Influence of Water Quality and Kind of Metal in the Secondary Cooling Zone of Casting Process

Dissertation

zur Erlangung des akademischen Grades

Doktoringenieur

(Dr.-Ing.)

vorgelegt von

M.Sc. Khalid Haroun Mohamed Abdalrahman

geb. am 17.06.1976

in Qena, Egypt

genehmigt durch die

Fakultät für Verfahrens- und Systemtechnik

der Otto-von-Guericke-Universität Magdeburg

Promotionskommission:

Prof. Dr.-Ing. Evangelos Tsotsas (Vorsitz)

Prof. Dr.-Ing. Eckehard Specht (Gutachter)

Prof. Dr.-Ing. Udo Fritsching (Gutachter)

Dr.-Ing. H. R. Müller (Gutachter)

eingereicht am: 03.07.2012

Promotionskolloquium am: 25.10.2012

Preface

I hereby declare that this submission is my own work and to the best of my knowledge it contains no materials previously published or written by another person, nor material which to a substantial extent has been accepted for the reward of any other degree or diploma at the University of Magdeburg or any other educational institution, except where due acknowledgement is made in the thesis. Any contribution made to the research by others, with whom I have worked at the University of Magdeburg or elsewhere, has been explicitly acknowledged in this thesis.

I also declare that the intellectual content of this thesis is the product of own work, except to the extent that assistance from others in the projects design and conception or in style, presentation, and linguistic expression is acknowledged.

Magdeburg, July 03, 2012

Khalid Haroun Mohamed Abdalrahman

This work is dedicated to ...
*The sweetest thing in the world-**ASMAA***

Khalid

Abstract

In the secondary cooling zone of the continuous casting of non-ferrous metals, the heat is transferred from the ingots using water sprays or water jets coming out of the mould. Unknown aspects of the heat transfer have been experimentally researched. Therefore, discs and sheets of different metals were heated in a furnace, removed and hung on a track in front of the quenching facility. The discs (140 mm diameter, 2-4 mm thickness) were cooled with a hydraulic nozzle with a constant impingement density of 3 kg/m^2/s. The sheets (length 140 mm, width 70 mm, thickness 2-4 mm) were cooled with a segment of a mould consisting of seven orifices with a diameter of 2.4 mm. The water jets of the mould impinge the sheets at an angle of 30^o. The temperature field of the back side of the samples was measured using an infrared camera. Therefore, the surface was coated with graphite in order to achieve a high emissivity. Its value was measured with dependence on temperature by using a specially calibrated device. The emissivity is about 0.9 and kept constant. The heat transfer was analyzed through two methods. In the first method, the temperature difference between both sides is neglected, because the Biot numbers are very small. The local heat transfer can then be calculated from a simple differential energy balance. In the second method, the temperature on the cooled side was calculated from the measured temperatures on the back side by using an inverse solution of the 2D Fourier differential equation. Both methods give similar results. In the film boiling region, the simple analysis is more suitable and in the nucleate boiling region, the inverse analysis is more suitable. In every method, the fluctuations of the originally measured temperatures, depending on time, require proper smoothing.

At first, the influence of the water quality was researched. For this, the deionized water was used as the reference water. This water was mixed with different typical additives. The addition of salts shortens the cooling time. The maximum heat flux, the DNB-temperature in the film boiling region, and especially the Leidenfrost temperature increase approximately linearly with the concentration. The salt $MgSO_4$ shows the strongest effect and the salt NaCl shows the weakest effect. The salts influence the electrical conductivity of the water because they dissociate. Therefore, for the salt mixture of real water, the electrical conductivity was found as a measurement to evaluate their cooling effect. Eight different waters which are commonly used in industrial process were tested. The cooling time of the discs varied within a factor of three. The maximum

heat flux, the DNB-temperature and the Leidenfrost temperature increase approximately linearly with the electrical conductivity for the real waters. The Leidenfrost temperature, for example, differs between the real water by 200 K. The pH value and the hardness of the water have no influence. The casting lubricant borax dissolves in water and increases the cooling rate. The casting lubricant graphite and carbon black have no influence. Neither dissolve in water. The surfactant which is used prolongs the cooling time. Dissolved CO_2 in the water prolong the cooling time and the gases O_2 and N_2 shorten the cooling time. The influence of the gases is comparably weak.

To research the influence of the kind of metal, discs of AA6082, nicrofer, nickel, inconel, pure copper (conductivity 385 W/m/K), copper alloy B14 (conductivity 118 W/m/K) and copper alloy L49 (conductivity 348 W/m/K) were cooled with the same conditions. The higher the heat penetration coefficient and the thermal diffusivity of metal, the lower the Leidenfrost and DNB- temperature. The copper discs formed an oxidized layer on the surface which splashed away during the cooling. Therefore, the heat transfer cannot be compared.

To research the influence of the surface roughness, samples with mean roughness values of 0.2, 1.7 and 7.7 μm and two samples of real ingot surfaces were used. A small increase of the roughness of about 2 μm prolongs the cooling. With a higher roughness, the cooling decreases. Real ingot surfaces with a high roughness have a significantly shorter cooling time and therewith, a high Leidenfrost temperature and heat transfer coefficient.

To research the quenching effect of the mould volume flow, the outflow water velocity was varied. The minimum velocity that the jets could impinge the sample was 0.9 m/s. The cooling time increased with higher velocities until a value in the range of 1.2 to 1.5 m/s and then the cooling decreased again. As a consequence, there is an optimum velocity for the highest cooling rate. This is the first time this effect has been researched and has not been reported in literature until now. The heat flux profile in the nucleate boiling region was analyzed. The range between the Leidenfrost temperature and the boiling temperature was defined as the range of the wetting front. This range increases with the flow distance and therewith, the maximum heat flux decreases. Due to of the opposite effects, the overall transferred heat in the wetting front range and therewith keep the wetting front velocity constant.

Zusammenfassung

In der Sekundärkühlzone beim kontinuierlichen Strangguss von Nichteisen (NE)-Metallen wird die Wärme mittels Wassersprays oder Wasserschleiern abgeführt. Noch nicht bekannte Einflüsse auf den Wärmeübergang wurden untersucht. Dazu wurden Scheiben und Platten aus verschiedenen Metallen in einem Ofen erwärmt und an Schienen hängend vor die Kühleinrichtung gezogen. Die Scheiben (Durchmesser 140 mm) wurden mit einer hydraulischen Düse mit einer konstanten Wasserbeaufschlagungsdichte von 3 kg/m^2/s gekühlt. Die Platten (140 mm Länge, 70 mm Breite, 2-4 mm Dicke) wurden mit einem Kokillensegment bestehend aus 7 Öffnungen mit einem Durchmesser von 2,4 mm gekühlt. Das Temperaturfeld auf der Rückseite wurde mit einer Infrarotthermokamera hochaufgelöst gemessen. Dazu wurde die Seite mit Graphit beschichtet, um eine hohe Abstrahlung zu erhalten. Der Emissionsgrad wurde temperaturabhängig mit einer kalibrierten Anlage gemessen. Der Wärmeübergang wurde mit zwei Methoden bestimmt. Bei der ersten Methode wurde die Temperatur über der Dicke der Probe als konstant angenommen. Der örtliche Wärmeübergang kann dann über eine einfache differenzielle Energiebilanz berechnet werden. Bei der zweiten Methode wurde der tatsächliche Temperaturverlauf auf der gekühlten Seite aus der inversen Lösung der zweidimensionalen Fourierschen Differenzialgleichung berechnet. Im Bereich der Filmverdampfung ist die erste Methode und im Bereich der Blasenverdampfung die zweite Methode besser geeignet.

Zuerst wurde die Qualität des Wassers untersucht. Hierzu wurde jeweils destilliertes Wasser als Referenz verwendet. Dieses Wasser wurde dann mit mehreren Zusätzen versehen. Die Zugabe von Salzen verkürzt jeweils die Kühlzeit. Die max. Wärmestromdichte, die DNB-temperatur (kritische Temperatur) und insbesondere die Leidenfrosttemperatur steigen linear mit der Konzentration an. Das Salz $MgSO_4$ hat den stärksten und NaCl den schwächsten Einfluss. Die Salze beeinflussen die elektrische Leitfähigkeit, da diese dissoziieren. Daher wurde für Salzmischungen die elektrische Leitfähigkeit als bestimmender Parameter für die Kühlwirkung ermittelt. Acht Wässer, die in verschiedenen Firmen zur Kühlung eingesetzt wurden, sind getestet worden. Die Kühlzeit der Scheiben variierte um den Faktor drei. Die max. Wärmestromdichte sowie die DNB- und Leidenfrosttemperatur steigen linear mit der elektrischen Leitfähigkeit an. Die Leidenfrosttemperatur z. B. schwankt bei den Wässern um 150 K. Der pH-Wert und die

Härte haben keinen Einfluss. Das Gieβhilfsmittel Borax verkürzt die Kühlzeit, da es in Wasser dissoziiert. Die Gieβhilfsmittel Grafit und Ruβ, die nicht dissoziieren, haben keinen Einfluss. Gelöstes CO_2 im Wasser verlängert die Kühlzeit, während O_2 und N_2 dagegen verkürzend wirken. Der Einfluss gelöster Gase ist vergleichsweise gering.

Um den Einfluss der Art des Metalls zu untersuchen, wurden Scheiben aus AA6082, Nicrofer, Nickel, Inconel, reinem Kupfer und zwei Kupferlegierungen mit sehr unterschiedlicher Wärmeleitfähigkeit unter sonst gleichen Bedingungen gekühlt. Je höher der Wärmeeindringkoeffizient und der Temperaturleitkoeffizient sind, desto niedriger sind die DNB- und die Leidenfrosttemperatur. Bei Kupfer bilden sich allerdings Oxidschichten auf der Oberfläche, die beim Kühlen abplatzen.

Um den Einfluss der Oberflächenrauigkeit zu untersuchen, wurden Scheiben mit 0,2, 1,7 und 7,7 μm Rauigkeit sowie Platten von realen Stranggussschalen aus Aluminium - Legierungen gekühlt. Kleine Rauigkeiten bis 2 μm verlängern die Kühlzeit. Erst bei höheren Rauigkeiten wird die Kühlzeit dann wieder verkürzt. Die realen Oberflächen weisen dagegen eine signifikant kürzere Kühlzeit und eine wesentlich höhere Leidenfrosttemperatur auf.

Zur Untersuchung der Kühlwirkung von Kokillen wurde deren Durchfluss und damit die Austrittsgeschwindigkeit variiert. Es zeigte sich, dass sich bei Geschwindigkeiten um 1,3 m/s ein Maximum in der Kühlwirkung einstellt. Die Profile der Wärmestromdichten wurden analysiert. Die Benetzungszone (Bereich von Siede-bis Leidenfrosttemperatur) steigt mit der Strömungslänge an, während die max. Wärmstromdichte abnimmt. Dadurch bleibt die Geschwindigkeit der Benetzungsfront und der dabei übertragene Wärmestrom konstant.

Acknowledgement

In particular, I wish to express my sincere appreciation to my supervisor, Professor **Prof. Dr.-Ing. E. Specht** for his continued encouragement and invaluable suggestions during this work. I would like to express my deep gratitude to everyone who helped me shape the ideas explored in this dissertation, either by giving technical advice or encouraging and supporting my work in many other ways. This dissertation would not have come into existence without their hands-on advice and motivation.

First of all, I am deeply indebted to my country **EGYPT** for accepting and supporting me to do my Ph.D. in Germany. As this Ph.D. was experimental in nature, it is most important to thank those personnel who helped and guided me in successfully performing those experiments. Dr. H. Woche made it possible to procure the required equipment as soon as possible and helped in communicating with machine shop personnel for building experimental set up. I am extremely thankful to him for his technical guidance. I would like to thank my friend Dr.-Ing. Umair Alam who is a part of my research work and who is helped me the technical aspects of executing experimental work in the lab. I would also like to thank Mr. R. Sühring, Mr. R. Timpe, Mr. D. Meinecke, Dipl.-Chem. M. Könnig and Mr. P. Fischer for providing technical help in building experimental set up. In spite of my below-average technical german language, I am so impressed by the fact that they used to understand all what I meant to say. I also thank Dr. J. Al-Karawi for providing the equipment for performing experiments. I would like to express my sincere thanks to Frau Christin Hasemann for helping me to solve the official issues and to handle the financial issues.

I always feel lucky to be with so many excellent researchers in my group. Thanks are due to all colleagues of my institute, who were always quite helpful during my stay. Thanks are due to all colleagues of my institute, who were always quite helpful during my stay. I am expressing my sincere gratitude to M.Tech. Gouri sankar, M.Tech. Koti Sunkara, M.Tech. Pavan Kumar, Dipl.-Ing. N. Lorenz, M.Sc. B. Hallak and M.Sc. Sabariman for their kind help in reviewing the text. I would like to thank M.Sc. Fabian Herz for helping me in some private things. In my daily work I have been blessed with a friendly and cheerful group of fellow students. I am thankful to my friend and group mate Dr.-Ing. Ashok Kumar Nallathambi who helped me in performing the numerical analysis and also discussed on many important aspects of this research. He also exposed me to

learn the modelling of quenching process. His systematic approach for the MATLAB programming is the basis for my work.

I am indebted to the personnel with whom I have worked on industrial project. Their advices and feedback has helped me to acquire an insight of the practical problems faced by industry. I am extremely thankful to Dr. H.R. Müller for reviewing and examining my thesis and his valuable advices in every project meeting. I thank Dr. H. Böttcher who has been a mentor and provided the Aluminum plates for performing experiments. I am grateful to Mr. P. Meslage and Mr. O. Siemon for their encouragement and full support. I am also thankful to Dr. W. Droste, Dr. E. Schmid, Mr. J. Buuren, Mr. H. Siewert for their keen interest in this project.

Khalid H. M. Abd Alrahman
Magdeburg, Germany

Table of Contents

Preface i

Abstract iii

Zusammenfassung v

Acknowledgement vii

Table of Contents ix

Nomenclature xi

1 Introduction 3
- 1.1 Problem definition . . . 3
- 1.2 Aluminum casting . . . 6
- 1.3 Copper casting . . . 7
- 1.4 Literature review . . . 10
  - 1.4.1 Wetting phenomenon . . . 10
  - 1.4.2 Spray cooling . . . 13
  - 1.4.3 Water qualities in casting process . . . 19
  - 1.4.4 Previous studies about surface morphology . . . 21

2 Experimental Works 23
- 2.1 Experimental setup . . . 23
- 2.2 Infrared system . . . 24
- 2.3 Emissivity . . . 26
- 2.4 High speed camera . . . 28
- 2.5 Samples . . . 29
- 2.6 Nozzles . . . 30
- 2.7 Mould (Array of jets) . . . 34
- 2.8 Mould movement mechanism . . . 34
- 2.9 Representative test . . . 39

3 Analysis Methods 41
- 3.1 Determination of Leidenfrost temperature . . . 41
- 3.2 Simple analysis of heat transfer . . . 41

3.3 Inverse analysis . . . 45
3.4 Measured data revision . . . 49
3.4.1 Methodology . . . 49
3.4.2 Calculated error of cooling rate . . . 52
3.4.3 Result analysis using revised data . . . 54
3.4.4 Effect of thermophysical property variations . . . 56

4 Water Quality **59**
4.1 Influence of single salts . . . 59
4.1.1 Magnesium sulfate ($MgSO_4$) . . . 59
4.1.2 NaCl, $NaHCO_3$, Na_2SO_4 and Na_2CO_3 . . . 62
4.1.3 $CaCO_3$ . . . 62
4.2 Casting lubricants . . . 63
4.2.1 Borax . . . 68
4.2.2 Graphite powder and carbon black . . . 68
4.3 Surfactant . . . 70
4.4 Mixtures of surfactant and dissolved matter . . . 70
4.5 Dissolved gases . . . 73
4.6 Water temperature . . . 76
4.7 Real waters . . . 76

5 Surface properties of metal **85**
5.1 Thermal material properties . . . 85
5.1.1 Temperature profiles . . . 85
5.1.2 Heat transfer . . . 90
5.1.3 Comparison with literature . . . 97
5.2 Surface Roughness . . . 99
5.2.1 Definition of roughness . . . 99
5.2.2 Roughness of disc samples . . . 100
5.2.3 Roughness of ingot samples . . . 102
5.2.4 Salt deposition . . . 103
5.2.5 Comparison with literature . . . 106

6 Heat transfer of mould jets **109**
6.1 Heat transfer mechanism . . . 109
6.2 Influence of initial temperature . . . 111
6.3 Influence of jet velocity . . . 111
6.4 Comparison with literature . . . 122

Bibliography **124**

A Appendix **135**

List of Publications **157**

Nomenclature

Symbols

A	[m^2]	Area
C_i	[mg/L]	Concentration of ionic
C_p	[J/kgK]	Specific heat
D	[m]	Diameter of the plate
d_t	[m]	Tube diameter
f	[-]	Force vector
f_i	[μS/cm]	Conductivity Factor
g	[m/s^2]	Gravitational acceleration
H	[m]	Width of the metal sheet
i	[-]	dissociation constant
K	[-]	Conductance matrix
K_b	[-]	Boiling point elevation constant
L	[m]	Length of the metal sheet
M	[-]	Capacitance matrix
$\dot{m}$	[$kg/m^2/s$]	Impinging density
m_{ml}	[mol/kg]	Salt molality
n	[-]	Previous time step
Q	[m^3/s]	Water flow rate
$\dot{q}$	[W/m^2]	Heat flux
$\tilde{q}$	[W/m^2]	Heat flux vector
r	[m]	Radius
R_a	[μm]	Arithmetical mean roughness
R_y	[μm]	Maximum peak
R_z	[μm]	Ten-point mean roughness
s	[m]	Thickness of the metal sheet

S	[-]	Instantaneous error norm
T	[^{o}C]	Temperature
t	[s]	Time
V	[m^3]	Volume
$\tilde{X}$	[-]	Sensitivity coefficient matrix
$\tilde{Y}$	[^{o}C]	Measured temperature vector
z	[m]	Distance between nozzle and metal sheet

Greek symbols

α	[W/m^{2}K]	Convective heat transfer coefficient
β	[kWs$^{0.5}$/m K]	Heat penetration coefficient
ϵ	[-]	Emissivity
ρ	[kg/m^3]	Density
θ	[^{o}C]	Temperature
θ_l	[^{o}C]	Liquidus temperature
θ_s	[^{o}C]	Solidus temperature
λ	[W/mK]	Thermal conductivity
σ	[W/m^{2}K^4]	Stefan-Boltzmann constant

Abbreviations

AA	Aluminum Alloy
BC	Boundary Condition
CCD	Charge Coupled Device
CGA	Conjugate Gradient Algorthim
CFD	Computational Fluid Dynamics
CHF	Critical Heat Flux
CT	Critical Temperature
DC	Direct Chill
DHCP	Direct Heat Conduction Problem
Di	Deionized
DNB	Departure from Nucleate Boiling
EC	Electrical Conductivity

FEM	Finite Element Method
FLIR	Forward Looking Infrared Radiometer
GDE	Governing Differential Equation
HF	Heat Flux
HTC	Heat Transfer Coefficient
ID	Impingement Density
IHCP	Inverse Heat Conduction Problem
IR	Infra-Red
LFP	Leidenfrost Point
LFT	Leidenfrost Temperature
MaxHF	Maximum Heat Flux
pH	Power of Hydrogen
pct	percentage
QWIP	Quantum Well Infrared Photo-Detector
TDS	Total Dissolved Salts
VDC	Vertical Direct Chill

Chapter 1

Introduction

1.1 Problem definition

Most non-ferrous (NF) metals are casted in the form of strands. For solidifying the strand, it must be cooled intensively using water as the coolant. The cooling methods depend on the kind of metal. Figure 1.1 shows schematically the cooling of Aluminum and its alloys. The shape and dimensions of the strand are predetermined by the mould. The mould is generally made of Aluminum or Aluminum alloy and cooling water flows through it. For copper casting, the copper moulds are lined with graphite coatings and for casting copper alloy, the moulds are made of copper or its alloys. The cooling of the strand within the mould is called the primary cooling. After emerging from the mould, the strand has a thin outer solidified layer, which must be sufficiently thick enough to prevent the break out of molten metal. The further cooling of the strand is performed

with the use of water which makes direct contact with the strand. The water from the primary cooling zone leaves the mould through the slots or holes. The cooling stage outside the mould is named as secondary cooling. Figure 1.2 shows the cooling water

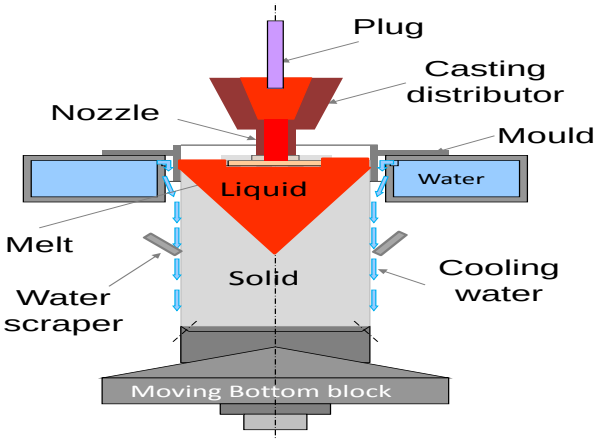

Figure 1.1: Schematic representation of the DC casting of aluminum ingots

Figure 1.2: Water exit from the mould

emerging out from the mould. The picture is taken with-out the strand, and the strand in fully solidified form is shown in Figure 1.3. In general, Aluminum billets are casted in a semi continuous method and copper and steel can be continuously casted based on the requirements. The secondary cooling process has a significant influence on the solidification microstructure, crack formation and thermal residual stresses. With the help of optimized secondary cooling, it is possible to minimize the thermal stresses, distortion, and hot cracks, which can improve the ingot quality. Therefore, it's highly important to characterize and study the secondary cooling in depth. In the continuous casting of copper alloys, the secondary cooling is independent of the mould. Below the mould, the strand is cooled by water sprays. Figure 1.4 schematically shows the arrangement of the nozzles. After spraying, the water runs down the strand again. The amount

of water from the individual nozzle can influence the cooling rate. The cooling system must be optimized in turn so that the surface remains free from cracks. Figure 1.5 shows a typical example of an edge crack, a cross crack and a center crack. With the introduction of the mathematical modeling of the continuous casting process in the operational practice, the exact description of the cooling process in the application of water on hot surfaces becomes indispensable. The combination of modeling and experimentation has contributed greatly to understanding the continuous casting processes. Operational ex-

periences and observations deliver some clear information that the specifically adjusted cooling water flow rates and the arrangements of cooling nozzles will improve the strand quality and reduce quality fluctuations. Therefore, there is a necessity to inspect the water quality and its influence on cooling rates. The results also showed that the direct relationship between the different water qualities and is not possible. Here, the question arises, what is the parameter, in which orders of magnitude at the operational cooling water treatment must be monitored and adjusted. For environmental reasons, nowadays, the cooling water is circulated and re-cooled by cooling towers. This leads to an increase in pollution of the water, e.g. dissolved salts, non-dissolved substance

Figure 1.3: Aluminum strand after casting (courtesy:NOVELIS INC.)

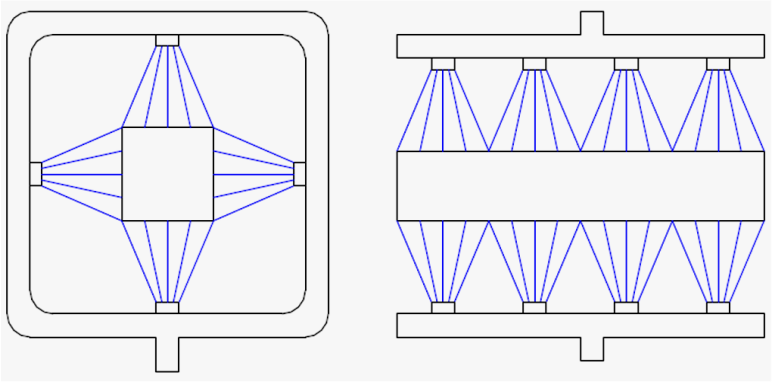

Figure 1.4: Nozzles register for secondary cooling of continuous cast copper

Figure 1.5: Typical cracks in the continuous casting of Copper alloys

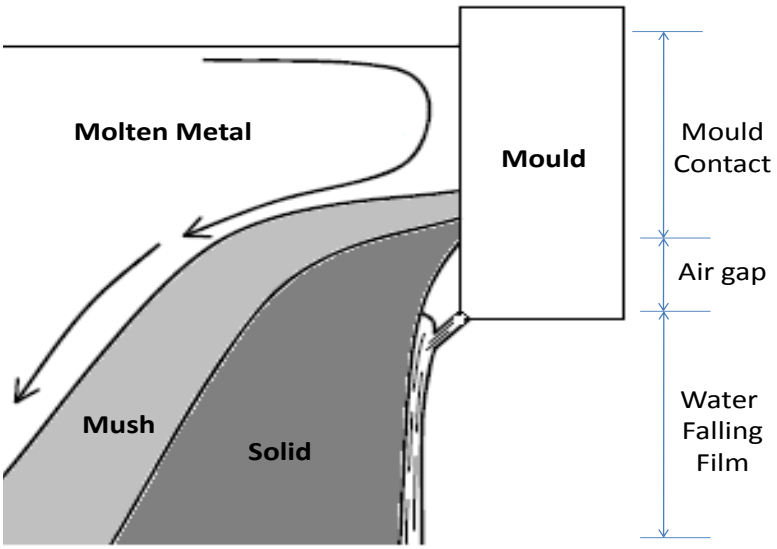

Figure 1.6: The three different heat transfer regimes commonly encountered in the DC casting process

and lubricants. In general, the pH, the value of electrical conductivity and hardness

are measured and monitored. The violation of the limits is prevented by replacement of subsets of the water. This monitoring does not have compliance with the cooling effect, but the goal is to protect the cooling system from corrosion. The main problem is that the effect of the various components and the quality of the water on the cooling effect is not well-known. Thus, there is no possibility to control the cooling effect and hence the quality of continuously cast metal. Therefore, no measures could be made to influence the quality of the cooling water. For the purposes of a more economical production by increasing the casting capacity without reducing the quality, the influence of the cooling water quality on the cooling rate must be examined.

1.2 Aluminum casting

During the continuous casting process, cracks and distortions in ingots can be found due to the non-uniform heat extraction rates. The accurate estimation of the heat transfer coefficients on the surface of the alloy is essential and useful in predicting the cracks during casting of metals. Generally, the surface of an ingot is divided into three different regions of heat transfer. The identification of the regions from the top to the bottom is as follows: the direct contact region with the surface of the mould, the air gap region between two surfaces, and the falling water film region. Figure 1.6 shows the three different heat transfer regimes. In the steady-state DC casting operation process, about 20 pct of the heat is extracted in the primary cooling, and about 80 pct is removed by secondary cooling water. In the secondary cooling zone, the water hits the hottest

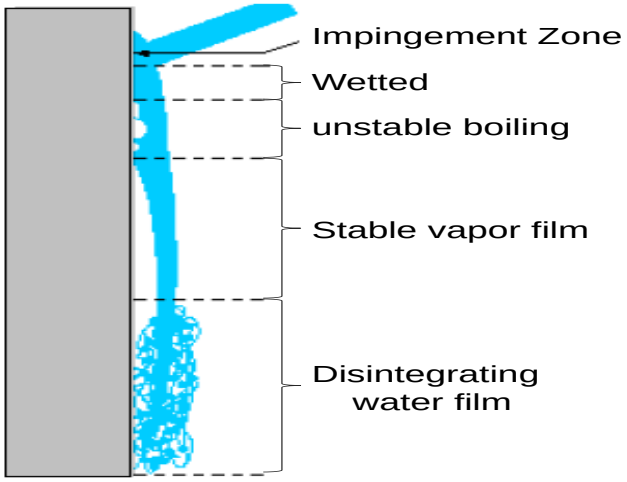

Figure 1.7: Structure regimes of the falling water

surface of the ingot and then forms a falling film down its surface. Water flows down the hot surface. Due to this, steam bubbles are rapidly swept away. A thin water vapor layer with low thermal conductivity, which prevents the heat flow from the hot surface, acts like an insulator. The cooling rate in this film boiling is comparatively low.

The moment that the ingot surface temperature falls below the Leidenfrost temperature, the vapor film collapses. When the film collapses, transition, nucleate boiling, and forced convection are the prevailing heat transfer mechanisms, during which the surface heat flux changes dramatically. While the cooling water flows along the length of the ingot, a thin wetting front, which separates the film boiling and nucleate boiling regions, moves continuously against the water flow direction with a velocity known as wetting front velocity. Vertically, the regimes of falling water film can be divided into impingement, wetted, unstable boiling, stable vapor film and disintegrating water film zone, as shown schematically in figure 1.7. The dimensions in the vertical direction of these regimes are not proportionally shown in the figure. The limits between different regions are schematically or qualitatively represented. In the unstable boiling regime, it is difficult for observing or visualizing the heat transfer phenomena because it is very narrow.

1.3 Copper casting

A copper strand leaving the mould is quenched directly by water sprays as shown in figure 1.8. The water droplets continuously impact the hot surface. Therefore, the secondary cooling contains different heat transfer phenomena in different regimes. The heat extraction by cooling water is governed by the phenomena of water boiling, which depends strongly on temperature. As shown in Figure 1.9, four heat mechanisms can

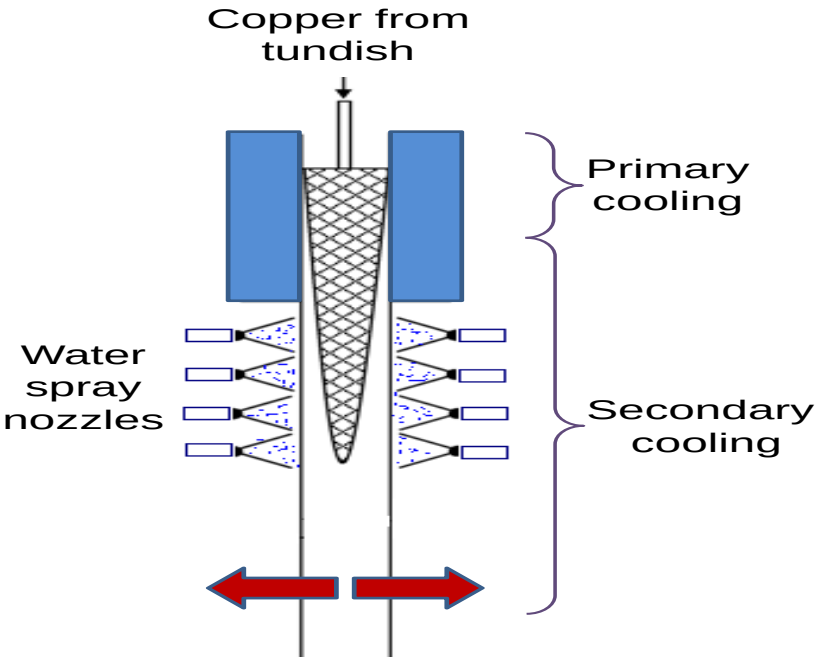

Figure 1.8: Schematic cooling processes for continuous casting of copper

be characterized when the water touches the a hot metal surface [1]. The heat transfer mechanisms are classified based on the surface temperature of the strand in the following way:

1. The film boiling regime, where the temperatures are higher than the Leidenfrost temperature.

2. Transition boiling, where the water bubbles start collapsing. In this regime, the heat transfer increases rapidly with decreasing surface temperature. When the metal surface is fully uncovered by vapor film, the heat transfer value reaches a maximum, which is referred to as the burnout temperature.

3. Nucleate boiling regime, which is located between 100 ^oC and CHF point. As the surface temperature goes down, the intensity of air bubbles continues to decrease. The nucleate boiling decreases until the surface temperature drops below the boiling point of water.

4. Convective heat at temperatures below 100 ^oC.

Experiments have been conducted to evaluate the heat transfer to the cooling water and to obtain the so-called boiling curves. Most of the empirical relationships are developed by the application of inverse analysis to the experimental measurements. The measured temperature data is recorded by thermocouples fixed in the metal surfaces.

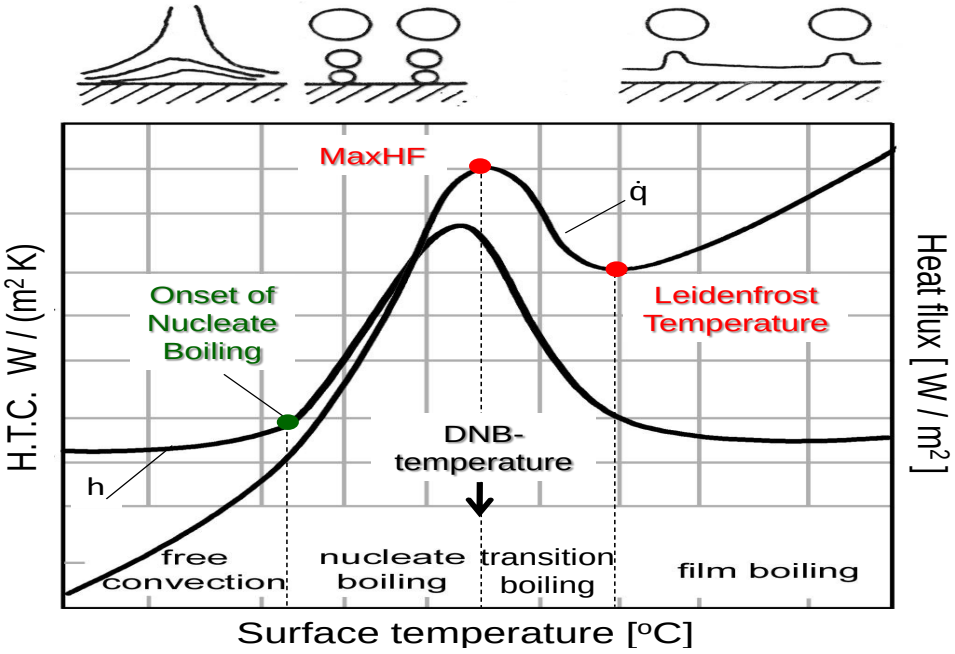

Figure 1.9: Boiling curve for water cooling indicating the different heat transfer regimes

Opstelten and Rabenberg [2] presented an empirical correlation for the heat flux as

$$\begin{aligned} q &= 27.3 \times 10^3\ \theta - 1.27 \times 10^6 \quad if \quad \theta < 120^oC \\ q &= 94.3 \times 10^3\ \theta - 9.24 \times 10^6 \quad if \quad 120^oC \leq \theta < 150^oC \\ q &= 12.3 \times 10^3\ \theta + 3.06 \times 10^6 \quad if \quad \theta \geq 150^oC \end{aligned} \tag{1.1}$$

In 1982, Weckman and Niessen [3] proposed the following correlation for estimating the nucleate boiling HTC in the free falling region as,

$$h(\theta) = \left(-1.67 \times 10^5 + 704\ \bar{\theta}\ \right) \left(\frac{Q}{\pi D}\right)^{1/3} + \frac{20.8}{\theta - \theta_{ref}} \left(\theta - 373.15\right)^3 \tag{1.2}$$

where θ represents the billet surface temperature in Kelvin, θ_{ref} is the bulk cooling water temperature in Kelvin, $\bar{\theta}$ $(= 0.5(\theta + \theta_{ref}))$ is the mean temperature in Kelvin, Q is the water flow rate in m^3/s, and D is the billet diameter in meter. The first term in Eq. 1.2 accounts for convective heat transfer due to the one-phase free falling turbulent film of water. The second term, which is taken into account only when $\theta > 373.15$ K, models the subcooled nucleate boiling. Sengupta et al. [4] extensively studied the secondary regime in the Aluminum DC casting process and compared it with the continuous casting of steel. Mortensen [5] presented a model for the time dependent heat and fluid flows during aluminum DC casting, where the aluminum alloy AA1050 was used. They used a constant heat transfer coefficient of 30000 W/m^2K in the model. Wiskel [6] studied the secondary cooling of AA5182 alloy to estimate HTC. An empirical co-relation is presented for HTC as a function of surface temperature. The boiling curves for the value of Maximum Heat Flux (MaxHF) and Leidenfrost points will differ due to the

differences in thermophysical properties of the metals, as well as surface effects such as surface roughness and oxide layers [7].

1.4 Literature review

1.4.1 Wetting phenomenon

Wetting front phenomenon can be located in many manufacturing processes which involves quenching, continuous castings and extrusions [8], [9], [10]. The wetting phenomenon occurs when the hot metal surface, that is initially covered with vapour film, becomes wetted with liquid film. So, the wetting is related to nucleate boiling, which considers direct cooling water contact with the portion of the metal surface. Hence, the knowledge of the wetting front and wetting velocity are important for the design and control of quench-based industrial processes. Ueda et al. [11] identified the wetting front position as the location at which the heat flux begins increasing sharply with decreasing surface temperature. Three different regimes exist on the hot surface undergoing a wetting process: (1) the film boiling regime, where water and the hot surface are separated by a vapor film, (2) the transition regime, and (3) the wetted regime [12]. The rewetting temperature can be defined as the temperature at which a transition occurs from the film boiling regime to the wetted regime. The rewetting temperature is essential to characterize the boiling regions in quenching processes. Carbajo [13] summarized the parameters that affect the rewetting temperature.

In order to clarify some further terms for discussing the quenching phenomena, the Figure 1.10 has been constructed. It shows the surface temperature and heat flux distribution during atomized spray quenching. The image was obtained from a high speed camera. From Figure 1.10, it is clear that the spray water covers up to 30 mm from the center of the disc. This 30 mm area of radius is usually named the wet zone. The visible area which lies to the outer of the wet zone is termed as the wetting front. The temperature gradient in this regime is very high and the position of the MaxHF also belongs to this regime. The influential parameters are cooling water velocity, material of the surface, and surface conditions. Both the material of the surface and its thickness affect the film boiling temperature [14]. A material, which has a high thermal conductivity, is able to supply high heat rate and delay the vapor film collapse to lower surface temperatures. Correspondingly, the lower heat fluxes have been measured for thinner materials. The combination, $\lambda\rho c$, of thermophysical properties has been designated as a heat penetration coefficient [15]. The heat penetration factor, $\sqrt{\lambda\rho C_p}$, can be used to verify the heat transfer to the water/metal interface.

Although the term Leidenfrost is used, it should be noted that the Leidenfrost temperature has special implications. Delhay et al [16] defined the Leidenfrost temperature

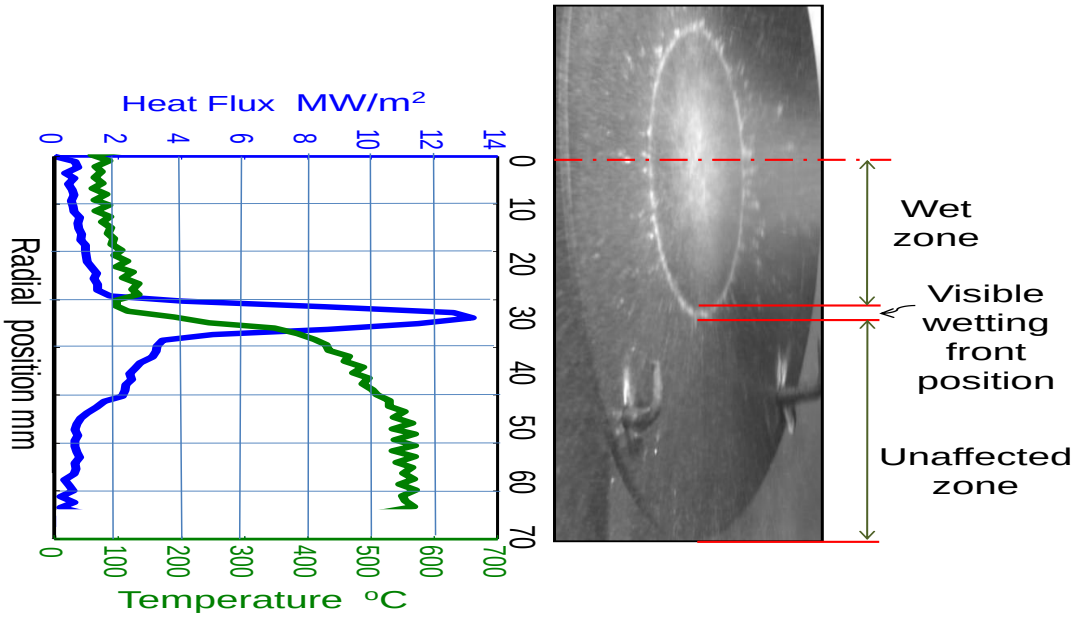

Figure 1.10: Surface temperature and heat flux distribution during atomized spray quenching

as the maximum temperature at which a water droplet floating on a vapor cushion eventually collapses and contacts the hot surface. Elias and Yadigaroglu [17] reported that the Leidenfrost rewetting temperature or the rewetting temperature is usually defined as the temperature at which a droplet eventually wets a hot surface. A large number of experimental and analytical studies on rewetting phenomena in various modes have been carried out during the last three decades and the important studies are tabulated in Table 1.1 [18]. From these studies, the fundamental concept of the main characteristics of rewetting phenomena (rewetting temperature, rewetting velocity and MaxHF) are mentioned here briefly along with a historical review which can provide necessary information to understand the rewetting phenomena.

Many investigations about the Leidenfrost point have been qualitative and used various correlations for predicting the Leidenfrost temperature. Baumeister and Simon [35] developed a semi-empirical expression in terms of the thermophysical properties of the heated surface. The semi-empirical expression is

$$T_{Leid} = T_f + \frac{0.844T_c\left\{1 - exp\left(-0.016\left[\frac{\left(\frac{\rho_s}{A_t}\right)^{1.33}}{\sigma_f}\right]^{0.5}\right)\right\} - T_f}{exp\left(3.066 \times 10^6\beta\right) erfc\left(1758\sqrt{\beta}\right)} \tag{1.3}$$

where,

$$\beta = \frac{1}{\lambda_s \rho_s c_{p,s}} \tag{1.4}$$

Table 1.1: Literature review of experimental studies on rewetting phenomena [18]

Authors	Temp.	Material	Liquid	Test section	Dimension (mm)	Quenching
Yoshioka et al. [19].1970	400	Stainless steel	Water	Tube	1 Thick, 13 O.D, 400 L	Top flood
Iloeje et al. [20].1975	382	InconelX750	Water	Tube	12.5 I.D, 13 O.D, 102 L	Bottom flood
Mitsutsuka et al. [21].1979	930	Carbon steel	Water	Plate	20 Thick, 200 Wide, 400 L	Top flood
Dhir et al. [22].1981	1127	Stainless steel	Water	Tube	0.88 Thick, 110 D, 12000 L	Bottom flood
Kokado et al. [23].1984	850	Stainless steel	Water	Plate	10 Thick, 200 Wide, 200 L	Jet
Lee et al. [24].1985	450	Stainless steel	Water	Tube	12 I.D, 16 O.D, 400 L	Bottom flood
Bamea et al. [25].1994	400	Inconel600	Water	Tube	44.8 I.D, 54 O.D, 800 L	Bottom flood
Mudawar et al. [26].1994	400	Aluminum	Water	Block	60 W, 120 H, 120 L	Spray nozzle
Filipovic et al. [27].1995	700	Copper	Water	Plate	25.2 Thick, 38 Wide	Jet
Kumagai et al. [28].1995	390	Copper	Water	Block	20 W, 120 H, 150 L	Jet
Ciofalo et al. [29].1999	300	Copper	Water	Slabs	1.1 W, 40 H, 50 L	Spray nozzle
Hall et al. [30].2001	650	Stainless steel	W + Air	Cy. block	107 D	Jet
Mitsutake et al. [31].2001	250	Copper, Brass	Water	Cy. block	89 D, 60 H	Jet
Liu et al. [32].2001	1000	Stainless steel	Water	Plate	2 Thick, 12 Wide, 12 L	Jet
Cui et al. [33].2003	240	Copper	W + Salts	Cy. block	25.4 D	Spray nozzle Jet
Jia et al. [34].2003	160	Copper	Water	Cy. block	10 D	Spray nozzle

Generally, the measured LFP temperature corresponds to the solid surface. To be more precise, it is better to calculate the LFP corresponding to the interface temperature (temperature of the liquid-solid). The LFP temperature is often lower than that measured by solid surface temperature within several degrees. During the droplet-surface contact, the interface temperature is dictated by the thermophysical properties of the liquid and solid. Eckert and Drake [36] used this interface temperature to solve the one-dimensional energy equation.

$$T_i = \frac{(\lambda\rho c_p)_s^{0.5} T_s + (\lambda\rho c_p)_f^{0.5} T_f}{(\lambda\rho c_p)_s^{0.5} + (\lambda\rho c_p)_f^{0.5}} \tag{1.5}$$

The discrepancies in these reported values arise from differences in the size of the liquid mass, the method of liquid deposition, the amount of liquid sub-cooling, solid thermal properties, surface material and finishing, pressure, and the presence of impurities. These parameters and their observed effects on the LFP are summarized in Table 1.2, along with the corresponding references [37].

1.4.2 Spray cooling

Most of the industrial spray applications involve complex phenomena and many operating parameters. The analytical modelling of spray cooling is not sufficient to understand interactions between the spray cooling and surface. Experimental studies are often chosen as the method used to estimate the thermal behaviour of a spray cooling effect on a heated surfaces [60] and [61]. Spray cooling is characterized by factors such as spray nozzle types, uniformity of heat removal, small droplet impact velocity (impingement density) and temperature limits. The mechanism of heat transfer during spray cooling is a highly complicated one, due to the interdependence of various parameters. Spray cooling dynamics have been experimented and investigated by many researchers. Pedersen and McGinnis [62] reported that the heat transfer from the hot surfaces directly depends on the droplet diameter and its velocity. The effect of the Weber number on heat transfer has been studied by Choi and Yao [63]. Sozbir et al. [64] pointed out that as the droplets quench the surface with high momentum, the increase in the impingement density of the spray increases the Leidenfrost temperature.

Müller et al. [65] presented the variation of the Heat Transfer Coefficient HTC with surface temperature for nickel. They investigated different values of the impingement density. In Figure 1.11, the parameter is the impingement density, which indicates how much liquid reaches the hot solid per unit of time and area. They found that a higher impingement density led to a higher HTC at a similar surface temperature point, either in the film boiling or the transition region. However, in the film boiling region, for the same impingement density they found that HTC is independent from surface temperature. Therefore, in this region, it can only be influenced by the impingement density. Other parameters, such as drop velocity, distance from nozzle to surface, and

Table 1.2: Summary of the influential LFP parameters [37]

Parameters	Observations/References
Droplet size	*LFP independent of droplet size [38], [39] *LPF increased with droplet volume [40]
Liquid deposition	*LFP differed between steady state drop size technique using a pipet and the transient sessile drop technique [41] *LFP increased with droplet velocity [39], [42], [43], [44] * LFP did not differ between sessile and impinging drops [45], [40]
Liquid subcooling	*Liquid subcooling had little effect on LFP for water on polished aluminum, brass, and stainless steel, but did cause an increased LFP on Pyrex [46] *Subcooling increased drop lifetime but did not influence the LFP [47] *Subcooling raised the LFP for water and other fluids at high pressures where both sensible and latent heat exchange are significant [48]
Thermal properties	*LFP increases as solid heat capacity decreases [39], [46], [40] *Baumeister et al. [46] developed a LFP correlation accounts for solid thermal properties *LFP independent of solid thermal diffusivity [48]
Surface conditions	* Gottfried et al. [38] estimated that the vapor layer beneath a film boiling sessile water drop was on the order of 10 microm, which is on the same length scale as surface. Thus, rough surfaces in comparison to polished surfaces would be expected to require a higher LFP to support a thicker vapor layer. *LFP increased as surface roughness and fouling increased [46] *LFP increased with increasing surface porosity [49] *LFP decreased with increased advancing contact angle in pool boiling [50], [51], [44], and [52]
Pressure	*LFP increased with pressure for various fluids [53], [47], and [54] (T_{leid} - T_{sat}) found to remain constant for various pressures [47], [40], and [55] * [56] et al. reported similar findings for four inorganic fluids * Rhodes et al. [57] observed (T_{leid} - T_{sat}) for Freon-114 to be constant over a reduced pressure range of 0.125 to 0.350 and found it to decrease with increasing pressure above this range
Water quality	* C. K. Huang et al. [58] found that the dissolved salt increases the Leidenfrost * Higher concentration of salt increases the Leidenfrost temperature [59], * [33] et al. reported that, the dissolved salts increased the Leidenfrost temperature in spray cooling by preventing bubble coalescence and producing particles which increase surface roughness

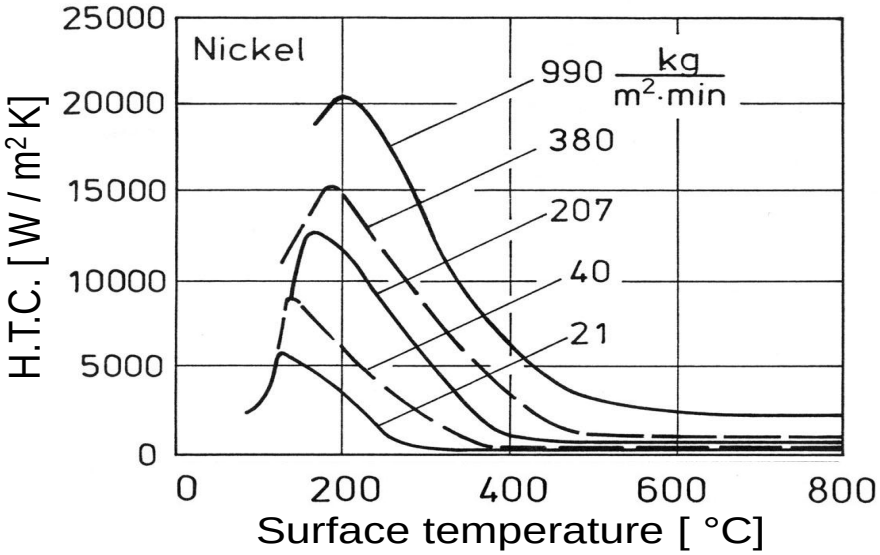

Figure 1.11: Heat transfer coefficient for spray quenching as a function of surface temperature and impingement density [65]

nozzle type, are not required to be considered separately, as they are contained in the impingement density [66], [67].

Müller et al. [65] also showed the characteristics of HTC over surface temperature for different types of materials, as shown in Figure 1.12. They compared four types of samples from Copper, Aluminum, Brass, and Nickel and used $\dot{m} = 120$ (kg/m^2.min) as the impingement density in this case to make the comparison. They found that Copper has the highest value, while Nickel has the lowest value. From two material types of interest, Aluminum and Nickel, they showed that Aluminum has a higher HTC than Nickel. However, for the Leidenfrost temperature, Nickel has the higher value compared to Aluminum.

As the impingement density is the only variable controlling the heat flow in the range of stable film boiling, the local distribution of the impingement density is of particular importance. In industrial practice, two fluid nozzles, i.e. water-air nozzles, are used. The addition of air as a second quenching medium serves mainly to influence the nozzle characteristics. The cooling effect of these nozzles is, however, determined only by the magnitude of the impingement density as shown in Figure 1.13 [68], [69].

Müller et al. [65] also presented the correlation between Leidenfrost temperature and impingement density. In this case, they used Nickel, Brass, Copper and Aluminum samples for the study. They concluded that the heat flow in the range of partial film boiling depends not only on the impingement density, but also on the type of metal. This influence can be described by the coefficient of heat penetration ($\sqrt{\lambda \rho C_p}$). Figure 1.14 shows the dependence of the Leidenfrost temperature for two metals. Their result

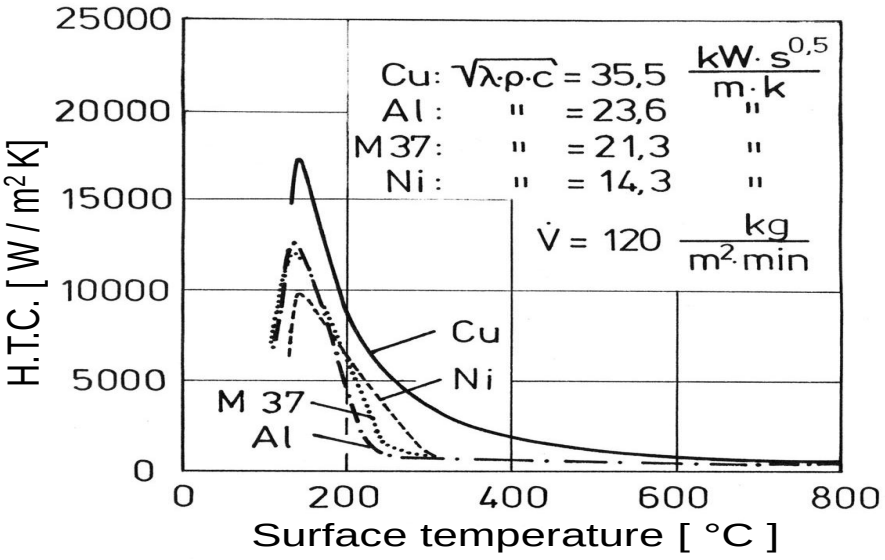

Figure 1.12: Heat transfer coefficient for spray quenching as a function of surface temperature and kind of metal [65]

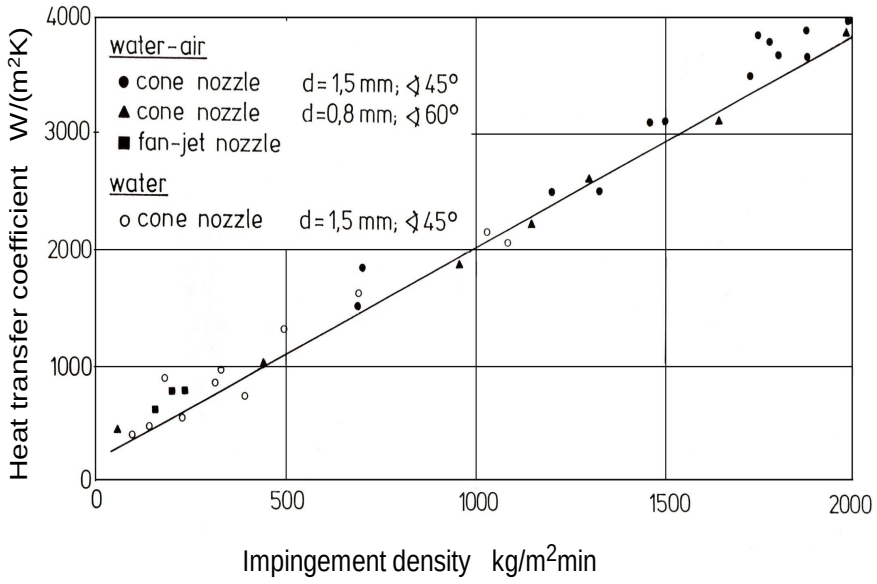

Figure 1.13: Heat transfer coefficient in the range of film boiling for spray quenching with water as a function of the impingement density [68], [69]

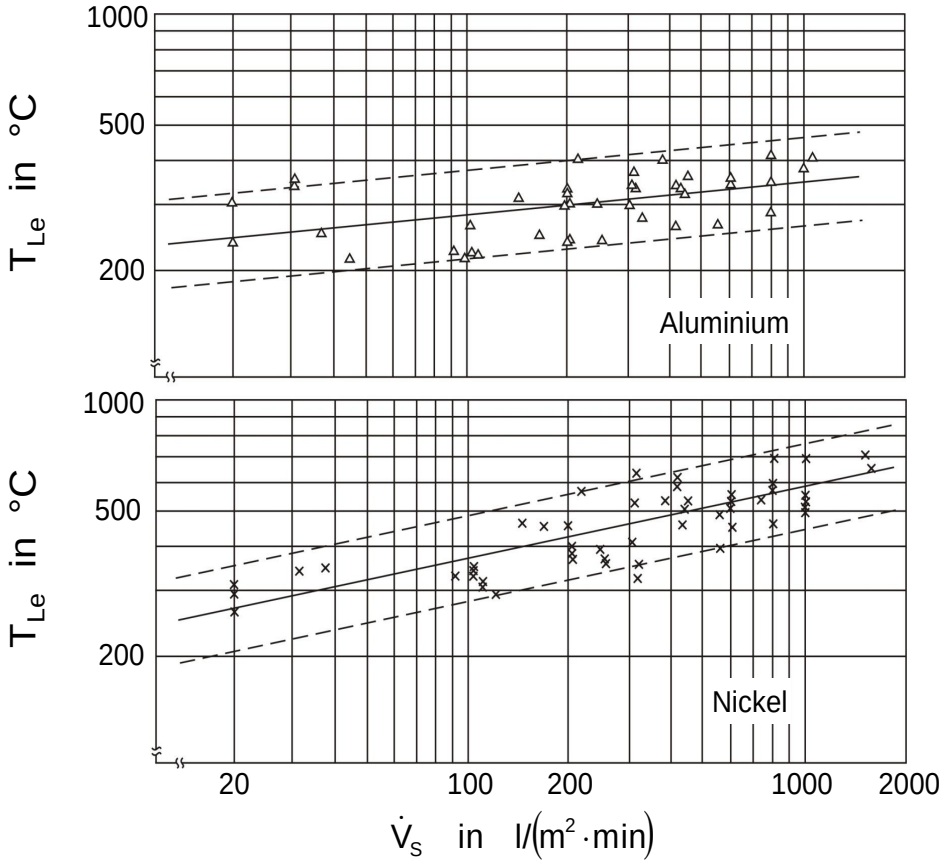

Figure 1.14: Leidenfrost temperature as a function of the impingement density for aluminum and nickel [65]

showed that both materials have a similar trend, the higher impingement density, the higher Leidenfrost temperature. From the same figure, we can easily conclude that at the same impingement density, Nickel has a higher Leidenfrost temperature compared to aluminum. To calculate the coefficient of the heat penetration, it must be taken into account that the material values at the surface are decisive. For Copper in particular, an oxide layer always forms at the surface in which $\sqrt{\lambda \rho C_p}$ contains considerably smaller values than in the metal itself.

The cooling of different metals and alloys were tested and investigated experimentally by many researchers. Shimada and Mitsutsuka [70] presented an experimental relation to describe and predict the heat transfer coefficient during spray cooling. They used similar nozzles to those which are used in the secondary cooling of the casting process. The experiments of the two different metals, such as steel and Aluminium, were tested by Sengupta et al. [4]. The results show that the maximum and minimum heat flux values for aluminum (380 ^oC and 200 ^oC) are at much lower temperatures than for steel (1000 ^oC and 600 ^oC), as shown in Figure 1.15.

The quenching experiments of 7055 alloy plate samples were made by Yu [71] at two

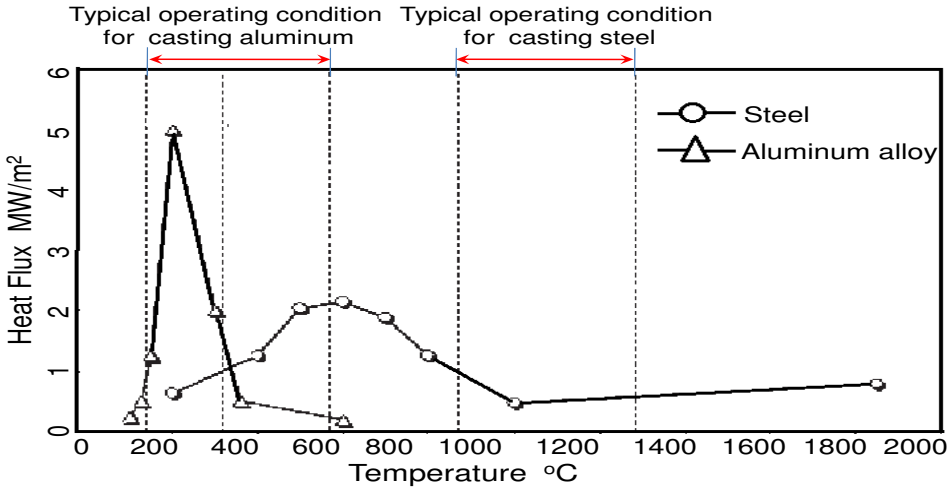

Figure 1.15: Typical boiling curves and operating temperature ranges in the secondary cooling regime for continuous casting of Steel and DC casting of Aluminium [4]

different operating conditions (cooling water with an oxidization inhibitor and cooling water without an oxidization inhibitor). The measured heat flux values show that the heat flux of the quenched sample by water with an oxidization inhibitor is higher than that of water without an oxidization inhibitor. Recently, a multi nozzle arrangement was investigated to calculate the heat transfer coefficient. Horizontal spray nozzle performance was studied to estimate the heat flux by Choi and Yao [72]. The maximum value of heat fluxes up to 2 MW/m^2 were calculated for a hot surface of 150 ^oC, and the Leidenfrost point was 250 ^oC.

Mizikar [73] studied the stainless steel plate samples cooled by three full-cone nozzles with an impingement density of up to 19 kg/m^2/s. The calculated heat transfer coefficients were found to be very linear with impingement density, as shown in Figure 1.16. In Mizikar's study, the angle of spray was mentioned and concluded that the influence of spray angle on heat transfer rate can be neglected. However, Ciofalo [29] reported much higher values of heat transfer rate at the same impingement density. More recently, Al-Ahamdi and Yao [74] used a cylindrical stainless steel plate. They observed the dependence of heat flux on impingement density. Many of researchers conducted experiments on spray cooling in metal casting and metal rolling. Most of these studies concentrated on operating parameters and atomized spray effects. Tseng et al. [75] tested a Steel roll cooling system and examined its roll life by combined methods (experimental and numerical methods). The values of heat transfer coefficients during that test were measured experimentally and then compared with a numerical simulation of the rolling processes. Horsky et al. [76] evaluated the heat fluxes on Steel plate samples. The plate is heated up to 620 ^oC and cooled by water spray nozzles.

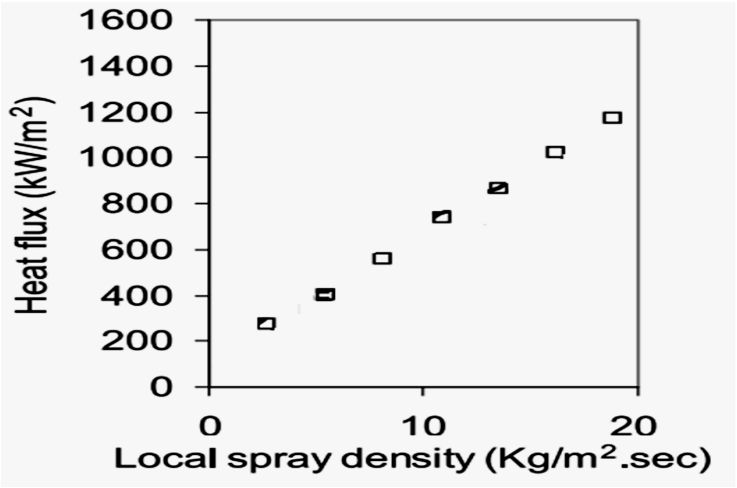

Figure 1.16: Heat flux of stainless steel versus local spray density [73]

The water pressure of the nozzles is considered to be another important operating parameter during the experiment. Bariani et al. [77], [78] presented an experimental and finite element simulation for estimating the heat flux during the cooling and deformation phases in the hot metal process. In Bariani's study, an inverse method is used to calculate the effect of impingement density and supply pressure to nozzles on the heat transfer coefficient. The results also have been compared between two different sprays: upward spray and downward spray. From the metallurgical point of view, the influence of cooling water quality during quenching processes has an important role. Water spray cooling can be found in various fields, such as air- conditioning and ventilation, protecting buildings from fire, painting walls and surfaces, combustion engines, and quenching hot surfaces, etc. Perhaps the most important application is the last one (metal quenching), which is discussed in this research. Most of the aluminum, steel, and other metal manufacturing industries apply spray cooling in the secondary cooling region.

1.4.3 Water qualities in casting process

In the three-phase system (water, solid surface, vapour), the interfacial tension force plays a significant role on the boiling phenomena, which is associated with the secondary cooling. Particularly, the propagation of the triple contact position (where the three phases meet) identifies the duration and the size of the wet contact region on the hot surface. The propagation of the wet zone strongly affects the heat flux in the transition boiling regime [79]. The surface tension and wetting front propagation of the cooling water can be varied with the addition of dissolved solids or oil, which can affect the water quality on the secondary cooling [80]. The influence of water quality is especially important when recirculation systems of the cooling water include lubricants, dissolved salts, water treatment chemicals, and solid particulates. These contents can accumulate in the cooling water cycle [81].

Castor oil is used in the DC casting process as a lubricant for the mould to prevent the ingot surface from tearing. The lubricant mixes with the cooling water and forms emulsion (water and oil mixture) [81]. Bergstrom found that the oil in the cooling water decreases the Leidenfrost point and thus the film boiling regime expands [82]. The concentration of lubrication oil in the coolant strongly affects the heat extraction rate [83]. The higher concentration of oil decreases the heat extraction rate and the bubble formation becomes the determining factor in the heat transfer mechanism [84]. They used a hot Aluminum block (slug) to examine the effect of water quality by placing the slug in front of a water spray in the mould. They found that the increase of solids concentration in the water reduces the cooling rate. Further, the oil concentration reduces the cooling rate significantly when it is above 10 ppm. Hamilton and Chen [85] immersed an Aluminium block into water. The block sample has dimensions of 200 mm long and 75 mm square cross-section, and it is heated to 460 ^oC. The results are consistent with Langlais et al work [83].

A surface tension lowering surfactant is often used to disperse the oil from the cooling water cycle. The surfactant promotes the bubble formation, thus the Leidenfrost temperature decreases dramatically and the heat transfer decreases also in the transition boiling region [81]. The cooling rate is higher when the water contains dissolved solids when compared to the deionized water. Grandfield et al. [86] studied the effect of various combinations of additives on the boiling curves. Grandfield found that some dissolved solids, such as NaCl and $CaCO_3$, increase the Leidenfrost temperature and promote the nucleate boiling over film boiling. The results showed that the water quality affects the critical heat flux, convection region, and nucleate region. The results also concluded that the difference in heat flux in the convection and nucleate regions is very small, but the difference in critical heat flux is large.

Ions can also be meaningfully introduced in the cooling water system during the quenching process. The *cations* (positively charged ions) such as Fe^{+3}, Al^{+3} and organic cationic polyectrolytes, reduce bubble adhesion and slightly increase the critical heat flux. The *anions* (negatively charged ions) promote the adhesion of bubbles, causing the Leidenfrost temperature to significantly lower. The critical heat flux also decreases [81]. The effect of the low concentrations, e.g. below 100 ppm, can be neglected [83]. The suspended solids, which are not dissolved in the cooling water and remain in the form of particulates, can promote the film boiling and increase the heat flux in the nucleate boiling regime [85].

The chemical treatment of the cooling water maintains the cleanliness and the quality of the water. As a result, the water quality becomes an important influencing factor on the heat transfer during the DC casting process. Ho Yu [87] quenched a hot aluminium block sample to show the effect of various additives on the heat transfer rate. Ho Yu found that the surfactant and the dissolved castor oil reduces the boiling heat transfer.

The results also indicate that the heat transfer rate can be increased by the addition of inorganic cations, whereas the heat transfer rate can be reduced by the presence of suspended solids.

1.4.4 Previous studies about surface morphology

Many experimental and industrial measurements have been investigated to quantify the heat transfer in the secondary cooling region during casting. Weckman and Niessen [3] quantified the heat transfer to model the heat transfer in DC casting. Watanabe and Hayashi [88] added further improvements to understand the heat transfer that occurs in the secondary cooling zone. They differentiated between the heat transfer magnitude that occurs at the water impingement point and the falling zone.

Some researchers have mentioned the importance of surface morphology on the heat transfer. However, no literature correlates the properties of the surface with the heat transfer during the DC casting process. However, some studies have been done to investigate the effect of the roughness during spray cooling. Berenson [89] measured the heat flux of two different copper alloys with different roughness. Berenson found that the increase of surface roughness shifts the nucleate boiling curve to the left.

Bui and Dhir [90] showed the effect of the roughness on Copper surfaces to the heat transfer during the nucleate and transition regions, as shown in Figure 1.17. The results are consistent with Berenson's work. However, in the transient region, the smooth surface produced a higher heat flux than the rough surface. Rammilison and Lienhard [52] conducted the experiments by using acetone on a Copper surface to show the effect of roughness on the heat transfer coefficient. They found that the heat transfer coefficient is significantly increased with the increase of the roughness in the nucleate boiling. It should be noted that the rough surfaces used in the experiments are only a few micrometers in difference, whereas the surface roughness of cast aluminium alloys can vary by many millimetres.

Wiskel [91] found that the heat flow varies significantly during the start-up phase of the DC casting process and related this variation to the difference in ingot surface morphology. The surface morphology observed near the ingot bottom is lapped and the surface morphology near the top is liquated. Based on the literature review, the influence of casting parameters (e.g., withdrawal rate and pour temperature), water properties (e.g., flow rate, temperature and quality) and ingot parameters (e.g., surface morphology) on the heat transfer to the ingot in the secondary cooling regime is extremely complex and difficult to rationalize experimentally. The water cooling rate and the temperature of the hot metal surface at the water contact point can change the ingot surface morphology, thus influence the heat extracted during the secondary cooling.

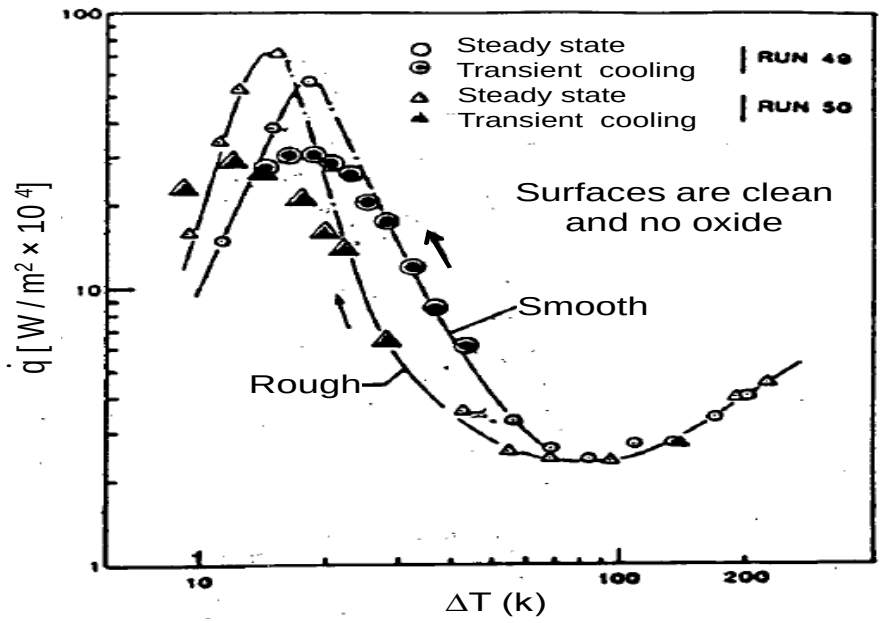

Figure 1.17: Effect of surface roughness on nucleate and transition boiling [90].

All of these studies show that the change in the surface morphology can have a significant effect on the heat transfer at a given surface temperature and also changes the shape of the boiling curve. These studies motivate the need to understand the heat transfer during the spray cooling for microelectronics and other material processes.

Chapter 2

Experimental Works

2.1 Experimental setup

Experimental set up is shown schematically in Figure 2.1. The experimental setup was constructed to analyze the influence of significant parameters on the heat transfer during the cooling of flat metal samples. It consists of a furnace, a cooling component e.g. a pneumatic atomizing nozzle (Lechler-156.35.13) or a hydraulic full cone nozzle or a mould with 7 or 8 orifices, an infrared camera FLIR SC3000, and metallic sheet samples of 2 or 3 mm thickness. At first, the metal sample is heated up by an electrically heated furnace to a temperature of 600 ^{o}C. This temperature can be adjusted according to the requirement. For example, if the sample is nickel, it can be heated to 800 ^{o}C, while in the case of Aluminum and its alloys, the set temperature is not more than 520 ^{o}C. Next, the sample is shifted to the cooling unit, where it is sprayed by an atomized spray, a hydraulic spray or an array of jets, depending on the method of quenching.

The water flow rate, pressure and air pressure are also adjusted according to the current objective of the experiments. The front side of the sheet is polished while the rear side is painted with black graphite paint in order to achieve an emissivity of 0.9. The surface temperature of the rear side is measured by an InfraRed(IR) camera. This IR camera has the capability of measuring the temperature with a frequency of 150 Hz within a window of 240 $\times$ 80 pixels. The temperature at every pixel can be measured. The distance between the two consecutive pixels is around 0.9 mm. The experiments are repeated with different concentrations of salts solutions, surfactant solution, deionized water, impingement densities and jet velocities.

From the infrared camera, the recorded data is saved in the computer. The parameters which influence the IR thermography are the emissivity of the surface, the ambient temperature, the relative humidity and the distance between the lens and measured surface. For the cooling by an array of jets, a metal sample with a rectangular shape is used and for the spray nozzle, a circular shape is used. However, in these two cases, the

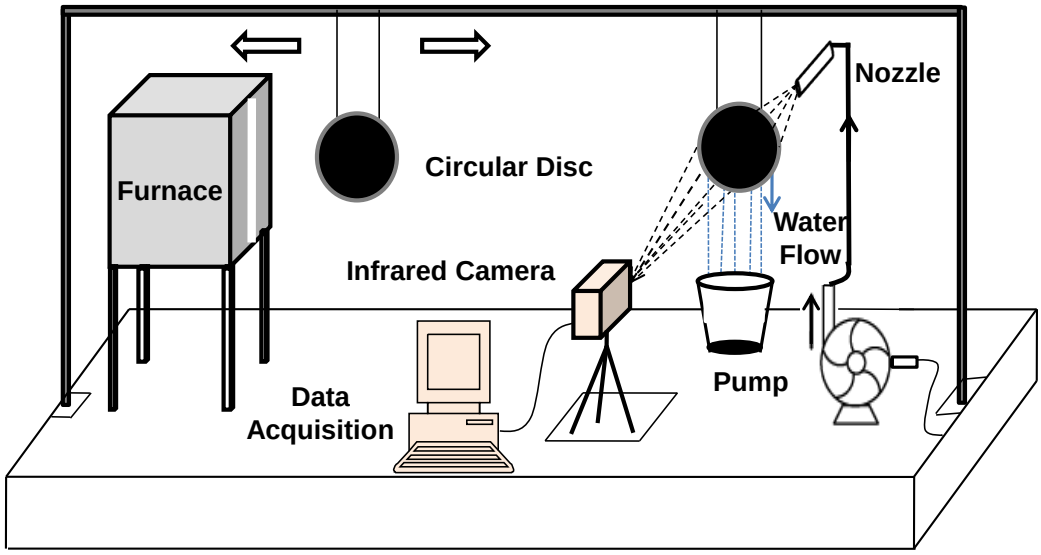

Figure 2.1: The experimental setup

Figure 2.2: ThermaCAM SC 3000 Researcher

water flow with respect to the plate significantly differs. When an array of jets is used, water flows parallel to the surface of the plate. When a spray nozzle is used, water flows perpendicular to the surface.

2.2 Infrared system

Hot metal samples emit thermal radiation from their surface. The lens of on the infrared camera senses this thermal radiation. The lens focuses the infrared (IR) energy by using a detector, which converts the energy into an electrical signal that can be displayed to have a certain frequency. This method facilitates the temperature measurement from a distance without contacting the object to be measured. The temperatures on the measuring side of the sample are recorded by using the ThermoCAM SC 3000 of the company FLIR, which is shown in Figure 2.2.

Table 2.1: Technical specifications and characteristics of ThermaCAM SC 3000.

Image frequency	50 up to 750 Hz
Detector type	Quantum Well Infrared Photodetector (QWIP) 320 × 240 pixels
Temperature range	−20 ^{o}C to 150 ^{o}C 100 ^{o}C to 500 ^{o}C 350 ^{o}C to 700 ^{o}C
Accuracy	1 ^{o}C(up to 150 ^{o}C)
	2 ^{o}C(above 150 ^{o}C)
Voltage	12V DC
Power consumption	22 watts
AC Adapter	Included
Weight	3.2 kg
Size	220 × 135 × 130 mm

Charge–Coupled–Device (CCD) chip of the camera converts electromagnetic radiation into electric current and process it into electronic signals. All of the pixels can be devoted to light capturing and its output is uniformly (a key factor in image quality) high. The camera also includes amplifiers, noise-correction, and digitization circuits, so that the chip gives the outputs as digital bits. All objects which radiate infrared energy can be converted into a visual representation of the thermal differences in the scene.

ThermaCAM feeds real-time data directly to the PC desktop for both recording and analyzing. During the measurements, the camera is installed on a stand and directed towards the measuring surface of the hot plate. ThermaCAM Researcher software analyzes the recorded thermal data of both static and dynamic images. To measure the transient temperatures of the experimental plate, the emissivity ϵ of this area (plate) is required as the setting parameter to the software. Therefore, the emissivity of the plate must be known. Table 2.1 shows the technical specifications of ThermaCAM SC 3000.

Data obtained from the IR-camera in thermal images format can be captured and stored at the extremely high frame rate of 150 Hz. The IR-camera software can transfer the thermal image data at a number of specific points to temperature-time data. The number of selected points on the surface could be sufficient in order to allow monitoring changes that occur in this region. In the case of mould quenching the selected points are placed vertically on the plate surface from top to bottom and in the direction which is parallel to the water flow. The distance between each point is equal to two pixels (one pixel distance 0.91 mm). Figure 2.3 a and b shows the thermal images obtained from the IR-cam during the mould and spray quenching respectively. The selected data points are also shown in the figure. This measured data from the IR-cam shows valuable

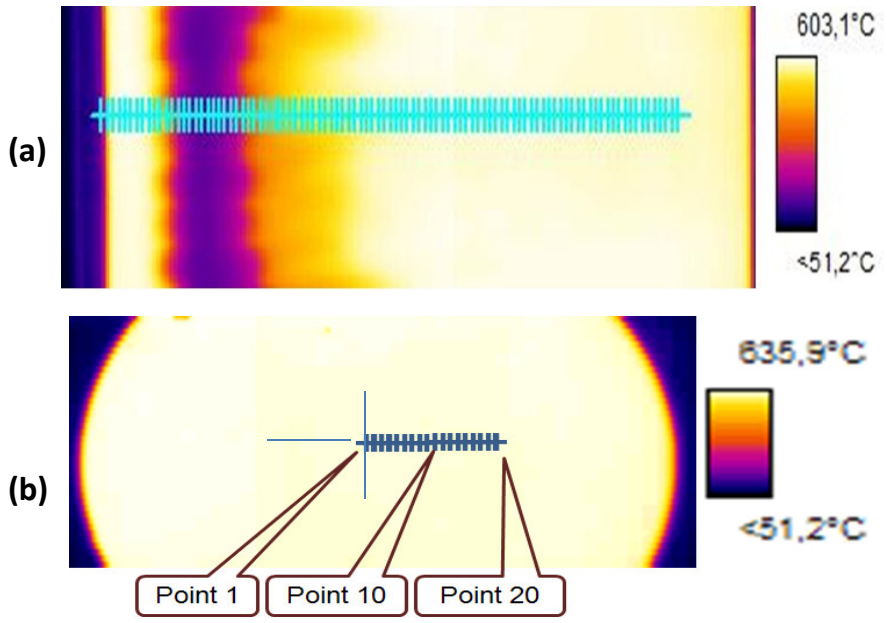

Figure 2.3: Selected points in thermal image of IR-cam

data for temperature with time at these points. The temperature gradient with time has been obtained for each selected point. The experimental measured data is supplied as input to the MATLAB program codes to estimate the heat flux of the metal surface.

2.3 Emissivity

The determination of the surface temperature by using the infrared camera requires a uniform and high surface emissivity on the measured side of the plate. The measured side of the metal sample is coated with a black paint. The initial temperature of the metal sample is approximately 550 ^{o}C. The measurement setup used to determine the temperature dependent emissivity of the coated surface ε is illustrated in Figure 2.4. Two similar kinds of metal samples are connected together and a thermocouple element is fixed between them. The exact temperature can be measured by a data logger connected to the thermocouple element. The metal sample is cooled by natural convection from the initial temperature to 150 ^{o}C. The measuring of temperature by infrared camera and data logger starts at the same moment. The recorded temperatures from the data logger are used to calibrate the measured temperatures from the infrared camera. The emissivity of the camera could be regulated until the shown temperature matches with that of the thermocouple. Figure 2.5 shows the measured emissivity of the black surface. The average emissivity for the black surface between 550 ^{o}C and 150 ^{o}C is 0.898. The same procedure has been applied to a higher temperature interval, 850 ^{o}C and 350 ^{o}C. Figure 2.6 shows the measured emissivity of the black surface at high range

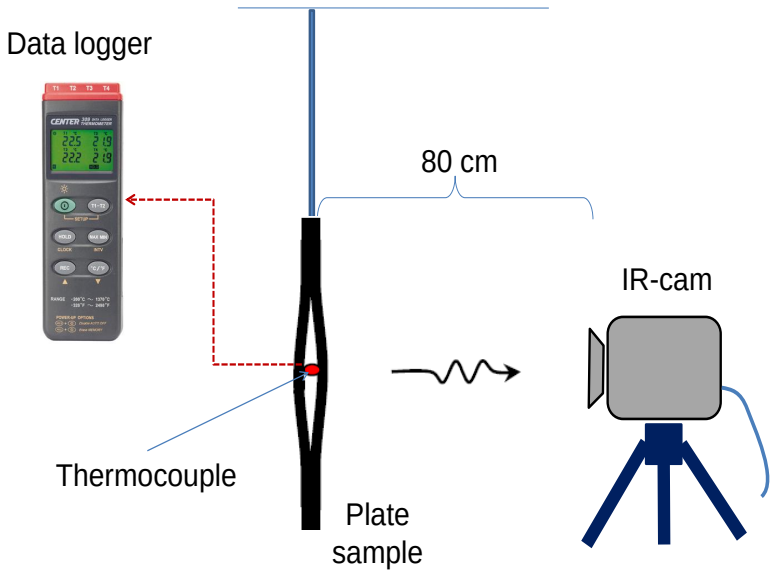

Figure 2.4: Measurement set-up for determining emissivity of the coating surface

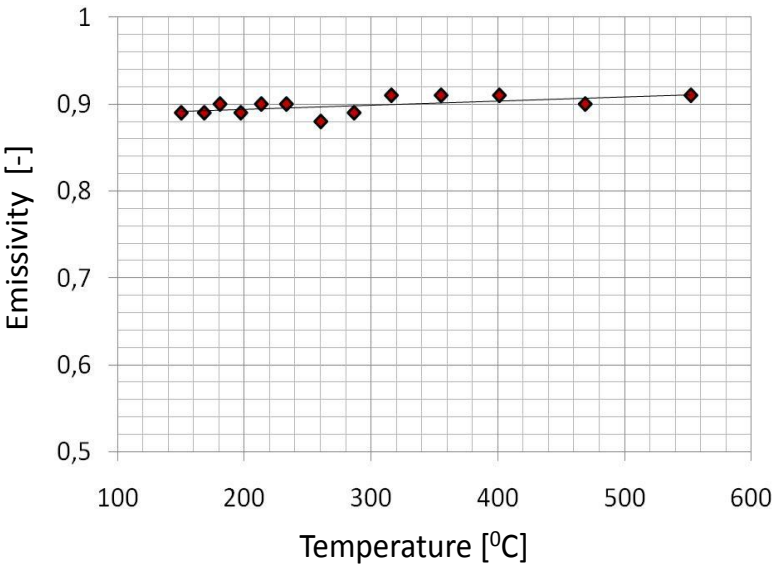

Figure 2.5: The emissivity variation of coated surface: At lower temperatures interval

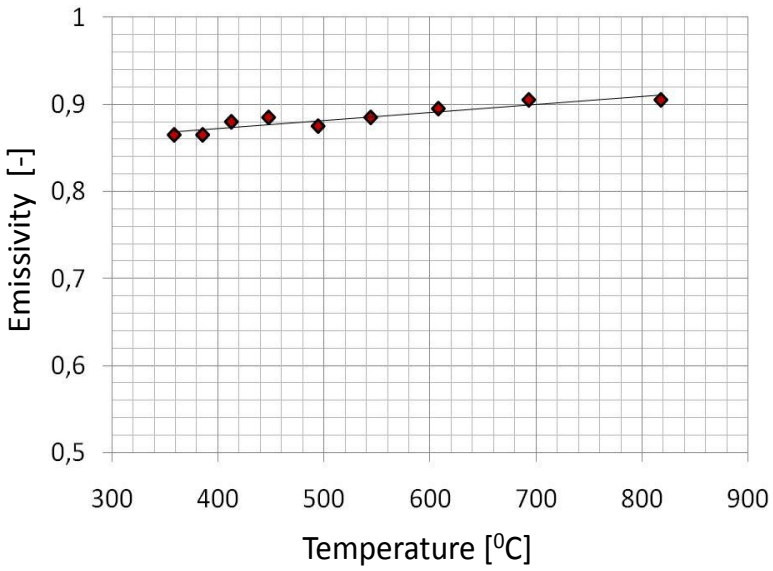

Figure 2.6: The emissivity variation of coated surface: At lower temperatures interval

temperature. Similarly, the average emissivity for the black surface between 850 ^{o}C and 350 ^{o}C is 0.884. The measured values of emissivity are slightly lower than the value of 0.95. This is caused by the extremely thin layer which is to avoid resistance for the heat conduction through it.

2.4 High speed camera

Two methodologies were followed to calculate or to measure the wetting front velocity i.e.

- by calculating the propagation of MaxHF using two dimensional analysis of solving inverse heat conduction problem
- by measuring the wetting front velocity using images at different times with accurate scaling using a high speed camera

A high speed camera is a device used for recording fast moving objects as a photographic image(s) onto storage media. After recording, the images stored on the media can be played back in slow motion. A normal motion picture camera is filmed and played back at 24 frames per second, while television uses 25 frames/s. High speed cameras can film up to a quarter of a million frames per second by running the film over a rotating prism or mirror instead of using a shutter, thus reducing the need for stopping and starting the film behind a shutter, which would tear at such speeds. The fastest cameras are generally used in scientific research, military testing and evaluation, and industries. An example of an industrial application is that of crash testing in order to understand the crash and what happens to the automobile and passengers during

Figure 2.7: High-speed camera

a crash. The problem of high speed cameras is that the need for stronger exposure. Therefore, one needs very bright light to be able to film at forty thousand frames per second, sometimes leading to the subject of examination being destroyed due to the heat of the lighting. The camera which was used for the visualization of wetting front phenomena was the High-SpeedStar 6 made by La Vision, as shown in Figure 2.7. Nickel, inconel 600 and AA2024 sheets and discs were quenched by atomized spray and water jets with different flow parameters and were visualized by high speed camera. This camera has different options, such as the size of the screen and frequency. Images can be captured at a maximum frequency of 5400 frames/sec when the screen resolution is selected as 1024 $\times$ 1024 pixels. Similarly, for the screen size of 512 $\times$ 512 pixels, the maximum frequency is 16000 frames/sec. However, the maximum frequency for this camera is 150 kHz. As the frequency of measurement increases, more intense lighting is required for illuminating the subject properly. Minimum inter-frame time is 4.8 μs and pixel size is 20 μm $\times$ 20 μm. A software called DaVis 7 is used for data acquisition and visualization of captured images. This arrangement is equipped with scaling the subject being analyzed to the real dimensional coordinates. Using this provision, first the disc or rectangular sheet is scaled on the screen to the actual dimensions and then the high speed movie is made with a selected frequency of frames/sec, exposure time and exposure time in the presence of high intensity lights. Once the images are saved, the position of the wetting front is related to real dimensions and its change is noted with respect to time, which is wetting front velocity. The results from these experiments are shown in Chapter 6.

2.5 Samples

Front and back sides of circular and rectangular sheets are shown in Figure 2.8. In this research Nickel, Aluminium alloy, Copper alloys and Nickel Inconel 600 were used. The thickness of sheets varied from 4 to 2 mm. Thermal conductivity, specific heat

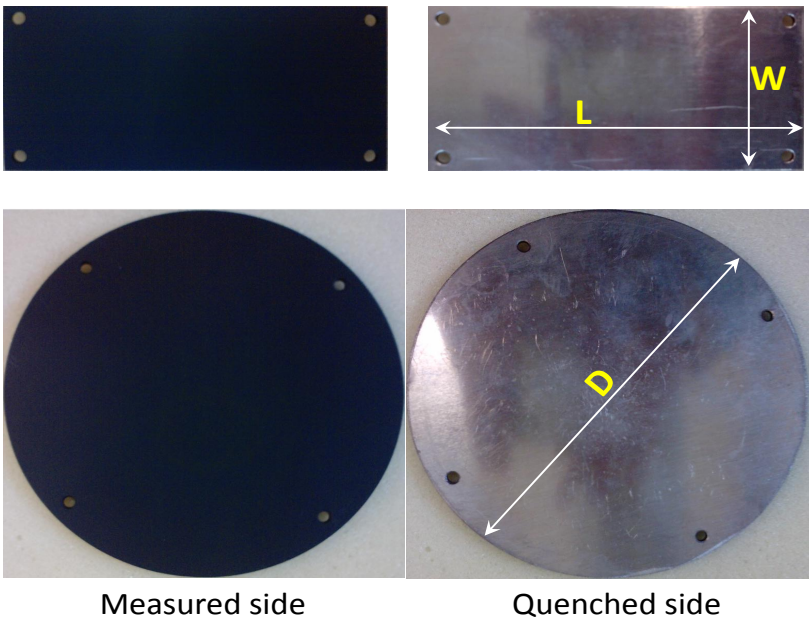

Figure 2.8: The rectangular and circular metal samples used in the experiments

capacity and density are the thermophysical properties of the material which must be known in order to calculate the heat transfer coefficient. The metals are cut into two shapes depending upon the method of quenching, i.e. rectangular shapes are machined for quenching by an array of jets, while circular disc shapes are formed for quenching by water spray or atomized spray. The width of the rectangular sheets depends on the size of the mould. 110 mm and 70 mm wide sheets were used for the small and big mould respectively. The sheets should have such a width that it stops the water flow and it should not wet the rear side of the sheet, which would disturb the measurements by the camera. The metal samples are cut by laser cutting. In the case of copper, they are cut by water jet cutting because laser cutting does not work precisely when the conductivity of the material is too high. After cutting, the sheets are painted with black graphite paint (the commercial name: SENOTHERM), heated to 250 ^{o}C and kept for 30 minutes for the proper fixation of the paint.

2.6 Nozzles

In this study, two different types of nozzles were used. The first type is a single-fluid nozzle or hydraulic nozzle, which has one input for liquid. For this nozzle type, as the fluid pressure increases, the flow through the nozzle increases and the droplet size decreases. While the second type is a two fluid nozzle or atomized spray nozzle (Lechler-156.35.13), which has two inputs for liquid and gas. The cooling water is connected with liquid input and compressed air is used as the atomizing gas. A homogeneous spray of fine droplets of about 20 μm is produced. The produced spray from the nozzle is full conical. The spray cone angle of the hydraulic nozzle is 45 ^{o} and distance between the

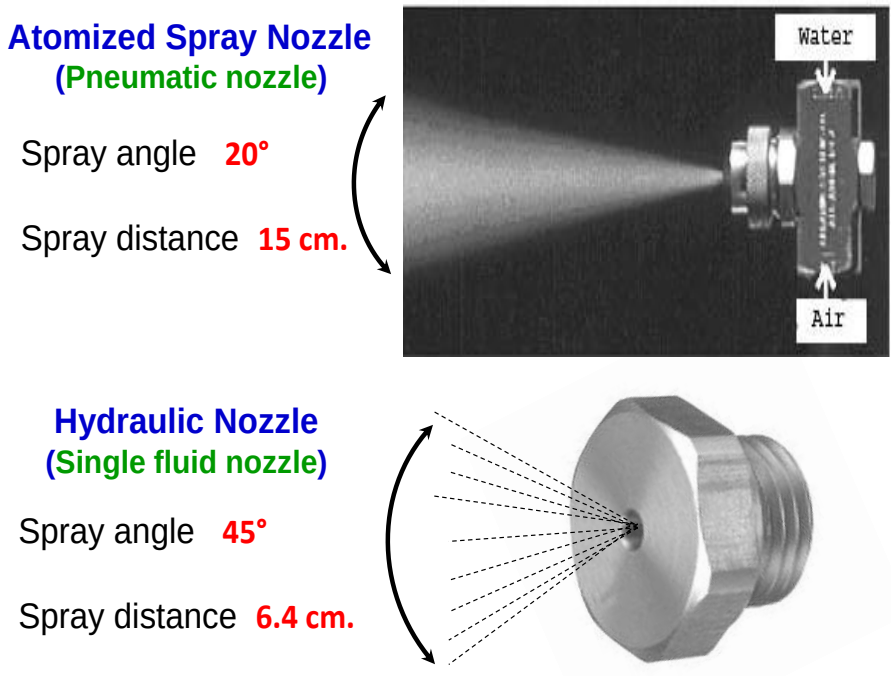

Figure 2.9: The two nozzle types used

nozzle and plate surface is 6.4 cm. The spray cone angle of an atomized nozzle is 20 ^{o} and the distance between the nozzle and plate surface is 15 cm. The two nozzle types described above are shown in Figure 2.9.

Impingement Density (ID)

The patternator shown in Figure 2.10 was used to measure spray distribution for both the single fluid nozzles and atomized spray nozzles. Water is sprayed for a specified period of time Δt and collected in vertical tubes with a diameter of $d_t = 10$ mm, each aligned perpendicular to the spray nozzle. Under these operating conditions, the vertical tubes carry the spray liquid into bottles. The mass of the collected liquid M_{water} into a particular bottle is measured separately. The mean impingement density was calculated from the following equation 2.1, where the impingement density unit is kg/m^2/s.

$$\dot{m} = \frac{4 \times M_{water}}{\Pi \times d_t^2 \times \Delta t} \tag{2.1}$$

Impingement density for the hydraulic full cone nozzle and pneumatic atomizing nozzle is measured using a patternator along the axis, perpendicular to the axis of the spray cone at a distance of 64 and 150 mm respectively. The value of impingement density distribution (IDD) is proportional to the amount of water flow at the inlet under constant air pressure . The Figure 2.11 shows the impingement density distribution for the single fluid nozzle. The average of three experimental data is taken as the nominal mass velocity of water. The spray distribution has been measured at three different water

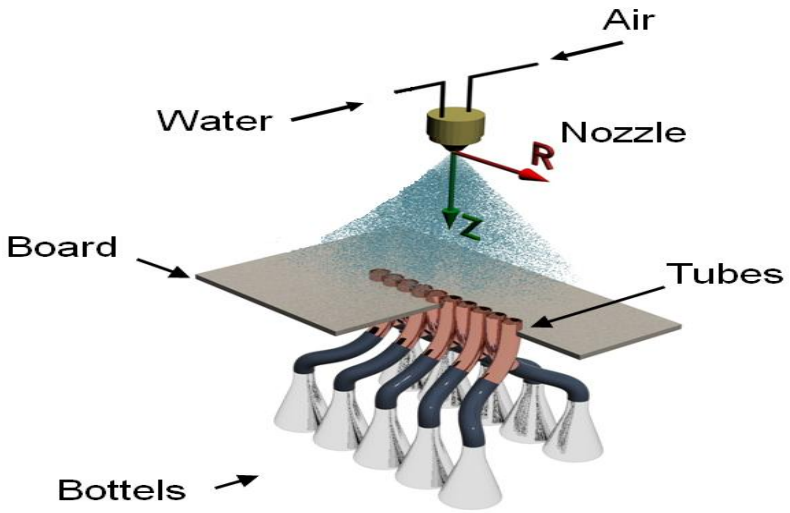

Figure 2.10: The patternator

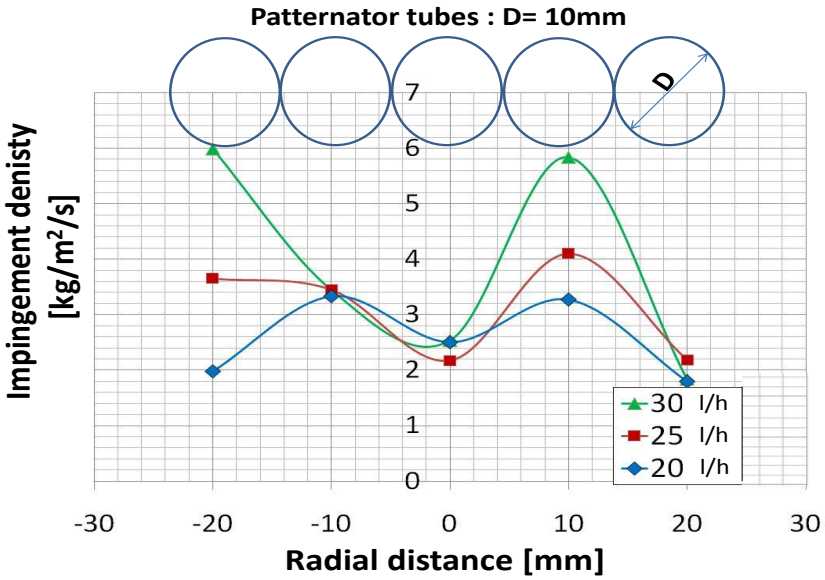

Figure 2.11: Distribution of ID of single fluid nozzle in radial direction

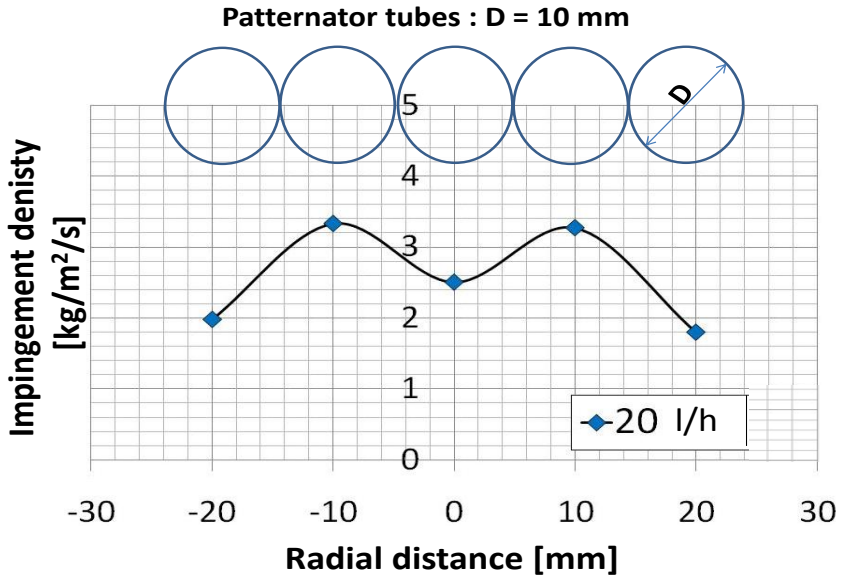

Figure 2.12: Distribution of ID of single fluid nozzle in radial direction at 20 liter/hr

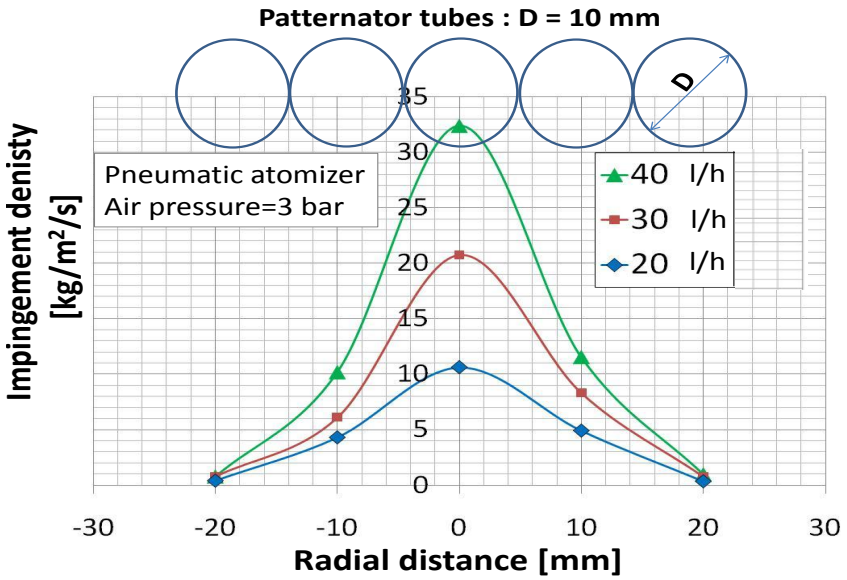

Figure 2.13: Distribution of ID of atomized spray nozzle in radial direction

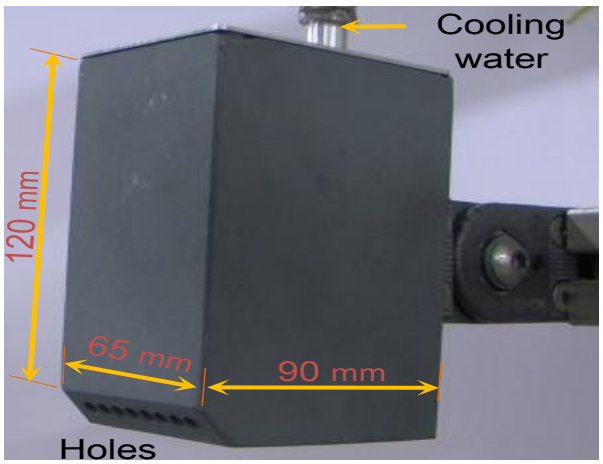

Figure 2.14: Mould used in experimental tests

flow rates of 20, 25, 30 l/h. The throughput of 20 l/h is distributed more uniformly and is separately shown in Figure 2.12. Due to this reason, the experiments for analyzing the effect of water quality on heat transfer during spray quenching have been performed at this flow rate with the hydraulic full cone nozzle. The Figure 2.13 shows the results for the impingement density of the atomized spray nozzle. In this case, the distributions are balanced and symmetrical at all flow rates. The heat transferred due to the single fluid nozzle spray is lower than the heat transferred due to the atomized nozzle. The cooling time of the single fluid nozzle is about five times longer. Therefore, the single fluid nozzle is used in the studies to investigate the heat transfer of different real waters, which are explained in detail in the next chapters.

2.7 Mould (Array of jets)

The designed mould has the dimensions of 120 × 90 × 65 mm, as shown in Figure 2.14. The cooling water is supplied through an array of small diameter holes. The water leaving from the holes produces water jets. These jets impinge on the rear side (quenched side) of the metal sample. The mould has eight holes of 2.4 mm diameter. The position of the water supply hole is designed to be on the top of the mould in order to make the flow from the jets more uniforml. A hydraulic pump with a flow regulating device delivers the cooling water to the mould.

2.8 Mould movement mechanism

Figure 2.15 shows the mould in fixed position. The mould weight is 2070 grams and the weight is increased slightly during the quenching process because water fills the inside of mould. The distance of stroke from the start position to the end position is about 120 mm. The required speed for the movement of the mould ranges from 10 mm/s to 50

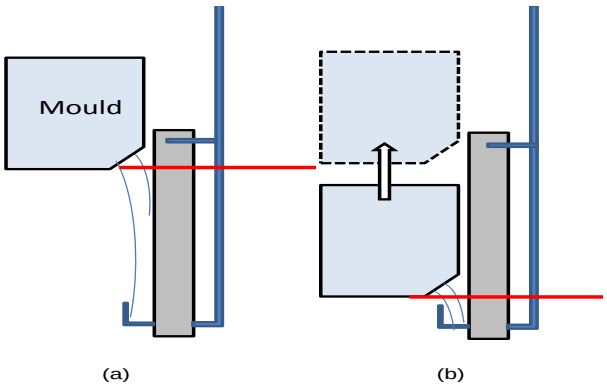

Figure 2.15: The mould positions (a)fixed position and (b)movement positions

mm/s. The regulating speed depends on operating conditions, which is completed by the stepper motor controller. The mould movement mechanism and mould itself are located in the quenching side and are installed as part of the experimental setup frame as the following Figure 2.16 shows the installation diagram of the mould movement mechanism. At the normal operating conditions, during the cooling tests, the heated plate is moved manually from inside the electrical furnace to the cooling zone. The optical sensor is fixed in a way not to hinder the camera function and does not affect the measurements. Therefore, the optical sensor sends a signal to the computer and the computer resends a signal to the controller and activates the stepper motor. Figure 2.17 shows the new installation of the experimental set up. The stepper motor speed is proportional to the applied voltage. The speed of the stepper motor is the same as the mould speed. Therefore, the controller is designed to vary the input voltage of the stepper motor in order to change its speed.

Optical device

An optical device known as Optris CT LT infrared sensor was also used for detecting the starting temperature of the metal sheet. As soon as the surface temperature of the hot metallic sheet reaches the desired starting temperature, the main IR camera is commanded to start the data acquisition. This starting temperature is communicated by the Optris CT by changing the color from yellow to blue. The working principle of Optris is the same as that of the infrared camera; however, the measurement is more tentative instead of very accurate, like the IR camera. It can measure the temperature from -50 ^{o}C to 975 ^{o}C. The spectral IR range for this device is 8 - 14 μm. Figure 2.18 shows the optical device used for the Optris CT infrared thermometry. The sensor is fixed in the face of the hot metal plate, as show in Figure 2.19(a). The sensor head is made of stainless steel (Figure 2.19(b)) and the sensor electronics are placed in a separate box (Digital Converter) made of casting zinc (Figure 2.19(c)). Figure 2.20 shows the position of the optical sensor in the experimental set up. The Optris CT can measure the

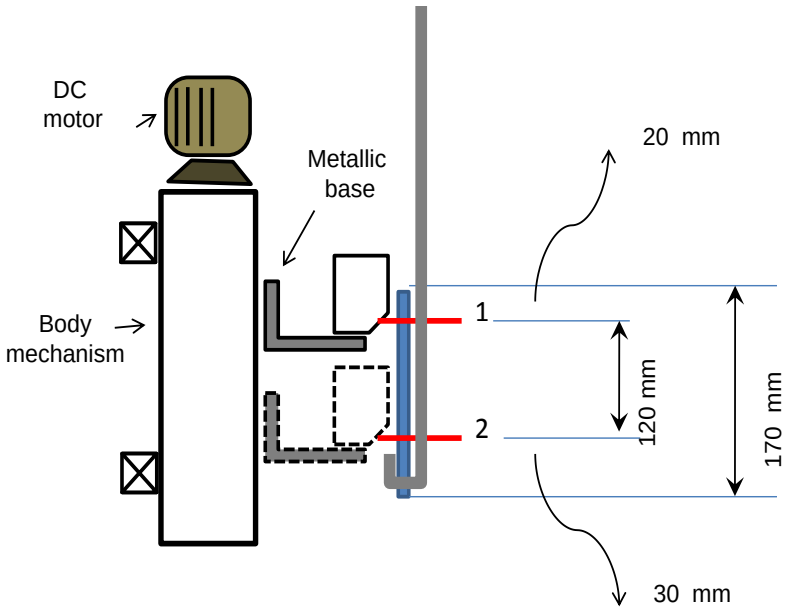

Figure 2.16: Installation diagram of mould movement mechanism

Table 2.2: Technical data of controller IT116 flash.

Dimensions (W × H × D)	(105 × 111 × 320)mm
Weight	2380 g
Power supply	115/230VAC
	50/60 Hz (switchable)
Signal voltage	24V DC
Power consumption	250 W
Peak current	4.2 A
Ambient temperature	0 ^{o}C to 50 ^{o}C
Integrated chip	32 bit, RISC processor
Program memory	128 KByte

surface temperature based on the emitted infrared energy of objects. The sensor head collects a small amount of energy (usually 0.0001 watt) radiated from the hot plate and generates an electrical signal. The generated electrical signal is amplified and converted into analog signal. The Digital Converter digitizes the signal into digital signal. Infrared thermometers of the optoelectronic sensor will send a signal to the controller when the hot metal is ready for testing. At this moment, the mould starts moving and thus begins the process of hot metal cooling.

Controller IT116 flash

The controller (IT116 flash), as shown in Figure 2.21, is a powerful one axis-controller for numerically controlled motion of a linear or rotary axis with a two phase-stepper

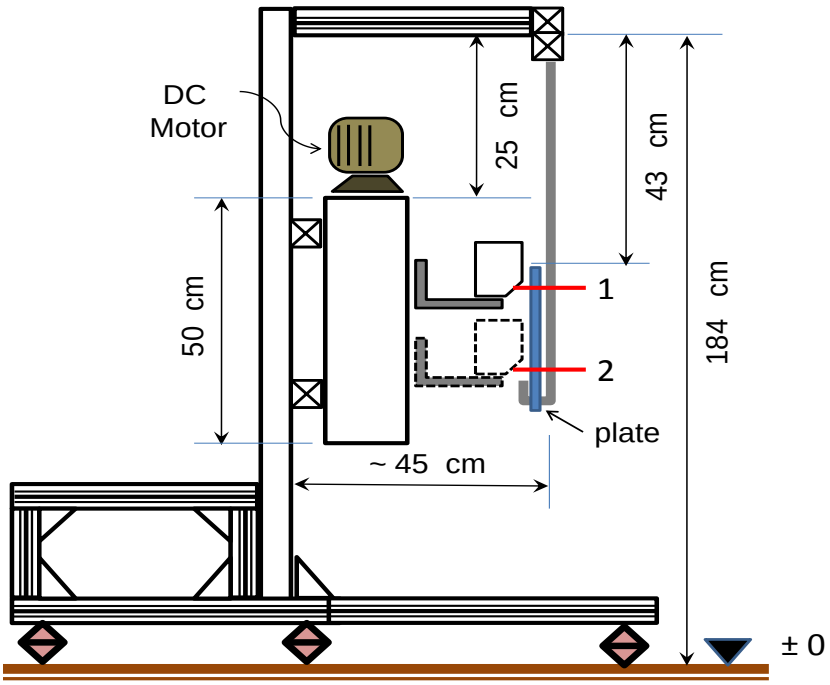

Figure 2.17: The new installation of the controller and optical sensor

motor. Table 2.2 shows the technical data of the controller IT116 flash. The controller has four binary inputs/outputs. For communication between a PC/Notebook (under Windows operation system) and the controller, a serial interface (RS232) is used. The microprocessor based controller includes an internal flash memory with a size of 128 KBytes for storing the firmware and the application program. The controller is prepared for loading application programs through the external memory. The controller (IT116 flash) has 128 micro steps for one full step. This feature allows very smooth motion of the connected two phase-stepper motor. The automatic current draw down reduces power dissipation as in the amplifier and the stepper motor. The peak current is 4.2 A.

Figure 2.18: Optical device for measuring starting surface temperature [Courtesy:optris]

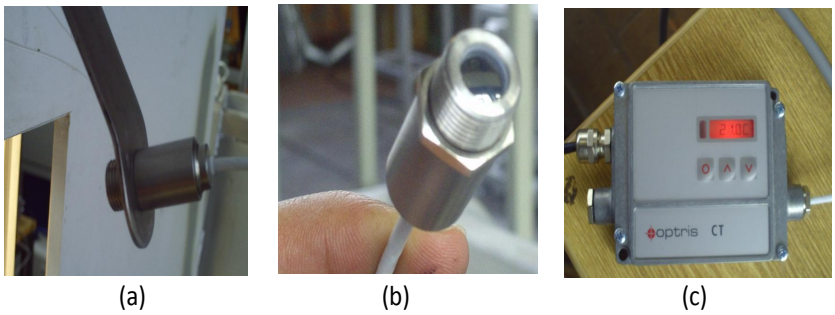

Figure 2.19: Optical device (a)Fixiation (b)The head (c)Digital Converter box

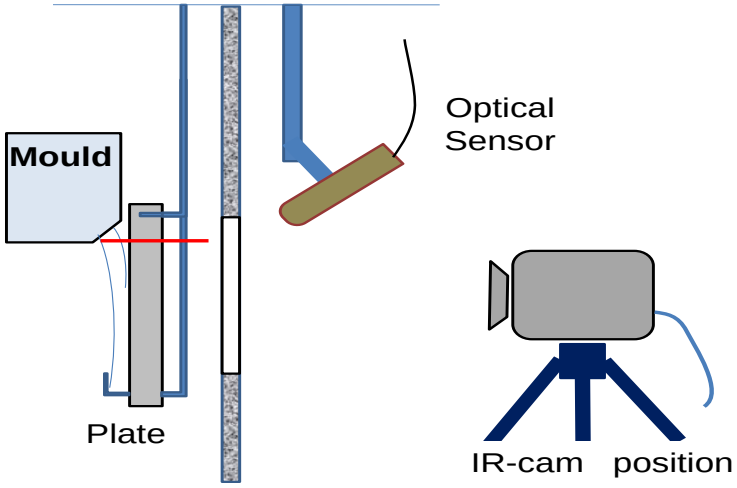

Figure 2.20: Optical device fixation

Figure 2.21: The controller IT116 flash

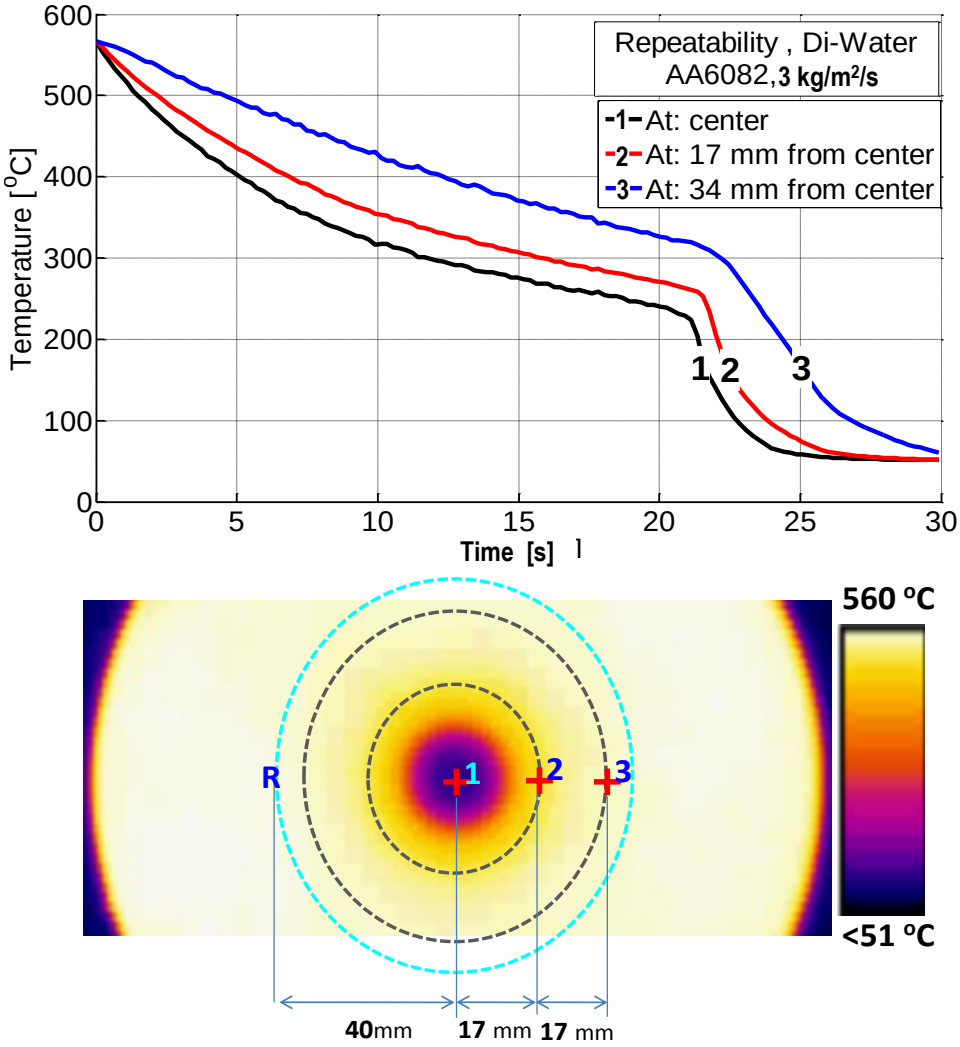

Figure 2.22: Cooling curves for three characteristic locations

It can be reduced to conform to parameters of different stepper motors.

2.9 Representative test

The principle temperature profiles are shown in Figure 2.22. An Aluminum sheet of alloy 6082 of 3 mm thickness is cooled with the single fluid nozzle (flow rate–20 kg/h). The temperature profiles at three different locations are shown: the center point (first point), the radial distance 17 mm (second point) and the radial distance 35 mm (third point). The spray cone has a radius of 40 mm. From this example, it can be seen that the temperature profiles are symmetrical in angular direction and thus independent of angular direction.

Chapter 3

Analysis Methods

3.1 Determination of Leidenfrost temperature

Figure 3.1 shows schematically the temperature-time curve during a cooling process. The cooling in the section of the film boiling is slow. The Leidenfrost point is defined as the temperature, at which the vapor film collapses. In the next transition boiling regime the heat dissipated increases by many times and reaches a maximum when the vapor layer is completely collapsed. In cooling processes it is of particular interest the region of stable film boiling and the location of the Leidenfrost temperature. The second derivative of the temperature profile can be used to detect the position of the Leidenfrost point. The second derivative is calculated by using discrete temperature measurements according to following equation

$$\left(\frac{d^2T}{dt^2}\right)_i = \frac{T_{i+1} - 2T_i + T_{i-1}}{\Delta t^2}. \tag{3.1}$$

Figure 3.2 shows an example for the calculated second derivative and the belonging temperature profile. It can be seen that the second derivation is constant along the time with one exception. Here a significant minimum value occurs. This peak correlates with the LFT. As a consequence, the LFT is determined in all test from the minimum peak of the second derivation of the temperature-time profile.

3.2 Simple analysis of heat transfer

For a simple analysis method, the temperature distribution is assumed to be stationary through the thickness of the metal sample. Therewith, the heat transfer of an annular ring of the disk with the width ∂r as shown in Figure 3.3 can be calculated from the energy balance

$$\frac{dh}{dt} = -\dot{q}_{sp} - \dot{q}_{\lambda} - \dot{q}_{\alpha} - \dot{q}_{R}. \tag{3.2}$$

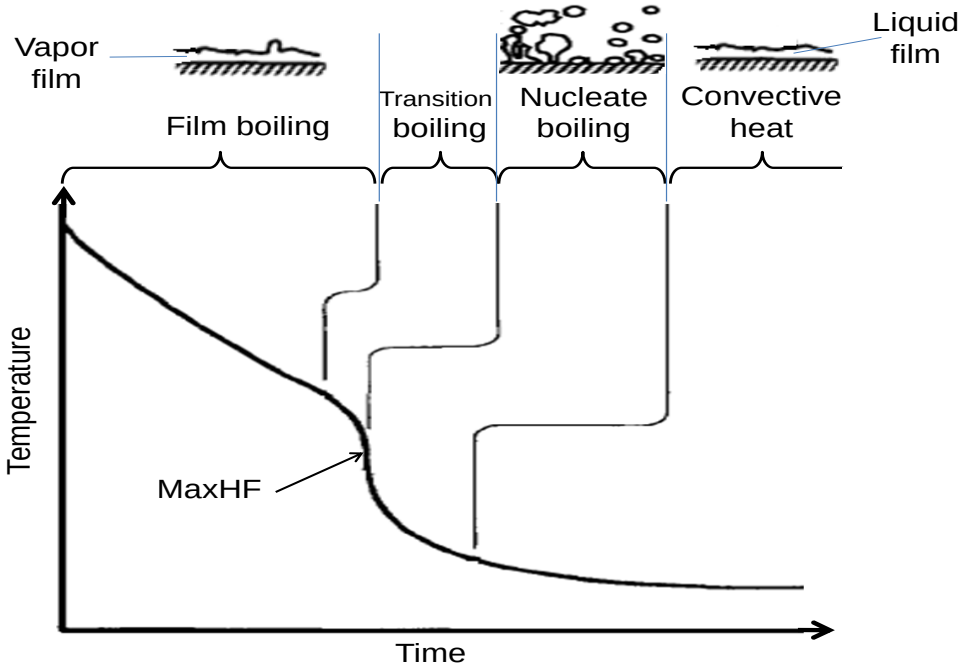

Figure 3.1: Temperature profile of a surface during quenching

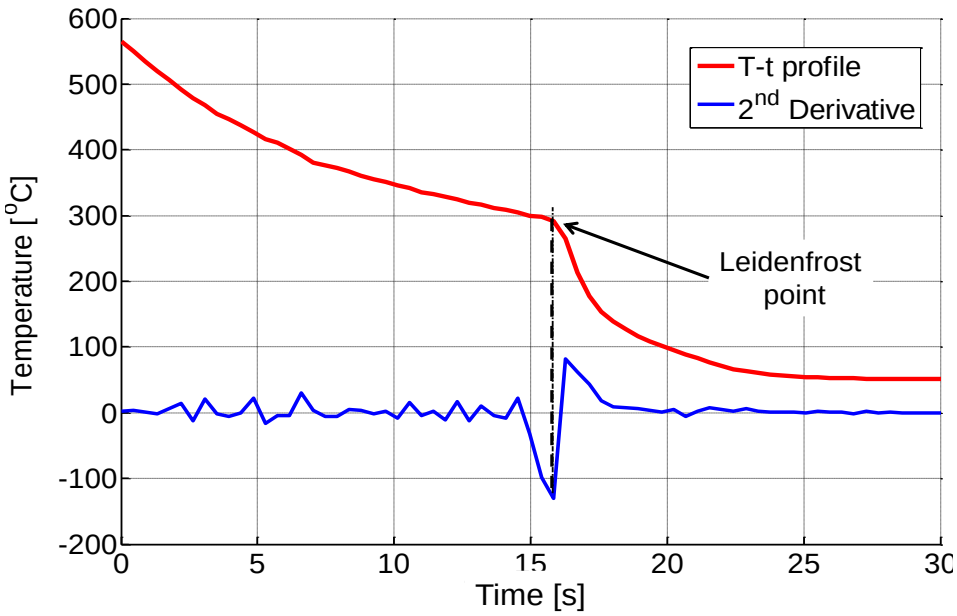

Figure 3.2: The second derivative of the temperature-time curve

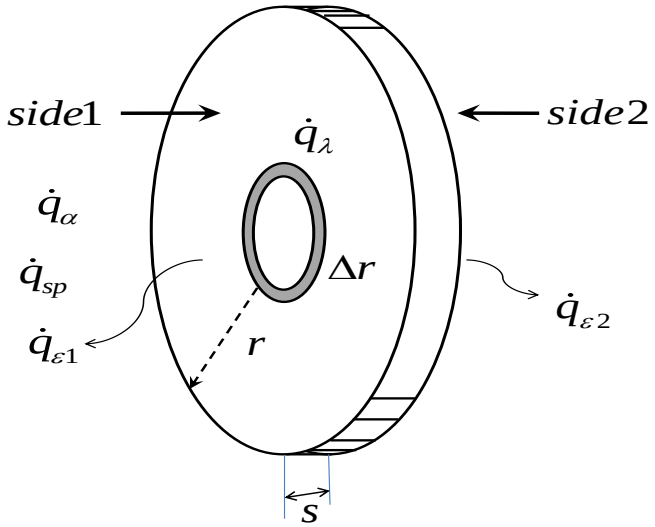

Figure 3.3: Heat losses during spray quenching

The decrease of the stored enthalpy with time is equal to the transferred heat fluxes by the spray $\dot{q}_{sp}$, by the radial conduction $\dot{q}_\lambda$, by natural convection $\dot{q}_\alpha$ and by radiation $\dot{q}_R$. The change of the enthalpy in the volume element is calculated by

$$\frac{dh}{dt} = \rho c_s s \frac{dT}{dt}. \tag{3.3}$$

The heat transfer coefficient of the water spray α_{sp} is defined with the water spray temperature T_{sp} by the equation

$$\dot{q}_{sp} = \alpha_{sp} \cdot (T_s - T_{sp}) \,. \tag{3.4}$$

where T_s is the surface temperature. The conductive heat flux is calculated using the Fourier approach

$$\dot{q}_\lambda = -s \cdot \lambda \frac{1}{r} \frac{\partial}{\partial r} \left(r \cdot \frac{\partial T}{\partial r} \right). \tag{3.5}$$

The natural convective heat loss is calculated by:

$$\dot{q}_\alpha = \alpha \cdot (T_s - T_\infty). \tag{3.6}$$

The HTC is assumed to be 5 $\mathcal{W}/m^2/K$. Convection is only considered on the side where surface temperature is measured. Radiation is considered on both sides of the metal sheet surface

$$\dot{q}_R = (\epsilon_1 + \epsilon_2) \cdot \sigma \cdot \left(T_s^4 - T_\infty^4 \right). \tag{3.7}$$

where ϵ_1 and ϵ_2 are the emissivities of the front and rear side of the sheets and σ is the Stefan Boltzmann Constant ($5.67 \times 10^{-8} W/m^2/K^4$). Since the front side is polished, its

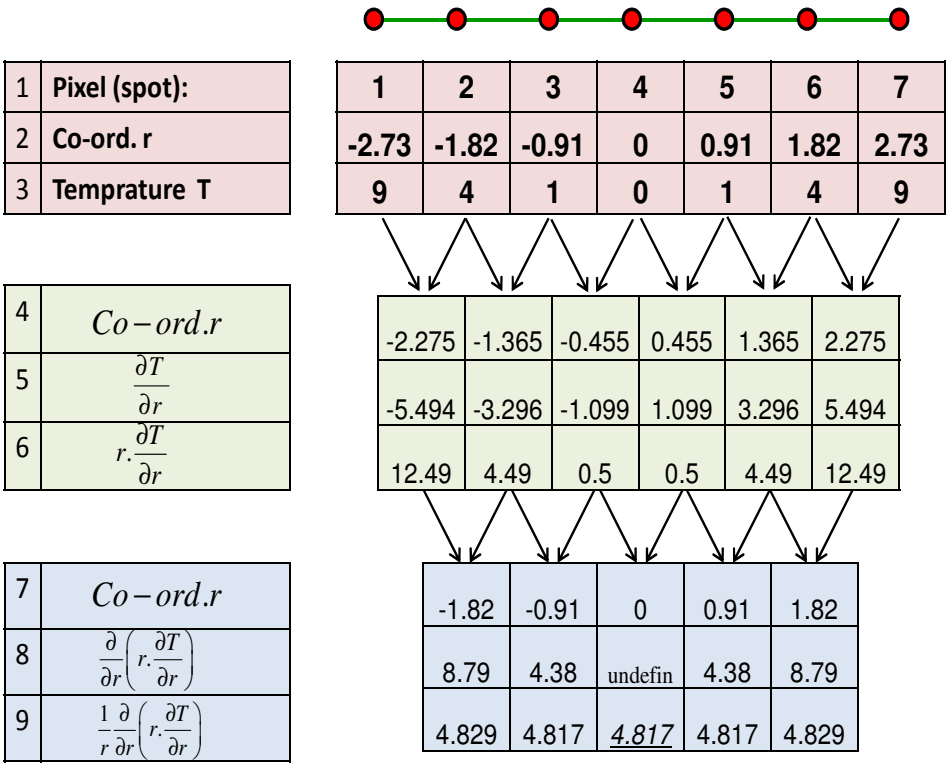

Figure 3.4: Flow diagram algorithm for the conduction factor calculation

emissivity is 0.3 and the rear side is painted black therefore its emissivity is increased to 0.9 approximately. Here T_∞ is the ambient temperature. The radiative and convective heat flows are only 5 % of the total heat loss as compared to conductive heat flow and heat transfer due to spray. In order to calculate the factor $\frac{1}{r}\frac{\partial}{\partial r}\left(r \cdot \frac{\partial T}{\partial r}\right)$, we have to follow

a step wise calculation procedure using the software Therma Cam 2001 Researchers. Seven spot measurements of temperature are carried out at the center of the spray jet on metal sheet in such a way that spot 4 is at the center and spot 1 and spot 7 are at the corners. Distance between two consecutive spots is equal to 2.3 mm, which is regarded as pixel size. In this example the pixel size equal to $3 \times \frac{156mm}{204totalpixels}$, where 156 mm is the measured diameter of the metal disc and 204 are the total pixels which are accommodated into this width. Therefore the distance between two consecutive spots is 2.3 mm.

The steps which are to be followed to calculate the conduction factor are explained by the following block diagram as shown in figure 3.4. The final value of factor $\frac{1}{r}\frac{\partial}{\partial r}\left(r \cdot \frac{\partial T}{\partial r}\right)$ is calculated by averaging two middle values in step (9) which is then used to calculated the heat transfer due to conduction.

3.3 Inverse analysis

In the region of nucleat boiling the heat transfer is so high that there is a temperature difference between the cooled front surface and the measured back surface. Therefore, alternatively a 2D inverse analysis of the heat transfer is used. The governing heat equation in 2D can be solved by a numerical analysis. The numerical analysis calculates the time dependent heat transfer coefficient for the position regarded at the metal plate surface from measured temperature at this position. In case of Direct Heat Conduction Problem (DHCP), the boundary conditions are well known and one has to solve the Governing Differential Equation (GDE) for finding the interior domain solution. In Inverse Heat Conduction Problem (IHCP), the boundary conditions are unknown and some part of the domain solution is known through experiments. Experimental temperature data are required to solve the GDE for the estimation of the boundary conditions. Nallathambi and Specht [92] used the Finite Element Method (FEM) to solve the IHCP using experimental data and DHCP temperature solution. The mathematical aspects of DHCP and IHCP are formulated separately in the following section.

Direct Heat Conduction Problem (DHCP)

Let an open bounded domain $\Omega \subset \mathbb{R}^n$ $(1 \leq n \geq 3)$ be the reference configuration of a non-linear thermo-plastic body $\mathfrak{B}$ with particles defined by $\vec{X} \in \tilde{\Omega}$, $\Gamma = \partial\Omega$ its smooth boundary and $\Upsilon \subset \mathbb{R}^+$ be the time interval of analysis $(t \in \Upsilon)$. As usual, $\tilde{\Omega} = \Omega \cup \Gamma$ and $\Gamma = \Gamma_\theta \cup \Gamma_q$. The metal quenching problem consists in finding an absolute temperature field $\theta : \tilde{\Omega}$ x $\Upsilon \to \mathbb{R}^+$ such that [93].

$$\rho\, c_p\, \dot{\theta} = -\nabla \cdot \vec{q} \qquad in\ \tilde{\Omega}\ \times\ \Upsilon \tag{3.8}$$

subject to the boundary conditions

$$\theta = \bar{\theta} \qquad in\ \Gamma_\theta\ \times\ \Upsilon \tag{3.9}$$

$$\vec{q} \cdot \vec{n} = -\bar{q} \qquad in\ \Gamma_q\ \times\ \Upsilon \tag{3.10}$$

and the initial condition

$$\theta(\vec{X}, t)|_{t=0} = \theta_0(\vec{X}) \qquad in\ \Omega \tag{3.11}$$

Eq. 3.8 represents the energy balance obtained from the First Law of Thermodynamics where the superposed dot denotes time derivative, ∇ is the gradient operator with respect to Cartesian reference system, ρ is the density at reference configuration and c_p is the specific heat capacity, both are functions of temperature. $\vec{q}$ is the heat flux vector. In Eq. 3.9, $\bar{\theta}$ is the prescribed temperature on temperature boundary Γ_θ. In the heat flux boundary Γ_q, q_s is the normal heat flux due to convection-radiation phenomena. Using temperature-dependent overall Heat Transfer Coefficient (HTC) α, q_s can be stated according to Newton's constitutive law as,

$$q_s = -\alpha(\theta)(\theta - \theta_\infty) \tag{3.12}$$

where θ_∞ is the ambient temperature. From Fourier's law of heat conduction, heat flux vector $\vec{q}$ can be defined as,

$$\vec{q} = -\bar{\mathbf{K}}(\theta) \cdot \nabla\theta \tag{3.13}$$

where $\bar{\mathbf{K}}$ is the temperature dependent second-oder thermal conductivity tensor. If the material considered is of isotropic nature, it can be reduced as a scalar k which is only a function of temperature and independent of direction.

Finite element form of the general governing differential equation with natural boundary conditions and also using Backward-Euler time difference scheme can be given as [94],

$$(\mathbf{M} + \Delta t\ \mathbf{K})\,\Theta^{n+1} = \mathbf{M}\Theta^n + \Delta t\ \mathbf{F}^{n+1} \tag{3.14}$$

where $\Delta t = t^{n+1} - t^n$, $\mathbf{M}$ is the global capacitance matrix , $\mathbf{K}$ is the global conductance matrix and $\mathbf{F}$ is global force vector and given as,

$$\begin{aligned}
\mathbf{M} &= \sum_{i=1}^{n} \int_{\Omega_e} \rho\ c\ \mathbf{N}\mathbf{N}^T\ d\Omega \\
\mathbf{K} &= \sum_{i=1}^{n} \int_{\Omega_e} k\ \nabla\mathbf{N}\ (\nabla\mathbf{N})^T\ d\Omega \\
\mathbf{F} &= \sum_{i=1}^{n} \int_{\Gamma_e} \mathbf{N}\ q\ d\Gamma
\end{aligned}$$

where n is the total number of elements and $\mathbf{N}$ is the element shape function. $\mathbf{M}$,$\mathbf{K}$ and $\mathbf{F}$ has the dimensions of $N \times N$ and $N \times 1$ respectively. N is the total number of nodes.

Inverse Heat Conduction Problem (IHCP)

Inverse Heat Conduction Problem (IHCP) is the determination of the surface heat flux (or temperature) from measured transient temperatures inside a heat conducting body. In this definition, the initial temperature distribution is considered to be known. Another definition estimates the surface heat flux from transient measured interior temperatures and simultaneously the initial temperature distribution.

Most of IHCP studies are devoted to the determination of transient and/or spatially distributed heat flux on the boundary of the body [95, 96] and the heat transfer coefficient at the boundary must be accurately determined as a function of temperature, before solving the IHCP when experimental data are used as additional information. Important applications of these methods have been studied in various branches of thermal engineering area: quenching, casting and phase change process, hot rolling and

welding [97]. Few of these works consider experimental situations involving unknown heat sources. Silva Neto and Ozisik [98] used the conjugate gradient algorithm (CGA) to estimate the time-varying strength of a line source placed in a rectangular region with insulated boundaries, but the location of the source was specified. Le Niliot [99] studied linear inverse problems with two-point heat sources, and experimental results were presented. Ohmichi and Noda [100] developed a method for the determination of rectangular heat sources for two-dimensional steady state problems.

Let an interior of the domain Ω bounded by the curve $\Gamma = \Gamma_\theta \cup \Gamma_q$, where Γ_θ is the temperature described boundary and Γ_q is the unknown heat flux boundary due to the water cooling. Using the standard finite element discretization technique, convective heat flux vector $\tilde{q}^{n+1}$ at current time step on the boundary Γ_q is represented as

$$\tilde{q}^{n+1} = \left[\tilde{q}_1^{n+1}, \tilde{q}_2^{n+1}, \cdots, \tilde{q}_J^{n+1}\right]^T \tag{3.15}$$

where J is the total number of nodes on Γ_q. In order to determine the vector $\tilde{q}^{n+1}$, we assume that instantaneous time-varying temperature measurements, $\tilde{Y}^{n+1}$, are available at I measurement site nodes

$$\tilde{Y}^{n+1} = \left[\tilde{Y}_1^{n+1}, \tilde{Y}_2^{n+1}, \cdots, \tilde{Y}_I^{n+1}\right]^T \tag{3.16}$$

where I is the total number of nodes on the measurement site. The objective of the IHCP is to estimate the surface heat flux at the quenched site using the measurement site temperature data. Assume that $\tilde{\Theta}^{n+1}$ is the calculated temperature vector using inverse FEM at the I measurement site nodes. Therefore, the instantaneous error norm is defined as in [101]

$$S \;=\; (\tilde{Y}^{n+1} \;-\; \tilde{\Theta}^{n+1})^T \,(\tilde{Y}^{n+1} \;-\; \tilde{\Theta}^{n+1}) \tag{3.17}$$

Using a non-iterative technique proposed by [101] while minimizing the error norm with respect to the surface heat flux ($\partial\, S/\partial\, \tilde{q} \;=\; 0$, called as *matrix normal equation*), yields the *sensitivity coefficient matrix* $\tilde{\mathbf{X}}$ as in [101]

$$\tilde{X}_{ij} \;=\; \frac{\partial \tilde{\theta}_i^{n+1}}{\partial \tilde{q}_j^{n+1}} \tag{3.18}$$

where superscript on $\tilde{X}_{ij}$ is suppressed. Exploiting the advantage of FEM, the force vector as mentioned in Eq. (3.14) modified as in [101]

$$F^{n+1} \;=\; \tilde{\mathbf{D}}\; \tilde{q}^{n+1} \;+\; c \tag{3.19}$$

where c is determined by the known temperature distribution on Γ_θ and $\tilde{D}_{Pj} \;=\; \partial\; F_P^{n+1}/\partial\; \tilde{q}_j^{n+1}$, is a constant matrix of dimension $N \times J$. N is the total number of

nodes on $\bar{\Omega}$, and P is the global node number. From the DHCP (Eq. 3.14), the temperature vector is rewritten as in [101]

$$\Theta^{n+1} \;=\; \psi^n \;+\; \Delta t\; \mathbf{U}\; F^{n+1} \tag{3.20}$$

ψ^n and $\mathbf{U}$ in Eq. 3.20 is given as in [101]

$$\begin{aligned} \mathbf{U} \;&=\; (\mathbf{C} \;+\; \Delta t\, \mathbf{K})^{-1} \\ \psi^n \;&=\; \mathbf{U}\, \mathbf{C}\, \Theta^n \end{aligned} \tag{3.21}$$

Substituting Eq. 3.19 in Eq. 3.20, the measurement site calculated temperature vector $\tilde{\Theta}^{n+1}$ is given as in [101]

$$\tilde{\Theta}^{n+1} \;=\; \tilde{\psi}^n \;+\; \Delta t\; \tilde{\mathbf{U}}\; [\tilde{\mathbf{D}}\; \tilde{q}^{n+1} + c\,] \tag{3.22}$$

where $\tilde{U}_{iP} \;=\; U_{GP}$ and $\tilde{\psi}_i^n \;=\; \psi_G^n$ are mapped from the global nodes to the nodes on the quenched boundary Γ_q. The sensitivity coefficient matrix is explicitly rewritten from Eq. (3.18), and Eq. (3.22)

$$\tilde{\mathbf{X}}^{n+1} \;=\; \Delta t\; \tilde{\mathbf{U}}\; \tilde{\mathbf{D}} \tag{3.23}$$

Finally, from the minimization of the error norm, the unknown surface heat flux is given as

$$\tilde{q}^{n+1} \;=\; \left(\tilde{\mathbf{X}}^T \tilde{\mathbf{X}}\right)^{-1}\; \tilde{\mathbf{X}}^T (\; \tilde{Y}^{n+1} \;-\; \tilde{\psi}^n \;-\; \Delta t\; \tilde{\mathbf{U}}\; c\;) \tag{3.24}$$

The inverse solution algorithm is summarized as follows: (i) Θ^n, $\mathbf{C}$, $\mathbf{K}$ and c are known from the previous time step. $\tilde{Y}^{n+1}$ is the known current experimental temperature vector. Using these quantities, $\tilde{q}^{n+1}$ can be determined from Eq. (3.24). (ii) Force vector F^{n+1} has to be determined using the current $\tilde{q}^{n+1}$ according to the relation given in Eq. (3.19). (iii) Global temperature vector Θ^{n+1} can be determined by substituting F^{n+1} in Eq. (3.20). The computation of conductance and capacitance matrices and force vector are as similar as the solidification problem. The only unknown matrix to be addressed in the inverse problem is the $\mathbf{D}$ matrix. It can be defined as the derivative of force vector with respect to the nodal heat flux vector. Assuming $c = 0$, the force vector can be written as

$$F^{n+1} \;=\; \mathbf{D}\; q^{n+1} \;=\; \tilde{\mathbf{D}}\; \tilde{q}^{n+1} \tag{3.25}$$

from $\mathbf{D}$ and q, $\tilde{\mathbf{D}}$ and $\tilde{q}$ can be computed from the global to local mappings as explained before. In Eq. (3.14), the element force vector can be modified by substituting the unknown heat flux q as $q \;=\; N^T\; q^e$ and becomes

$$F^e \;=\; \int_{\Gamma_q^e} N\; N^T\; q^e\; d\Gamma_q^e \tag{3.26}$$

where q^e is the element unknown nodal heat flux vector. Now, the element form of **D** matrix can be given as

$$\mathbf{D}^e = \frac{\partial F^e}{\partial q^e} = \int_{\Gamma_q^e} N\, N^T\, d\Gamma_q^e \tag{3.27}$$

This matrix is a constant one because there is no material properties inside the integral. This can be easily computed without much difficulty.

3.4 Measured data revision

3.4.1 Methodology

Experimental and numerical analysis techniques for the heat transfer from the hot surfaces in the cooling experiments have been explained. A developed technique has applied to find the solutions. The developed technique uses MATLAB program which consists of steps to dispose non-logical data and purify such data. This technique depends on the revision of the measured data from the surface, which is supplied as the input to the numerical methods in calculating the heat flux. In the way of the solution, a developed technique is applied to the measurement data collected from experiments. Many researchers suggested some processings to the measurement data. Sengupta [4] suggested that the mathematical models based on thermo fundamentals should include the optimization practices. Bakken [102] interested to reduce the measurement error by using a special jag used to ensure that the thermocouples were placed near the surface and axially aligned each other. Also, the data smoothing techniques are used to eliminate noise and extract real trends and patterns. Schneider [103] applied a smoothing technique to all measured temperature values in order to remove any random noise. This technique was found applicable to achieve the stable inverse solution of heat transfer. In this research, the heat flux of aluminum samples has been estimated by using experimental results on inverse mathematical model.

A circular plate made of Aluminium alloy AA6082 is used during these experiments. The plate has been heated to an initial temperature of 560 ^{o}C. Then, it is cooled with water by spraying from a hydraulic nozzle. The measurement data of twenty selected points have been used. The distance between two points is 2 pixels, which is equal to 1.82 mm. First, the unrevised data is used as inputs to the numerical method. Further, one more time the data is revised and used as inputs to the numerical method. The heat fluxes were estimated and compared for the two different data (revised and unrevised data). The temperature profiles of the twenty points for deionized water are plotted as shown in figure 3.5. Especially in the film boiling region, a small fluctuation of the temperature can be seen. This fluctuation is caused by the fluctuation of the droplets cooling the surface. A closer view of the region marked with the square in figure 3.5 is shown in figure 3.6. A revised data technique is required in order to increase the accuracy

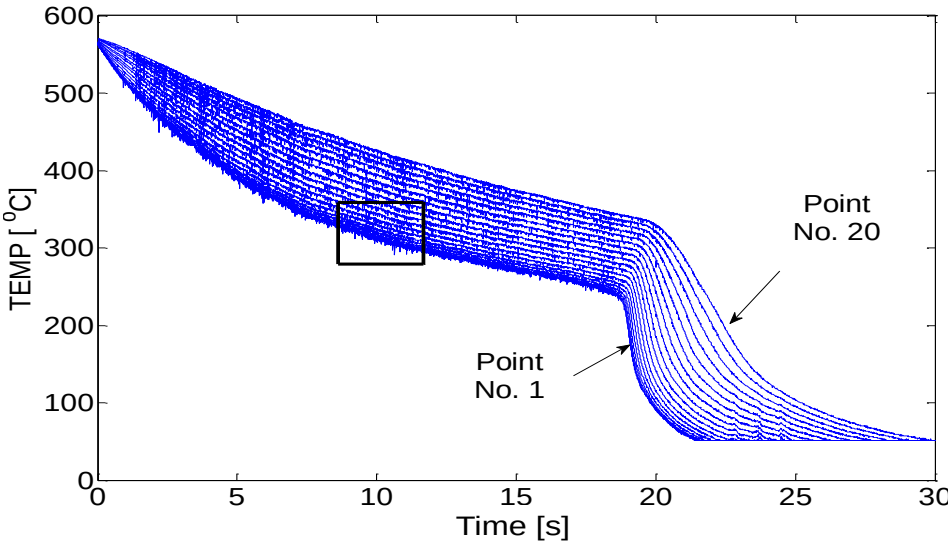

Figure 3.5: Real temperature profiles for twenty selected points

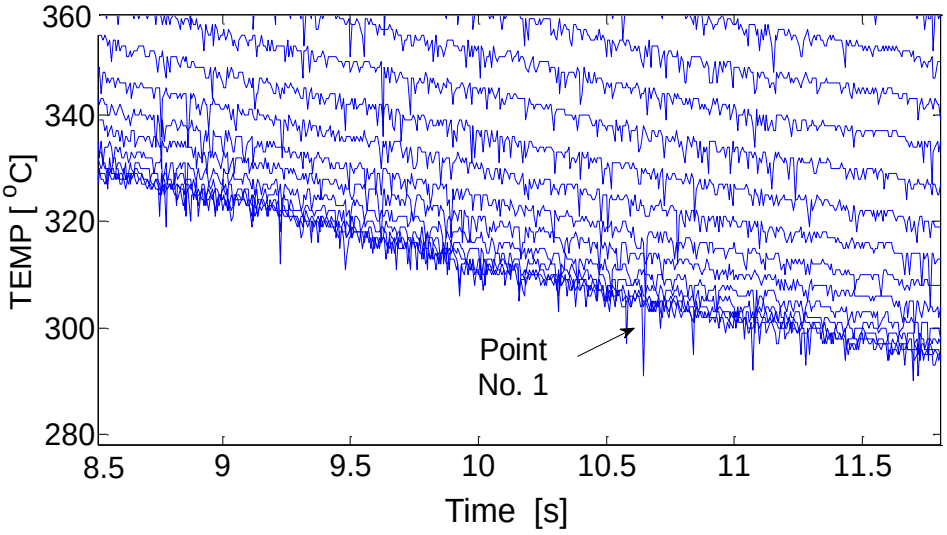

Figure 3.6: Real temperature profiles with an enlarged scale

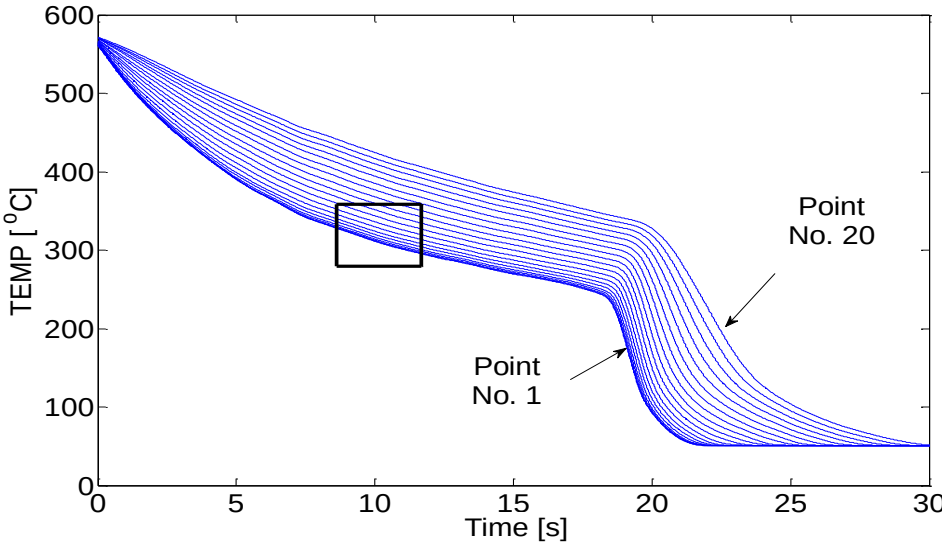

Figure 3.7: Revised temperature profiles for twenty selected points

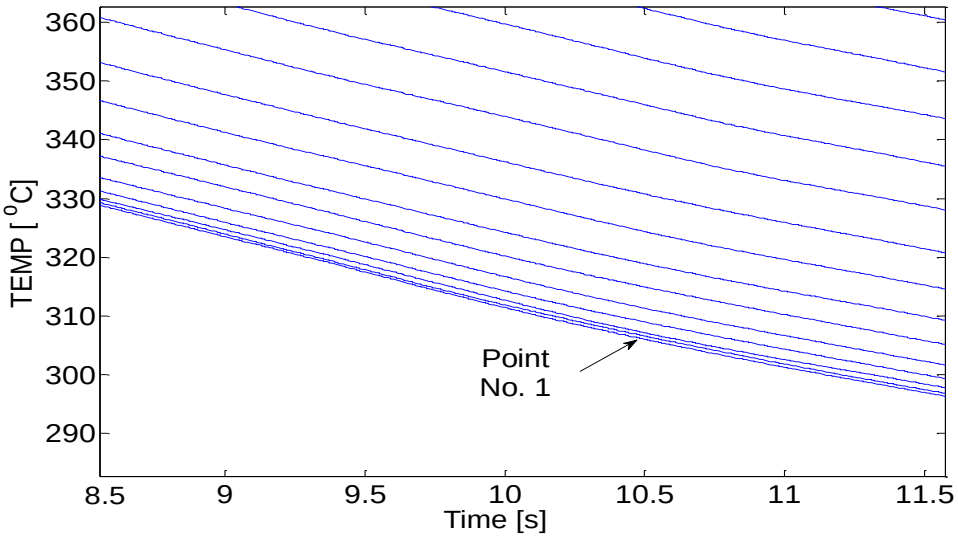

Figure 3.8: Revised temperature profiles with an enlarged scale

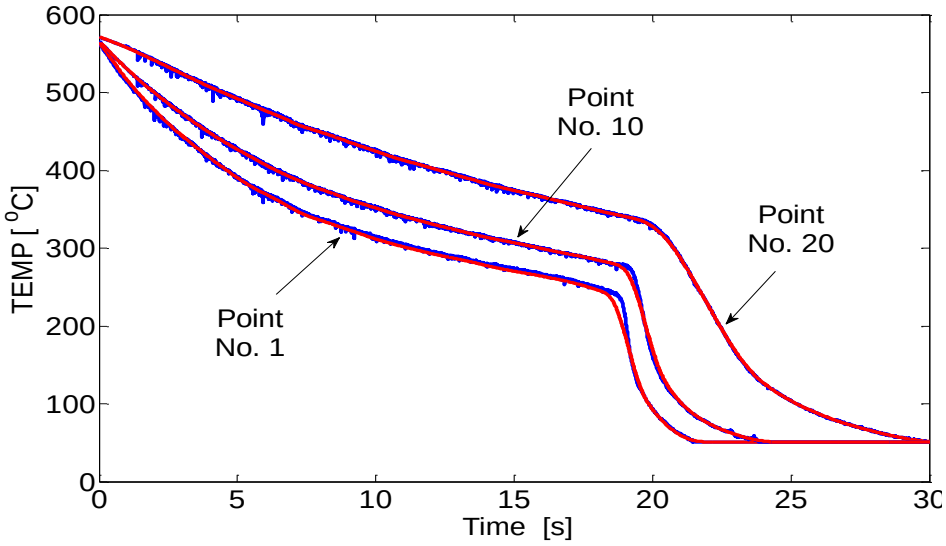

Figure 3.9: Three different points of measured data before and after using a revision

of the results. The revised temperatures are used as input data, which facilitates the use of numerical solutions. Figure 3.7 shows the same twenty points plotted after using MATLAB program where the temperature profiles appear without any fluctuations. The closer view is also shown in figure 3.8.

3.4.2 Calculated error of cooling rate

To confirm these results the errors of cooling rate were calculated in two cases (revised data and not revised data) at three different positions (three different points). The unit of the cooling rate is temperature/time (^{o}C/sec), it can be estimated by dividing each temperature data point by its corresponding time. The calculation for percentage error is used to evaluate the degree of error in measured data. The assessing percentage of the cooling rate error was formulated as.

$$\frac{RealValues - RevisedValues}{RealValues} \times 100\% \tag{3.28}$$

Figure 3.9 shows the temperature profiles at three different points 1,10 and 20. Each point is represented by two curves. One curve for the revised data, while the other for non revised data (original data). Figure 3.10 shows the temperature curves (same as in figure 3.9) for the first 18 seconds of the cooling (film boiling regime for this example). The calculated error percentage of the cooling rates in this regime is equal to zero because there is no difference between the revised and original data. The percentage of cooling rate error was evaluated at the position of Leidenfrost point. The absolute values of calculated errors at the Leidenfrost position for the three points 1,10 and 20 are equal to 2.79%, 1.85%, and 0.0% respectively. Figure 3.11 in enlarged scale of axes shows the error of the three different points at the Leidenfrost positions.

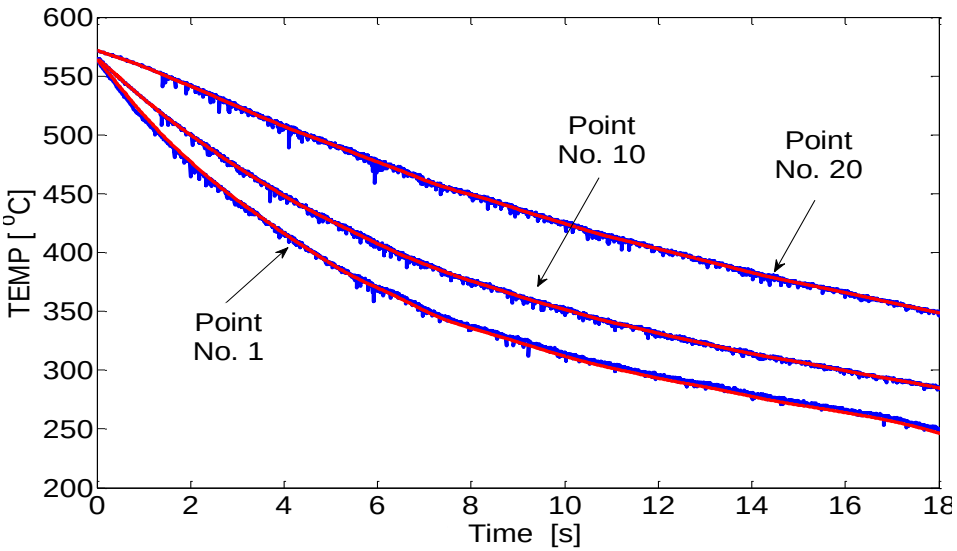

Figure 3.10: A real measured values and revised measured values of three points during film boiling

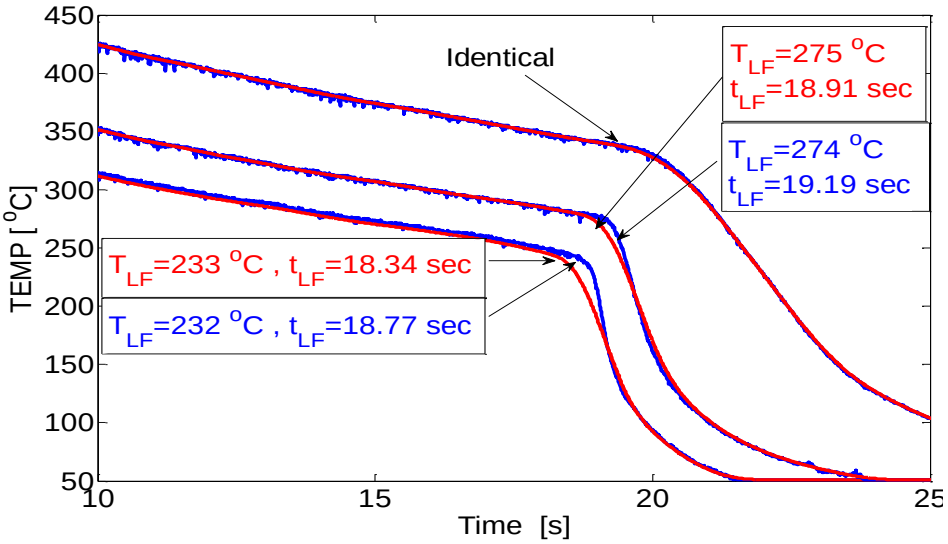

Figure 3.11: Errors in cooling rates at LFT regions of three points

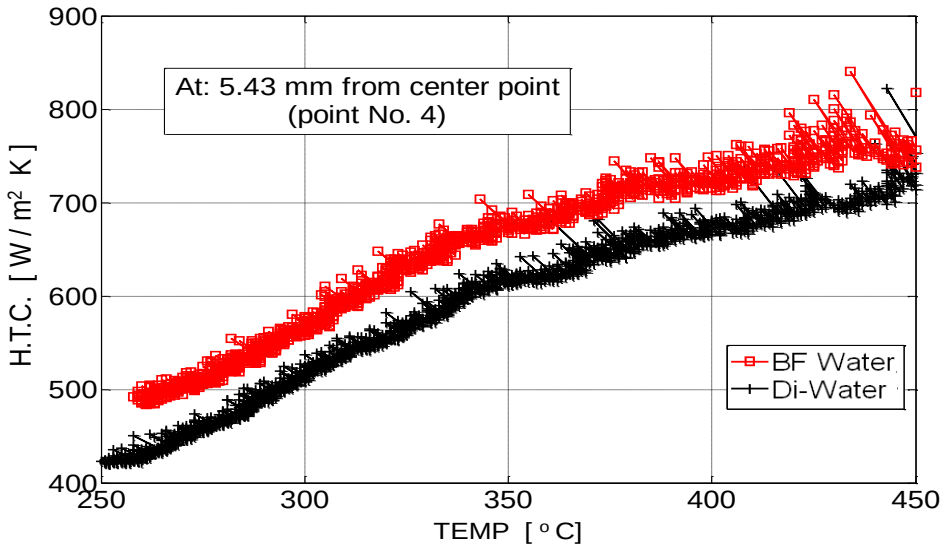

Figure 3.12: Heat transfer coefficients in film boiling region by using non revised data (simple analysis)

Table 3.1: LFT, MaxHF, and DNB-temperatures values

parameter	Di-water	BF-water
LFT ^{o}C	255	264
MaxHF MW/m^2	1.7	2.2
DNB-temperature ^{o}C	180	186

3.4.3 Result analysis using revised data

Figure 3.12 shows the heat transfer coefficients in film region for deionized and BF-water at the position 5.43 mm from center point of the plate. The original data has been used as an input data for the numerical method. It can be seen that the range of the fluctuation is about 25 $\mathcal{W}/m^2/K$. Figure 3.13 has been drawn with revised input data. The values represent the mean values of the HTC from Figure 3.13. Also, the inverse method (IHCP) has been applied to calculate the heat fluxes by using the experimentally revised and not revised data Figure 3.14 shows the estimated heat fluxes for these two coolants when a non-revised data is applied to the inverse method. The fluctuations are so high that the HTC can not be determined. Further, the inverse method is used again to estimate and plot the two heat fluxes by using revised measured data as input as shown in figure 3.15. Now the boiling heat transfer profiles are clearly seen. However, the fluctuations in the film boiling region are larger than using the simple analysis in Figure 3.12. The values of LFT, Max. Heat Flux (MaxHF), and DNB-temperature from figure 3.15 are estimated and compared as shown in Table 3.1. Also, the Table 3.1 shows the values of LFT temperatures and HTC which inferred from figure 3.12. From the results it can be concluded that, some improvements could be made to the measured

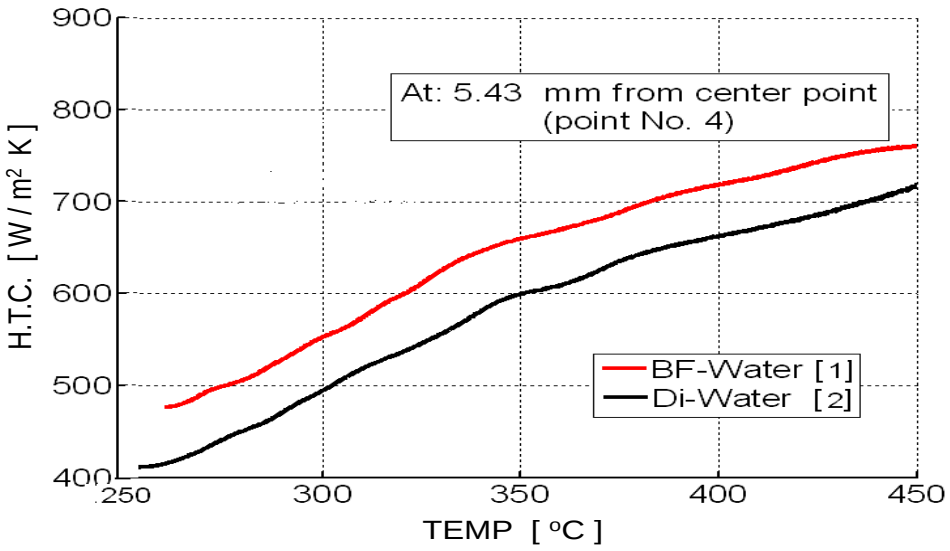

Figure 3.13: Heat transfer coefficients in film boiling region by using revised data (simple analysis)

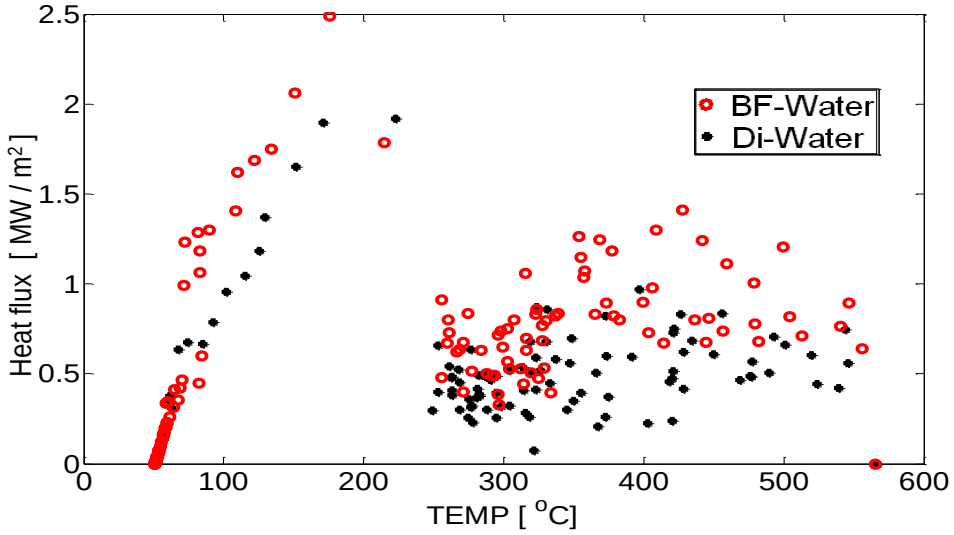

Figure 3.14: Heat fluxes results region by using non revised data (IHCP method)

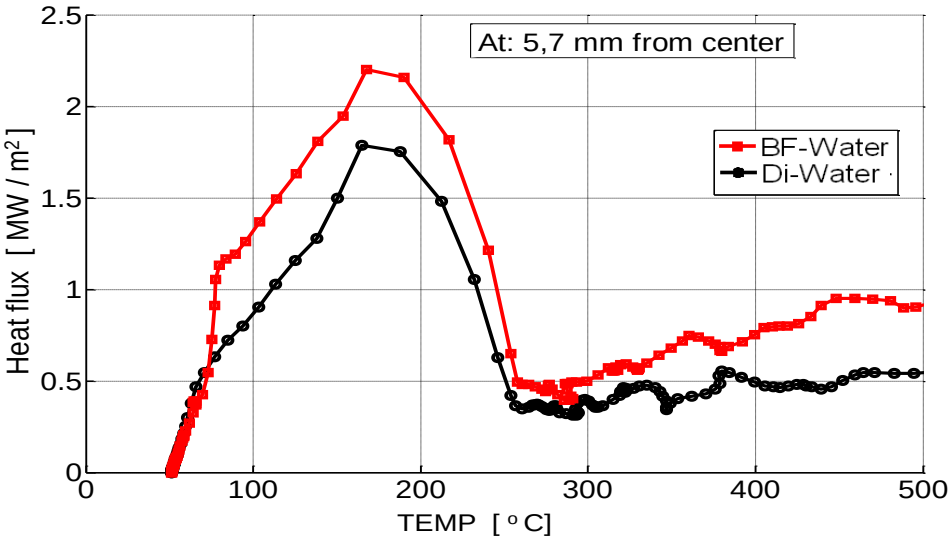

Figure 3.15: Heat fluxes results by using revised data (IHCP method)

data in order to make the results more useful and clear.

3.4.4 Effect of thermophysical property variations

The figure 3.16 shows the effect of the thermophysical properties variation on the calculated heat flux of the metal sample (AA6082) during cooling process. The figure is plotted based on the simple analysis (as explained in equation 3.2). In this equation, the numerator includes the conductive part and the storage energy part. These parts are all over the denominator of temperature difference. The conductive part includes the thermal conductivity λ while the second part includes the specific heat $C_p$of the metal sample. In this experiment, combination of some factors in the simple analysis is tested with the following illustration that can be noticed from the figure:

- The black solid line (1) shows the heat flux characteristic over temperature when the factor of conductive heat transfer is neglected and all the thermophysical properties are fixed (combination 1)
- The black dashed line (2) shows the heat flux characteristic over temperature when the factor of conductive heat transfer is neglected and C_p to be the only variable (combination 2)
- The blue solid line (3) shows the heat flux characteristic over temperature when the factor of conductive heat transfer is considered and all the thermophysical properties are fixed (combination 3)
- The blue dashed line (4) shows the heat flux characteristic over temperature when the factor of conductive heat transfer is considered and C_p to be the only variable (combination 4)

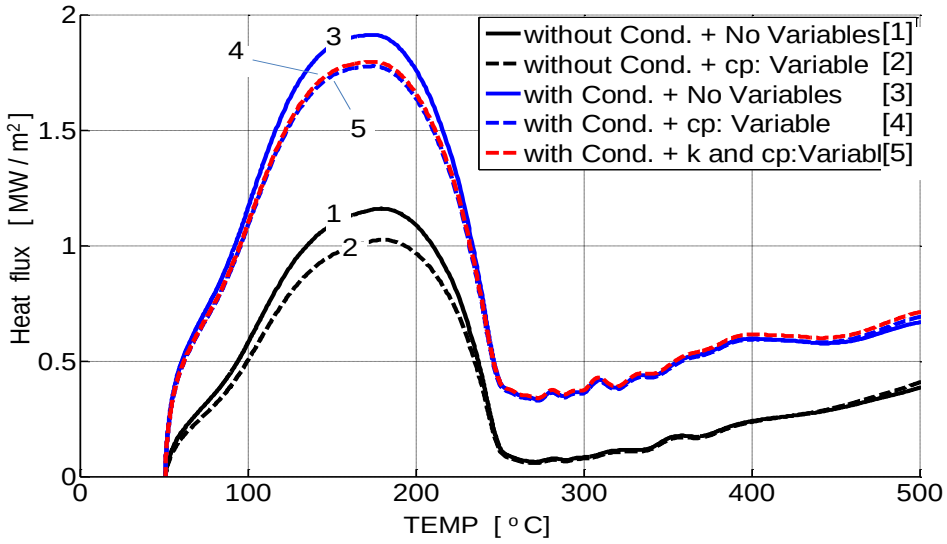

Figure 3.16: Effect of thermophysical property variations

- The red dashed line (5) shows the heat flux characteristic over temperature when the factor of conductive heat transfer is considered and λ dan C_p to be the only variable (combination 5)

From the figure, it is noticed that the DNB-temperature of the heat flux of any combination is of 180 ^{o}C. In the first and the second combinations, the calculated heat transfer is merely due to the total heat loss which depends on the specific heat (C_p) of the metal sample. However, from the heat flux calculation, the combination (1) shows the heat flux of about 1.17 W/m^2 while the combination (2) is of about 1 W/m^2. It means that by taking cp into consideration will decrease the calculated heat flux by 14.5 % when the factor of conductive heat transfer is not taken into consideration.

The other three combinations, the calculated heat transfer is taking conductive heat transfer into consideration. In the combination (3), the calculated heat flux value is of 1.9 W/m^2. In the combination (4), the calculated heat flux is of about 1.77 W/m^2 and the (5) is of about 1.8 W/m^2. It means that by taking C_p as variable (combination 4), it decrease 6.8 % of calculated heat flux. But when thermal conductivity (λ) is considered as well as variable (combination 5), it will increase the value of calculated heat flux by 1.7 % compared to the combination (4) and decrease of about 5.2 % to the combination (3). It means that the significant different of the 3, 4, and 5 combination is much more due to the C_p variation. Other comparison can be done by taking at the same condition with and without conductive heat transfer factor is taken into consideration during calculation. By comparing the combination (1) to the combination (3), the calculated heat flux

difference is about of 38.4 % while the combination (2) compared to combination (4) resulting the difference is of about 43.5 %. It means that the conductive heat transfer contribute about 38.4 - 43.5 % to the calculated heat transfer of the experiment.

Chapter 4

Water Quality

4.1 Influence of single salts

4.1.1 Magnesium sulfate ($MgSO_4$)

At first, the influence of the salt $MgSO_4$ will be discussed. All previous studies showed that this salt has the strongest effect. As reference water deionized water was used. This water was mixed with different amount of MgSO4. Figures 4.1, A.1 and A.2 depicts the cooling profiles at the three characteristic points (center point, 17 mm within spray cone and 34 mm outside spray cone) of the disc for all used salt concentrations. It can be seen that the Leidenfrost temperature is strongly shifted to higher values with increasing salt concentration. This results in a much faster cooling time. Figure 4.2, A.3 and A.4 shows the analysed heat flux with dependence on the surface temperature at these points. The parameter is again the salt concentration. From this figure, it can be seen that not only the Leidenfrost temperature is shifted to higher values with the salt concentration, but also the MaxHF, the belonging DNB-temperature and the heat flux at the Leidenfrost temperature.

Figure 4.3 shows the heat transfer coefficient at the center point as an example. Also, the HTC is influenced by the salt concentration in the same way. In the following, the two characteristic temperatures and the MaxHF will be discussed with dependence on the electrical conductivity for the composition of the salt mixture. All dissolved salts in water disintegrate into positively charged ions (cations) and negatively charged ions (anions). The electrical conductivity is a measure of the solution for the amount of the ions. The different cations and anions have an individual effect on the conductivity [104]. These conductivity factors are summarized in Table 4.1. The electrical conductivity is the sum of the factors f_i multiplied with the concentration C_i in mg/l.

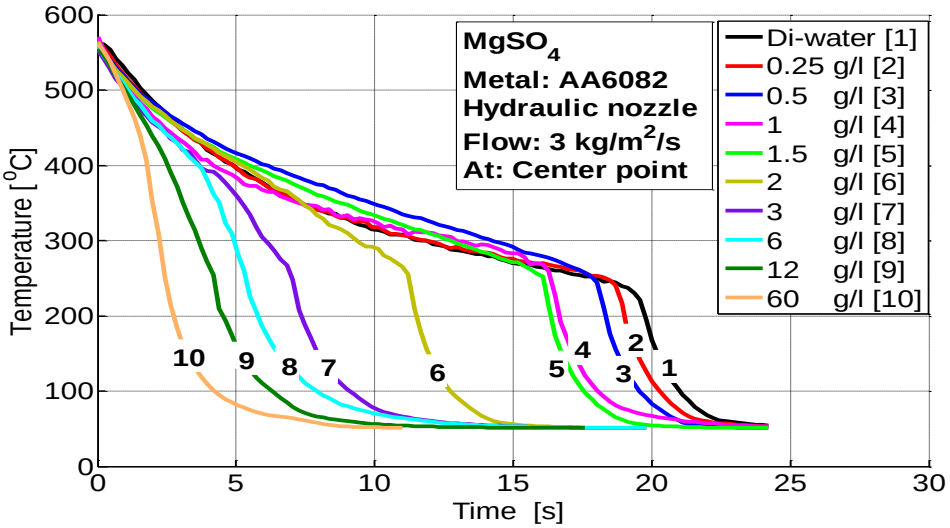

Figure 4.1: Temperature profiles for $MgSO_4$ solutions at center point

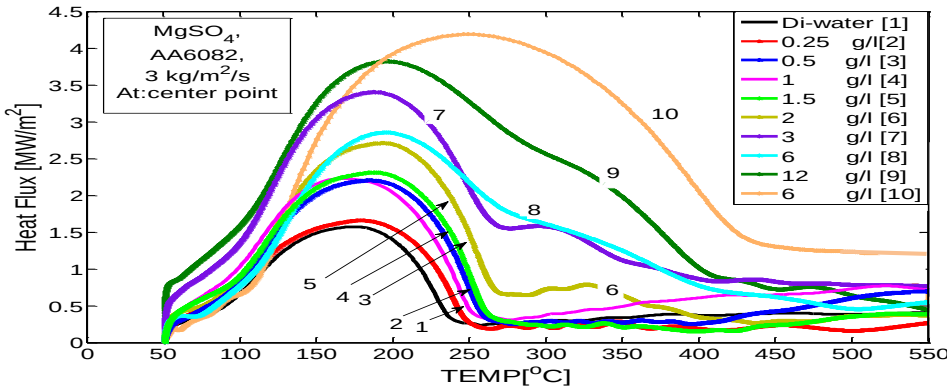

Figure 4.2: Heat fluxes for $MgSO_4$ solutions at 34 mm from the center

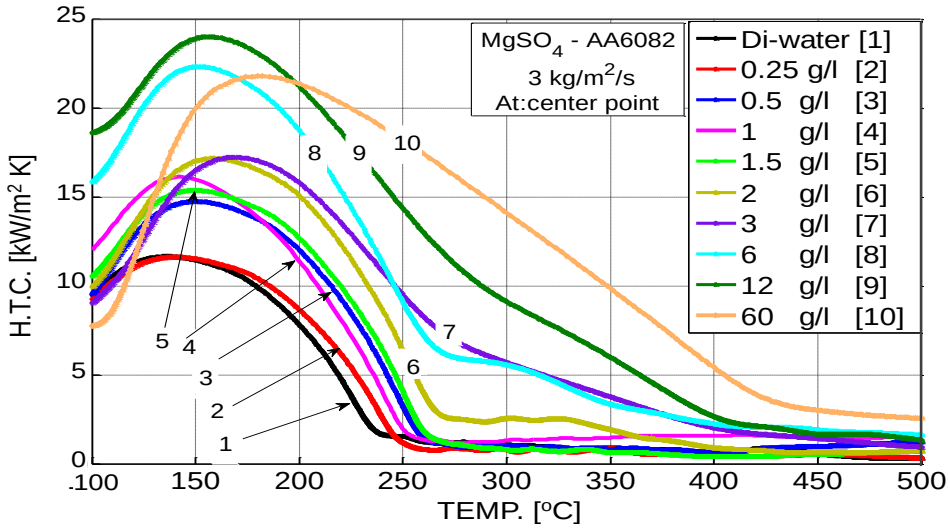

Figure 4.3: Heat transfer coefficient for $MgSO_4$ solutions at center point

Table 4.1: Conductivity factors for major ions [104]

Ion	Conductivity Factor μS/cm
Calcium (Ca^{+2})	2.6
Magnesium (Mg^{+2})	3.82
Potassium (K^{+1})	1.84
Sodium (Na^{+1})	2.13
Bicarbonate ($HCO_3{}^{-1}$)	0.715
Chloride (Cl^{-1})	2.14
Sulfate ($SO_4{}^{-2}$)	1.54
Nitrates ($NO_3{}^{-2}$)	1.15

$$EC = \sum (C_i \times f_i) \tag{4.1}$$

As an example for $MgSO_4$, the electrical conductivity is

$$EC = \left[\left(10^3 \times \frac{24}{120} C_i \times 3.82 \right) + \left(10^3 \times \frac{96}{120} C_i \times 1.54 \right) \right] \tag{4.2}$$

where 24, 96 and 120 are the molecular weights of Mg, SO_4 and $MgSO_4$ respectively. Figure 4.4 shows the calculated values as explained before with dependence on the concentration and the measured conductivity. It can be seen that the conductivity is proportional to the concentration until a value of 6 g/l. The calculated and measured values match well in this range.

Figure 4.5 shows the three characteristic parameters, Leidenfrost temperature, MaxHF and DNB-temperature, with dependence on the electrical conductivity for the three locations on the disc. The selected range is chosen until a value of 12000 μS/cm, in which the conductivity is proportional to the concentration. It can be seen that all three parameters seem to increase linearly with the conductivity and the concentration, respectively. Qiang et al. [105] measured also the heat transfer with spray cooling of deionized water and dissolved $MgSO_4$. They used the same impingement density of 3 kg/m^2/s, as in this study. Their values for the MaxHF of the deionized water and the increase with the salt concentration match perfectly with the results of this study. Their DNB-temperature also increased with salt concentration, but the values cannot be compared because they used copper as

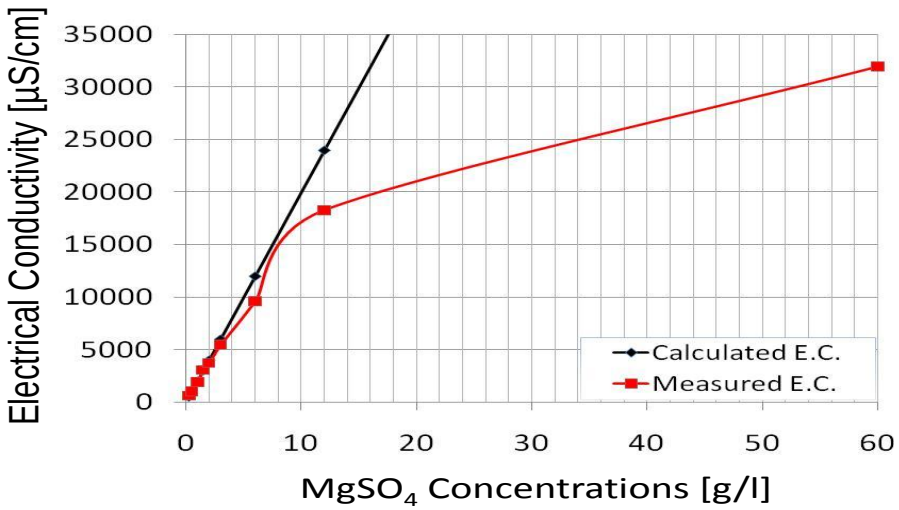

Figure 4.4: The calculated and measured ECs of $MgSO_4$ solutions

the metal sample. The Leidenfrost temperature could not be measured because the initial temperature was only 240 ^oC.

4.1.2 NaCl, $NaHCO_3$, Na_2SO_4 and Na_2CO_3

Real waters include different kinds of salts. The Figures 4.6 to 4.9 show the cooling profiles for the salts NaCl, $NaHCO_3$, Na_2SO_4 and Na_2CO_3, respectively at center point. The cooling profiles at 17 mm and 34 mm from center have been shown in A.5 to A.12. In these cases, a pneumatic nozzle and Nickel as the metal type was used. Therefore, the cooling times cannot be compared with those of $MgSO_4$. Also for these salts, the cooling time is shortened with increasing concentrations. In Figure 4.10, the cooling profiles of the used salts are compared for the same concentration of 0.5 mol/l. All salts increase the cooling rate. The salt $MgSO_4$ has the strongest effect, while the salt NaCl has the weakest effect. This principal fact matches with the results reported from Qiang et al. [105], Huang [58] and Jeschar et al. [106]. These authers also report that the salts $MgCl_2$, KCl and $CaCl_2$ increase the Leidenfrost temperature and MaxHF.

4.1.3 $CaCO_3$

In Figures 4.11, A.13 and A.14 the cooling profiles are shown for three concentrations of dissolved $CaCO_3$. Here the hydraulic nozzle and AA6082 as a metal were used again. Also in this case, the cooling times are shortened with the concentration. Figures 4.12 and Figure 4.13 show the corresponding heat flux and the HTC, respectively, with dependence on the surface temperature. Figure 4.14 shows the

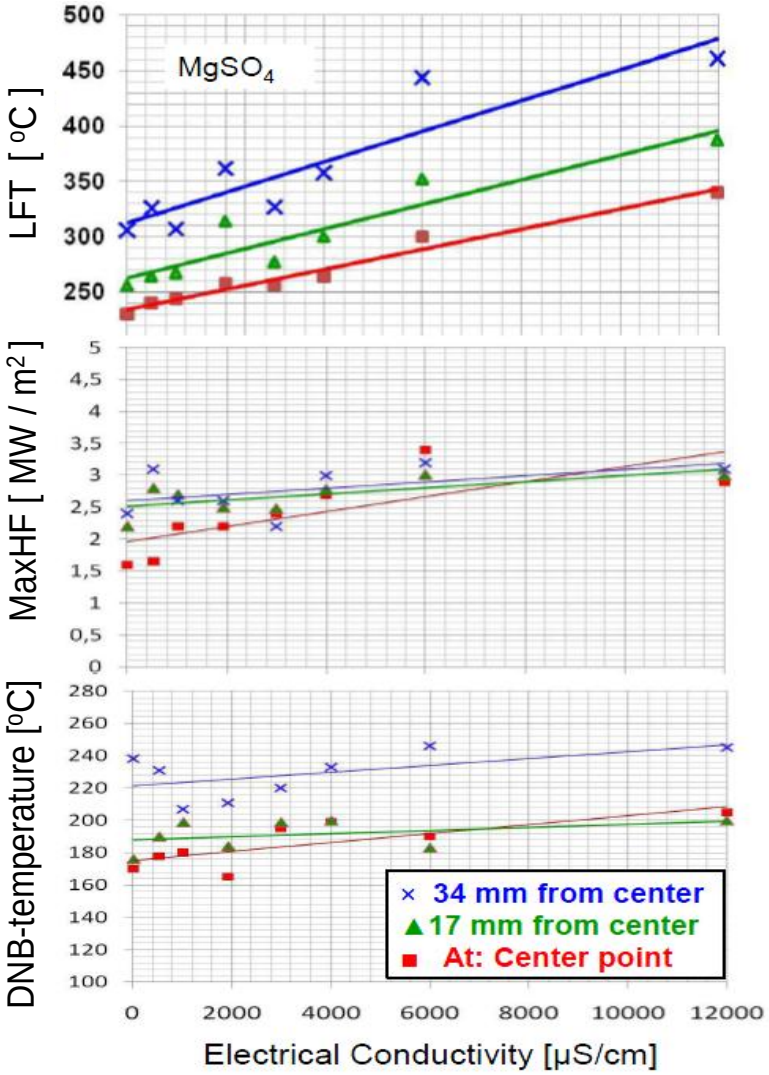

Figure 4.5: LFT, MaxHF and DNB-temperature of $MgSO_4$ solutions at the three different positions

LFT, MaxHF and DNB-temperature with dependence on the concentration. All properties seem to increase linearly with the concentration, as it was already the case with the salt $MgSO_4$.

4.2 Casting lubricants

In the continuous casting process lubricants are often used. Typical lubricants are Borax ($Na_2B_4O_7.10H_2O$), graphite powder and carbon black. Borax dissolves in water, as is the case for salts. Graphite powder and carbon black don't dissolve.

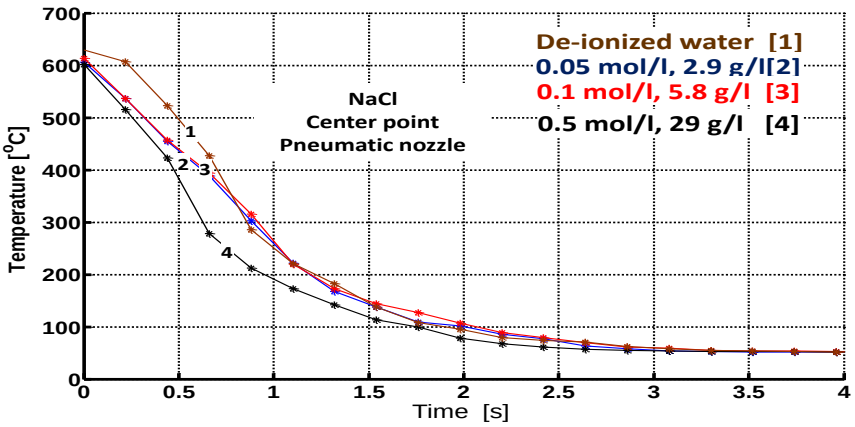

Figure 4.6: Temperature profiles for NaCl solutions at center point

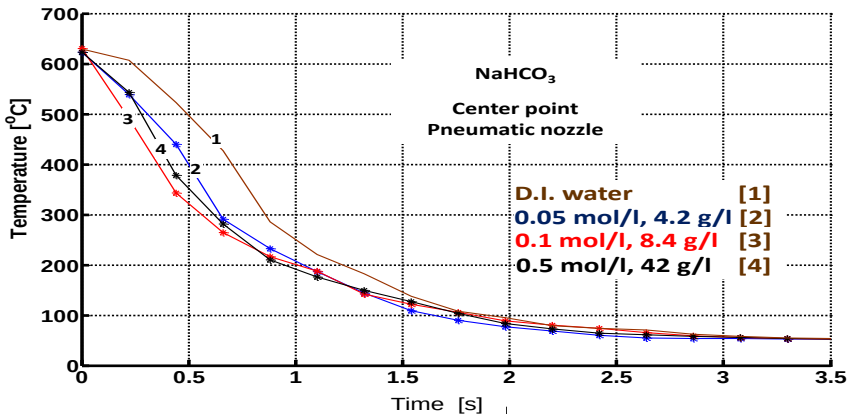

Figure 4.7: Temperature profiles for $NaHCO_3$ solutions at center point

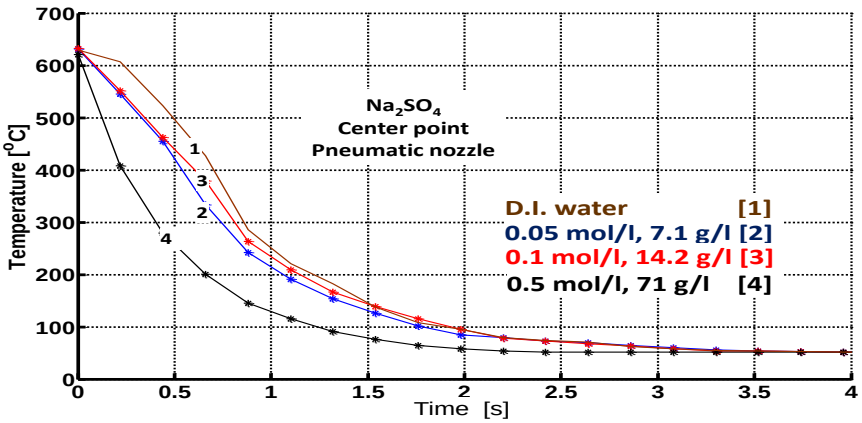

Figure 4.8: Temperature profiles for Na_2SO_4 solutions at center point

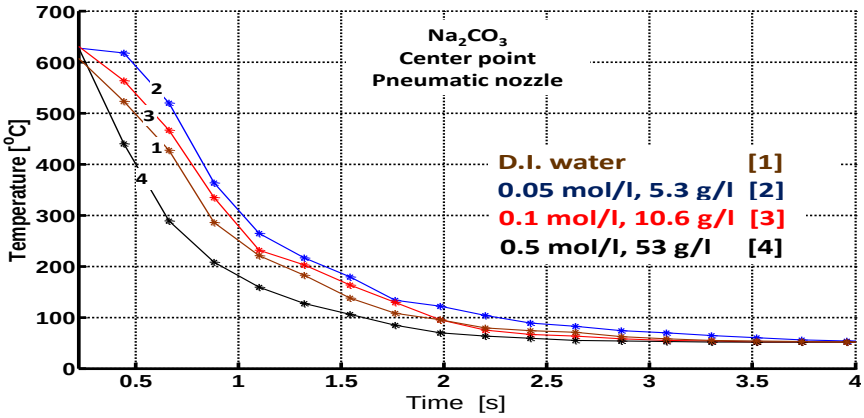

Figure 4.9: Temperature profiles for Na_2CO_3 solutions at center point

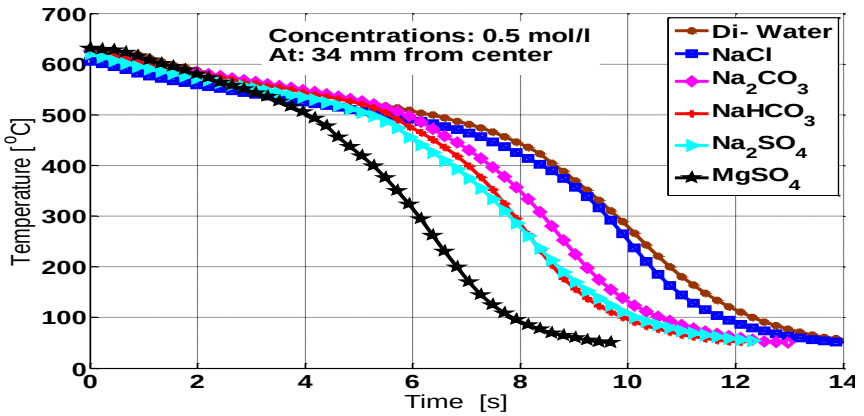

Figure 4.10: Temperature profiles of five salt solutions used in atomized spray at 34 mm from center

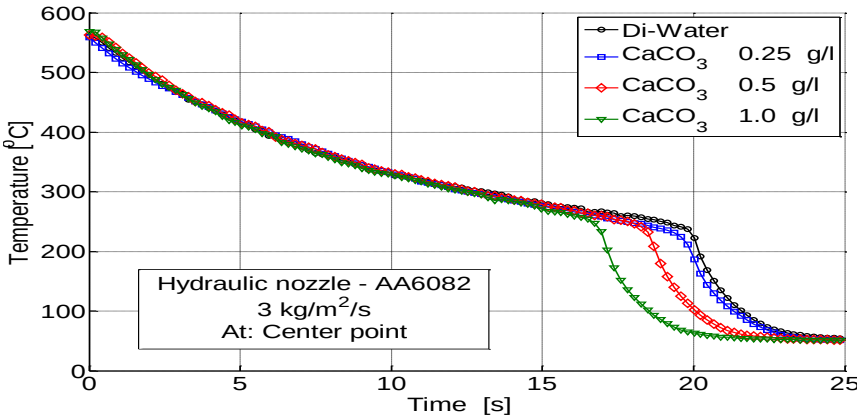

Figure 4.11: Temperature profiles for $CaCO_3$ solutions at center point

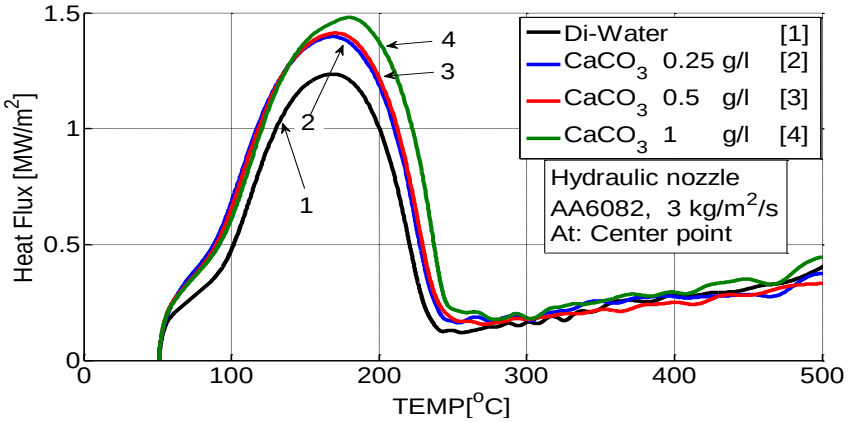

Figure 4.12: Heat flux vs. surface temperature for $CaCO_3$ at center point

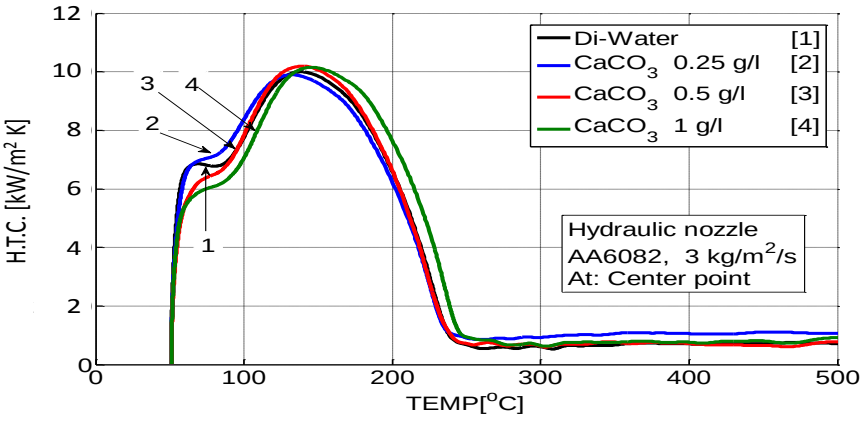

Figure 4.13: Heat transfer coeffcient vs. surface temperature for $CaCO_3$ at center point

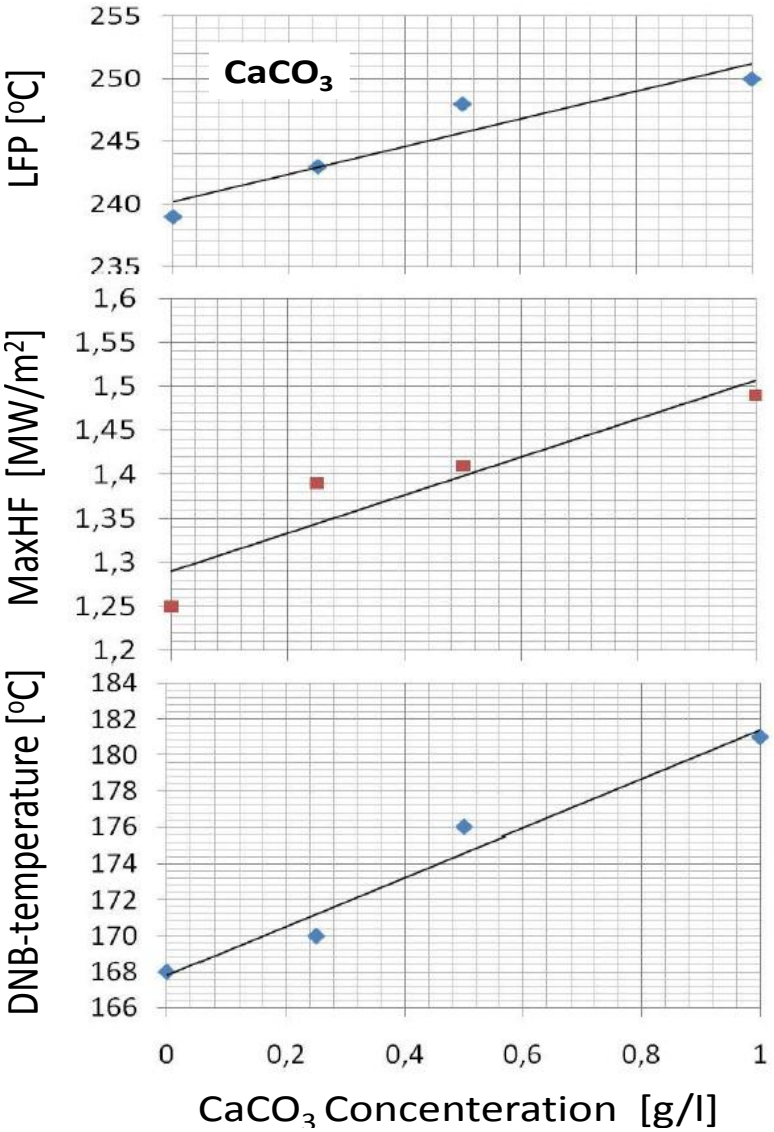

Figure 4.14: LFT, MaxHF and DNB-temperature of $CaCO_3$ at center point

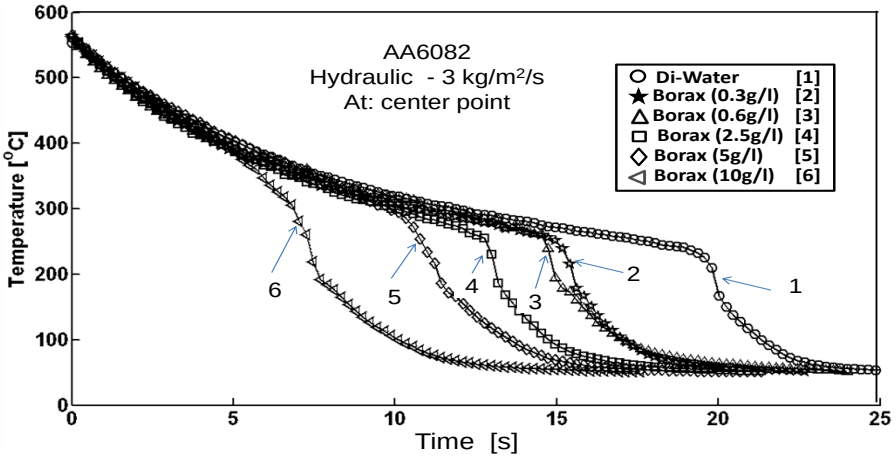

Figure 4.15: Temperature profiles for Borax at center point

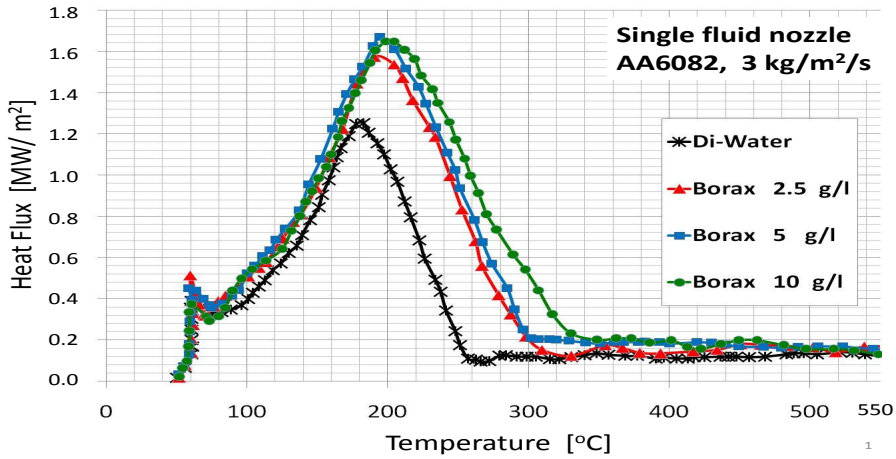

Figure 4.16: Heat flux vs surface temperature for Borax at center point [107]

4.2.1 Borax

Figures 4.15, A.15 and A.16 shows the cooling profiles for different borax concentrations in the same method as before of the three characteristic positions. As the concentration of Borax increases the cooling times are shortened again. Figure 4.16 shows the heat flux with dependence on the surface temperature. The LFT and the MaxHF are shifted to higher values with the concentration. Their values can be seen in Figure 4.17 with dependence on the borax concentration. All three parameters increase linearly with the concentration.

4.2.2 Graphite powder and carbon black

In Figure 4.18, photographs depict the water with graphite powder. The left photo shows the water after it was well stirred. The following two photographs show the water after 5 and 10 minutes. It can be seen that the graphite powder sinks to

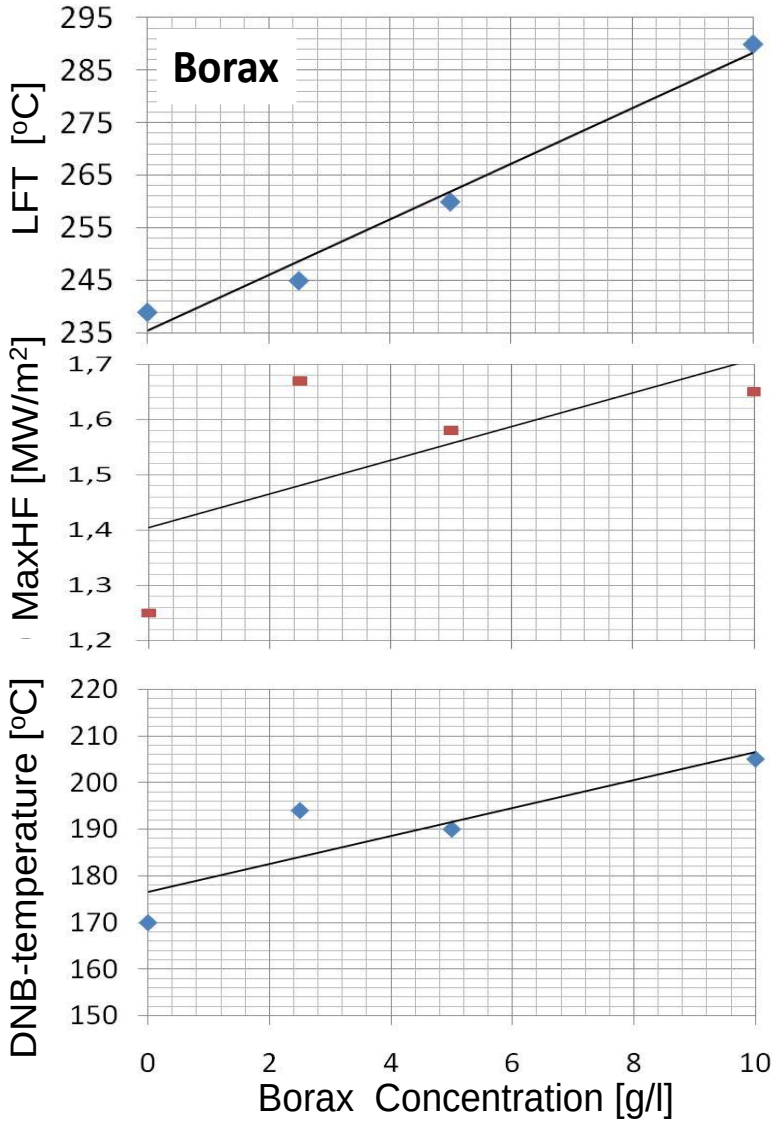

Figure 4.17: LFT, MaxHF and DNB-temperature of Borax at center point

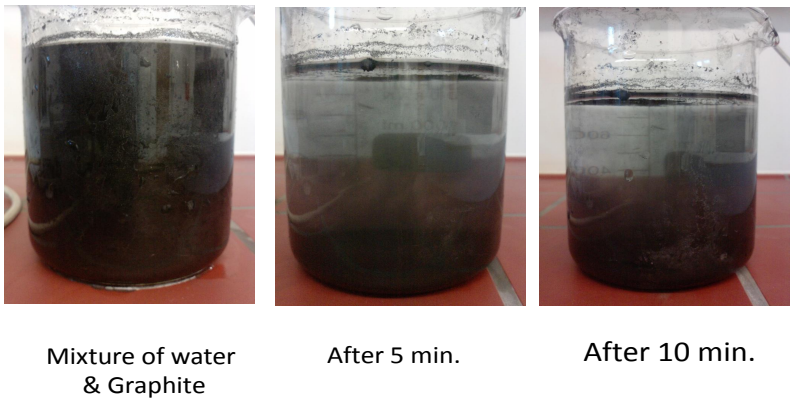

Figure 4.18: Graphite after (a) mixing (b) 5 minutes (c) 10 minutes

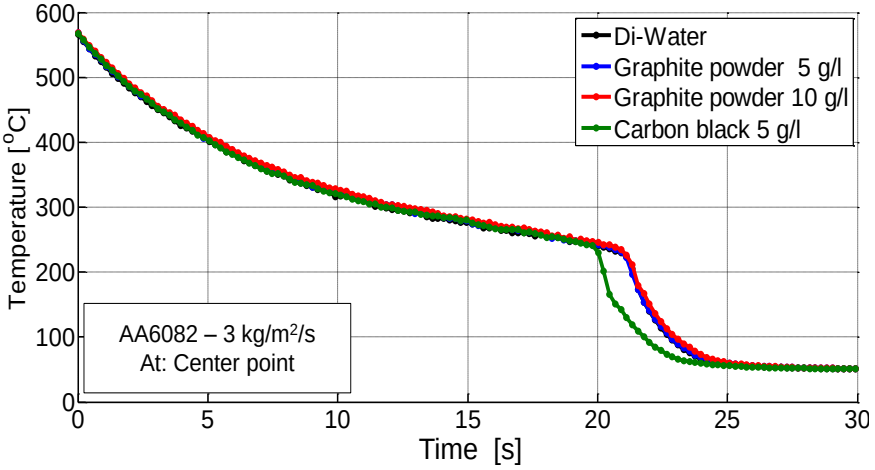

Figure 4.19: Temperature profiles for graphite and carbon black at center

the bottom. Therefore, it doesn't dissolve. Figure 4.19, A.17 and A.18 shows the cooling profiles for graphite powder with the two concentrations and for carbon black. A significant influence cannot be seen. Typical concentrations are much lower than those used in the experiments. Therefore, these non-dissolved solids have no influence on the heat transfer.

4.3 Surfactant

In casting processes of aluminium alloys and also in hardening processes of steel alloys surfactants are deposited into the water to prolong the cooling rate. Figures 4.20 A.19 and A.20 shows the cooling profiles for different concentrations of a typical surfactant used in industry. It can be seen that with the addition of the surfactant in the range of ppm, the cooling time is prolonged. In Figure 4.21 and Figure 4.22, the HF and the HTC, respectively, are shown with dependence on the surface temperature. The HTC in the region of the film boiling is dependent on the concentration. However, the LFT and the MaxHF decrease with the concentration. This decrease is shown in Figure 4.23 for the characteristic positions. The LFT, MaxHF and DNB-temperature appear to decrease linearly with the concentration.

4.4 Mixtures of surfactant and dissolved matter

As seen in the chapters before, surfactants prolong the cooling time, while dissolved matter, such as Borax and $MgSO_4$, decrease the cooling time. Therefore, in this chapter, it will be considered what the impact is of mixtures between lubricants and dissolved matter. Figures 4.24, A.21 and A.22 show the cooling profiles

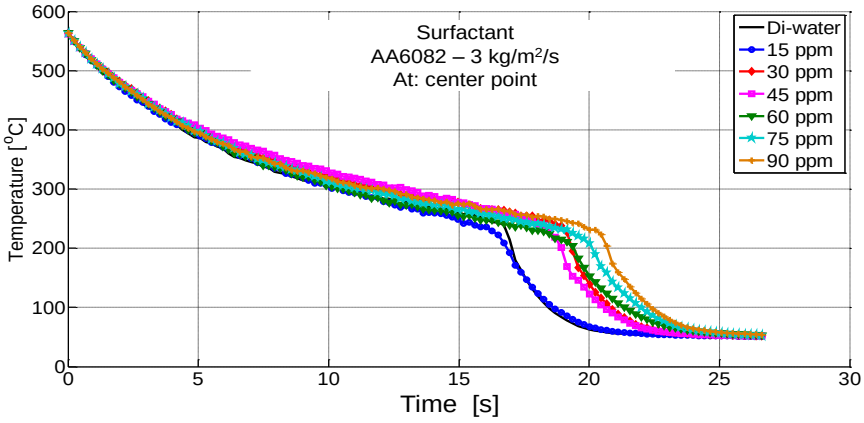

Figure 4.20: Temperature profiles for surfactant at center point

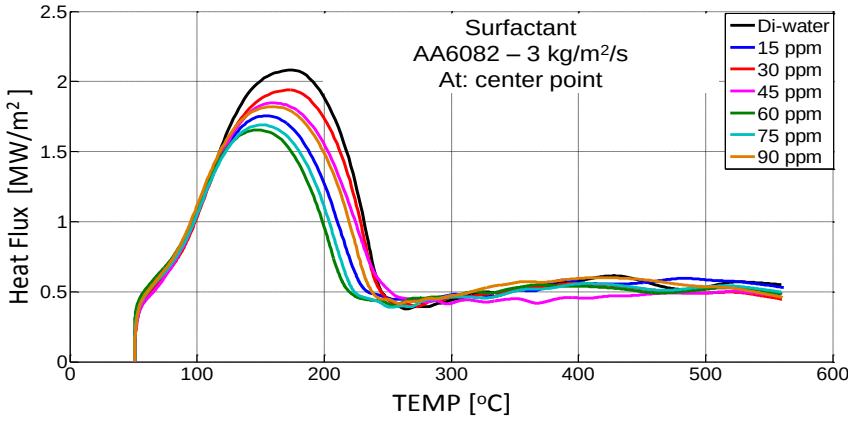

Figure 4.21: Heat flux vs. surface temperature for surfactant at center point

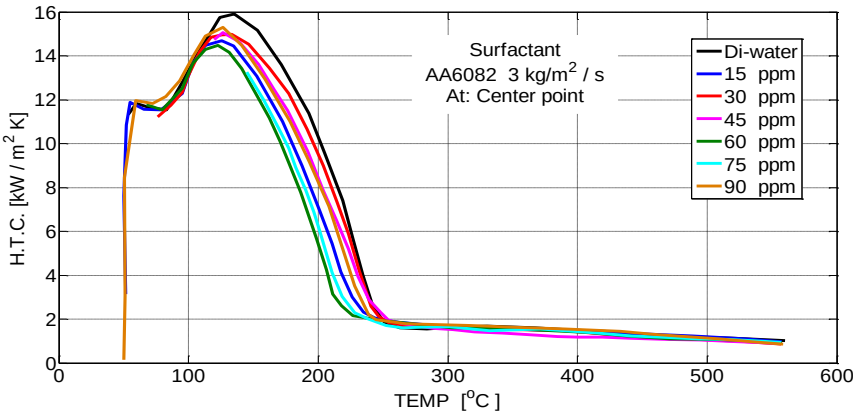

Figure 4.22: Heat transfer coeffcient vs. surface temperature for surfactant at center

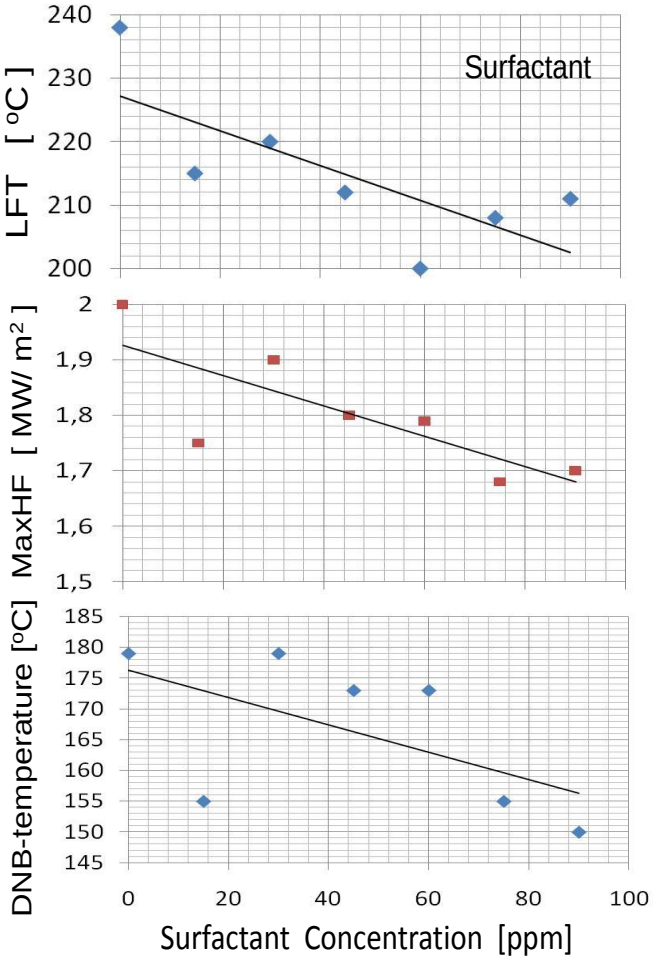

Figure 4.23: LFT, MaxHF and DNB-temperature of surfactant at center point

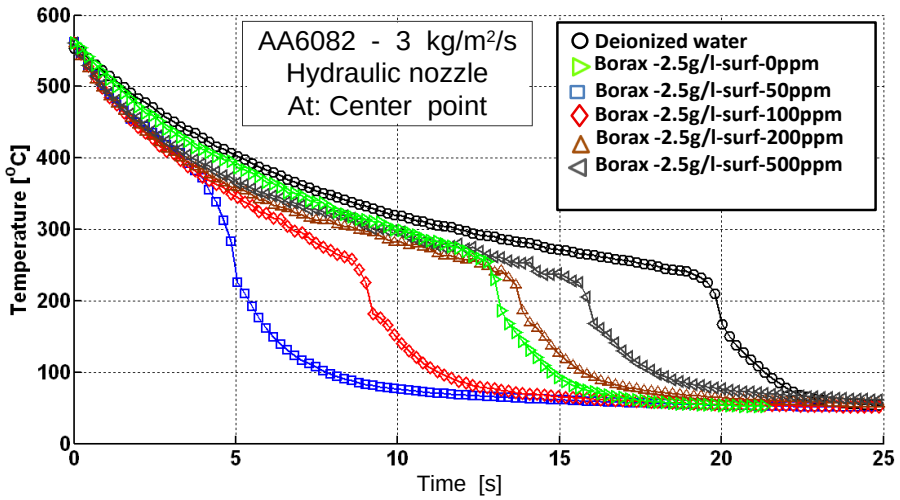

Figure 4.24: Temperature profiles for Borax/surfactant mixture [107]

of deionized water and deionized water with 2.5 g/l dissolved borax, which was mixed with different concentrations of the surfactant. The lowest concentration of the surfactant with 50 ppm has an unexpected effect. This concentration produces the shortest cooling time. In comparison to the deionized water with only dissolved Borax, the cooling time is dramatically shortened, approximately by a factor of two. The surfactant concentrations above 50 ppm continuously prolong the cooling time. However, the mixture with 100 ppm surfactant has an even a shorter cooling time compared to the 2.5 g/l borax water without surfactant. All mixtures up to the very high concentration of 500 ppm surfactant have a significantly shorter cooling time than the deionized water. The borax has a stronger effect for shortening the cooling time than the surfactant for prolonging the cooling time. However, the levels of the concentrations are in a different range.

Figures 4.25, A.23 and A.24 show the cooling profiles for deionized water, deionized water with 3 g/l $MgSO_4$ and again four different concentrations of the surfactant. At the center point and the distance 17 mm, the surfactant shortens the cooling time. The highest concentration of 500 ppm has the shortest cooling time. The principal effect is similar to borax. At high concentrations of dissolved matter, the surfactant seems to decrease the cooling time instead of prolonging the time. As a consequence, if surfactants are used to prolong the cooling time, the water should be free of dissolved matter, especially salts.

4.5 Dissolved gases

Water can also dissolve different amounts of gases. The gas components with the highest concentration are oxygen, nitrogen and carbon dioxide. The ratio of N_2

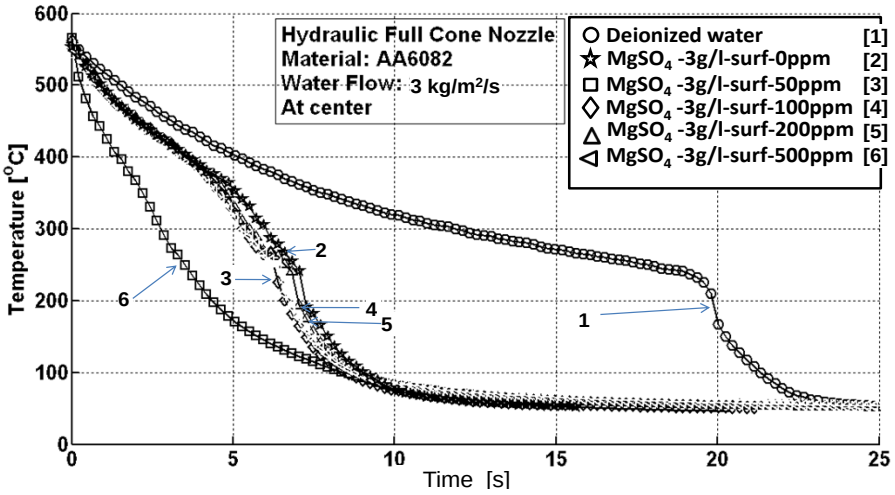

Figure 4.25: Temperature profiles for $MgSO_4$/surfactant [107]

to O_2 in water is approximately 2:1, instead of 4:1 in the atmosphere. Dissolved carbon dioxide dissociates into HCO_3 and H, which is designed as carbon acid. To measure the impact of these gases, deionized water was dispersed with a flow of O_2, N_2, CO_2 and air for a time period of 15 minutes. Therefore, it is assumed that the water has the equilibrium concentration which is the maximum value. Also for comparison, drinking mineral water (sparkling water) was used which has a high concentration of CO_2 and includes salts.

Figures 4.26, A.25 and A.26 show the cooling profiles for the water with the different dissolved gases. It can be seen that CO_2 significantly prolongs the cooling time. The water with the dissolved air has the shortest cooling time. The oxygen seems to have no effect. The nitrogen shortens the cooling time. As a consequence, the water with the dissolved air should have the same cooling time as the water with dissolved nitrogen. However, the air shows a stronger influence than the pure nitrogen. This effect cannot be explained. Therefore in the future, further experiments with dissolved gases should be done. Figure 4.27 and Figure 4.28 show the HF and HTC, respectively. The dissolved air and nitrogen shift the MaxHF and the LFT to higher values. Also, the HTC in the film boiling region has higher values. These effects are also reported from Jeschar et al. [106] for the cooling of a nickel sphere immersed in a bath of water. In the figures concerning the dissolved gases, the profiles for carbonated mineral water (sparkling water) are also included. Its profiles lie between the deionized water and the deionized water with dissolved pure carbon dioxide. This can be explained by the two opposite effects of this mineral water. The carbon dioxide prolongs the cooling time, while the salts decrease.

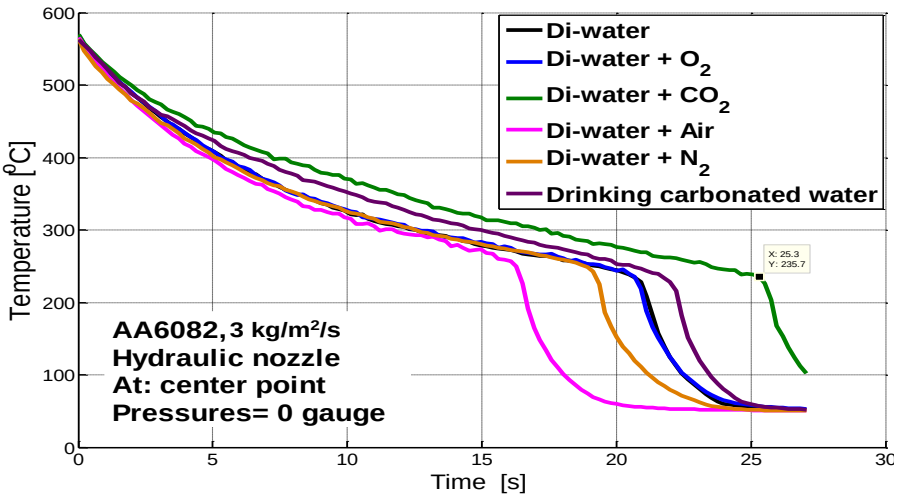

Figure 4.26: Temperature profiles for dissolved gases at center point

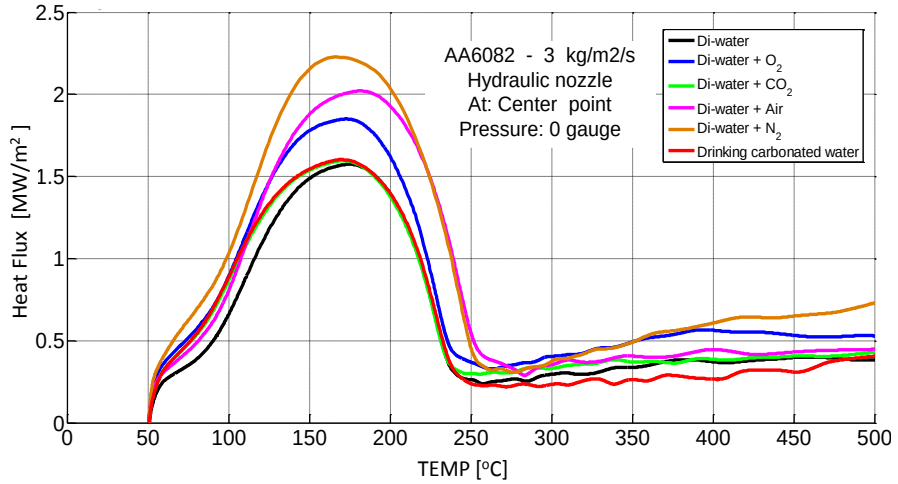

Figure 4.27: Heat flux vs. surface temperature for dissolved gases at center point

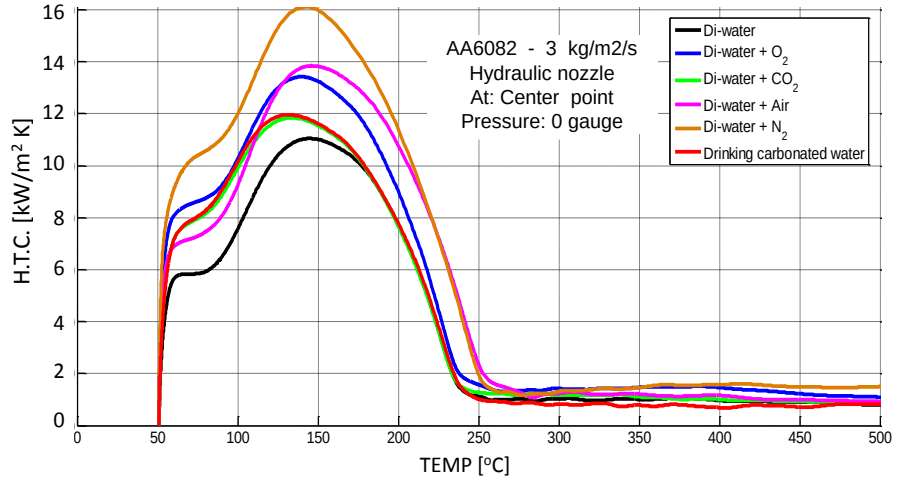

Figure 4.28: Heat transfer coeffcient of dissolved gases at center point

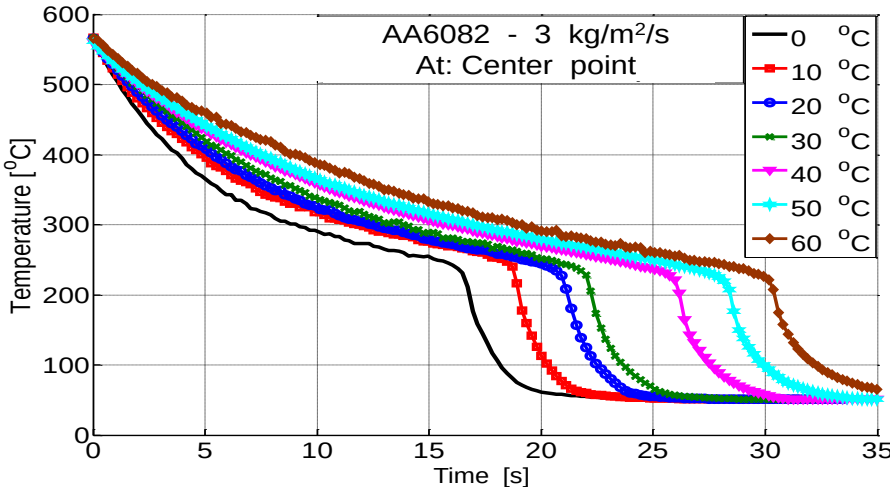

Figure 4.29: Temperature profiles for spray water temperature at center point

4.6 Water temperature

As it is known from literature, the temperature of the water also influences the cooling rate. Therefore, Figure 4.29, A.27 and A.28 shows the cooling profiles for different temperatures of the water. With increasing temperature, the cooling rate is decreased. Figure 4.30 and Figure 4.31 show the HF and the HTC, respectively, again with independence on the surface temperature. The decrease of the LFT, MaxHF and DNB-temperature are shown in Figure 4.32. The values decrease approximately linearly with the temperature in the range of 0 ^oC to 60 ^oC. Figure 4.33 shows the HTC in the film boiling region. From these last figures it can be seen that the temperature of the water has a strong impact on the cooling rate. Therefore, all experiments in this study were conducted with a constant temperature of 15 ^oC.

4.7 Real waters

In real waters, various salts are dissolved. Therefore, the cooling rate was measured for eight different waters which were used in some plants for the continuous casting of Aluminium and Copper alloys. In Table 4.2, the analysis of these waters are summarized. The analysis of the deionized water used is also included. All waters are ranked by the measured electrical conductivity, which is named as E.C. LAB. The conductivity was also calculated from the concentrations using Eq.(4.1) and the factors given in Table 4.1 and named as E.C. CAL. It can be seen that these values differ in some cases from the measured values. The differences are in the range of 0 to 20 % related to the measured values. The table also includes the pH value and the hardness. The pH value varies in a range of 7.1 to 9.1. A relation

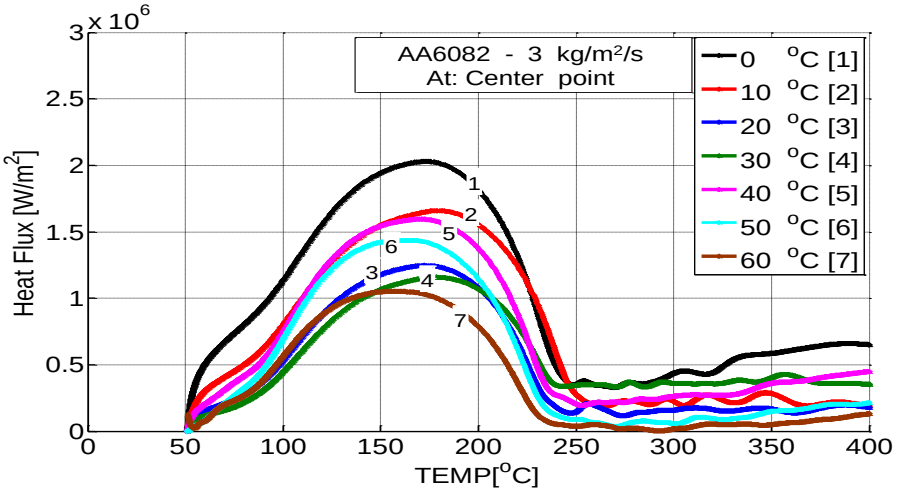

Figure 4.30: Heat flux vs. surface temperature for spray water temperature at center point

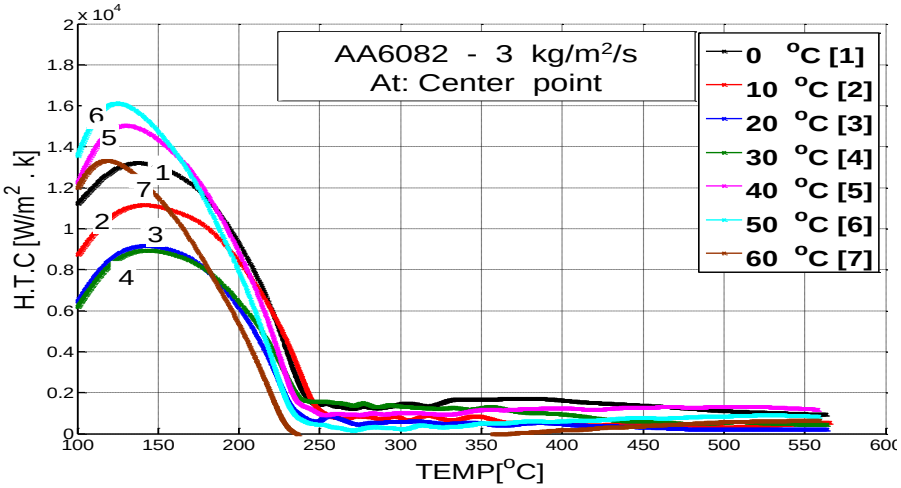

Figure 4.31: Heat transfer coeffcient vs. surface temperature for spray water temperature at center point

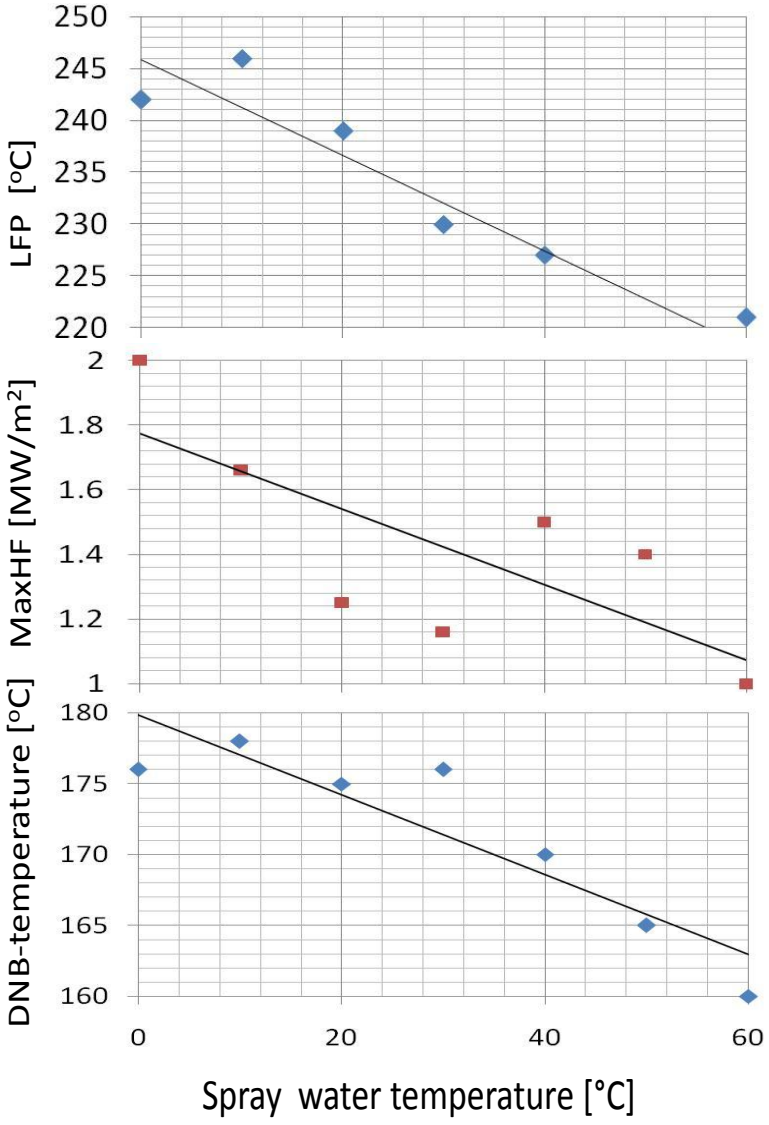

Figure 4.32: Effect of spray water temperature on LFT, MaxHF and DNB-temperature at center point

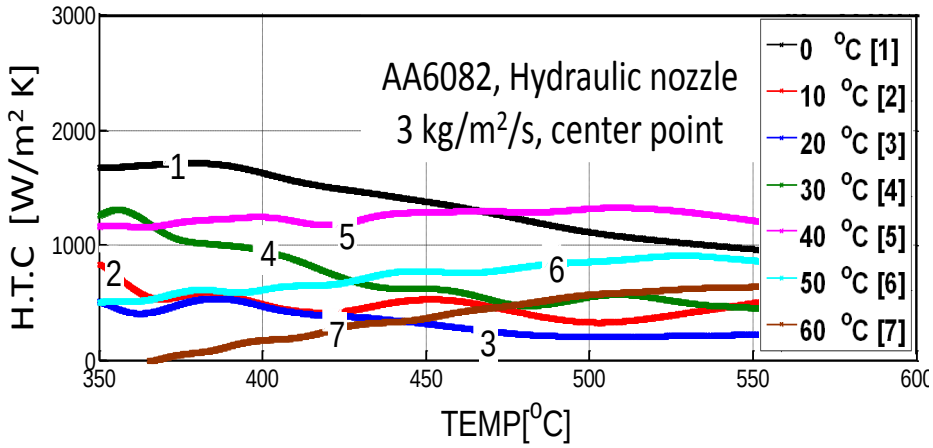

Figure 4.33: Heat transfer coeffcient of spray water temperature in the film boiling region at center point

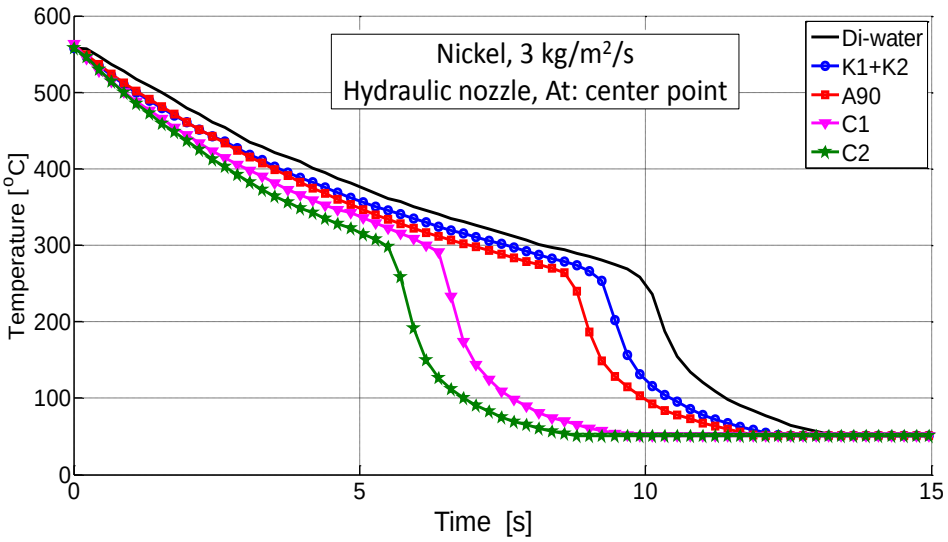

Figure 4.34: Temperature profiles for K1+K2,A90, C1, C2 and Di-water at center point

to the conductivity is not recognizable. The same fact is valid for the hardness.

Figure 4.34 compares the cooling profiles of real waters at the center point position as an example. All other positions show the same effects. The waters with a high electrical conductivity have a significantly higher cooling rate than the other waters. In Figure 4.35, the calculated heat flux is shown with dependence on the surface temperature. It can be seen that all characteristic parameters, Leidenfrost temperature, MaxHF, DNB-temperature and film boiling heat flux, differ considerably between all waters. The higher the conductivity is, the higher are their values.

Table 4.2: Analyzed compositions of used industrial and deionized waters

Parameters	Di-water	AG	K1	BF	A90	AL	AF	C1	C2
Magnesium mg/l	<0.03	14	7.8	<2	17	11	53	106	93
Sulfate mg/l	<5	<5	<5	62	36	180	301	867	628
Calcium mg/l	<2	84	38.5	2	49.7	138	150	248.5	88
Sodium mg/l	<0.03	88	96	186	94.4	149	91	77	305
Nitrate mg/l	0.81	21	31.8	36.3	42	0.5	<0.5	41	445
Chloride mg/l	3	11	62	43	121	241	195	170	191
E.C LAB μS/cm	6.7	530	692	841	869	1477	1565	2190	2580
E.C CAL μS/cm	9.6	700	716	997	926	1476	1336	2480	2890
pH value	7	8	8.4	9.1	8.5	7.9	7.1	7.7	7.7
Carbonate ^odH	0.28	14.3	13.2	14.14	10.8	10.4	11.8	3.78	4.6

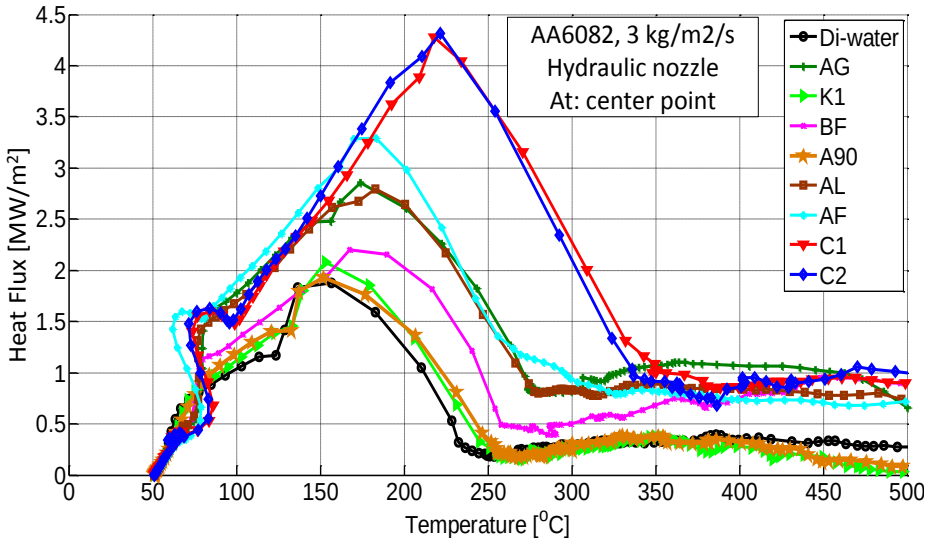

Figure 4.35: Heat flux vs surface temperature of the real waters at center point

Therefore, in Figure 4.36, the Leidenfrost temperature, the MaxHF and the DNB-temperature are plotted versus the electrical conductivity. All three parameters seem to increase linearly with the electrical conductivity. In particular, the Leidenfrost temperature differs considerably by 150 K between the real waters. The MaxHF increases approximately by a factor of two and the DNB-temperature by approximately by 50 K. Therewith, the electrical conductivity seems to be the relevant parameter which characterizes the cooling effect and heat transfer of real waters. An influence of the pH value and the hardness of the waters cannot be detected.

It is remarkable that the impact of the electrical conductivity is different between the single salt and the salt mixtures. It can be seen from the Figure 4.36, that the salt mixture causes the Leidenfrost temperature value to increase in the range of the electrical conductivity (0 - 2500 μS/cm). For the distance 34 mm as an example, the temperature increases from 300 ^oC to 450 ^oC. For the single salt $MgSO_4$, it can be seen from Figure 4.5, that within this range the Leidenfrost temperature only increases from 300 ^oC to 350 ^oC. Also the MaxHF and the DNB-temperature for the single salt $MgSO_4$ increase with a significant lower gradient than for the salt mixture. An explanation cannot be given. Further tests with defined mixtures of salts are planned.

After the center point has reached the LFT, a wetting front occurs and moves in radial direction. With the following two figures it will be researched if the wetting front velocity is a measure for the quenching effect of the water. Figure 4.37 shows the position of the wetting front for the nine different waters. It can be seen that the wetting occurs at the center point after 8 seconds for the water C1 and after

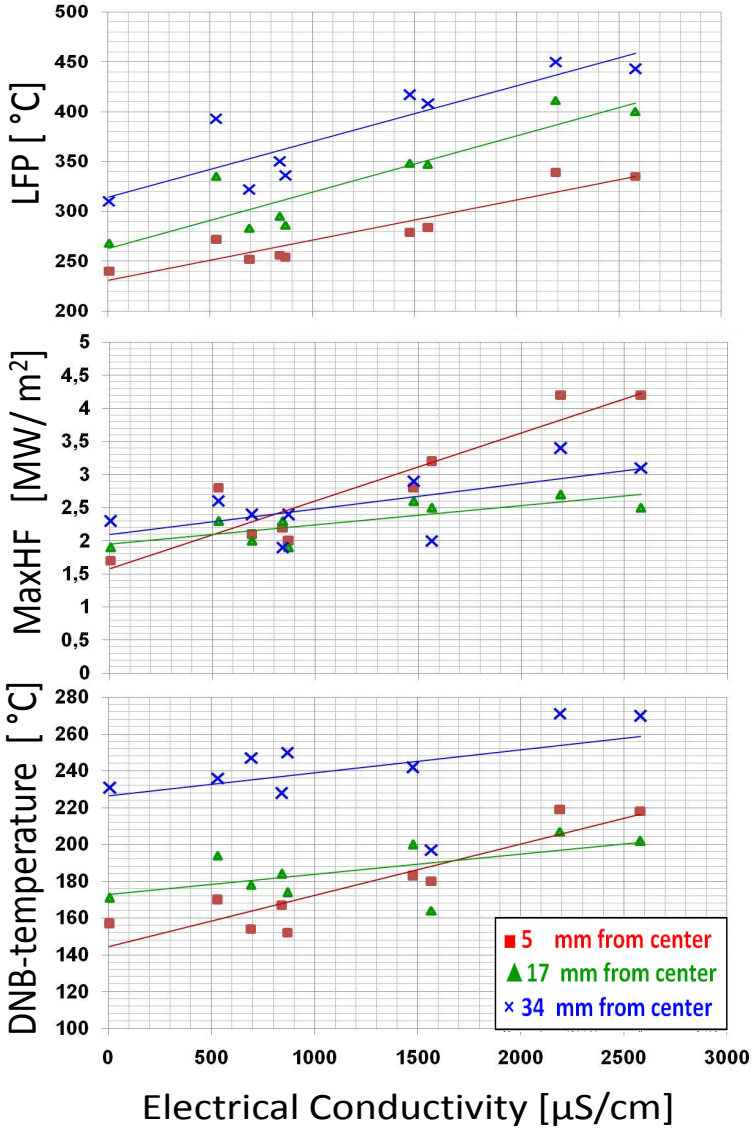

Figure 4.36: Dependence of Leidenfrost, MaxHF and DNB-temperature on the electrical conductivity at impingement density $\dot{V}_s = 3$ kg/m^2/s

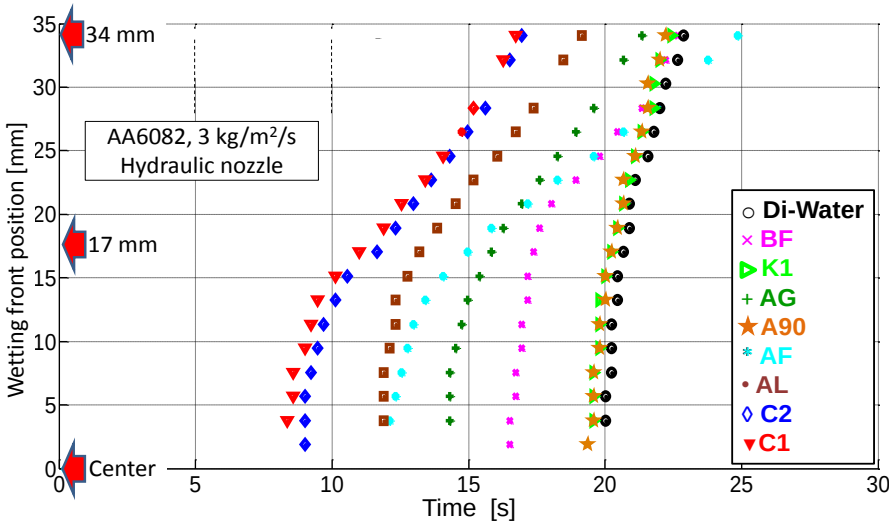

Figure 4.37: Position of the wetting front for the nine different waters

20 seconds for the DI-water. All the other waters are between these values. The higher the LFT, is the shorter is, of course, the time after which the wetting occurs. At the position 34 mm, the wetting occurs after 17 seconds for the water C1 and after 23 seconds for the DI-water. Here the difference between the two times is much smaller than at the center point.

The movement of the wetting front for one water with the time is the wetting front velocity. Its values are depicted in Figure 4.38. It is remarkable that the Di-water with the weakest quenching effect has the highest wetting front velocity. This can also be seen from figure 4.37. The wetting position moves for the Di-water after 20 seconds beginning from the center and only within 3 seconds to the position 34 mm. For this distance, the moving time for the water C1 needs about 9 seconds and therewith, three times more. During the movement of the wetting front, heat has to be transferred to cool the metal from the LFT to the boiling temperature. The higher the LFT is, the more heat has to be transferred. The water C1 has a much higher LFT than the Di-water. Therefore, the wetting front of the water C1 has to transfer more heat than that of the Di-water, which results in slower moving velocity. Therefore, the wetting front velocity is not a useful measurement for the quenching effect. The most important parameter is the LFT.

From Figure 4.38 is can be concluded that most waters have a similar wetting front velocity. At the beginning, the value decreases rapidly and after a length of approximately 15 mm, the value seems to keep constant. The rapid decrease at the center region can be explained with the profile of the impingement density, as shown in Figure 2.12. The impingement density has the maximum value at a distance of 10 mm and not in the center. The HTC is proportional to the

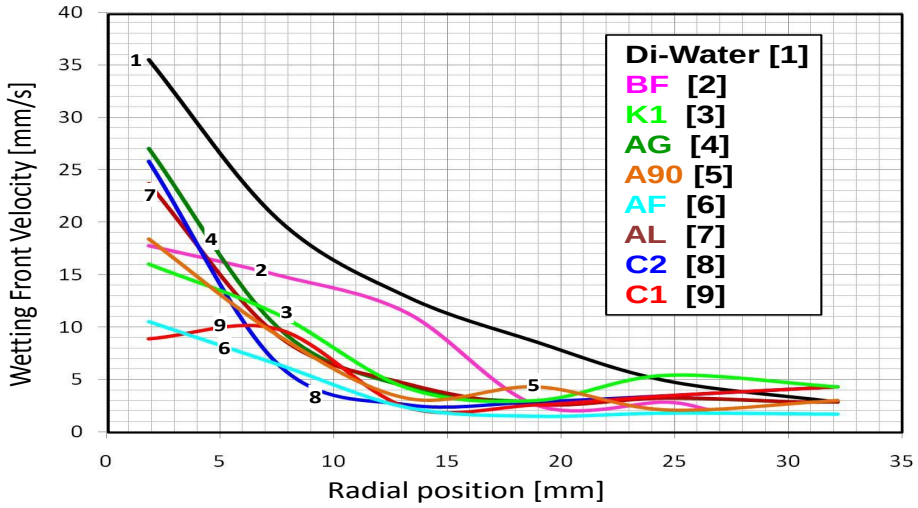

Figure 4.38: Wetting front velocity for the nine different waters

impingement density. Therefore, the vapor films collapse nearly at the same time in the range of ± 10 mm, which results in a high value of the velocity. Behind the wetting front, which has the LFT, follows a wetting range in which the temperature falls to the boiling temperature. In this range, the heat is transferred by nucleate boiling according to the boiling profile with the DNB-temperature and the MaxHF. The transferred heat also depends on the width of the range. This range can be principally analyzed from the radial temperature profiles by searching the LFT and boiling temperature. However, the width of this range was not of interest in this study.

Chapter 5

Surface properties of metal

5.1 Thermal material properties

5.1.1 Temperature profiles

Seven different kinds of metals were used to research the influence of the thermal material properties: the density, the specific heat capacity and the conductivity. The values are summarized in Table 5.1. The two materials Nicrofer and Inconel are steel alloys with a high contents of nickel and chromium. Therefore, their conductivities are very low. Nickel has a mean value of the conductivities, while the Aluminum alloy 6082 has a relatively high conductivity. The three copper alloys significantly differ in the conductivity. The copper K14 is a very pure metal with the highest conductivity of the sample metals. The Copper alloy L49 has an eight times lower conductivity. The table also includes the values for the heat penetration coefficient and the thermal diffusivity. The thickness of the used plates differed between 2, 3 and 4 mm. For this study it was not possible to obtain plates of the same thickness for all materials.

For all cooling tests with the different plates, the hydraulic nozzle with the impingement density of 3 kg/m^2/s was used again. The initial temperature was stayed constant 560 ^oC. This is the highest possible temperature for the aluminum alloy. In the Figures 5.1, 5.2, 5.3, A.29, and A.30 the temperature profiles along the radial distance are shown. The parameter is the time in full seconds. Between the profile is therewith a time interval of one second. It can be seen that Nickel has much more even profiles than Nicrofer. The reason is the 4.5 higher thermal conductivity. It is remarkable that Nicrofer has a much faster cooling rate in the core. After six seconds, the core has a temperature below 100 ^oC. After this time, the nickel plate core has still a temperature of about 350 ^{o}C.

Table 5.1: The thermal properties of metal samples and heat penetration coefficients

Property	Nickel	Nicrofer	AA6082	Inconel	Copper-B14	Copper-L49	Copper-K14
Compsitions	Pure nickel	NiCr25FeAlY	AlSi1MgMn	NiCr15Fe10	CuSn4	CuNi9Sn2	Pure copper
Density Kg/m^3 ρ	8908	7900	2770	8470	8850	8890	8940
Thermal conductivity W/m.K λ	91	20	170	14.9	118	48	385
Specific heat J/Kg.K C_p	440	600	1050	444	400	400	400
Penetration coefficient kWs$^{0.5}$/m^2 K $\sqrt{\lambda\rho C_p}$	18.89	9.74	22.24	7.39	20.44	13.07	37.11
Thermal diffusity Kg/m^3 α	23×10$^-$6	4.2×10$^-$6	58.5×10$^-$6	4×10$^-$6	33.3×10$^-$6	13.5×10$^-$6	108×10$^-$6
Thickness mm s	2	2	3	3	4	4	4

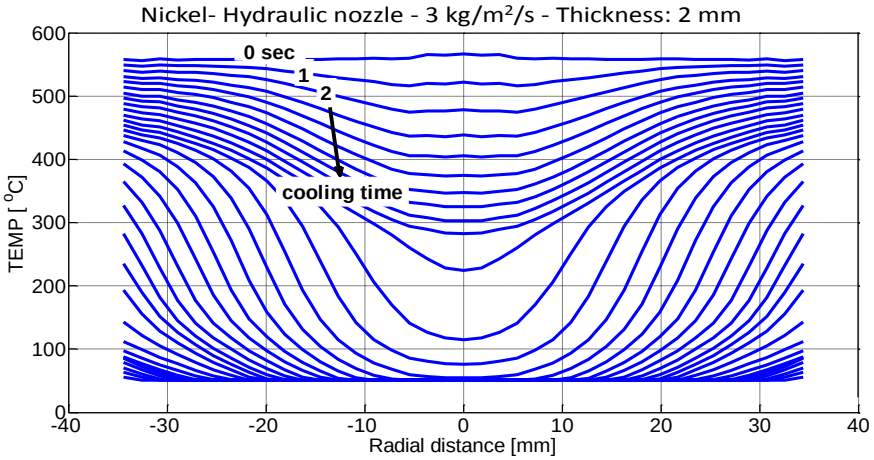

Figure 5.1: Temperature distribution along the radial distance for the Nickel plate with 2 mm thickness

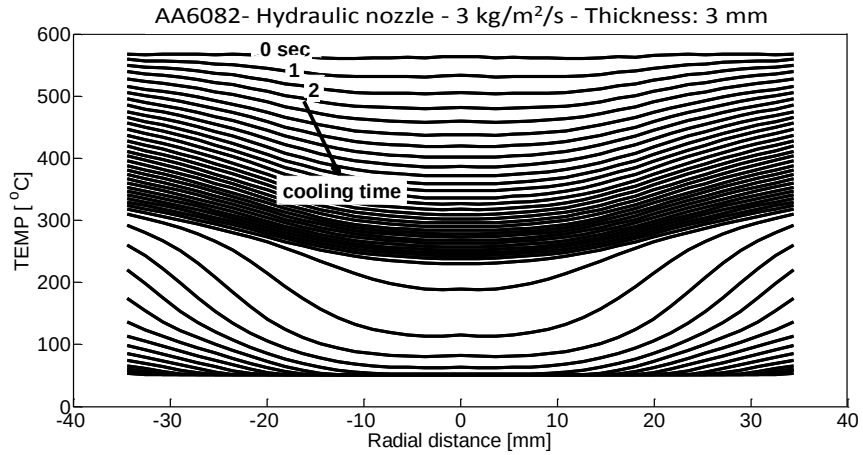

Figure 5.2: Temperature distribution along the radial distance for the AA6082 plate with 3 mm thickness

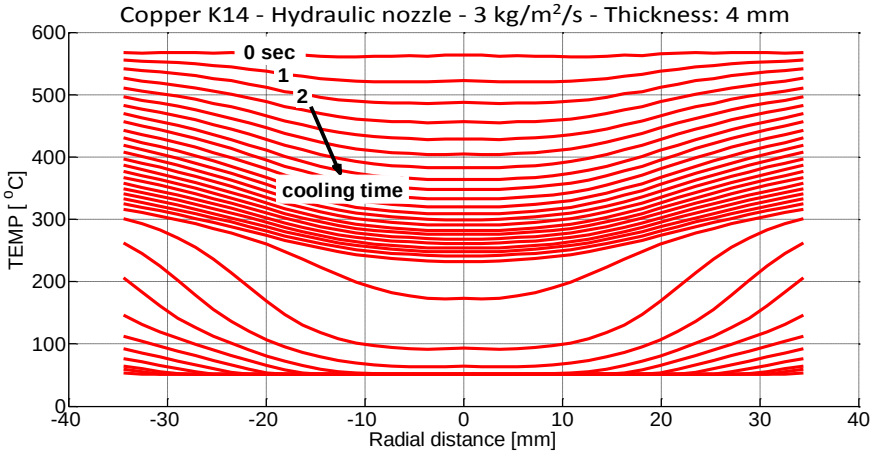

Figure 5.3: Temperature distribution along the radial distance for the Copper K14 plate with 4 mm thickness

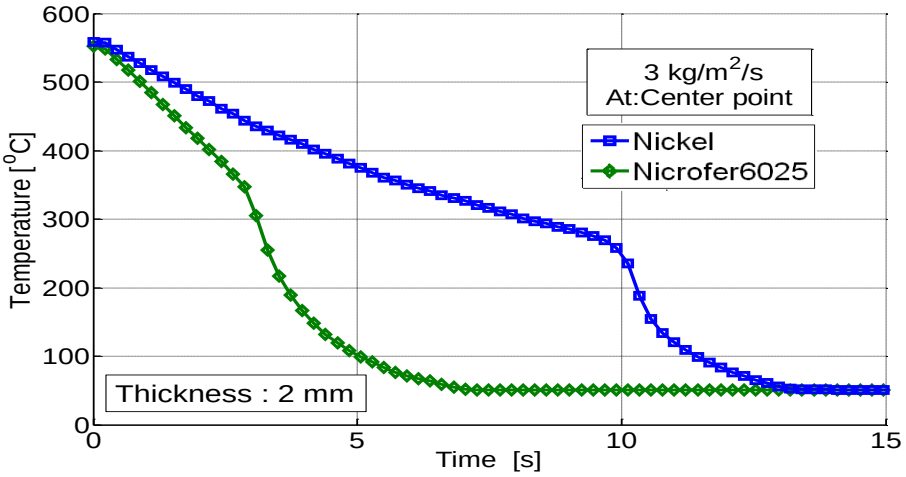

Figure 5.4: Temperature profiles of metals with the thickness of 2 mm at center

From the theory of transient heat transfer, the cooling time is proportional to the thermal diffusity according to the Fourier number. However, in this case, the Nicrofer with the lower thermal diffusity has the higher cooling rate. The material with the lower conductivity, here Inconel, has again the higher gradients. Figure 5.3 shows the radial profiles for copper K14, which is the material with the highest conductivity. As a consequent, these profiles are most often compared with all other profiles. The Figures 5.4, 5.5 and 5.6 and Figures A.31 to A.36 show the temperature profiles with dependence on time for the 2, 3 and 4 mm plates, respectively, again at the three characteristic positions: the center point, 17 mm and 34 mm distance from the center.

From Figure 5.4, it can be seen that the two materials nickel and Nicrofer have the same cooling rate at the beginning (except center point). However Nicrofer has a significantly higher Leidenfrost temperature. Therefore, the region of nucleate boiling starts earlier for Nicrofer, which results in the much shorter cooling time. From Figure 5.5, it can be seen that at the beginning of the film boiling region, the Aluminum has a higher cooling rate than the Inconel. The reason is the much lower density. Therewith, less stored heat has been transferred. However, the Inconel material, with the much lower conductivity, has again a higher Leidenfrost temperature. Figure 5.6 compares the cooling profiles of the copper alloys with the 4 mm plate thickness. Here, the alloy B14 with the mean conductivity of 118 W/m.K has the shortest time. The alloy K14 with the highest conductivity (385 W/m.K) and the alloy L49 with the lowest conductivity (48 W/m.K) have a similar cooling time. During the heating of the copper discs, oxide layers are formed on the surface. These layers splash away during the spray cooling. The surface behavior will be discussed in the next chapter.

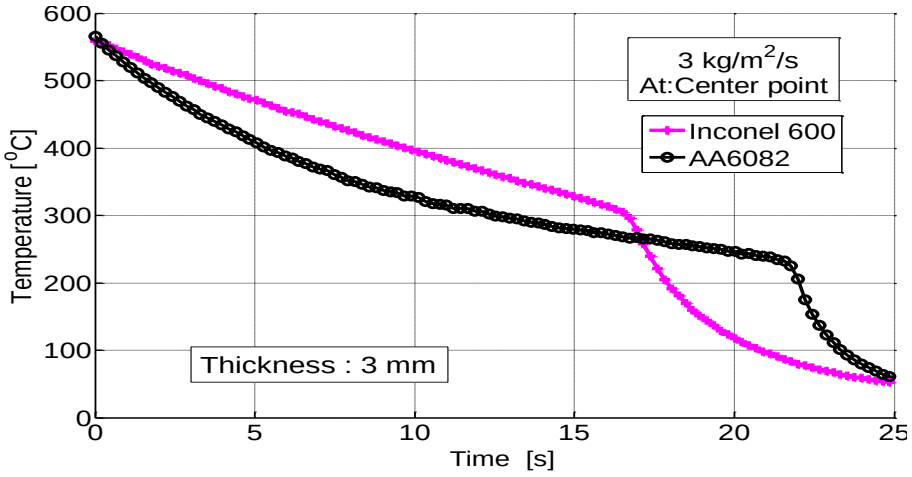

Figure 5.5: Temperature profiles of metals with the thickness of 3 mm at center

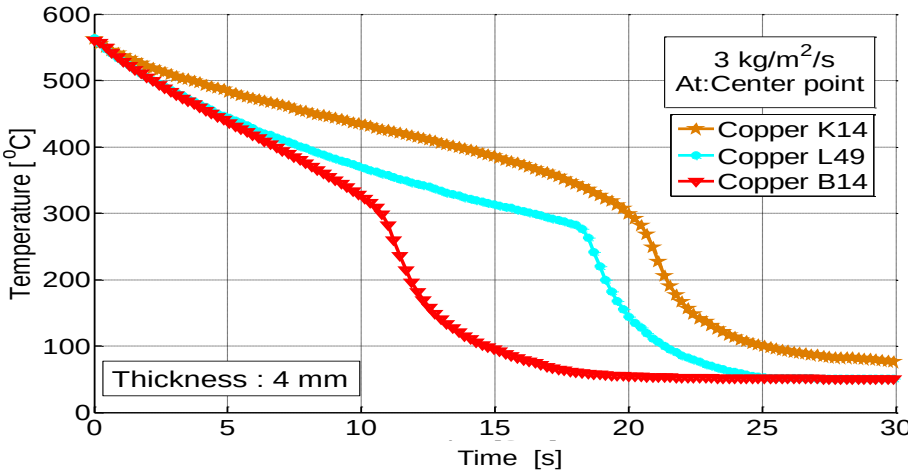

Figure 5.6: Temperature profiles of metals with the thickness of 4 mm at center

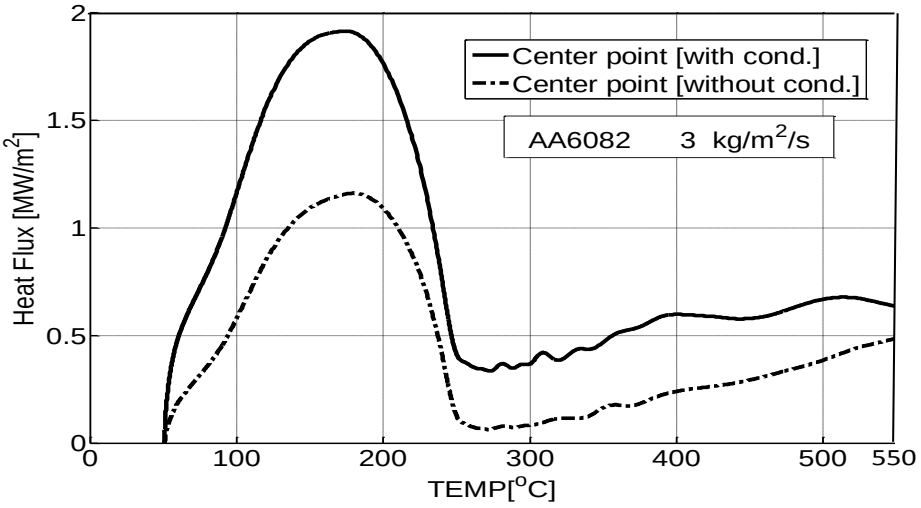

Figure 5.7: Heat flux for AA6082 at center point

5.1.2 Heat transfer

In the following, the heat transfer from the different discs will be compared. The heat transfer coefficient in the film boiling region is in the range of 400 to 800 $W/m^2/K$. Therewith, the Biot numer (Bi = α × s / λ) is in the range of 0.006 and 0.08. For these small values, it can be assumed that the temperature on both sides of the disc are similar. Therefore, the transfer heat flux can be calculated at radial position from the energy balance

$$\dot{q} = -\rho c_s s \frac{dT}{dt} - s \cdot \lambda \frac{1}{r} \frac{\partial}{\partial r} \left(r \cdot \frac{\partial T}{\partial r} \right) \tag{5.1}$$

as already explained in Chapter 3. The transferred heat flux is the decrease of the local enthalpy plus the heat conduced to this radial position. Figures 5.7, A.37 and A.38 shows this heat flux with dependence on the surface temperature for the material AA6082 as an example for the three characteristic positions. Two profiles are shown. The dotted line is for the heat flux because of the change of enthalpy. The continuous line stands for the heat flux from the change of enthalpy and the radial conduction. It can be concluded that the transferred heat flux from the radial conductivity is in the magnitude of 50 % of the change of enthalpy. The profiles for the center point were calculated using the temperature dependent material properties and using mean values of the temperature range from 100 to 600 ^oC. The differences are negligibly small, especially for the heat transfer in the film boiling region and for the Leidenfrosttemperature. The Figures 5.8, 5.9 and 5.10 and Figures A.39 to A.44 compare the heat flux profiles of the different metals for the 2 mm, 3 mm and 4 mm discs, respectively. All profiles differ, especially the Leidenfrost and DNB temperatures, such as the value of the MaxHF. Figures 5.11, A.45 and A.46 show the corresponding profiles of the heat transfer coefficient

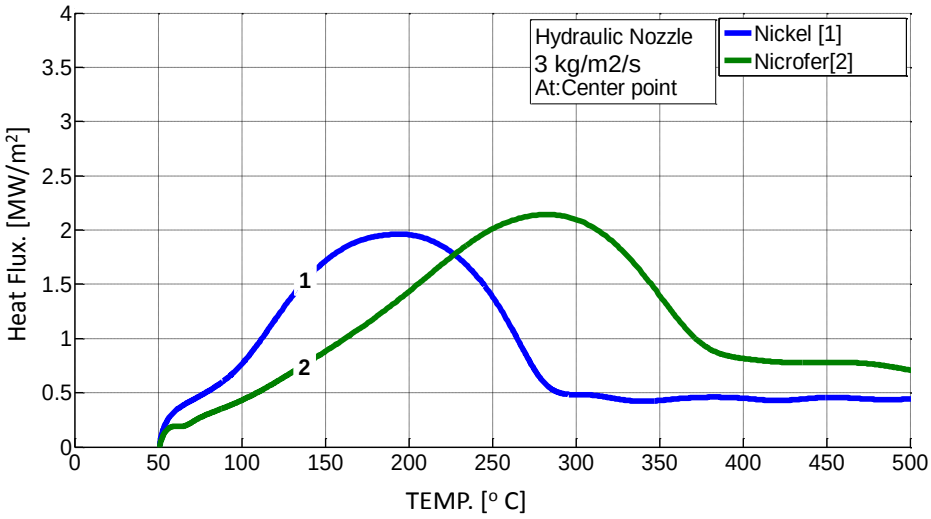

Figure 5.8: Heat flux of Nickel and Nicrofer plates at center point

at the center point as an example. In Figures 5.12, A.47 and A.48 the HTCs in the film boiling region are compared for the metals at the three characteristic positions. At the center point, Nicrofer has the highest value and the Aluminum the lowest. At the distance 34 mm, it is quite opposite. Here, the Aluminum has the highest value and Nicrofer has nearly the lowest value. Nickel always has one of the lowest values.

Figure 5.13 compares the LFT for all metals at the center point. For the Nickel, Aluminum, Inconel and Nicrofer, it seems that the LFT decreases with the heat penetration coefficient. For the Copper alloys, the LFT is influenced by the heat penetration coefficient of the oxide layer. This value is unknown, but the value must be much lower than that of the non-oxidized metal. Figure 5.14 compares the LFT of the metal at all three positions. The higher the distance from the center is, the higher are the values for the LFT. At all positions, the LFT decreases again with the heat penetration coefficient, except for the copper alloys. The Figures 5.15, 5.16 and 5.17 compare the influence of the kind of metal on the MaxHF, the DNB-temperature and the mean value of the heat flux in the film boiling region at the center point, as an example. A significant influence of the MaxHF cannot be detected. The DNB-temperature seems to decrease such as the LFT. The heat flux in the film boiling region seems to decrease with the heat penetration coefficient, except for the Copper alloys.

Figure 5.18 and 5.19 show the LFT and the heat flux in the film boiling region dependent on the thermal diffusivity of the metals. Here, the same trend can be seen as in the figures before. The values seem to decrease with the thermal diffusivity in a similar way as with the heat penetration coefficient. Therefore, it

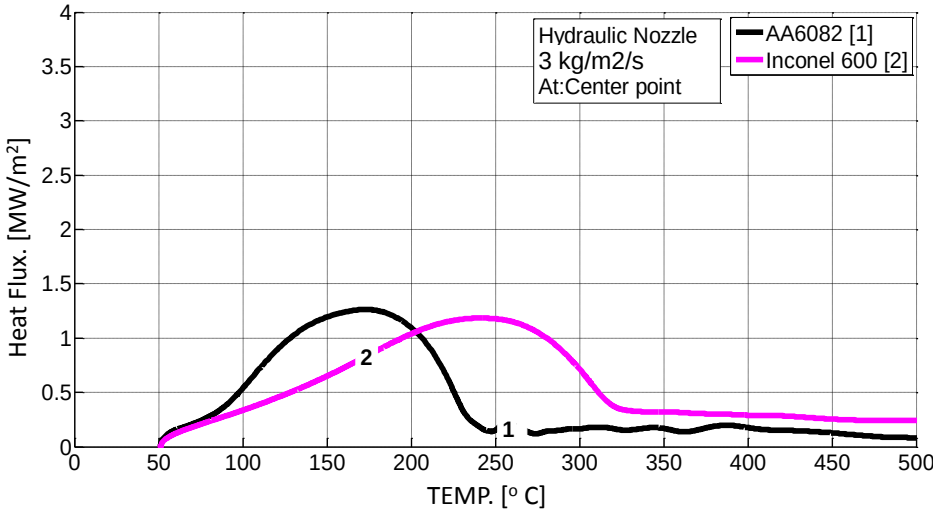

Figure 5.9: Heat flux of AA6082 and Inconel plates at center point

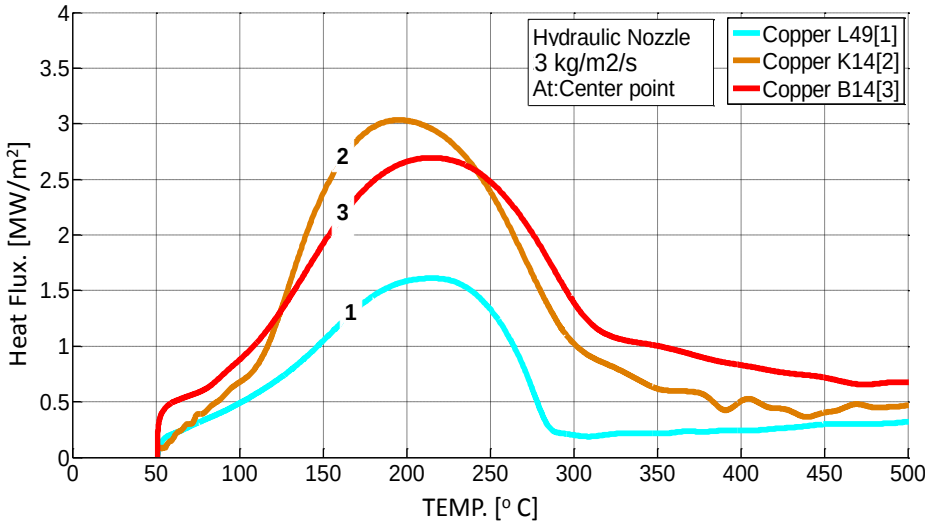

Figure 5.10: Heat flux of Copper alloys L49, K14 and B14 at center point

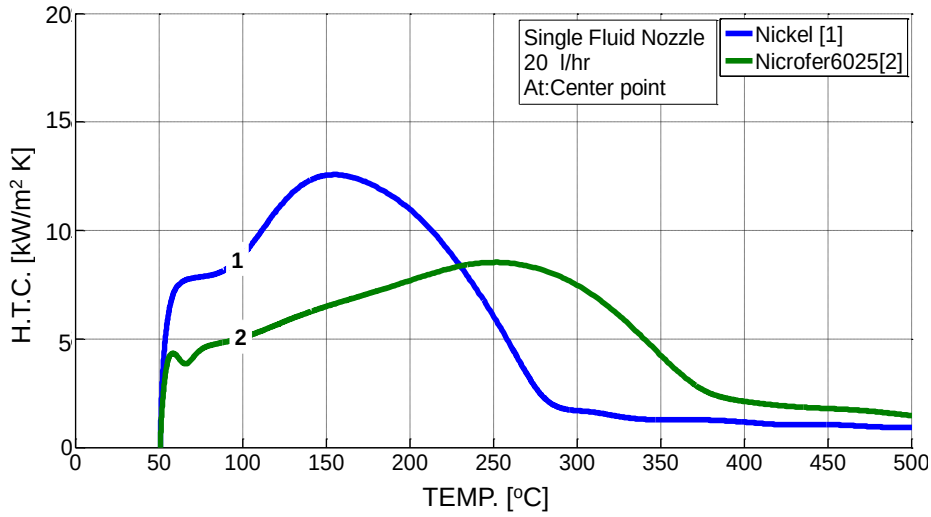

Figure 5.11: Heat transfer coefficient of Nickel and Nicrofer at center poin

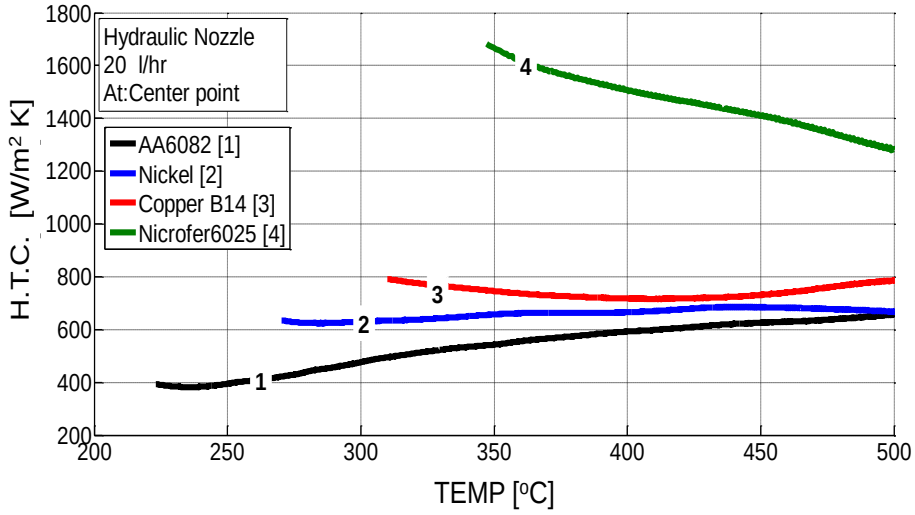

Figure 5.12: Heat transfer coefficient in film boiling region of metal plates used at center point

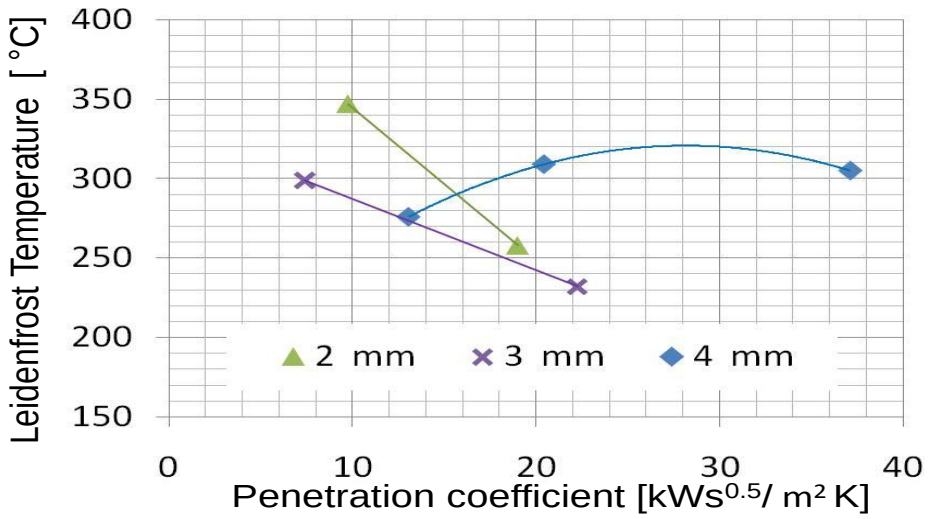

Figure 5.13: Effect of penetration factor on LFT for different metal at center point

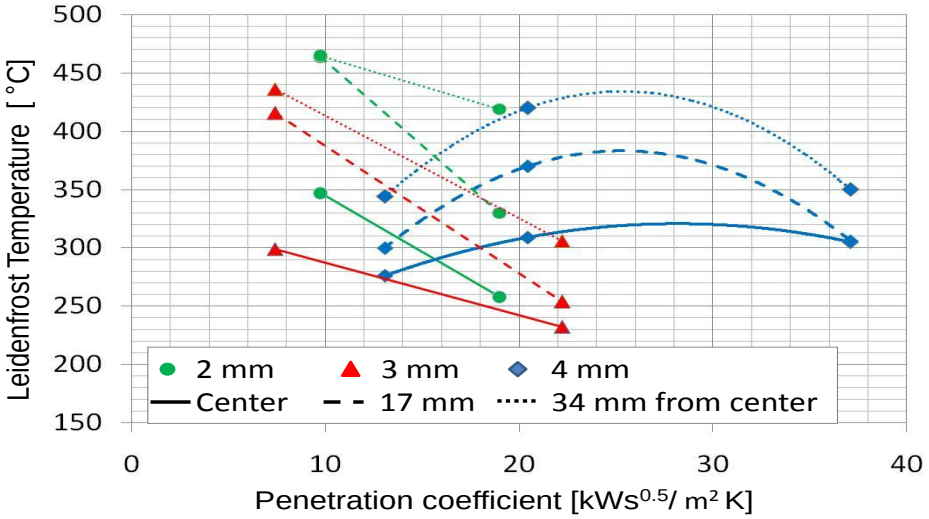

Figure 5.14: Effect of penetration factor on LFT at all three positions

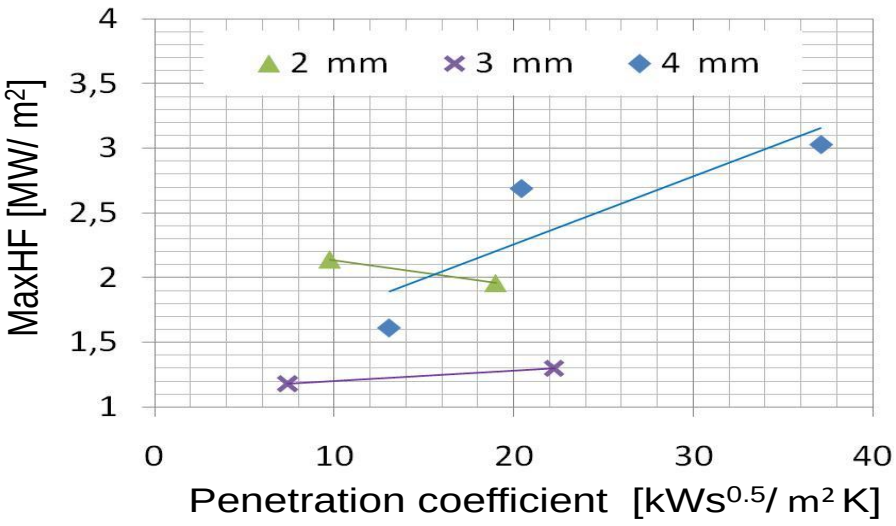

Figure 5.15: Influence of the kind of metal on the MaxHF

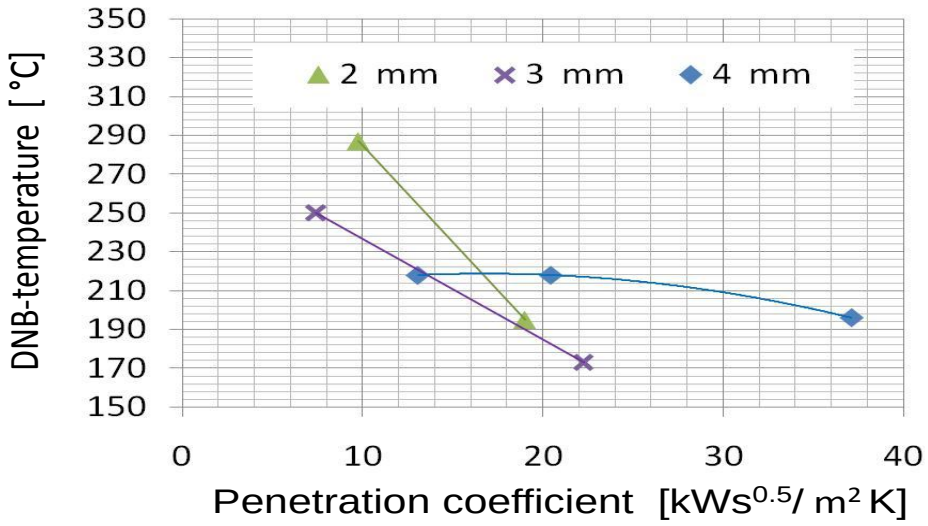

Figure 5.16: Influence of the kind of metal on the DNB-temperature

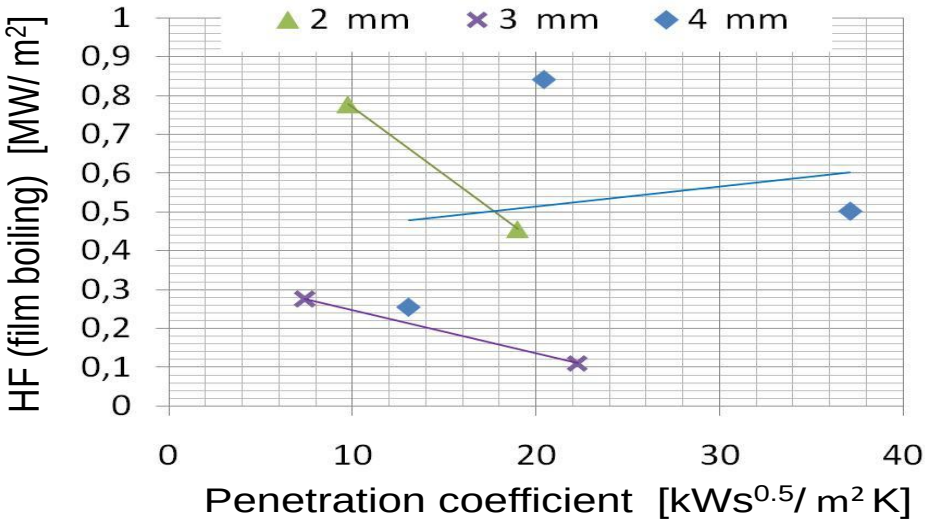

Figure 5.17: Influence of the kind of metal on the mean value of the heat flux in the film boiling region

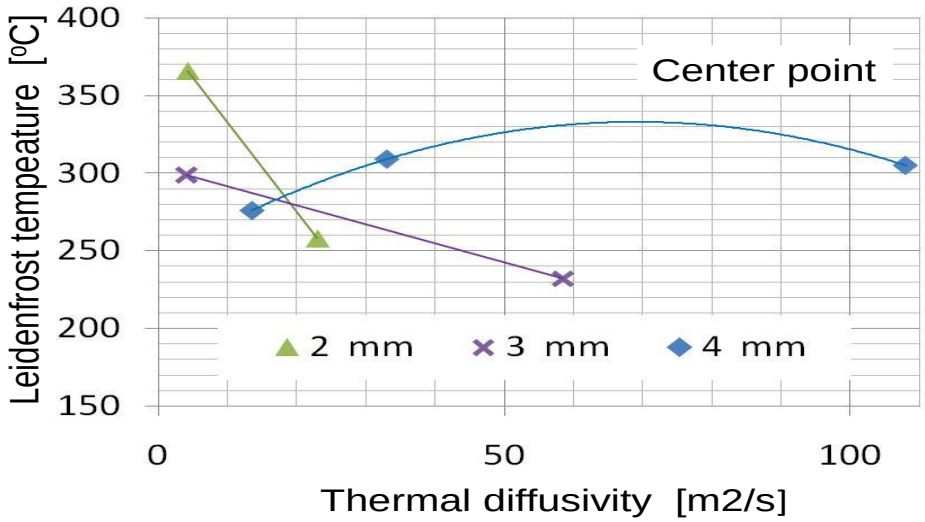

Figure 5.18: LFT dependent of the metals on the thermal diffusivity

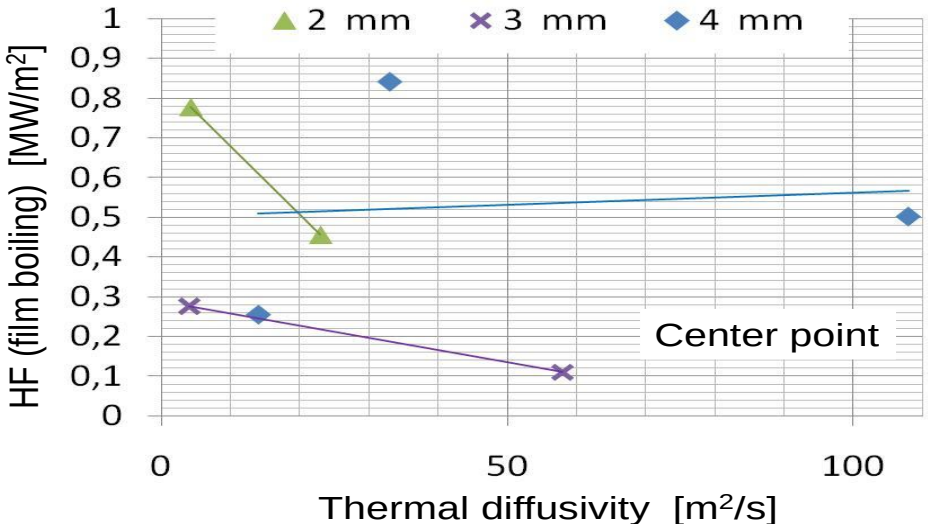

Figure 5.19: Heat flux of the metals dependent on the thermal diffusivity

is not clear which material property is decisive for the influence on the LFT. In all experiments, the Biotnumber was so small that the temperature difference in the thickness can be neglected. In this case, the thermal diffusivity is the proper material value. The authors in literature, who used thick samples and measured the temperatures using thermocouples, conclude the surface near effects are important, which are described by the heat penetration coefficient. As a consequence, a theory of the Leidenfrost problem is required to predict the correct influence of the material properties. As conclusion of these experiments, a clear influence of the kind of metal cannot be given. More experiments are necessary, especially tests with the same thickness of all discs. Additionally, tests with higher initial temperatures should be done to obtain better information about the heat flux and the HTC in the film boiling region. However, in these experiments, non Aluminum alloys can be used.

5.1.3 Comparison with literature

The results will be compared with those from literature in the following. Müller et al. [65] measured the LFT and the DNB-temperature in spray cooling for Copper, Nickel, Aluminum and Brass. He showed that both temperatures increase with the impingement density. For the value 3 kg/m^2/s, he measured a LFT of 300 ^{o}C for Aluminum and 400 ^{o}C for nickel. From Figure 5.14, it can be seen that the LFT for Aluminum increases from 230 ^{o}C at the center to 300 ^{o}C at the distance of 34 mm. The LFT for nickel increases from 260 ^{o}C to 420 ^{o}C. In both studies, Nickel has a higher LFT than Aluminum. The values for both metals are in the similar range. Müller et al. measured a DNB-temperature of 180 ^{o}C for Nickel and 160 ^{o}C for Aluminum, which are similar values as in Figure 5.16.

Al-Ahamdi and Yao [74] measured the LFT and the DNB-temperature for stainless steel. Both temperatures increase again with the impingement density. For the value 3 kg/m^2/s, they measured LFT in the range of 500 to 650 ^{o}C and DNB-temperatures of 270 to 370 ^{o}C. Nicrofer has similar material properties as stainless steel. From Figure 5.14, it can be seen that Nicrofer has a LFT of 350 ^{o}C at the center and 470 ^{o}C at the position of 34 mm. From Figure 5.16, it can be seen that the DNB-temperature is 290 ^{o}C for Nicrofer.

All three studies agree that the LFT and the DNB-temperature are higher, the lower the heat penetration coefficient is. The LFT in this study is lower than the values given by the other authors. The difference for the center point is about 140 K for Nickel, 70 K for Aluminum and 200 K for Nicrofer. One reason is that in this study Di-water was used, while in the other studies real water was used with an unknown quality. As it was explained in the previous Chapter, Di-water has the lowest quenching effect. Another reason is that the sizes of the samples were different and that the initial temperature in the other studies was higher. In the next Chapter, it will be shown that the higher the initial temperature is, the higher is the LFT temperature.

As mentioned before, Müller et al. [65] and Al-Ahamdi and Yao [74] report that the LFT increases with the impingement density. As a consequence, the LFT at the position of 34 mm should be lower than at the center position, because the impingement density of the nozzle used is much higher at the center than at the position of 34 mm. However, the values presented in the literature are only valid for the center point. Here, small samples were used and were arranged at the center line of the nozzle. The impingement density was varied by changing the distance between the nozzle and the sample. Therefore, the flow conditions represents the stagnation point. However, for large flat samples and therewith real work pieces, the flow conditions depend on the radial distance if the LFT is reached at the center. Next, a wetting front occurs, which moves in radial direction. The position 34 mm is still in the film boiling region, while the wetting front already moves. As a consequence, a radial flow supposes the spray. Due to the splashing effect at the wetting front droplets flow with a high velocity over the plate in radial direction. From other cooling methods, such as immersion quenching, it is known that the LFT is higher when the flow velocity is higher.

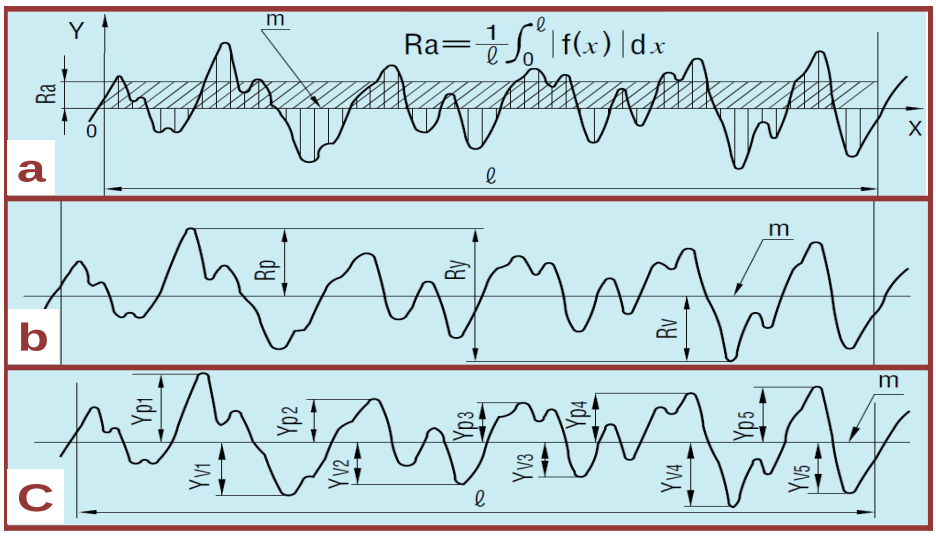

Figure 5.20: Typical ways for obtaining surface roughness

5.2 Surface Roughness

5.2.1 Definition of roughness

To determine the roughness of a surface, the height variations along the distance are measured. Figure 5.20 shows the principle profile of the height along the distance of a surface. Three different methods are used to define the roughness of the surface, which will be explained with this figure.

A) Arithmetical mean roughness R_a: In this method, the fluctuations (zigzag line) in relation to the basic line are summarized according to

$$R_a = \frac{1}{l} \int_0^l |f(x)|\, dx \tag{5.2}$$

The area $\int_0^l |f(x)|\, dx$ represents the area of the peaks below and above the basic line.

B) Maximum peak height R_y: In this method, the heights of the maximum peaks of the surface above and below the basic line are searched and added

$$R_y = R_p + R_V \tag{5.3}$$

C) Ten-point mean roughness R_z: In this method, the sum of five peak heights and five peak depths is calculated and divided by the factor five

$$R_z = \frac{|Y_{p1} + Y_{p2} + Y_{p3} + Y_{p4} + Y_{p5}| + |Y_{V1} + Y_{V2} + Y_{V3} + Y_{V4} + Y_{V5}|}{5} \tag{5.4}$$

The relation of these three different roughness values are $R_y > R_z > R_a$

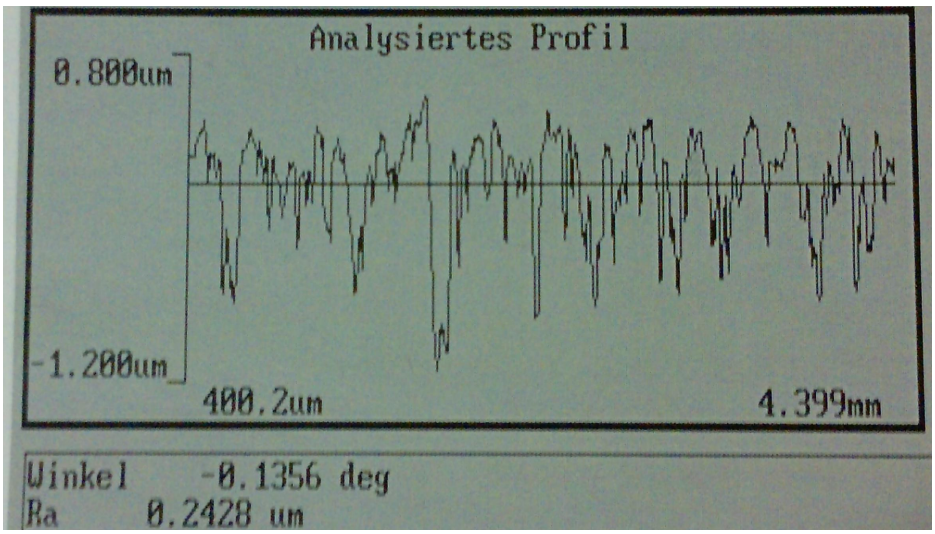

Figure 5.21: Real fluctuations on AA6082 surface

5.2.2 Roughness of disc samples

To study the effect of small roughness values, discs of the Aluminum alloy AA6082 with a thickness of 3 mm were used. They were heated to 560 ^{o}C and cooled with the hydraulic nozzle. Deionized water was used with an impingement density of 3 kg/m^2/s. These are the standard conditions.

Figure 5.21 shows the measured roughness profile of the standard disc of AA6082, which was used for all experiments explained before. The arithmetical mean roughness is 0.24 μm. Some of these discs are polished with sand paper and some are scratched with saws. Figure 5.22 shows photos of the three surfaces. The roughness of the surface using the sand paper was measured as Ra = 1.7 μm and using the saw as Ra = 7.7 μm. Figures 5.23, A.49 and A.50 show the cooling profiles of the Aluminum disc at the three characteristic positions. It is surprising that the smooth surface (R_a = 1.7 μm) has the shortest cooling time. The surface with the low roughness of 1.7 μm has a significantly longer cooling time than the smooth surface. With the higher roughness of 7.7 μm, the cooling time decreases in comparison with the mean roughness of 1.7 μm. The plates were heated and cooled using two methods. During the first method, water was sprayed on the smooth surface and during the second method, the water was sprayed on the original ingot surface. The non-sprayed surface of the plates were coated with graphite and their surface temperature was measured with the IR-camera.

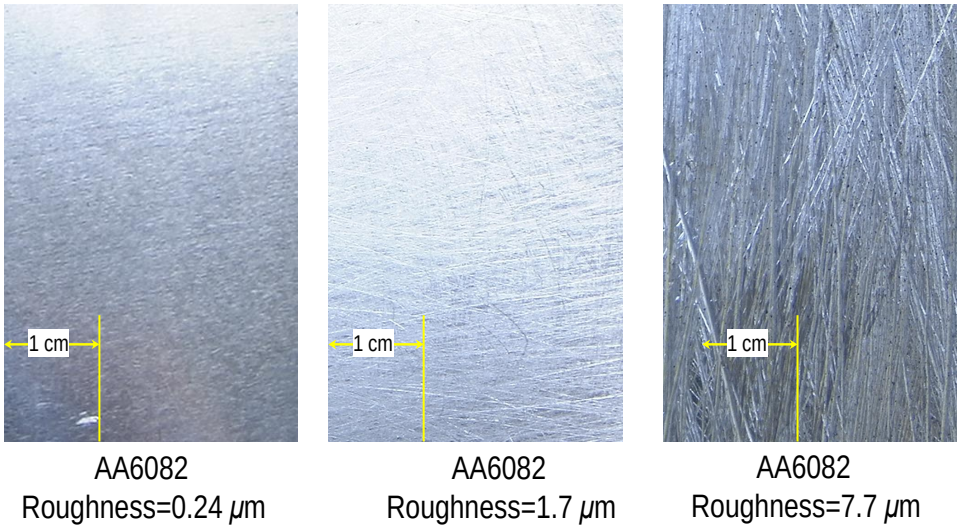

Figure 5.22: Arithmetical mean roughness of three AA6082 surfaces

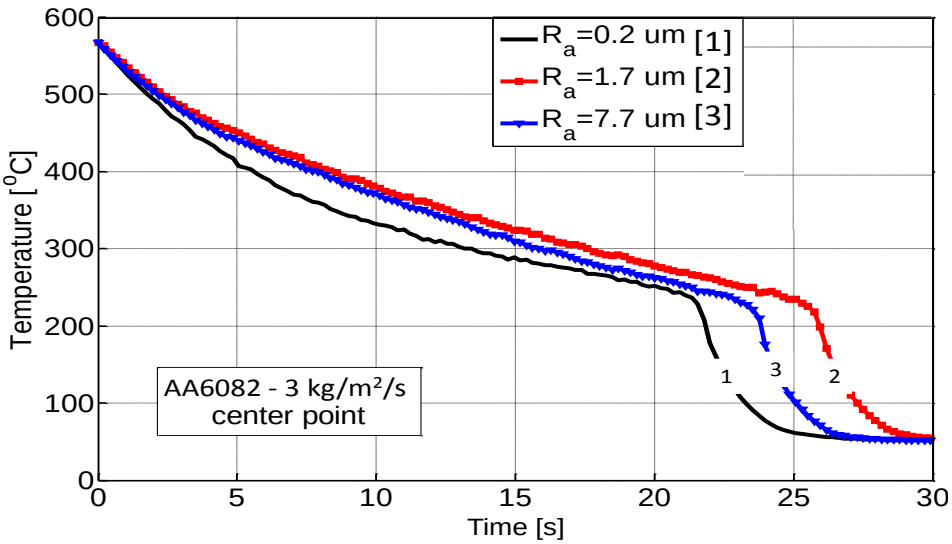

Figure 5.23: Temperature profile of rough AA6082 surfaces at center point

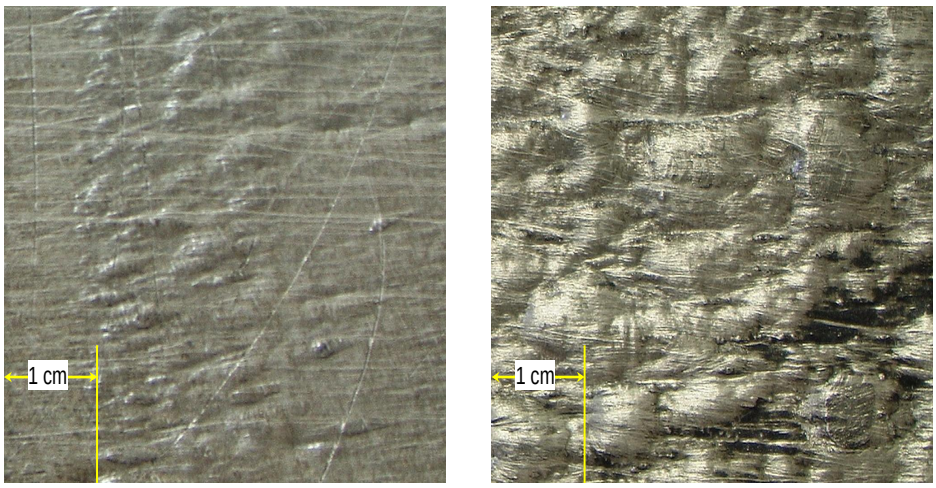

Figure 5.24: Real surfaces of Aluminum ingots used

5.2.3 Roughness of ingot samples

The surface of ingots after the casting process is creats an unsmooth structure. Figure 5.24 shows a photo of the structure of two ingots from different casting processes. From these two ingot plates with a thickness of 10 mm and 6.5 mm respectively, were cut. The cut side was polished. With this method, one side of the prepared plates had the surface shown in Figure 5.24, while the other side had a relatively smooth surface.

Figure 5.25 shows the cooling profiles at the three characteristic positions for the 10 mm plate. It is obvious that the spray on the ingot surface has a much higher cooling effect than the spray on the smooth surface. The surface temperature of 100 ^{o}C, as an example, is reached after approximately 60 seconds, instead of 120 seconds for the cooling of the smooth surface. However, not only the LFT is shifted to a higher value, the heat transfer in the film boiling region is also increased. It is remarkable that for this thick plate the cooling profile is similar for all three distances.

Figure 5.26 shows the cooling profiles at the three characteristic positions for the plate with the thickness of 6.5 mm. Also in this case, the spray on the ingot surface gives a much faster cooling rate than the spray on the smooth surface. The temperature of 100 ^{o}C is reached after approximately 30 seconds instead of 60 seconds, which is within half of the time. Again, the cooling profiles for all three positions are similar. In the Figures 5.27 and 5.28, the heat transfer coefficient is shown with dependence of the surface temperature for the plate with the thickness of 10 mm and 6.5 mm, respectively. It can be seen, that especially in the film

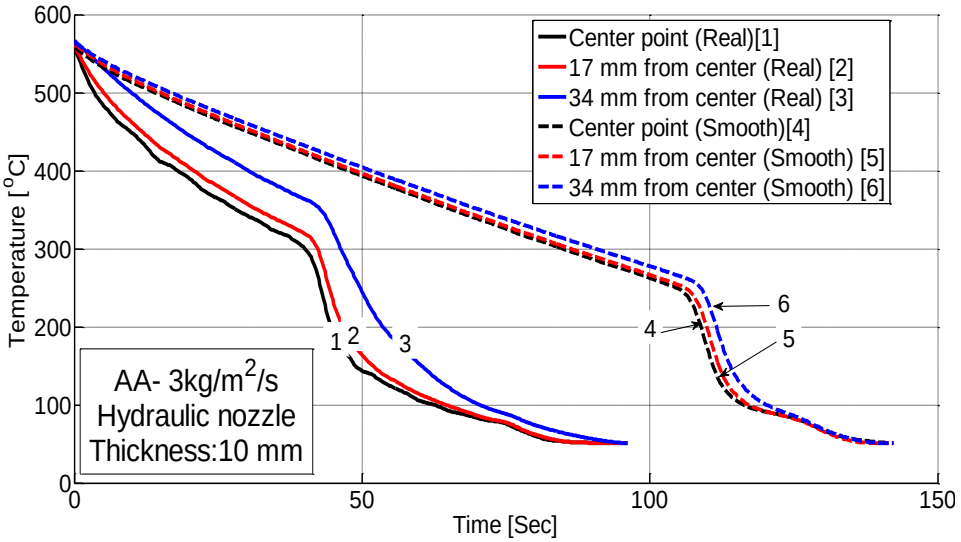

Figure 5.25: Temperature profile of Aluminum ingot (thickness: 10 mm)

boiling region, the heat transfer of the ingot surface is more times higher than of the smooth surface. One reason is that the ingot surface has a higher area than the smooth surface. Another reason is the higher roughness of the ingot surface.

5.2.4 Salt deposition

Dissolved salts reduces the cooling time, as shown in Chapter 4. It is still unknown what may be the cause. The salts influence the material properties of the water only such low that this can be excluded as a reason. The question remains to be answered if salts influence the surface structure through particle deposition during the cooling process. Figure 5.29 shows photos of the Aluminum disc after quenching with the water in which 60 g/l $MgSO_4$ was dissolved. From the upper photo it can be seen, that a white annular ring is formed with a diameter of approximately 60 mm. Outside the ring, the disc has the color and the structure as it was prior to the quenching. However within the ring, the color of the surface has changed. Both lower photographs show the surface in the range of the white ring in greater detail. It can be seen that there are salt deposits in the magnitude 0.1 to 1 mm.

Figure 5.30 shows photographs of the Aluminum disc after quenching with the water in which 1 g/l $CaCO_3$ was dissolved. Also, in this case, it can be seen that there are small white deposits on the surface. The number of these deposits are much smaller than for the $MgSO_4$ before the concentration was much lower. It is unknown if this change in the surface structure and the salt deposits influence the cooling time. More research in this behavior is necessary.

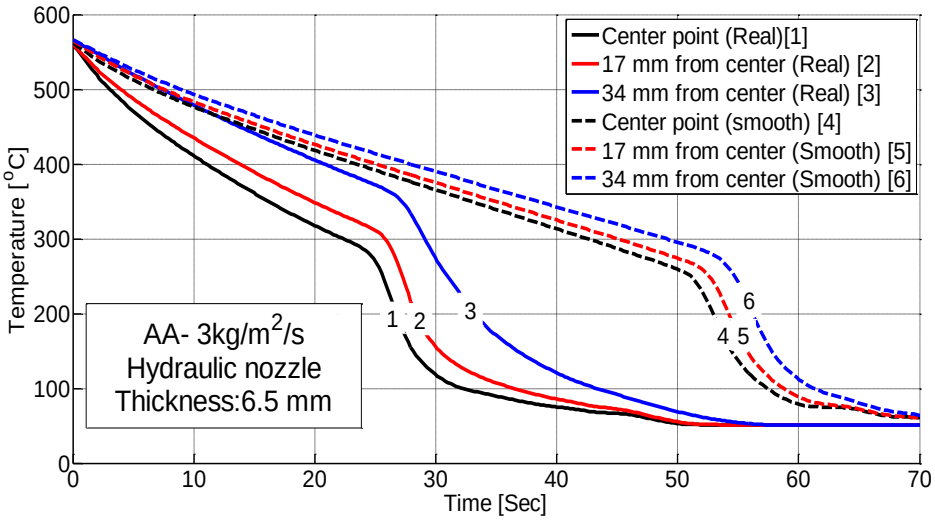

Figure 5.26: Temperature profile of Aluminum ingot (thickness: 6.5 mm)

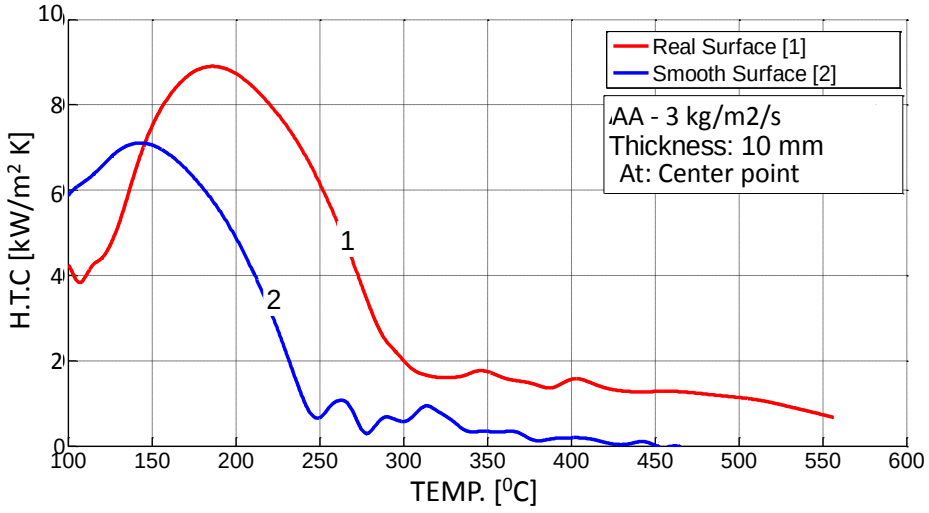

Figure 5.27: Heat transfer coefficient of Aluminum ingot (thickness: 10 mm)

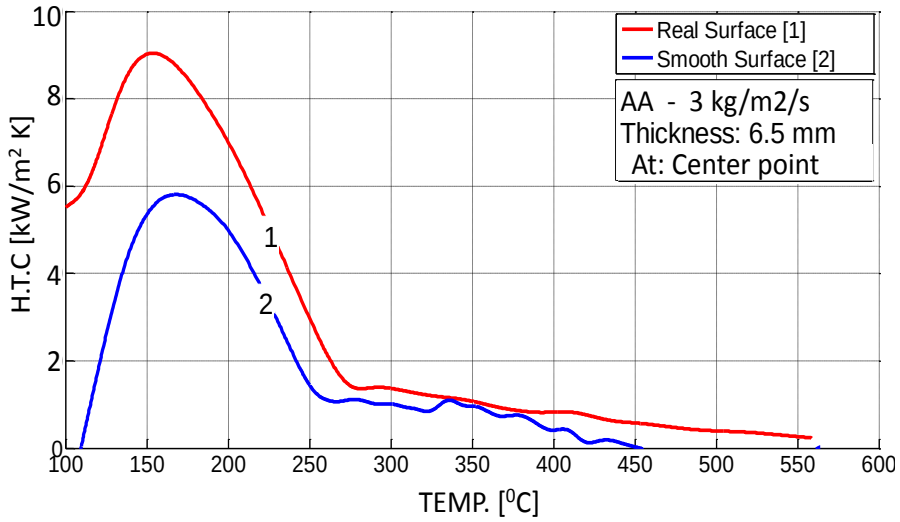

Figure 5.28: Heat transfer coefficient of Al. ingot with the thickness of 6.5 mm

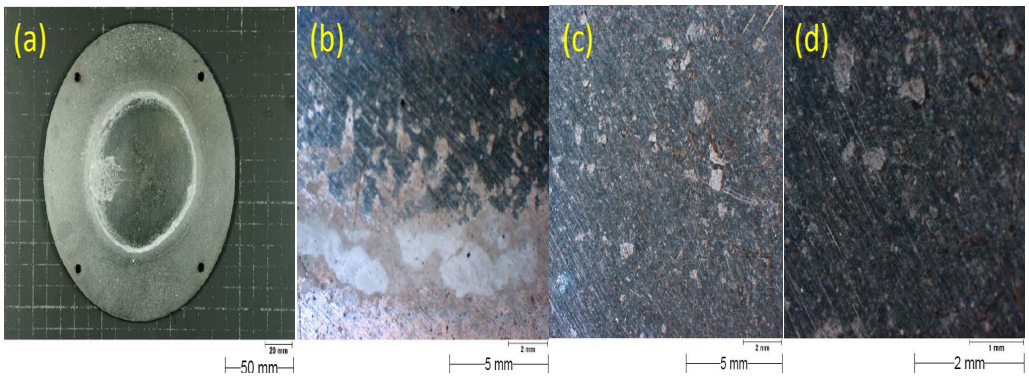

Figure 5.29: Salt deposition on AA6082 surface of $MgSO_4$ solution of 60 g/l

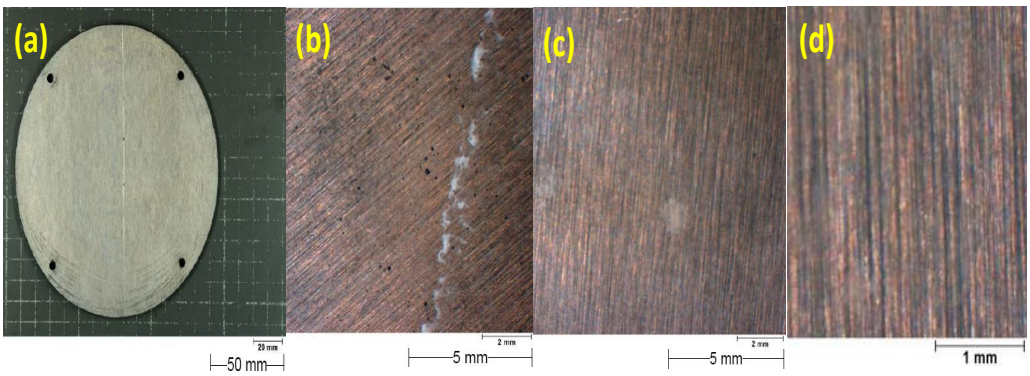

Figure 5.30: Salt deposition on AA6082 surface of $CaCO_3$ solution of 1 g/l

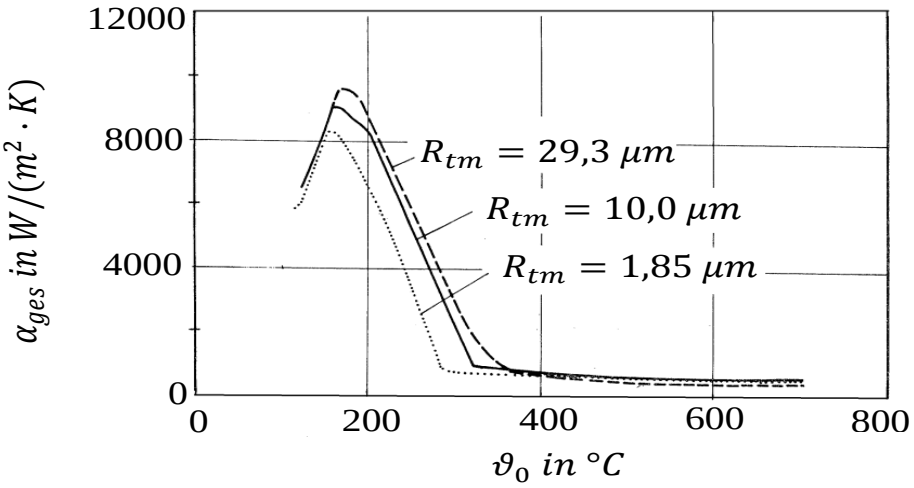

Figure 5.31: Influence of surface temperature on the overall heat transfer coefficients with the average surface roughness [67]

5.2.5 Comparison with literature

Reiners et al. [67] measured the cooling of a Nickel cylinder with an impingement density of 2 kg/m^2/s for three values of surface roughness: 2 μm, 10 μm and 30 μm. The profile of the HTC with dependence on the surface temperature is shown in Figure 5.31. The LFT increases from 290 ^{o}C to 360 ^{o}C, the DNB-temperature from 160 ^{o}C to 175 ^{o}C and the max. HTC increases from 8000 to 9500 W/m^2/K. The HTC in the film boiling region was independent on this roughness. Parabhu et al. [108] measured the effect of the surface roughness with steel plates, which had a roughness of 1 μm and 3 μm and a grooved surface. They immersed the plates in a different baths of liquids. The range of nucleate boiling immediately occurred so that a LFT could not be detected. The heat flux profiles with dependence on surface temperature were similar for the 1 μm and 3 μm roughness. For the grooved surface, the value of the MaxHF was about 10 % higher.

Bernardin et al. [110] sprayed water on plates made of Al-1100 with a particle blasted and a milled finished surface. This Aluminum alloy is relatively high oxidation-resistant. The roughness of the particle blasted surface increased after the cooling process from 0.9 μm to 1.6 μm. The roughness of the milled surface kept constant at 1.4 μm approximately. The LFT was independent on the surface temperature with 220 ^{o}C. However, the HTC in the film boiling region was for the particle blasted surface slightly larger than for that of the milled surface. Values for the HTC and the impingement density were not reported.

Dianfeng Li [111] researched the heat flux of plates which were cut out of real

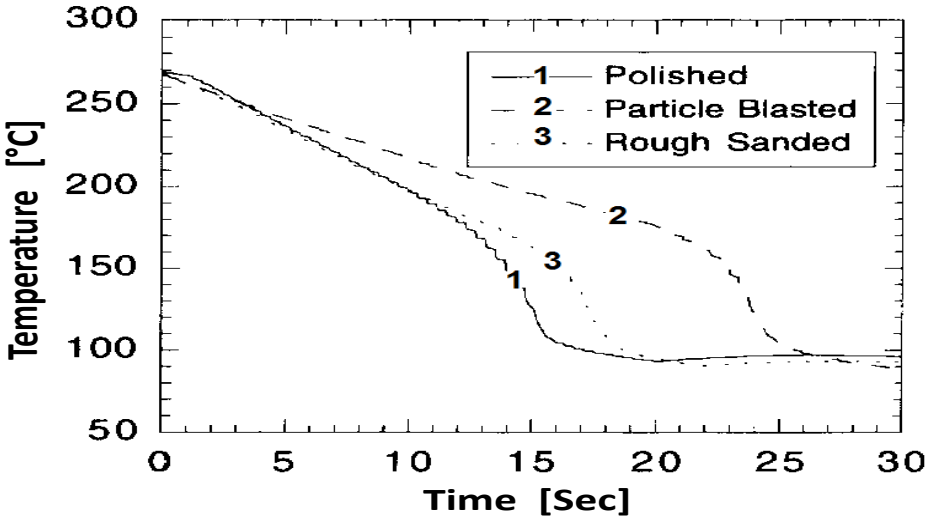

Figure 5.32: Influence of surface roughness for single water droplets on horizontal copper discs [109]

ingots, which were casted of three different Aluminum alloys. The plates with the dimension of 13 cm by 30 cm, had a thickness of 5 cm. The roughness was 470 μm for AA5182 , 120 μm for AA3004 and 25 μm for AA1005. The plates were quenched with water jets from a mould. The region of nucleate boiling immediately occurred. They compared the heat flux profiles of the sample with the real surface with a sample with a polished surface of about 5 μm roughness and which was made of the same alloy. For the alloy AA5182, the value of the MaxHF was 5.1 MW/m^2 for the high roughness of 470 μm and 3.8 MW/m^2 for the polished surface. For the alloy AA1050, the MaxHF was 6.9 MW/m^2 for the real surface, with 25 μm and 6.2 MW/m^2 for the polished surface. The results principally match with the results from Figure 5.28, in which the MaxHF is much higher for the real ingot surface as for the polished surface.

Bernardin et al. [109] researched the effect of surface roughness for single water droplets on horizontal copper discs. Polished discs with a roughness of 0.1 μm, particle blasted discs with 1 μm and rough sanded discs with 3 μm were used. The measured cooling profiles are shown in Figure 5.32. The cooling time of the droplets was shortest for the polished (0.1 μm) disc and longest for the particle blasted (1 μm) disc. The LFT was similar for all three surfaces. The differences in the cooling time were caused by the different HTC in the film boiling region. These results matched principally with those seen in Figure **??**. The values of the roughness are in the same magnitude. Also in this case, the LFT is nearly constant and only the HTC in the film boiling region changes with the roughness. The small increase of the roughness from 0.2 to 1.7 μm prolongs the cooling time considerably. The increase of the roughness to 7.7 μm shortens is the cooling time.

However this time is still longer than that for the smooth surface.

Chapter 6

Heat transfer of mould jets

6.1 Heat transfer mechanism

In continuous casting processes of copper alloys, the strand leaving the mould is cooled by sprays. The heat transfer of impinging sprays has been extensively researched because this cooling method is also applied in the continuous casting of steel. However, in continuous casting processes of aluminum alloys, the strand leaving the mould is cooled by jets which are coming out of the mould. The influencing parameters for this cooling method are still unknown, as explained already in the introduction. The mechanism of the measuring method and the heat transfer is explained in Figure 6.1. The jets leave the mould with an angle of approximately 30^o and impinge the test plates as described in Chapter 2. The impinging position is about 53 mm away from the top of the plate. The water pours down, touching the surface. In these tests, the plates are cooled first at the top. Therefore, the upper part of the plate has a lower temperature, while the lower part has still the initial temperature of the heating. When the water

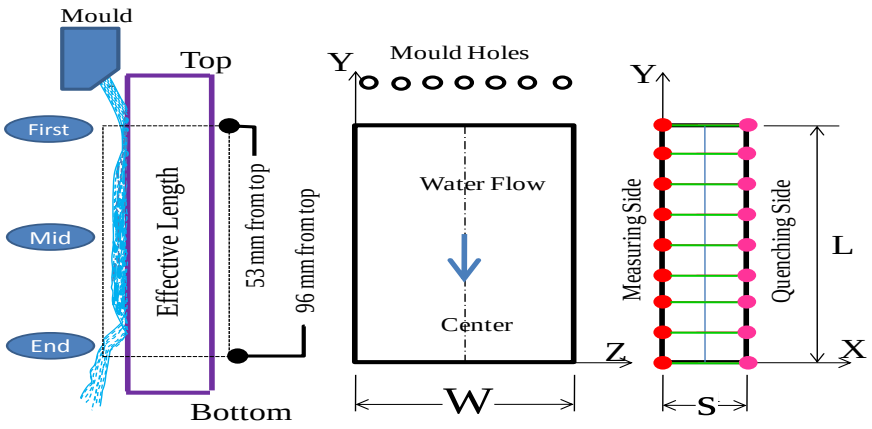

Figure 6.1: Mechanism of mould quenching

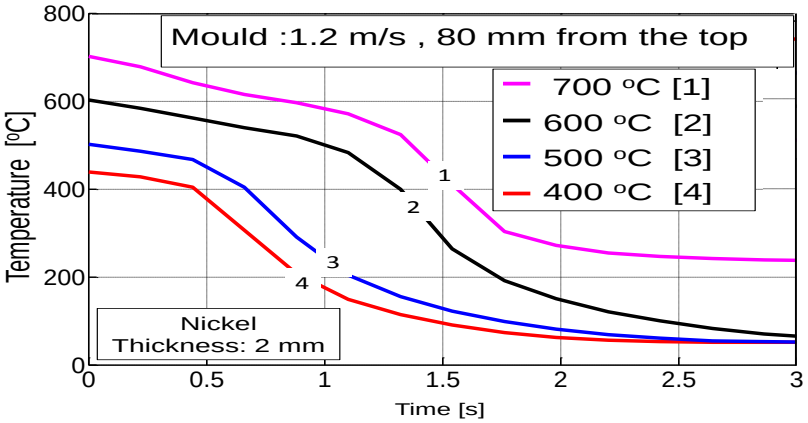

Figure 6.2: Temperature profiles with respect to initial surface temperature

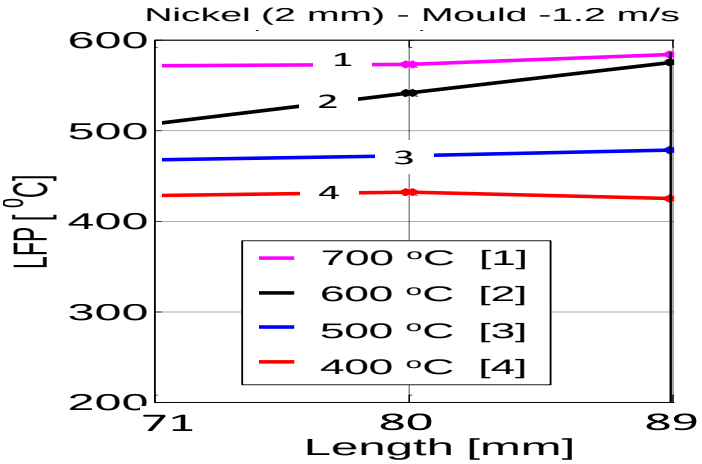

Figure 6.3: LFT along the length for different initial temperature

film reaches the position where the plate has the LFT, the water is splashed away from the surface. For discussing the heat transfer, the temperature profiles at the positions 53 mm (impingement point) and 96 mm away from the top of the plate will be considered. In reality of the casting process, the temperature of the strand is hot at the top and cold at the bottom. This is the opposite profile as in the test of this study, because a continuous moving of the plate was not possible. Therewith, the jet hits the hot surface which is above the LFT. The falling water film cannot splash away because the temperatures down the strand are below the LFT. In spite of this lack of the testing plant principal, effects of the heat transfer can be researched.

6.2 Influence of initial temperature

The middle of Figure 6.1 shows a top view of the plate with the width W = 70 mm. The water flows from seven holes to the plate with a diameter 2.4 mm. It is assumed that the temperature profiles down the center line are representative for a mould with many more holes. The plates had a thickness of s = 2 mm for Nickel and s = 3 mm for Aluminum alloy 2024 and Inconel. The temperatures of the quenched and measured sides are assumed to be similar as before.

At first, tests have been conducted with a plate of Nickel, which had initial temperatures between 400 ^oC and 700 ^oC. Figure 6.2 shows the temperature profiles at the impinging position. All profiles show the film boiling region at the beginning and then a transfer to the nucleate boiling region. However, in all four cases the LFT is different. This LFT is shown separately in Figure 6.3 for all initial temperatures at three positions below the impingement point. It can be seen that the higher the initial temperature is, the higher is the LFT. Therefore, for all tests described in the following, a constant initial temperature of 520 ^oC was always used.

6.3 Influence of jet velocity

For a given mould with fixed orifices, the only parameter which can be influenced is the volume flow of the water and therewith, the velocity of the jets. Figures 6.4 and 6.5 show the temperature profiles with dependence on time for two distances, 53 mm and 96 mm from the impingement point, as an example. The parameter is the jet velocity. The minimum value is 0.9 m/s. For lower values, the jets do not hit the plate. It can be seen that this velocity has the longest cooling time. An increase of the velocity to 1.2 m/s shortens the cooling time considerably. However, a further increase of the velocity prolongs the cooling time. Therewith, an optimum velocity exists which will be discussed later in more detail.

In Figures 6.6 and 6.7 the LFT is shown with dependence on the length for the four velocities. It is remarkable that the LFT is independent from the length. However, it is dependent on the velocity. For the optimum velocity with the shortest cooling time, the LFT has the lowest value. Figures 6.8, 6.9, 6.10 and 6.11 show the cooling profiles for inconel and nickel, respectively. Again the minimum velocity of 0.9 m/s has the longest cooling time. The velocities 1.2 m/s and 1.5 m/s have the shortest times. With increasing velocities, the cooling prolongs again. Figures 6.12 and 6.13 show the profiles of the heat flux for the Aluminum sheet at the two previously defined distances with the velocity as the parameter. The profiles rapidly increase

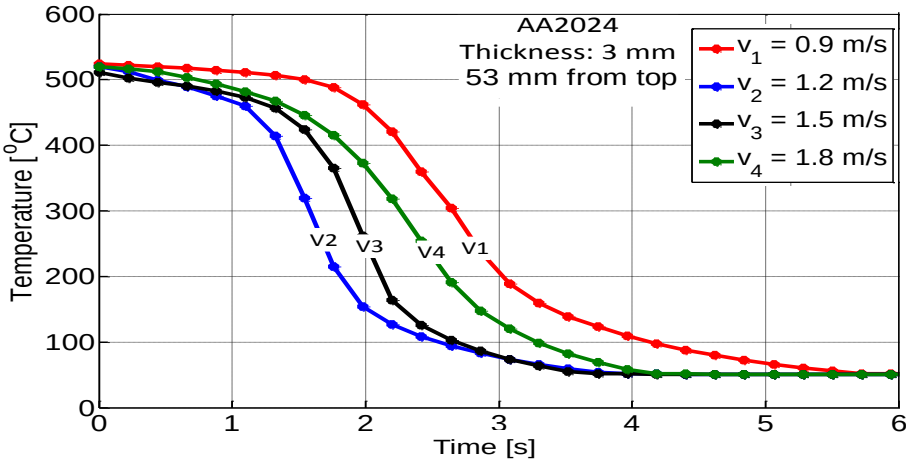

Figure 6.4: Temperature profiles of the AA2024 plate at 53 mm from the top

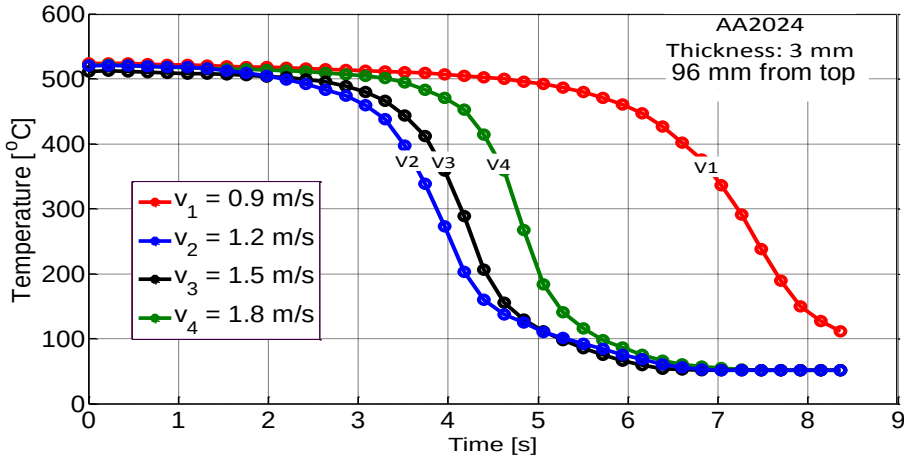

Figure 6.5: Temperature profiles of the AA2024 plate at 96 mm from the top

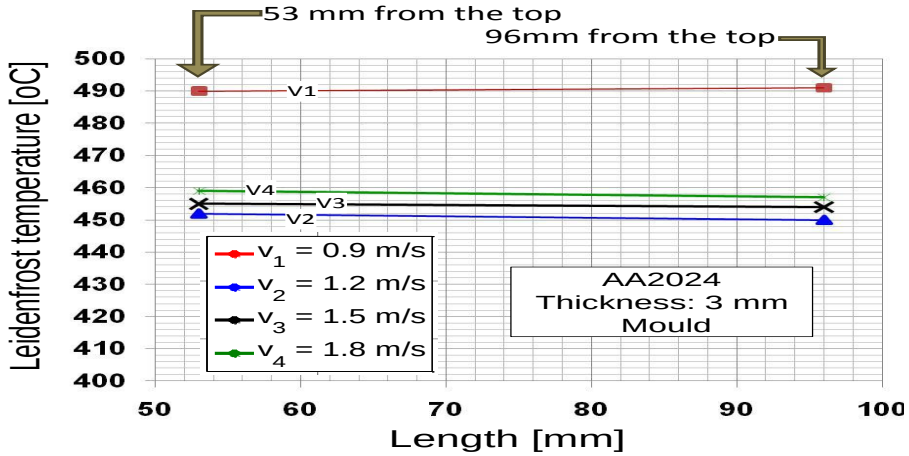

Figure 6.6: Leidenfrost temperature of AA2024 for four velocities at 53 and 96 mm from the top

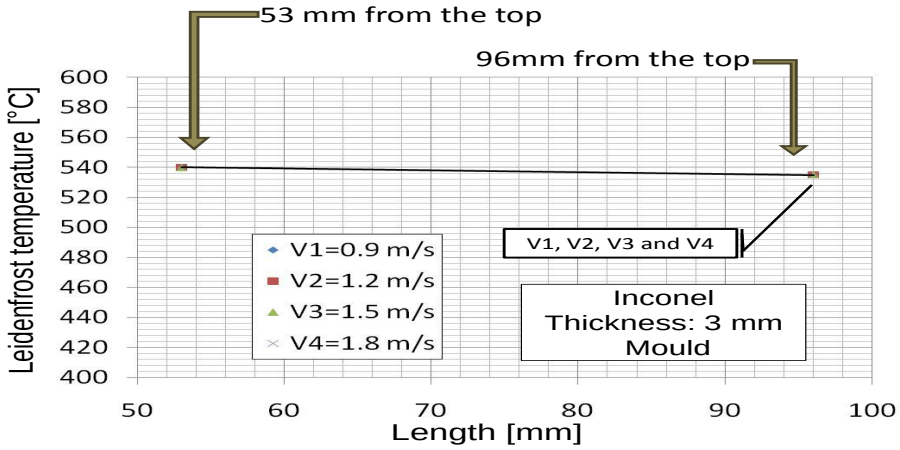

Figure 6.7: Leidenfrost temperature of Inconel for four velocities at 53 and 96 mm from the top

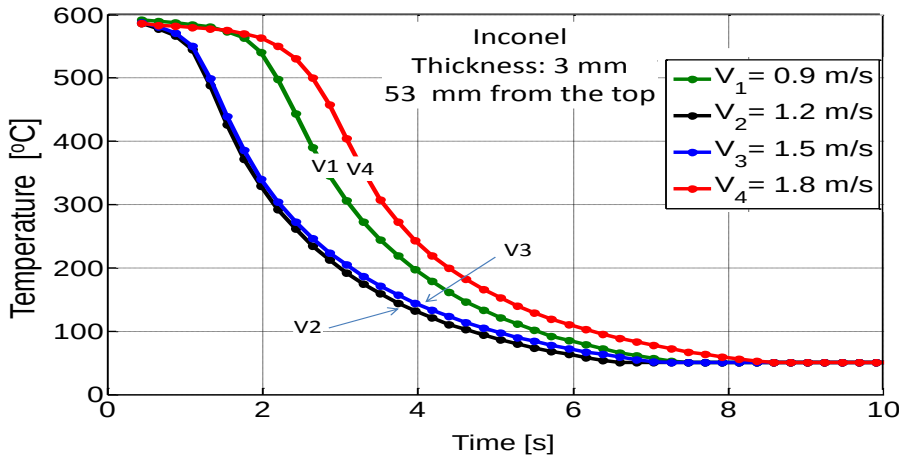

Figure 6.8: Temperature profiles of the Inconel plate at 53 mm from the top

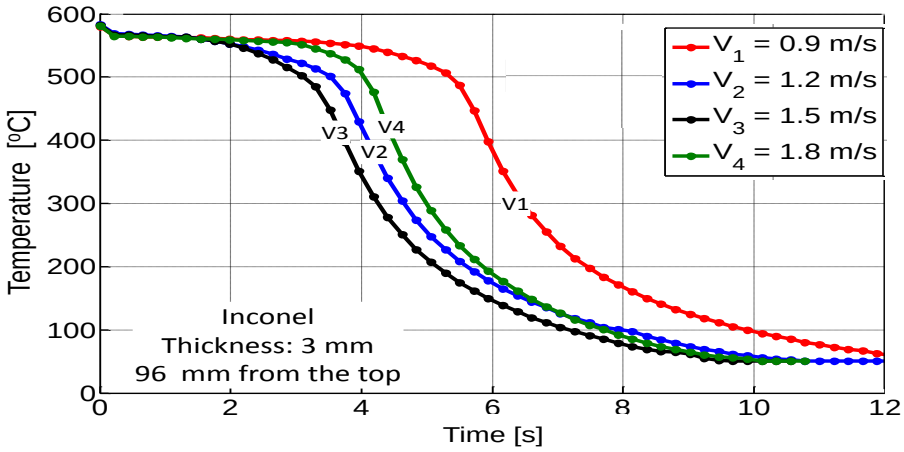

Figure 6.9: Temperature profiles of the Inconel plate at 96 mm from the top

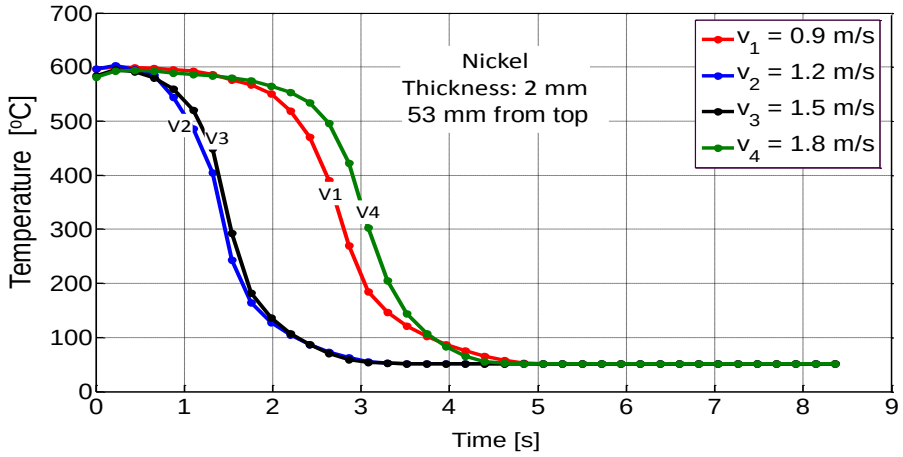

Figure 6.10: Temperature profiles of the Nickel plate at 53 mm from the top

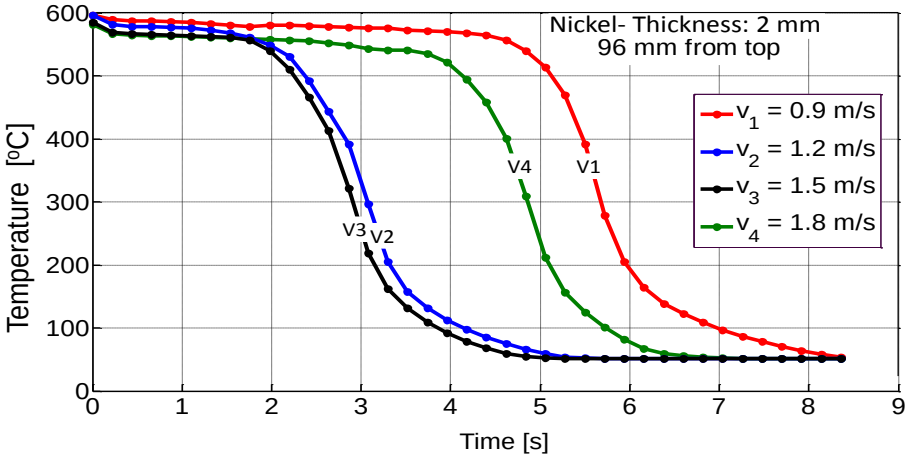

Figure 6.11: Temperature profiles of the Nickel plate at 96 mm from the top

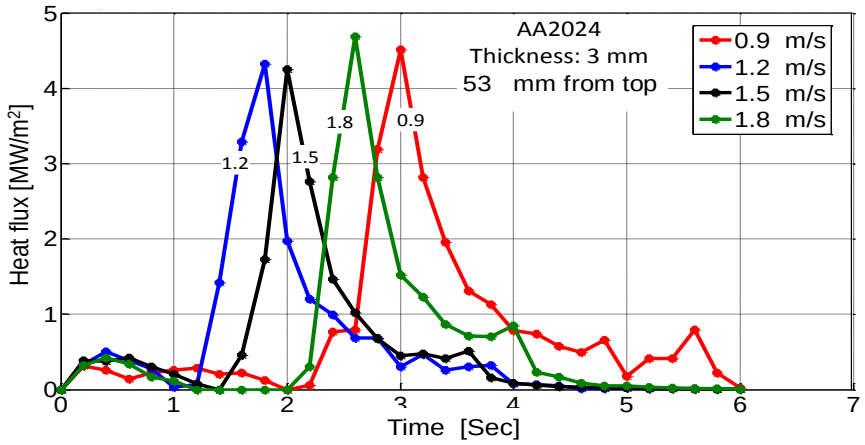

Figure 6.12: Heat flux distribution of AA2024 at 53 mm from the top

approximately linear to the max. value, decreases again approximately linear at the beginning and then the gradient becomes lower.

From the comparison of Figure 6.4, it can be seen, using the velocity of 1.2 m/s as an example and, at the position 53 mm after 1.2 sec. the LFT is reached. At that time, the heat flux increases rapidly. From Figure 6.4, it can be seen that the temperature 100 ^oC , the end of the boiling region, occurs after 2.3 sec. This is the time where the heat flux turns from the linear and decreases into the horizontal direction. Therewith, the time for passing the wetting front at the distance 53 mm is 1.1 seconds. The corresponding range will be discussed later. At the distance 96 mm, the LFT is reached after 3.0 sec. At this time, the heat flux increases again rapidly. The temperature 100 ^oC is reached after 5.0 sec. The time interval for passing of the wetting front is therewith 2.0 seconds. It seems that the value of the MaxHF is slightly lower at the position 96 mm in comparison to 53 mm. As an example, for the velocity 1.2 m/s, the value decreases from approximately, 4.4 to 3.4 MW/m^2 and for the 1.5 and 1.8 m/s form 4.4 to 4.0 MW/m^2.

Figures 6.14 and 6.15 show the heat flux for the Inconel in the same form as before. From Figures 6.8 and 6.9, it can be seen that at the position 53 mm, the LFT is reached after approximately 0.8 sec. for the velocities 1.2 and 1.5 m/s. At this time, the heat flux increases again rapidly. The temperature 100 ^oC is reached after 4.5 sec. This time does not have a special mark in the heat flux profile. The time interval for passing of the wetting front is 3.7 sec. and therewith, much longer than for the metal AA2024. However, the value of the MaxHF is about 2.3 MW/m^2 considerably lower. For the distance 96 mm, the LFT is reached after approximately 3.0 sec. and the boiling temperature after 7.0 sec. The time interval again increases slightly with the distance from 3.7 to 4.0 seconds and the MaxHF

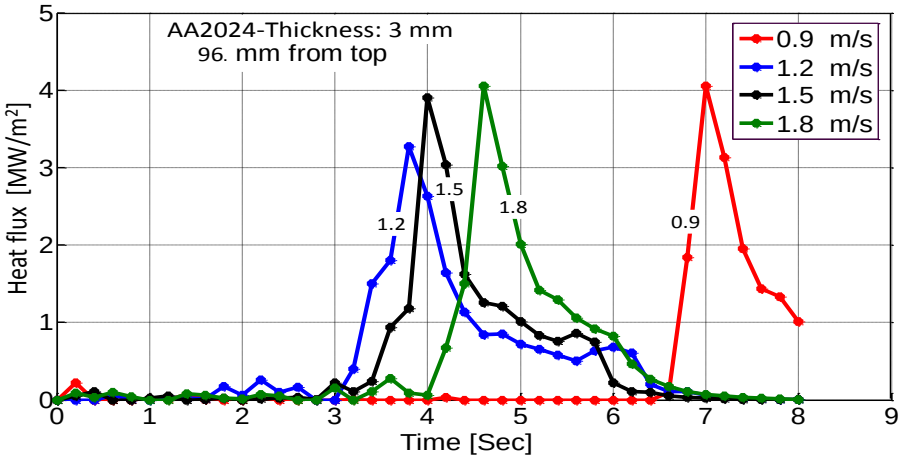

Figure 6.13: Heat flux distribution of AA2024 at 96 mm from the top

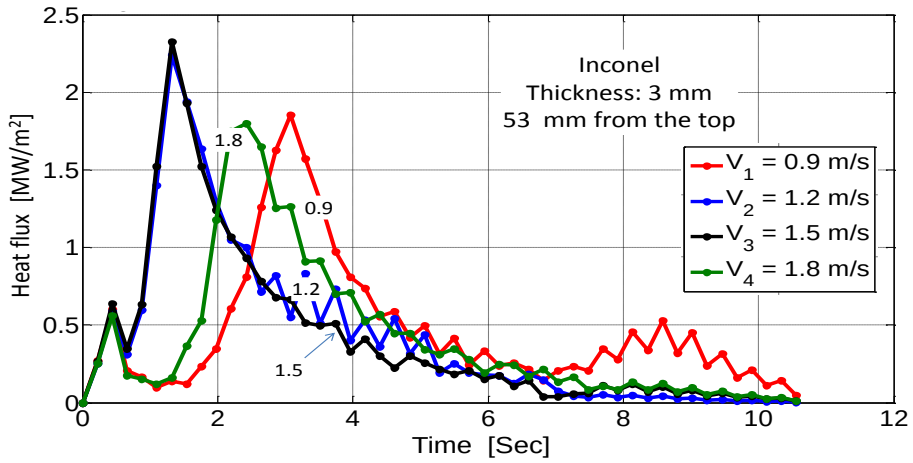

Figure 6.14: Heat flux distribution of the Inconel at 53 mm from the top

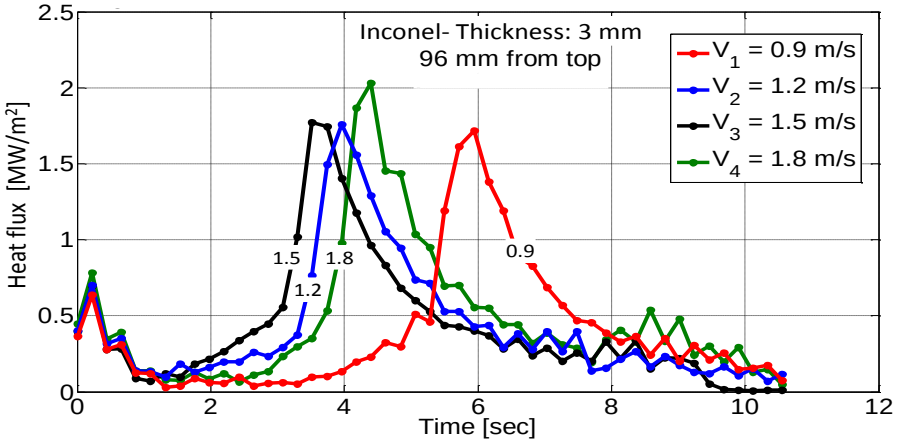

Figure 6.15: Heat flux distribution of the Inconel at 96 mm from the top

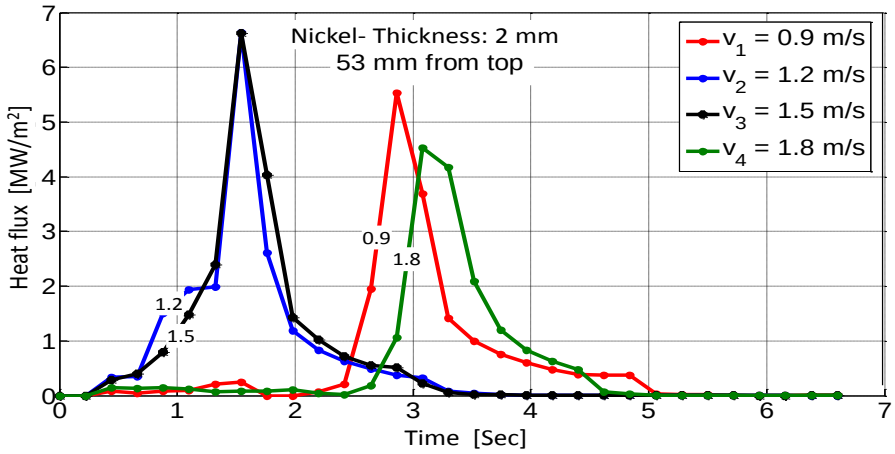

Figure 6.16: Heat flux distribution of the Nickel plate at 53 mm from the top

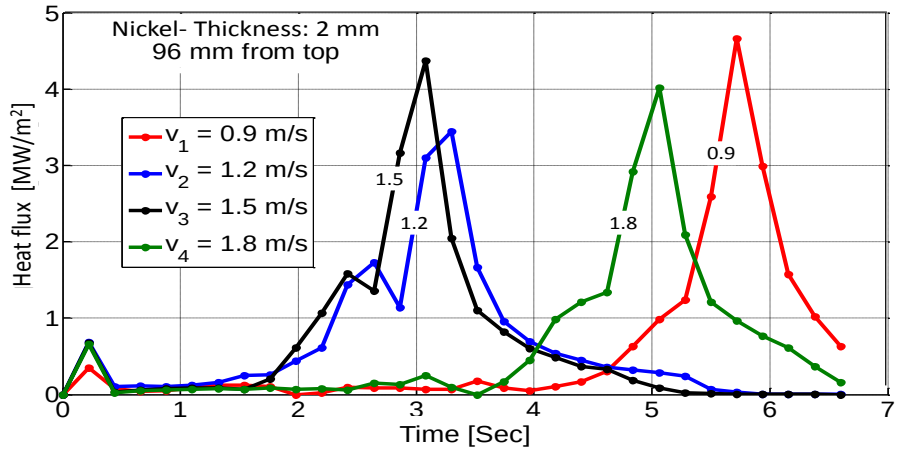

Figure 6.17: Heat flux distribution of the Nickel plate at 96 mm from the top

decreases again from 2.3 to 1.7 MW/m^2. The value of the MaxHF for Inconel is lower than for AA2024. This matches with Figure 5.15 for the spray cooling. Figure 6.16 and 6.17 shows the heat flux profiles for nickel. From Figure 6.8, it can be seen that for the velocity 1.2 m/s and 1.5 m/s, the LFT and the boiling temperature are reached after 1.0 sec. and 2.1 sec., respectively, and at 53 mm and 96 mm, after 2.5 sec and 4.0 sec. If in Figures 6.16 and 6.17 both linear lines for the heat flux are prolonged from the max. value to the value zero, then this time matches with the time of the LFT. The time interval for the passing of the wetting increases again with the distance from 1.1 sec. to 1.5 sec. The HF decreases again from about 6.6 to 4 MW/m^2.

The movement of the MaxHF with time is shown is Figures 6.18, 6.19 and 6.20 for all three metals with the jet velocity as the parameter. It can be seen that for all cases the position of the MaxHF increases linearly with time. Therewith, the wetting front velocity stays constant. The gradient gives the velocity of the

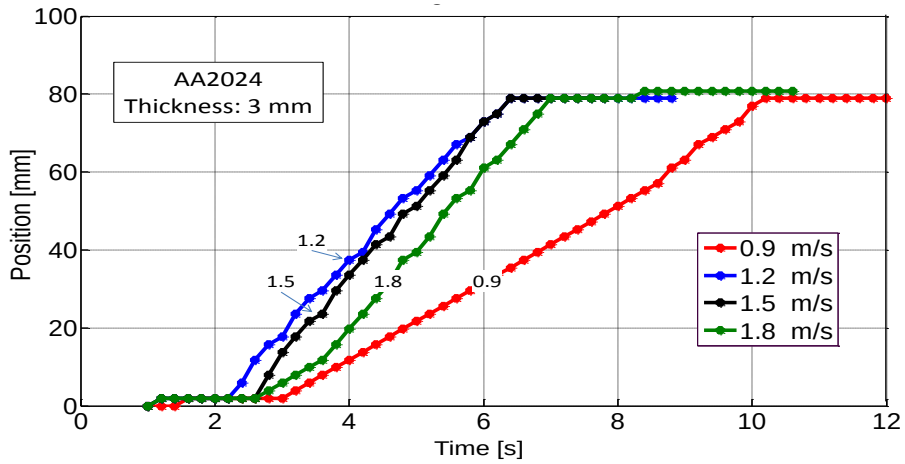

Figure 6.18: MaxHF propagation of AA2024 for four cooling water velocities

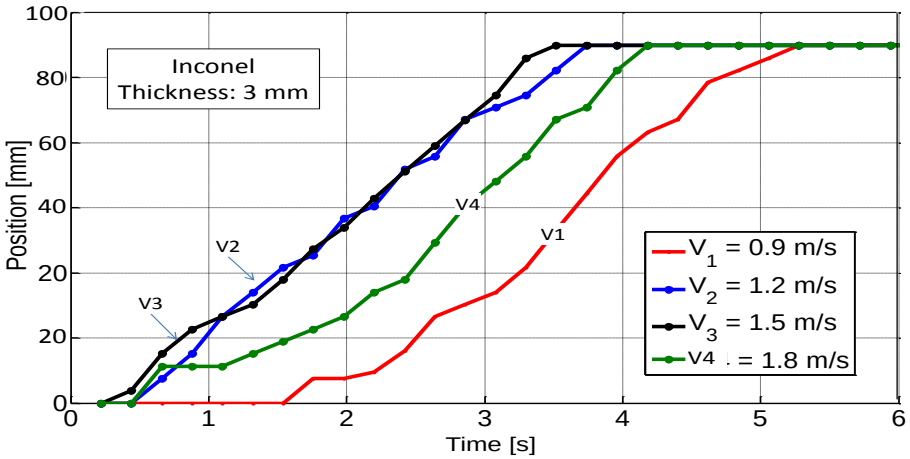

Figure 6.19: MaxHF propagation of Inconel for four cooling water velocities

wetting front. This velocity is depicted in Figure 6.21. Its value increases with the water jet velocity to a maximal value and then decreases. This is similar to the cooling times. Inconel has slightly higher wetting velocity than AA2024. The wetting front velocity of the nickel cannot be compared because the plate has a lower thickness which results in a higher value.

Figure 6.22 shows photographs of the wetting front at four different times. The photographs were taken from the film of the high speed camera. The movement at the center line is again used for the analysis. Figures 6.23, 6.24 and 6.25 shows the position of the wetting front with dependence on the frequence which is proportional to time. It can be seen that the position moves again approximately linear with time. The values of the wetting front velocity were calculated again from the gradient and shown in Figure 6.26. The tendency is similar, as before. Therefore, the values analyzed with this high speed camera and with the Infrared-Images are compared in Figure 6.27. Both methods of analyzing match.

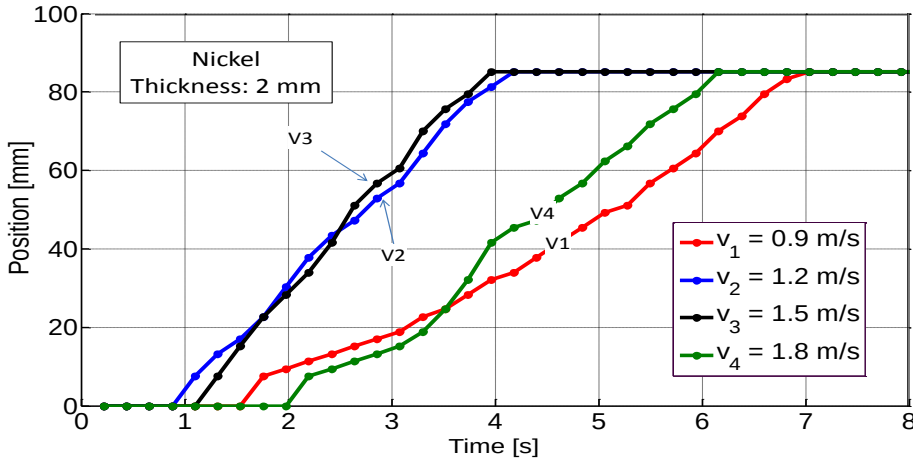

Figure 6.20: MaxHF propagation of Nickel for four cooling water velocities

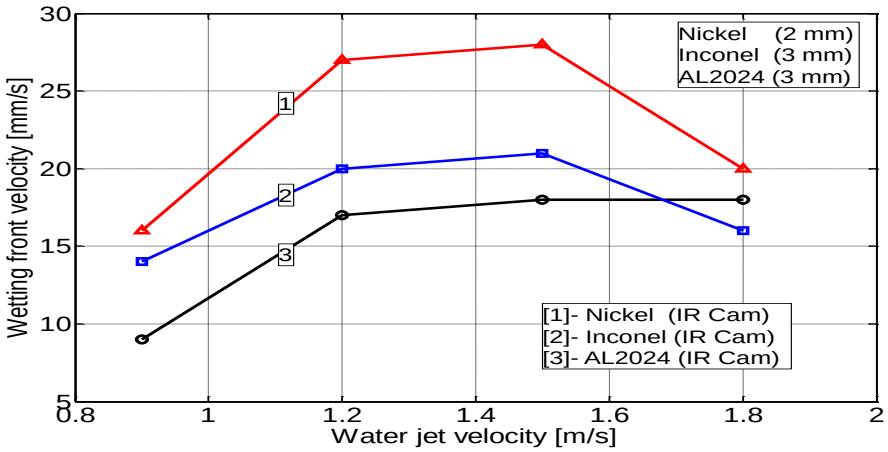

Figure 6.21: Wetting front velocity of three different metals using IR cam

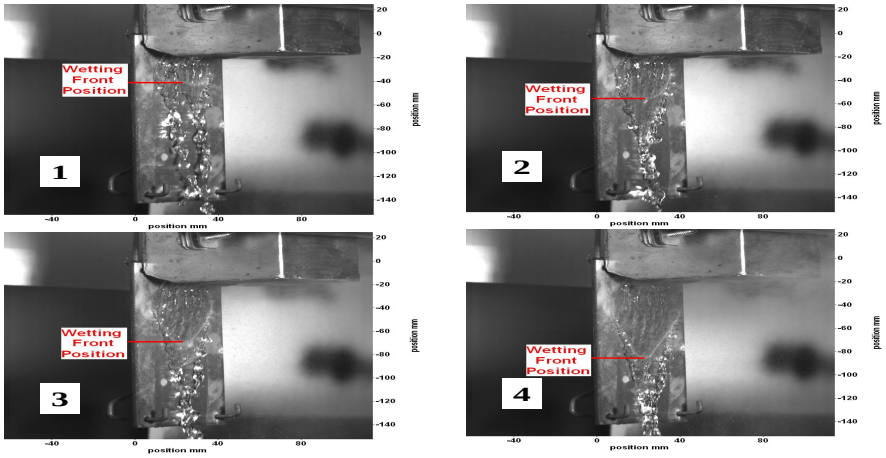

Figure 6.22: Wetting front position at four different positions on the surface

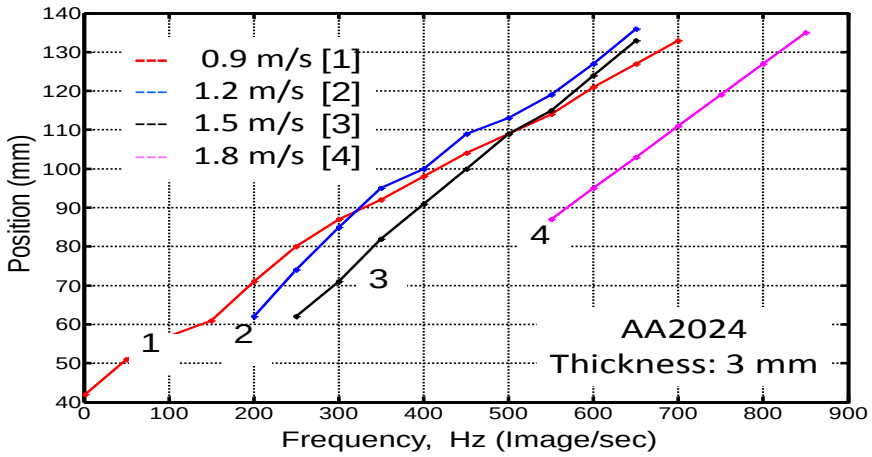

Figure 6.23: Wetting front propagation of AA2024 by using high speed cam

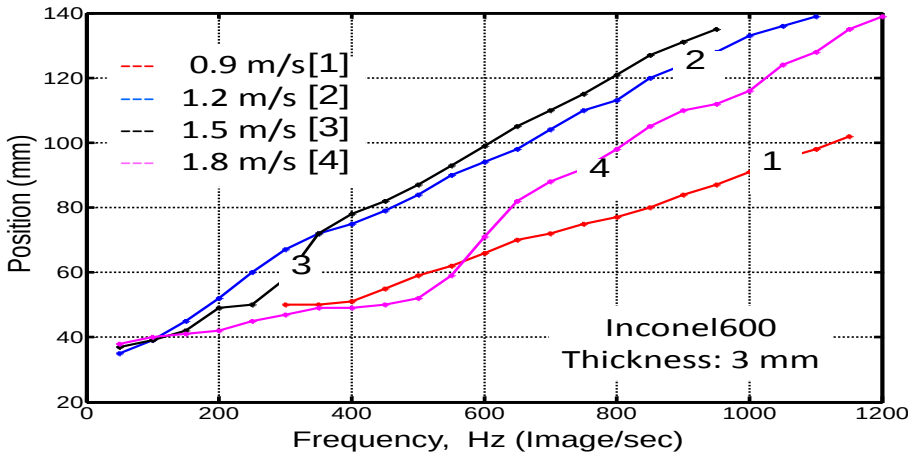

Figure 6.24: Wetting front propagation of Inconel by using high speed cam

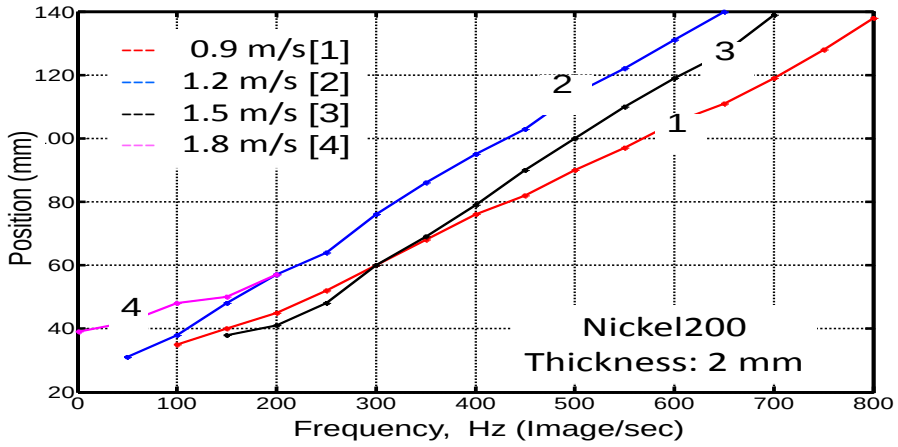

Figure 6.25: Wetting front propagation of Nickel by using high speed cam

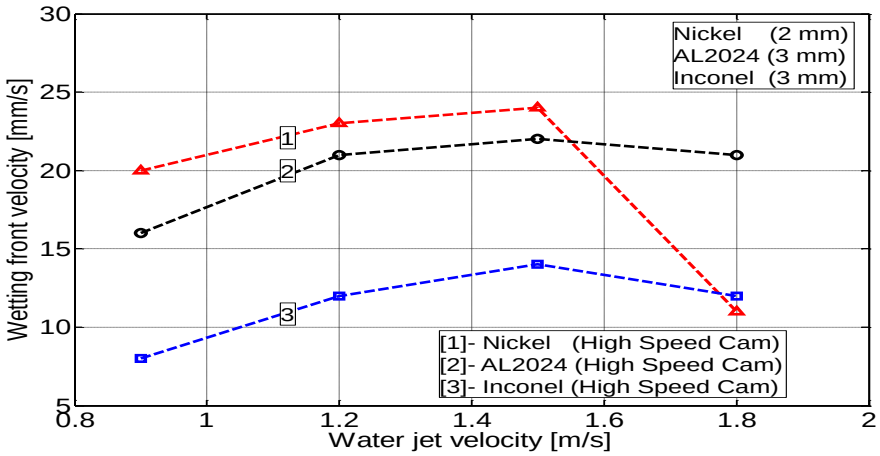

Figure 6.26: Wetting front velocity of three different metals using high speed cam

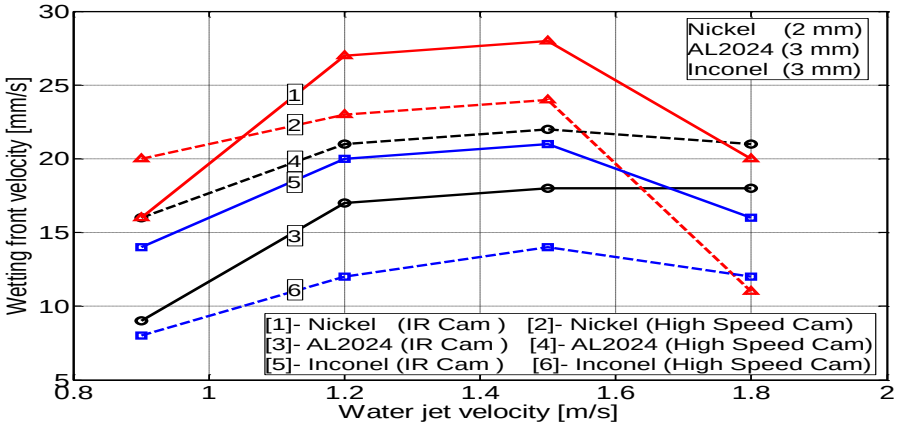

Figure 6.27: Variation of wetting front velocity with respect to water jet velocity for three materials

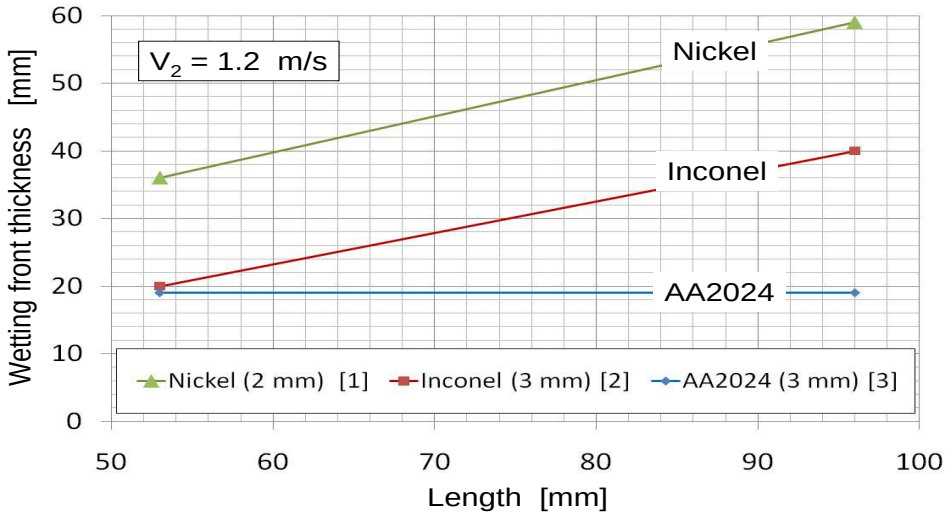

Figure 6.28: Wetting front range of the three metals at water jet velocity 1.2 m/s

From the cooling profiles, the time interval can be determined, in which the temperature falls from LFT to boiling temperature. Using the wetting front velocity now the range of the wetting front can be calculated. This range is shown in Figure 6.28 with dependence on the length of the plate with the jet velocity 1.2 m/s as an example. For AA2024, the range is 20 mm and seems to be constant. For Inconel and Nickel, the range increases with the length. Nickel has a much larger range than the other two metals. From the Figures **??**, **??** and **??**, it can be concluded that the MaxHF is in the middle of the period between the times at which LFT and boiling temperatures are reached. Therefore, the heat flux profile can be approximated by a triangle. The area within this triangle is the heat flow, which is transferred by the wetting front. This heat flow is half of the value of the MaxHF multiplied by the area of the wetting front, which is the range multiplied with the width of the plate. In Table 6.1, the heat flow per meter of width is summarized for the three metals and the two positions. It seems that this heat flow is dependent on the position and therewith, on the length of the plate. A lower MaxHF is compensated by a larger range. It is remarkable that the heat flow depends on the kind of metal. The very high value of Nickel can not be explained by the lower plate thickness of 2 mm instead of 3 mm. The reason cannot be explained. More tests with plates of the same thickness must be conducted.

6.4 Comparison with literature

Heat transfer measurements for moulds are unknown. Therefore, a comparison will be done for the heat transfer of one jet which impinges vertically a plate. Such experiments are conducted from the research group M. Monde [112]. In this

Table 6.1: Heat flow per meter of width of metals at water jet velocity 1.2 m/s

Metal	Position mm from the top	MaxHF MW/m^2	Range MW/m^2	Heat flow kW/m
AA2024	At 53	4.4	0.02	88
	At 96	4.0	0.02	80
Inconel	At 53	2.5	0.02	50
	At 96	1.8	0.04	68
Nickel	At 53	6.5	0.036	234
	At 96	3.5	0.06	210

quenching case, in the stagnation point immediately wetting occurs. Then the wetting front moves in radial direction. The sample was a block with a 94 mm diameter and 59 mm thickness. The metal was copper, steel and brass. The initial temperature varied from 250 ^oC to 600 ^oC. The wetting front was researched using a high speed camera. In Woodfield [112] et al., the MaxHF and the range of the wetting front are described. For a jet velocity of 3 m/s, the range is 16 mm at the radius 8 mm and increases with the radius to 30 mm at a radius of 15 mm. The MaxHF decreases with the radius from 4.5 MW/m^2 at the radius 8 mm to 1.5 MW/m^2 at the radius 15 mm. These results principally match with the mould. The MaxHF decreases with the distance to the jet and therefore, the range of the wetting front increases. The values of the MaxHF and the range of the wetting front are in the same magnitude.

References

[1] L. Burmeister, *Convective Heat Transfer*. Wiley, 1983.

[2] I. J. Opstelten and J. M. Rabenberg, "Determination of the thermal boundary conditions during aluminum DC casting from experimental data using inverse modeling," in *Light Metals: Proceedings of Sessions, TMS Annual Meeting (Warrendale, Pennsylvania)* (C. E. Eckert, ed.), pp. 729–735, 1999.

[3] D. C. Weckman and P. Niessen, "A numerical simulation of the D.C. continuous casting process including nucleate boiling heat transfer," *Metallurgical Transactions B*, vol. 13, no. 4, pp. 593–602, 1982.

[4] J. Sengupta, B. Thomas, and M. WELLS, "The use of water cooling during the continuous casting of steel and Aluminium alloys," *Metallurgical and Materials Transactions A*, vol. 36, pp. 187–204, 2005.

[5] D. Mortensen, "A mathematical model of the heat and fluid flows in direct-chill casting of aluminum sheet ingots and billets," *Metallurgical and Materials Transactions B: Process Metallurgy and Materials Processing Science*, vol. 30, no. 1, pp. 119–132, 1999.

[6] J. Wiskel, *Thermal analysis of the startup phase for D.C casting of an AA5182 aluminum ingot*. PhD thesis, The University of British Columbia, Canada, 1995.

[7] H. Tansi and G. Totten, "Proceedings of the 3rd International Conference on Quenching and Control of Distortion," *Czech Republic*, pp. 50–61, 1999.

[8] J. Filipovic, R. Viskanta, F. P. Incropera, and T. A. Veslocki, "Behavior of a Steel Strip Cooled by an Array of Planar Water Jets," *Steel Res.*, vol. 63, pp. 438–446, 1992.

[9] C. Kohler, E. Specht, and R. Jeschar, "Heat Transfer with Film Quenching of Vapourizing Liquids," *Steel Res.*, vol. 61, pp. 553–559, 1990.

[10] T. A. Deiters and I. Mudawar, "Optimization of Spray Quenching for Aluminum Extrusion, Forging, or Continuous Casting," *J. Heat Treatment*, vol. 7, pp. 9–18, 1989.

[11] T. Ueda, S. Tsunenari, and M. Koyanagi, "An Investigation of Critical Heat Flux and Surface Rewetting in Flow Boiling Systems," *Int. J. Heat Mass Transfer*, vol. 26, pp. 1189–1198, 1983.

[12] M. Ishii, "Study on Emergency Core Cooling," *Nucl. Energy Soc. J.*, vol. 14, pp. 237–242, 1975.

[13] J. J. Carbajo, "A Study on the Rewetting Temperature," *Nucl. Eng. Design*, vol. 84, pp. 21–52, 1985.

[14] O. C. Iloeje, D. N. Plummer, W. M. Rohsenow, and P. Griffith, "Effects of Mass Flux, Flow Quality, Thermal and Surface Properties of Materials on Rewet of Dispersed Flow Film Boiling," *J. Heat Transfer*, vol. 104, pp. 304–308, 1982.

[15] H. S. Ragheb, S. C. Cheng, and D. C. Groeneveld, "Observations in Transition Boiling of Subcooled Water under Forced Convection Conditions," *Int. J. Heat Mass Transfer*, vol. 24, pp. 1127–1137, 1981.

[16] J. M. Delhaye, M. Giot, and M. L. Riethnuller, *of Two-Phase Systems for Industrial Design and Nuclear Engineering*. McGraw-Hill, New York, 1981.

[17] E. Elias and G. Yadigaroglu, "A General One-Dimensional Model for Conduction- Controlled Rewetting of a Surface," *Nuclear Engineering and Design*, vol. 42, pp. 185–194, 1977.

[18] J. A. Hammad, *Characteristics of heat transfer and wetting front during quenching high temperature surface by jet impingement.* PhD thesis, Saga University, march 2004.

[19] K. Yoshioka and S. Hasegawa, "A Correlation in Displacement Velocity of Liquid Film Boundary Formed on a Heated Vertical Surface in Emergency Cooling," *Journal of Nuclear Science and Technology*, vol. 7, pp. 418–425, 1970.

[20] O. C. Iloeje, D. N. Plummer, W. M. Rohsenow, and P. Griffith, "An Investigation of the Collapse and Surface in Film Boiling in Forced Vertical Flow," *Trans ASME, Journal of Heat Transfer*, vol. 14, pp. 166–172, 1975.

[21] M. Mitsutsuka and K. Fukuda, "Boiling Phenomena and Effects of Water Temperature on Heat Transfer in the Process of Immersion Cooling of a Heated Steel Plate," *Transactions of the Iron and Steel Institute of Japan*, vol. 19, pp. 162–169, 1979.

[22] V. K. Dhir, R. B. Duffey, and I. Catton, "Studies on a Zircaloy Rod Bundle," *Journal of Heat Transfer*, vol. 103, pp. 293–299, 1981.

[23] J. Kokado, N. Hatta, H. Takuda, J. Harada, and N. Yasuhira, "An Analysis of Film Boiling Phenomena of Subcooled Water Spreading Radially on a Hot Steel Plate," *Arch. Eisenhüttenwes*, vol. 55, pp. 113–118, 1984.

[24] Y. Lee and W. Shen, "Effect of Coolant Vapor Quality on Rewetting Phenomena," *J. Heat Mass Transfer*, vol. 28, pp. 139–146, 1985.

[25] Y. Barnea and E. Elias, "Flow and Heat Transfer Regimes During Quenching of Hot Surfaces," *Int. J. Heat Mass Transfer*, vol. 37, pp. 1441–1453, 1994.

[26] I. Mudawar and T. A. Deiters, "A Universal Approach to Predicting Temperature Response of Metallic Parts to Spray Quenching," *Int. J. Heat Mass Transfer*, vol. 37, pp. 347–362, 1994.

[27] J. Filipovic, F. P. Incropera, and R. Viskanta, "Quenching Phenomena Associated with a Water Wall Jet: I. Transient Hydrodynamic and Thermal Conditions, Experimental Heat Transfer," *Journal of Heat Transfer*, vol. 8, pp. 97–117, 1995.

[28] S. Kumagai, S. Suzki, Y. Sano, and M. Kawazoe, "Transition Cooling of a Hot Metal Slab by an Impinging Jet with Boiling Heat Transfer," *ASME/JSME Thermal Engineering Conference*, vol. 2, pp. 347–352, 1995.

[29] M. Ciofalo, I. Piazza, and V. Brucato, "Investigation of the Cooling of Hot Walls by Liquid Water Sprays," *Int. J. Heat Mass Transfer*, vol. 42, pp. 1157–1175, 1999.

[30] D. E. Hall, F. P. Incropera, and R. Viskanta, "Jet Impingement Boiling from a Circular Free-Surface Jet During Quenching: Part 2-Single-Phase Jet," *ASME Journal of Heat Tramfer*, vol. 123, pp. 911–917, 2001.

[31] Y. Mitsutake and M. Monde, "Heat Transfer During Cooling of High Temperature Surface with an Impinging Jet," *Heat and Mass Transfer*, vol. 37, pp. 321–328, 2001.

[32] Z. H. Liu and J. Wang, "Study on Film Boiling Heat Transfer for Water Jet Impinging on High Temperature Flat Plate," *Int. J. Heat Mass Transfer*, vol. 44, pp. 2475–2481, 2001.

[33] Q. Cui, S. Chandra, and S. McCahan, "The Effect of Dissolving Salts in Water Sprays Used for Quenching a Hot Surface: Part 2-Spray Cooling," *ASME Journal of Heat Transfer*, vol. 125, pp. 333–338, 2003.

[34] W. Jia and H. H. Qiu, "Experimental Investigation of Droplet Dynamics and Heat Transfer in Spray Cooling," *Experimental Thermal and Fluid Science*, vol. 27, pp. 829–838, 2003.

[35] K. J. Baumeister and F. F. Simon, "Leidenfrost Temperature Its Correlation for Liquid Metals, Cryogens, Hydrocarbons, and Water," *ASME Journal of Heat Tramfer*, vol. 95, pp. 166–173, 1973.

[36] E. R. G. Eckert and R. M. Drake, *Analysis of Heat and Mass Transfer*. McGraw-Hill, 1972.

[37] J. D. Bernardin and i. Mudawar, "The Leidenfrost Point: Experimental Study and Assessment of Existing Models," *ASME*, vol. 121, pp. 894–903, 1999.

[38] B. S. Gottfried, C. J. Lee, and K. Bell, "The Leidenfrost Phenomenon: Film Boiling of Liquid Droplets on a Flat Plate," *Int. J. Heat Mass Transfer*, vol. 9, pp. 1167–1187, 1966.

[39] B. M. Patel and K. J. Bell, "The Leidenfrost Phenomenon for Extended Liquid Masses," *Chem. Eng. Progress Symposium Series*, vol. 62, pp. 62–71, 1966.

[40] S. Nishio and M. Hirata, "Direct Contact Phenomenon between a Liquid Droplet and High Temperature Solid Surface," *International Heat Transfe*, vol. 1, pp. 245–250, 1978.

[41] E. S. Godleski and K. J. Bell, "The Leidenfrost Phenomenon for Binary Liquid Solutions," *International Heat Transfer*, vol. 4, pp. 51–58, 1966.

[42] S. C. Yao and K. Y. Cai, "The Dynamics and Leidenfrost Temperature of Drops Impacting on a Hot Surface at Small Angles," *Exp. Thermal Fluid Sci*, vol. 1, pp. 363–371, 1988.

[43] W. P. Klinzing, J. C. Rozzi, and I. Mudawar, "Film and Transition Boiling Correlations for Quenching of Hot Surfaces with Water Sprays," *J. Heat Treating*, vol. 9, pp. 91–103, 1992.

[44] V. C. Labeish, "Thermo hydrodynamic Study of a Drop Impact Against a Heated Surface," *Exp. Thermal Fluid Sci.*, vol. 8, pp. 181–194, 1994.

[45] K. Bell, "The Leidenfrost Phenomenon," *Chem. Eng. Prog. Symposium Series AIChE*, vol. 63, pp. 73–82, 1967.

[46] K. J. Baumeister, R. E. Henry, and F. F. Simon, "Role of the Surface in the Measurement of the Leidenfrost Temperature," *Augmentation of Convective Heat and Mass Transfer, A. E. Bergles and R. L. Webb, eds., ASME*, pp. 91–101, 1970.

[47] H. Hiroyasu, T. Kadota, T., and Senda, "Droplet Evaporation on a Hot Surface in Pressurized and Heated Ambient Gas," *JSME*, vol. 17, pp. 1081–1087, 1974.

[48] G. S. Emmerson, "The Effect of Pressure and Surface Material on the Leidenfrost Point of Discrete Drops of Water," *Int. J. Heat Mass Transfer*, vol. 18, pp. 381–386, 1975.

[49] C. T. Avedisian, "Effect of Pressure on Bubble Growth Within Liquid Droplets at the Superheat Limit .," *ASME Journal of Heat Tramfer*, vol. 104, pp. 750–757, 1982.

[50] S. A. Kovalev, "An Investigation of Minimum Heat Fluxes in Pool Boiling of Water," *Int. J. Heat Mass Transfer*, vol. 9, pp. 1219–1226, 1966.

[51] C. Unal, V. Daw, and R. A. Nelson, "Unifying the Controlling Mechanisms for the Critical Heat Flux and Quenching: The Ability of Liquid to Contact the Hot Surface.," *ASME Journal of Heat Tramfer*, vol. 114, pp. 972–982, 1992.

[52] J. M. Ramilison and J. H. Lienhard, "Transition boiling heat transfer and the film transition regime," *J. of heat transfer*, vol. 109, pp. 746–752, 1987.

[53] G. P. Nikolayev, V. V. Bychenkov, and V. P. Skripov, "Saturated Heat Transfer to Evaporating Droplets from a Hot Wall at Different Pressures," *Heat Transfer Soviet Research*, vol. 6, pp. 128–132, 1974.

[54] C. W. Snoek and G. S. Emmerson, "The Effect of Pressure on the Leidenfrost Point of Discrete Drops of Water and Freon on a Brass Surface," *Int. J. Heat Mass Transfer*, vol. 21, pp. 1081–1086, 1978.

[55] P. Testa and L. Nicotra, "Influence of Pressure on the Leidenfrost Temperature and on Extracted Heat Fluxes in the Transient Mode and Low Pressure," *Journal of Heat Transfer*, vol. 108, pp. 916–921, 1986.

[56] V. V. Klimenko and S. Y. Snytin, "Film Boiling Crisis on a Submerged Heating Surface," *Thermal Fluid Sci.*, vol. 3, pp. 467–479, 1990.

[57] T. R. Rhodes and K. J. Bell, "The Leidenfrost Phenomenon at Pressures up to the Critical," *International Heat Transfer Conference Toronto, Canada, Hemisphere, New York*, vol. 1, pp. 251–255, 1978.

[58] C. Huang and V. Carey, "The effect of dissolved salt on the leidenfrost transition," *Intl. J. Heat and Mass Transfer*, vol. 50, pp. 269–282., 2006.

[59] U. Alam, K. Abdalrahman, and E. Specht, "Experimental investigation of influence of dissolved salts and surfactant on heat transfer in atomized spray quenching of metal," in *2010 14th International Heat Transfer Conference, IHTC14*, pp. 779–786, 2010.

[60] S. Chandra and C. Avedisian, "On the collision of a droplet with a solid surface," *Proc. R. Soc. London*, vol. A 432, p. 1341, 1991.

[61] B. Kang and D. Lee, "On the dynamic behavior of a liquid droplet impacting upon a inclined heated surface," *Expt. Fluids*, vol. 29, p. 380387, 2000.

[62] F. McGinnis and J. Holman, "Individual Droplet Heat Transfer Rates for Splattering on Hot Surfaces," *Int. J. Heat Mass Transfer*, vol. 12, pp. 85–105, 1969.

[63] K. Choi and S. Yao, "Mechanisms of Film Boiling Heat Transfer of Normally Impacting Spray," *Int. J. Heat Mass Transfer*, vol. 30, pp. 311–318, 1987.

[64] N. Sozbir, C. Y, and S. Yao *Trans, ASME*, vol. 125, pp. 71–74, 2003.

[65] H. R. Müller and R. Jeschar, "Wärmeübertragung bei der Spritzwasserkühlung von Nichteisenmetallen," *Metallkunde*, vol. 74, pp. 257–264, 1983.

[66] R. Jeschar, U. Reiners, and R. Scholz, "Heat Transfer During Water and Water Air Spray Cooling in the Secondary Cooling Zone of Continuous Casting Plants," in *Proceedings of the 69th Steelmaking Conference, Washington D. C., April 6-9, Vol. 69, Book 1, pp 511-521*, 1986.

[67] U. Reiners, R. Jeschar, and R. Scholz, "Wärmeübertragung bei der Stranggusskühlung durch Spritzwasser," *Steel Research*, vol. 60, pp. 442–450, 1989.

[68] R. Jeschar, U. Reiners, and R. Scholz, "Wärmeübertragung bei der zweiphasigen Spritzwasserkühlung," *In Gaswärme int.*, vol. 33, pp. 299–308, 1984.

[69] R. Jeschar, U. Reiners, and R. Scholz, "Heat transfer during one and two-phase water spray cooling in hot metals," *Sixth Japan-Germany Seminar*, vol. 33, pp. 146–159, 1984.

[70] M. Shimada and M. Mitsutsuka, "On Heat Transfer Coefficient by Forced Water Cooling to Carbon Steel," *Tetsu-to-Hagane*, vol. 52, pp. 1643–1651, 1966.

[71] H. Yu, "Method of Preventing Cracking in Direct Chill Cast Ingots," tech. rep., United States Patent, 2006.

[72] K. Choi and S. Yao, "Mechanisms of Film Boiling Heat Transfer of Normally Impacting Spray," *Int. J. Heat and Mass Transfer*, vol. 30, pp. 311–318, 1987.

[73] E. Mizikar, "Spray Cooling Investigation for Continuous Casting of Billets and Blooms," *Iron Steel Enging*, pp. 53–70, 1970.

[74] H. M. Al-Ahamdi and S. C. Yao, "Experemintal study on the spray cooling of Cooling high temperature metal using full cone industrial sprays," *ASME 2006 International Mechanical Engineering Congress and Exposition*, vol. 2, pp. 679–687, 2006.

[75] A. Tseng, F. Lin, A. Gungeria, and D. Ni, "Roll cooling and its relationship to roll life," *Metallurgical Transactions*, vol. 20A, 1989.

[76] J. Horsky, M. Raudensky, and W. Sauer, "Experimental study of cooling characteristics in hot rolling," *J. Mater. Proc*, vol. 45, pp. 131–135, 1994.

[77] P. F. Bariani, T. D. Negro, and S. Masiero, "Experimental evaluation and FE simulation of thermal conditions at tool surface during cooling and deformation phases in hot forging applications," *CIRP Annals - Manufacturing Technology*, vol. 51/1, pp. 219–222, 2002.

[78] P. F. Bariani, T. D. Negro, and S. Masiero, "Influence of coolant spray conditions on teat transfer at die surface in hot forging," in *Proc. 7th ICTP*, vol. 1, pp. 781–786, 2002.

[79] L. Kiss, T. Meenken, A. Charette, Y. Lefebvre, and R. Levesque, "Effect of water quality and water type on the heat transfer in DC casting," *TMS Light Metals*, p. 829834, 2003.

[80] L. Kiss, T. Meenken, A. Charette, V. Lefebvre, and R. Levesque, "Experimental Study of the Heat Transfer Along the Surface ofa Water-Film Cooled Ingot," *Light Metals*, pp. 981–985, 2002.

[81] H. Vu, "The Effect ofCooling Water Quality on Aluminum Ingot Casting," *Light Metals*, pp. 1331–1347, 1985.

[82] T. Bergstrom, "Transfer in the Continuous DC Casting Process of Aluminium," *Light Metals*, 1987.

[83] J. Langlais, T. Bourgeois, Y. Caron, G. Beland, and D. Bernard, "Measuring the Heat Extraction Capacity of DC Casting Cooling Water," *Light Metals*, pp. 979–986, 1995.

[84] M. Bamberger and B. Prinz, "Determination of Heat Transfer Coefficients during Water Cooling of Metals," *Journal of Material Science and Technology*, vol. 2, pp. 410–415, 1986.

[85] S. Hamilton, "Heat Transfer and Water Quality in DC Casting," *Chemical and Materials Engineering*, 1995.

[86] J. Grandfield, A. Hoadley, and S. Instone, "Water Cooling in Direct Chill Casting: Part 1, Boiling Theory and Control," *Light Metals*, pp. 691–699, 1997.

[87] H. Yu, "The effect of cooling water quality on aluminium ingot casting," *Light Metals*, pp. 1331–1347, 1985.

[88] Y. Watanabe and N. Hayashi, "3-D solidification analysis of the initial state of the DC casting process," *Light Metals*, pp. 979–984, 1996.

[89] P. J. Berenso, "Experiments on pool boiling heat transfer," *Int. J. Heat and Mass transfer*, vol. 15, pp. 985–999, 1962.

[90] T. D. Bui and V. K. Dhir, "Boiling heat transfer on a vertical surface," *ASME, J. Heat transfer*, vol. 107, pp. p756–763, 1985.

[91] J. B. Wiskel and S. L. Cockcroft, "Heat-Flow-Based Analysis of Surface Crack Formation During the Start-Up of the Direct Chill Casting Process: Part II. Experimental Study of an AA5182 Rolling Ingot," *Metallurgical and Materials Transactions B*, vol. 27B, pp. 129–137, 1996.

[92] A. K. Nallathambi and E. Specht, "Estimation of heat flux in array of jets quenching using experimental and inverse finite element method," *Journal of Materials Processing Technology*, vol. 209, pp. 5325–5332, 2009.

[93] D. Celentano, E. Orate, and S. Oller, "A temperature-based formulation for finite element analysis of generalized phase-change problems," *International Journal for Numerical Methods in Engineering*, vol. 37, pp. 3441–3465, 1994.

[94] K. Bathe, *Finite Element Procedures in Engineering Analysis*. Prentice-Hall, 1982.

[95] J. Beck, *Inverse Heat Conduction. Ill-posed Problems*. Wiley / Inter science, 1985.

[96] Y. Jarny, M. Ozisik, and J. Bardon, "A general optimization method using adjoint equation for solving multidimensional inverse heat conduction," *International Journal of Heat and Mass Transfer*, vol. 34, pp. 2911–2919, 1991.

[97] A. Osman and J. Beck, "Investigation of transient heat transfer coefficient in quenching experiments," *International Journal of Heat and Mass Transfer*, vol. 112, pp. 843–848, 1990.

[98] A. S. Neto and M. Ozisik, "Two-dimensional inverse heat conduction problem of estimating the time-varying strength of a line heat source," *J. Appl. Phys.*, vol. 71, pp. 5357–5362, 1992.

[99] C. L. Niliot, "The boundary-element method for the time-varying strength estimation of point heat sources: application to a two-dimensional diffusion system," *Heat Transfer*, vol. 33, pp. 301–321, 1998.

[100] M. Ohmichi and N. Noda, "Inverse analysis of two-dimensional steady-state heat conduction problem with many plane heat sources," *Trans. Information Processing Soc. Jpn.*, vol. 36, pp. 2566–2572, 1995.

[101] X. Ling, R. Keanini, and H. Cherukuri, "A non-iterative finite element method for inverse heat conduction problems," *International Journal for Numerical Methods in Engineering*, vol. 56, pp. 1315–1334, 2003.

[102] J. Bakken and Bergstrom, "Heat transfer Measurements During D.C. Casting of Aluminium," in *Light Metals*, 1986.

[103] W. Schneider and E. Jensen, "Investigation About Starting Crackes In D.C. Casting of 6063 Type Billets. Part I: Experimental Results," *Light Metals*, pp. 931–936, 1990.

[104] R.D.More, G.Richards, and A.Story, "Electrical Conductivity as an Indicatornof Water Chemistry of Hydrologic Process," *Streamline Watershed Management Bulletin*, vol. 11, pp. 25–29, 2008.

[105] C. Qiang, S. Chandra, and S. McCahan, "The effect of dissolving salts in water sprays used for quenching a hot surface: Part 2-Spray cooling," *Journal of Heat Transfer*, vol. 125, pp. 333–338, 2003.

[106] R. Jeschar, E. Specht, and J. Köhler, "Heat Transfer During Cooling of Heated Metal Objects With Evaporating Liquids, ," *Tensi, H., Liscic, B., Luty, W. Theory and Technology of Quenching-Springer*, pp. 73–92, 1992.

[107] U. Alam, *Experimental Study of Local Heat Transfer during Quenching of Metals by Spray and Multiple Jets*. PhD thesis, Otto-von-Guericke-University Magdeburg, 2011.

[108] K. N. Prabhu and P. Fernandes, "Effect of surface roughness on metal/quenchant interfacial heat transfer and evolution of microstructure," *International Journal of Materials and Design*, vol. 28, pp. 544–550, 2007.

[109] J. D. Bernardin, J. Stebbins, and I. Mudawar, "Effect of surface roughness on water droplet impact history and heat transfer regimes," *International Journal of Heat and Mass Transfer*, vol. 40, pp. 73–88, 1997.

[110] J. D. Bernardin and I. Mudawar, "An Experimental Investigation Into the Relationship Between Temperature-Time History and Surface Roughness in the Spray Quenching of Aluminum Parts," *Journal of Engineering Materials and Technology*, vol. 118, pp. 127–134, 1996.

[111] D. Li, "Boiling water heat transfer study during casting of aluminum alloys," Master's thesis, The University of British Culombia, November 1999.

[112] P. Woodfield and M. Monde, "On the size of the boiling in jet impingement quenching," *Int. J. Heat and Mass TransferTramfer*, vol. 52, pp. 460–465, 2009.

Appendix A

Appendix

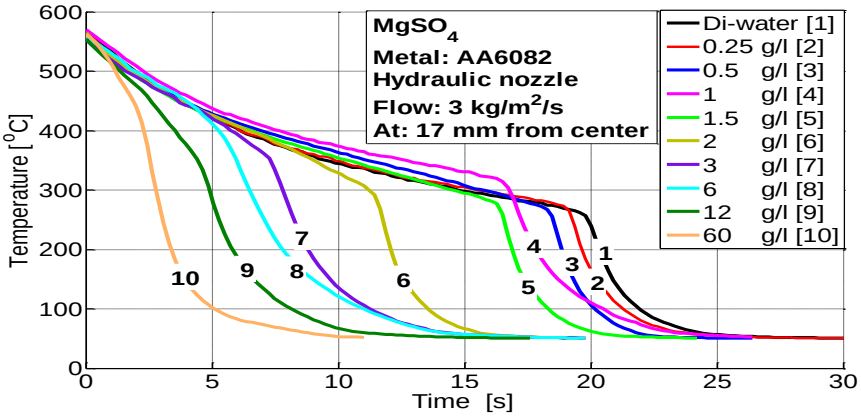

Figure A.1: Temperature profiles for $MgSO_4$ solutions at 17 mm from the center

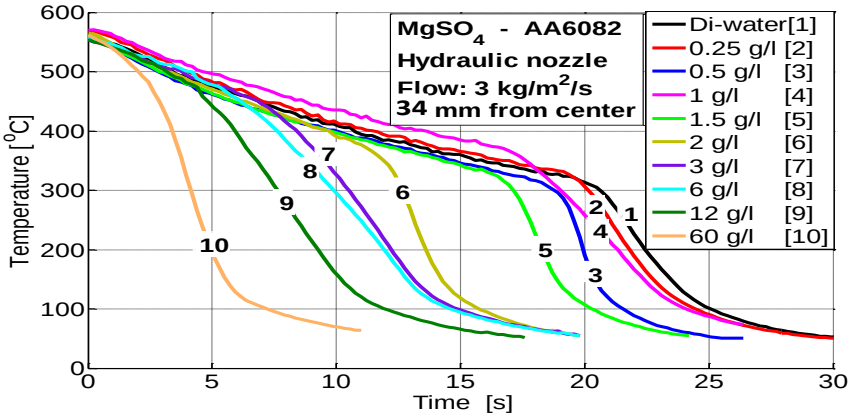

Figure A.2: Temperature profiles for $MgSO_4$ solutions at 34 mm from the center

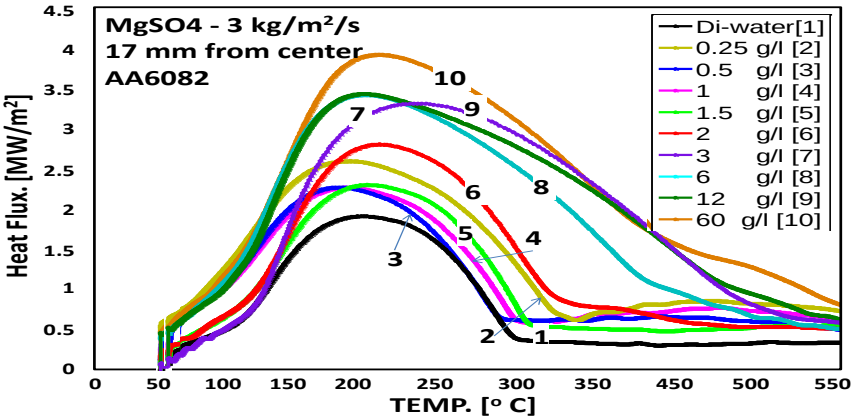

Figure A.3: Relation between heat flux and surface temperature for $MgSO_4$ solutions at 17 mm from the center

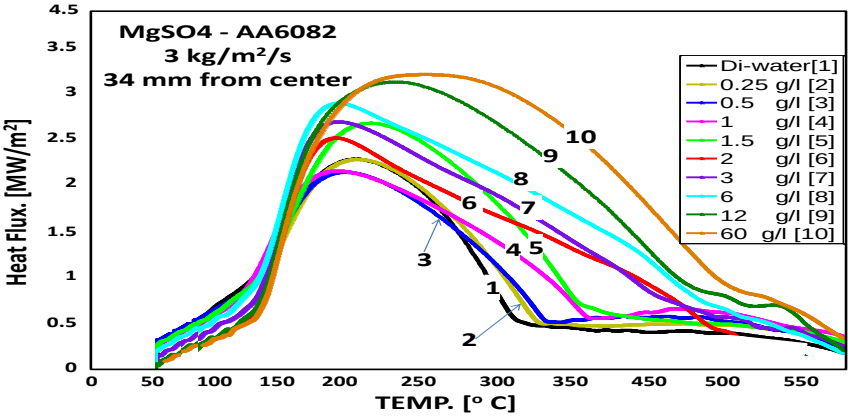

Figure A.4: Relation between heat flux and surface temperature for $MgSO_4$ solutions at 34 mm from the center

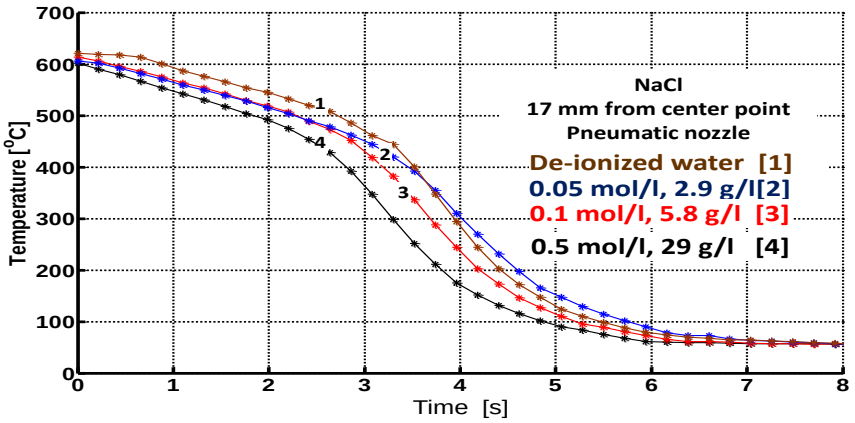

Figure A.5: Temperature profiles for NaCl solutions at 17 mm from the center

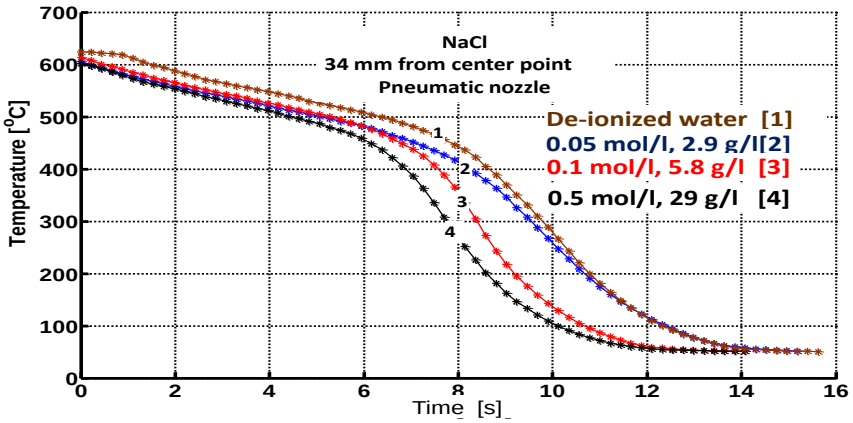

Figure A.6: Temperature profiles for NaCl solutions at 34 mm from the center

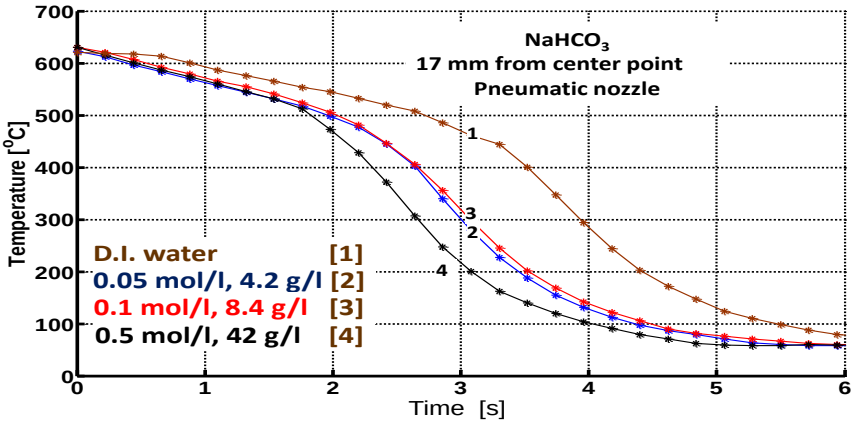

Figure A.7: Temperature profiles for $NaHCO_3$ solutions at 17 mm from the center

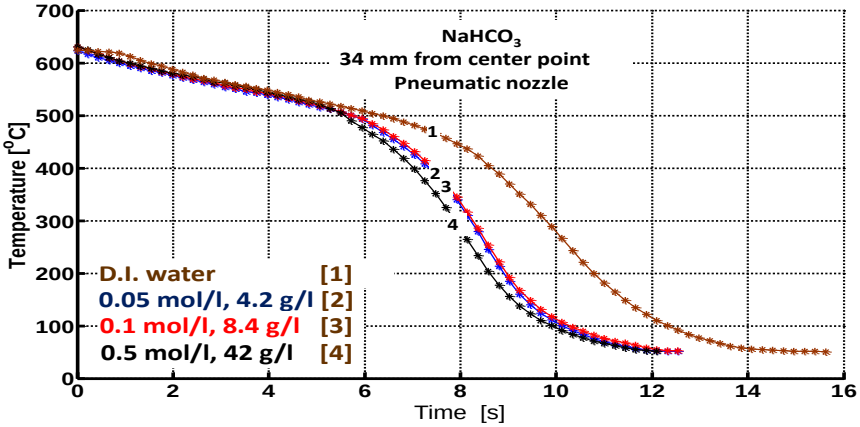

Figure A.8: Temperature profiles for $NaHCO_3$ solutions at 34 mm from the center

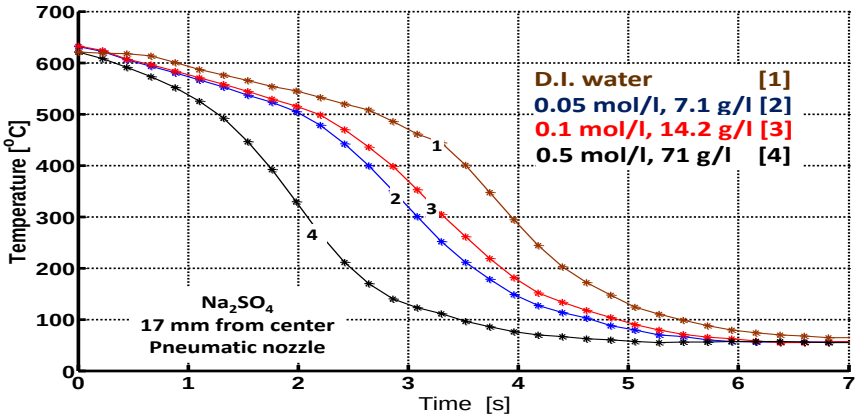

Figure A.9: Temperature profiles for Na_2SO_4 solutions at 17 mm from the center

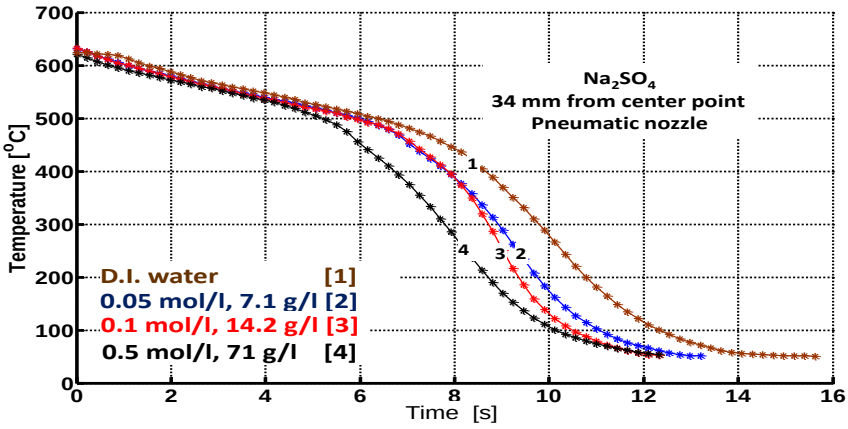

Figure A.10: Temperature profiles for Na_2SO_4 solutions at 34 mm from the center

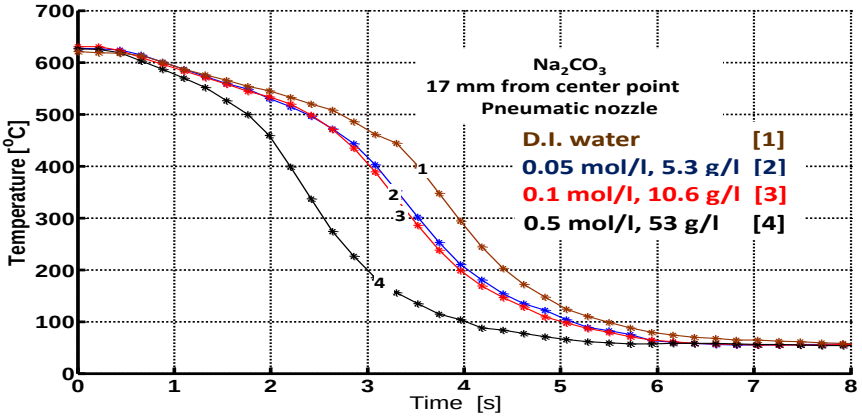

Figure A.11: Temperature profiles for Na_2CO_3 solutions at 17 mm from the center

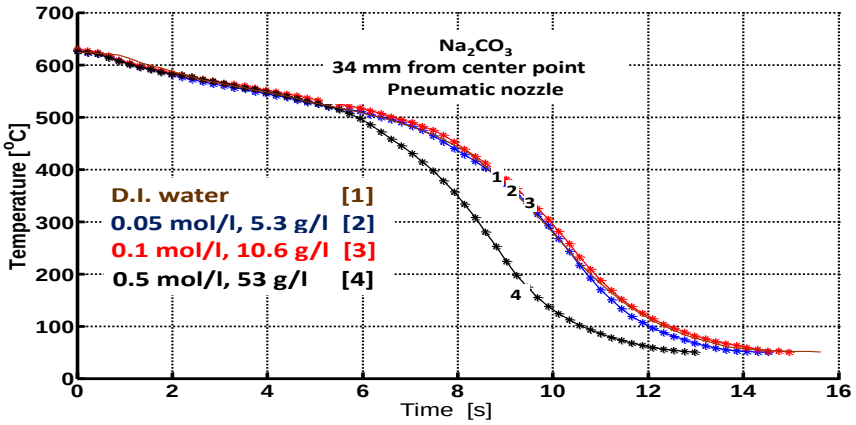

Figure A.12: Temperature profiles for Na_2CO_3 solutions at 34 mm from the center

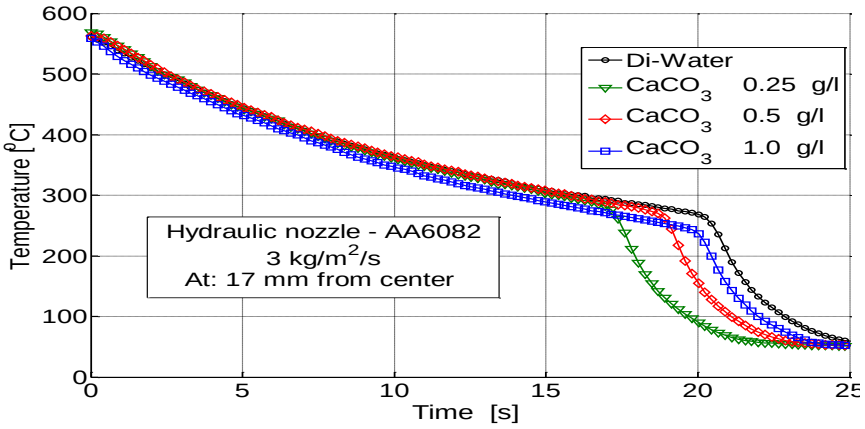

Figure A.13: Temperature profiles for $CaCO_3$ solutions at 17 mm from the center

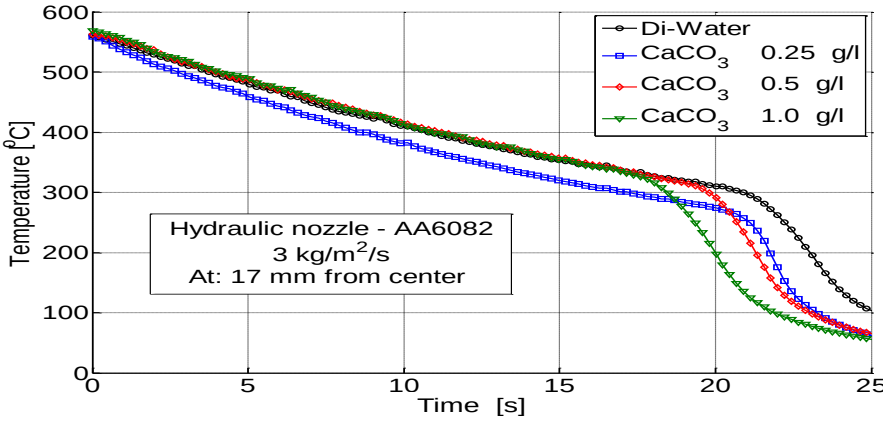

Figure A.14: Temperature profiles for $CaCO_3$ solutions at 34 mm from the center

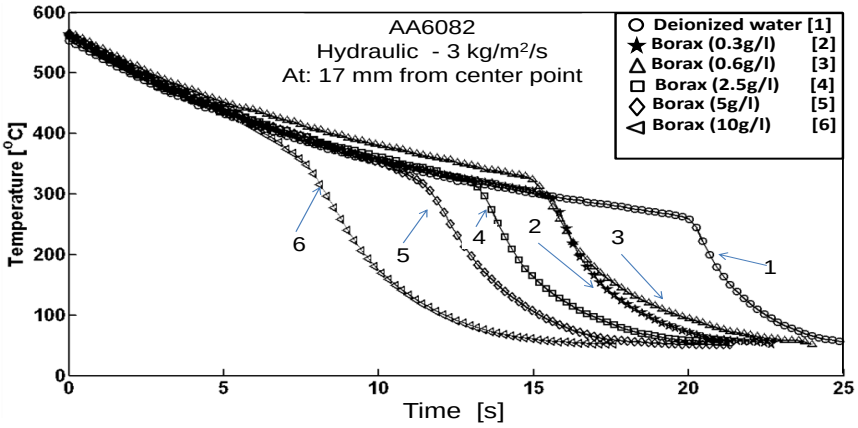

Figure A.15: Temperature profiles for Borax solutions at 17 mm from the center

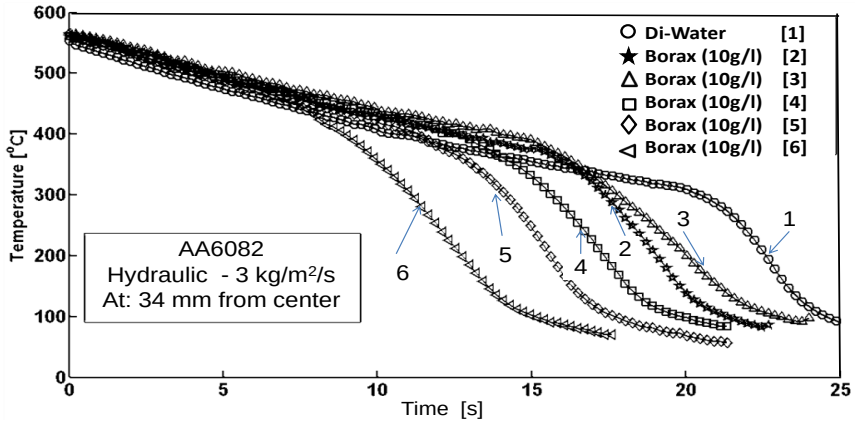

Figure A.16: Temperature profiles for Borax solutions at 34 mm from the center

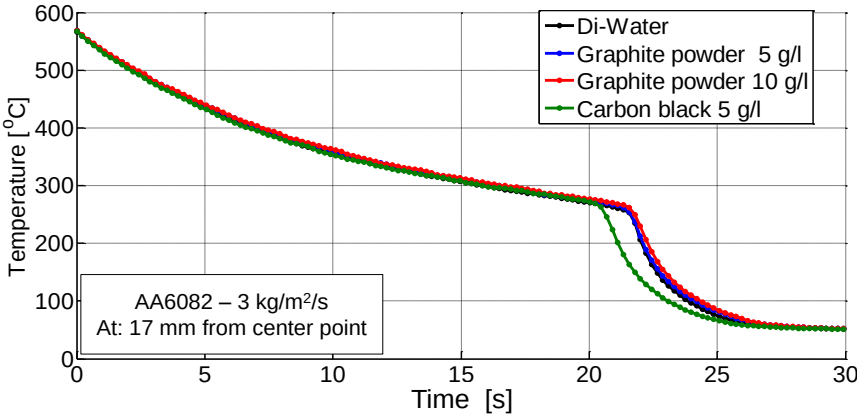

Figure A.17: Temperature profiles for graphite powder and carbon black solutions at 17 mm from the center

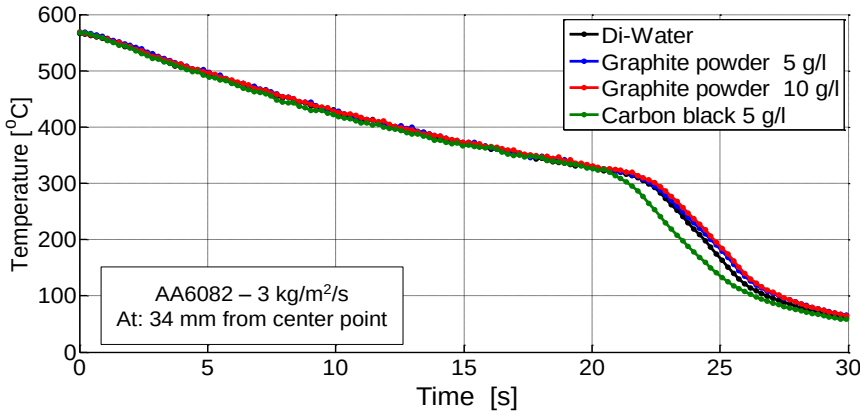

Figure A.18: Temperature profiles for graphite powder and carbon black solutions at 34 mm from the center

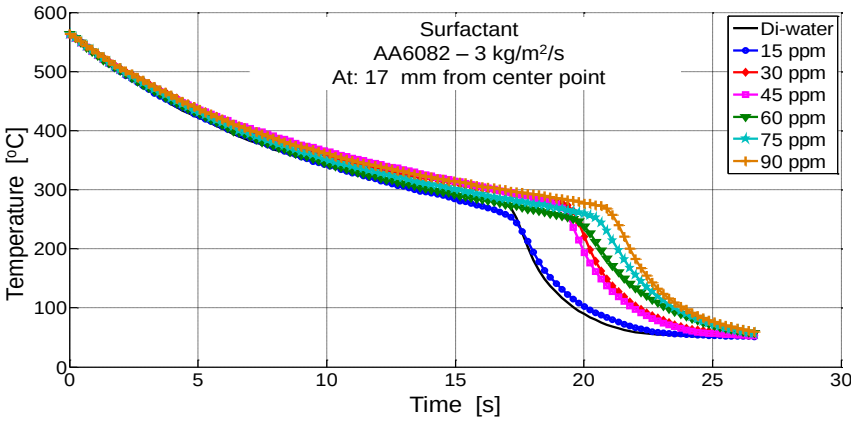

Figure A.19: Temperature profiles for surfactant at 17 mm from the center

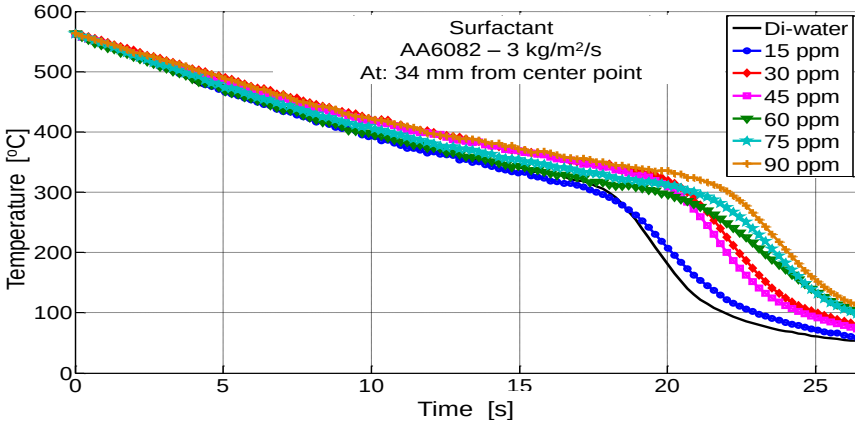

Figure A.20: Temperature profiles for surfactant at 34 mm from the center

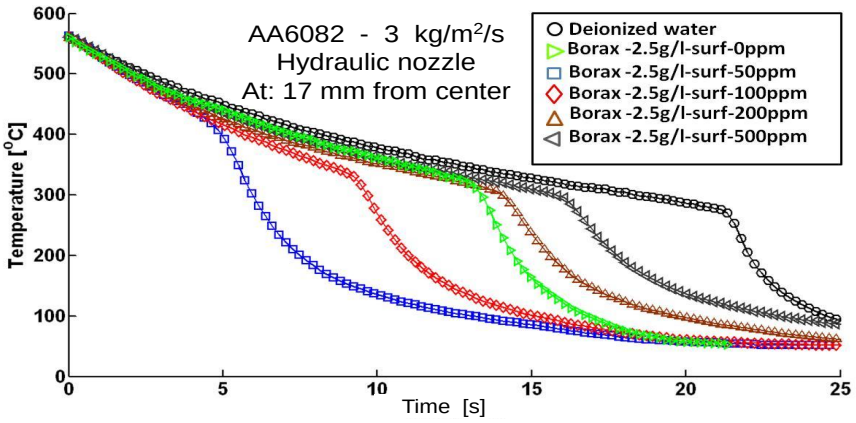

Figure A.21: Temperature profiles for Borax/surfactant mixture at 17 mm from the center [107]

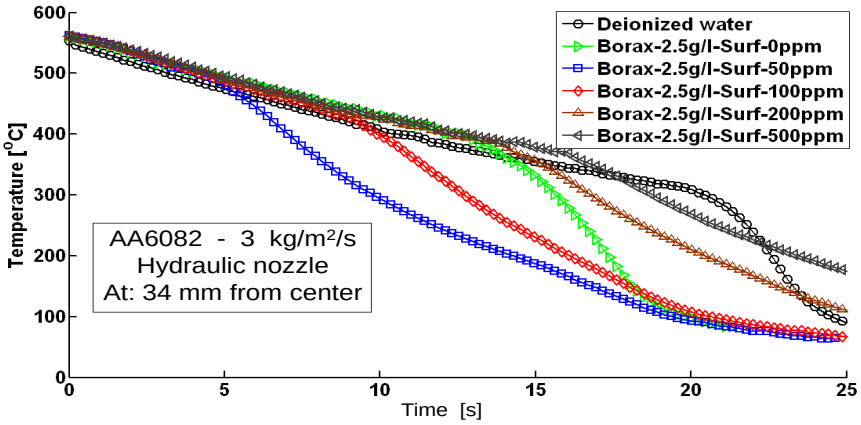

Figure A.22: Temperature profiles for Borax/surfactant mixture at 34 mm from the center [107]

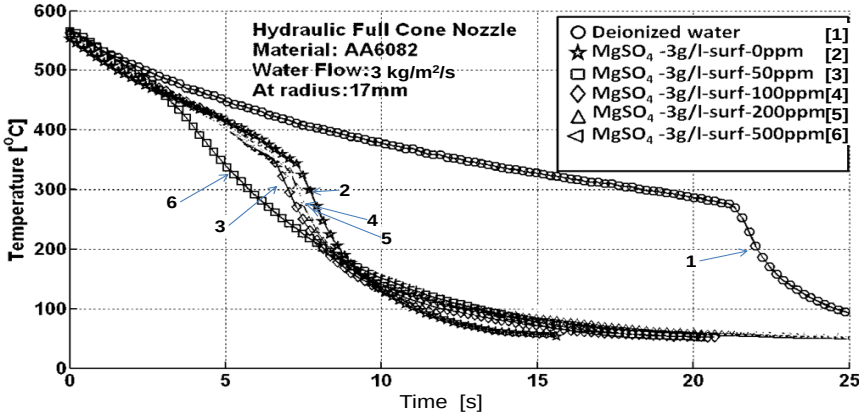

Figure A.23: Temperature profiles for $MgSO_4$/surfactant at 17 mm from the center [107]

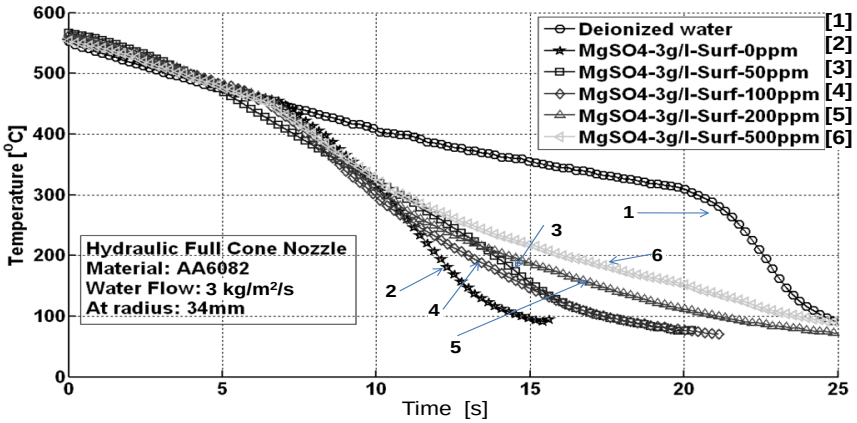

Figure A.24: Temperature profiles for $MgSO_4$/surfactant at 34 mm from the center [107]

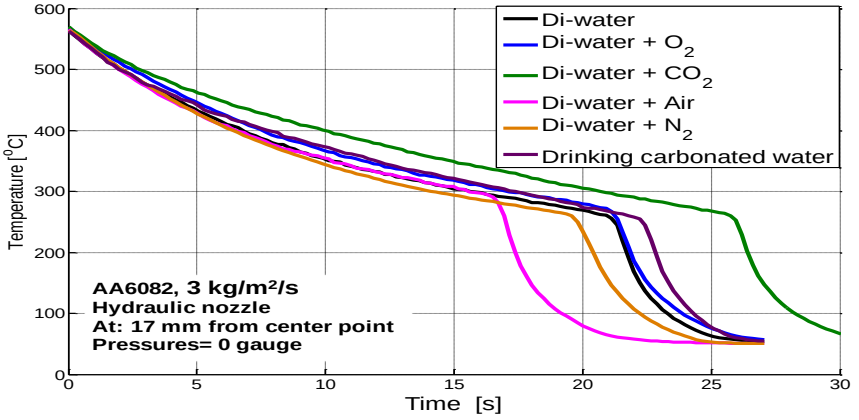

Figure A.25: Temperature profiles for dissolved gases at 17 mm from the center point

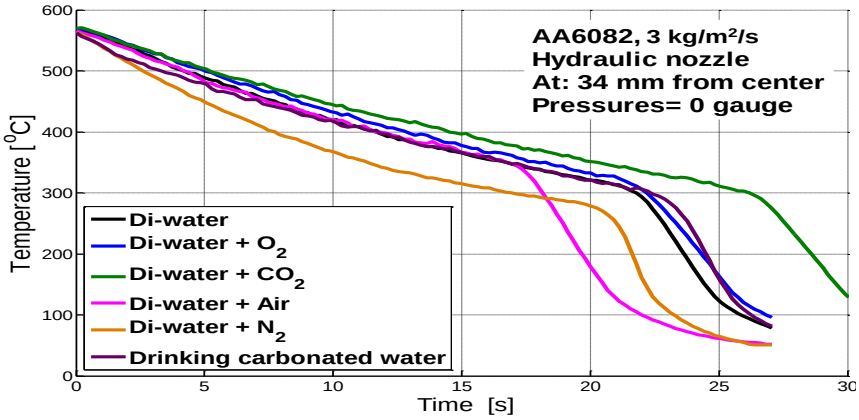

Figure A.26: Temperature profiles for dissolved gases at 34 mm from the center point

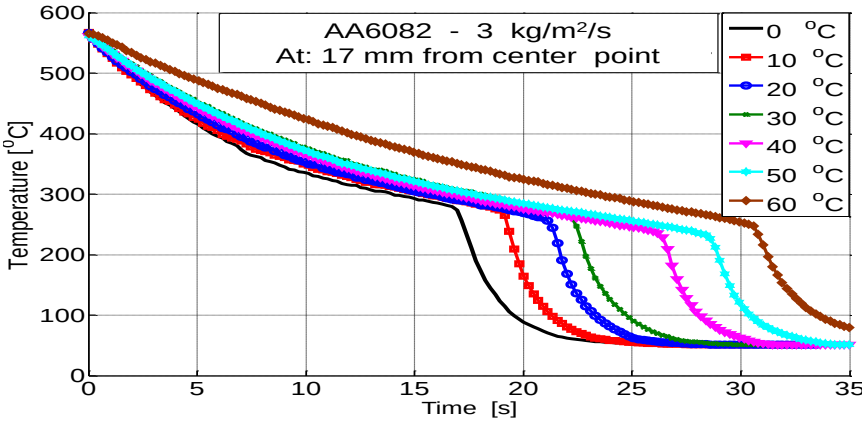

Figure A.27: Temperature profiles for spray water temperature at 17 mm from the center point

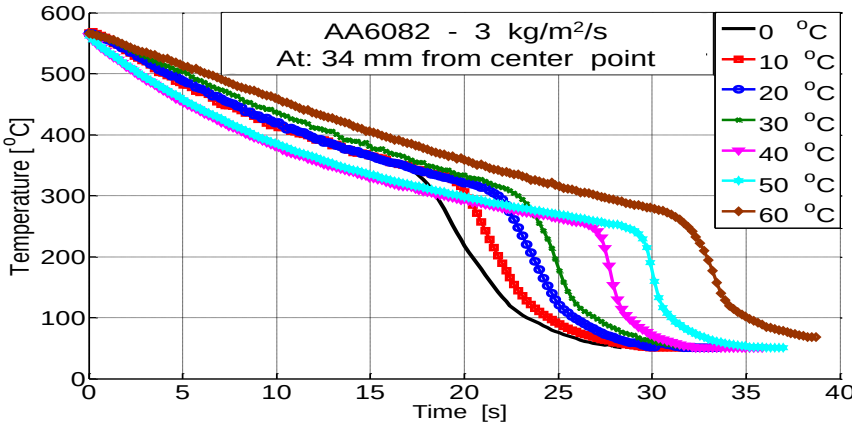

Figure A.28: Temperature profiles for spray water temperature at 34 mm from the center point

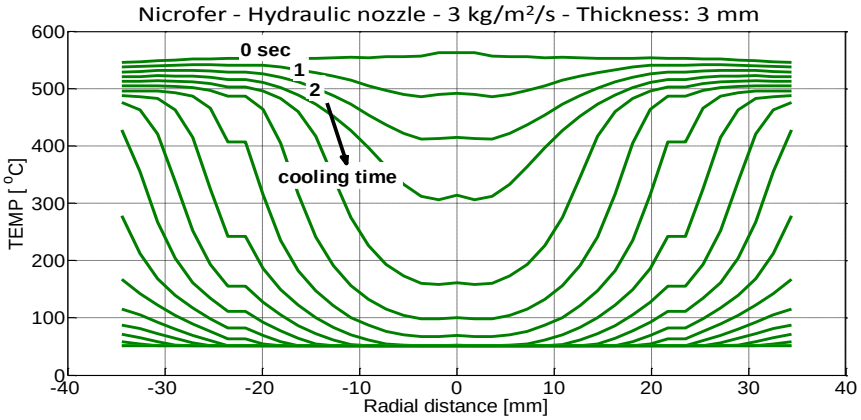

Figure A.29: Temperature distribution along the radial distance for the Nicrofer plate with 2 mm thickness

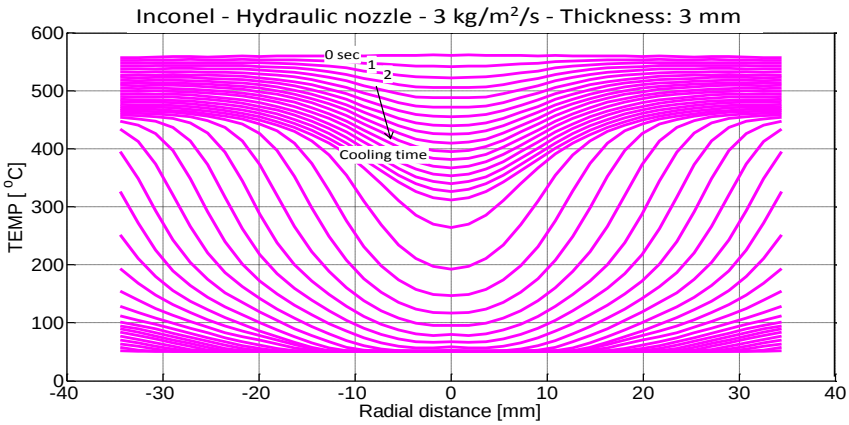

Figure A.30: Temperature distribution along the radial distance for the Inconel plate with 4 mm thickness

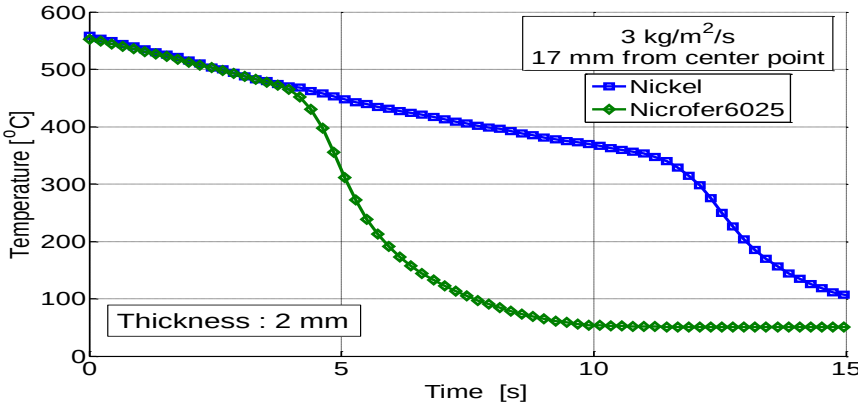

Figure A.31: Temperature profiles of metals with the thickness of 2 mm at 17 mm from center point

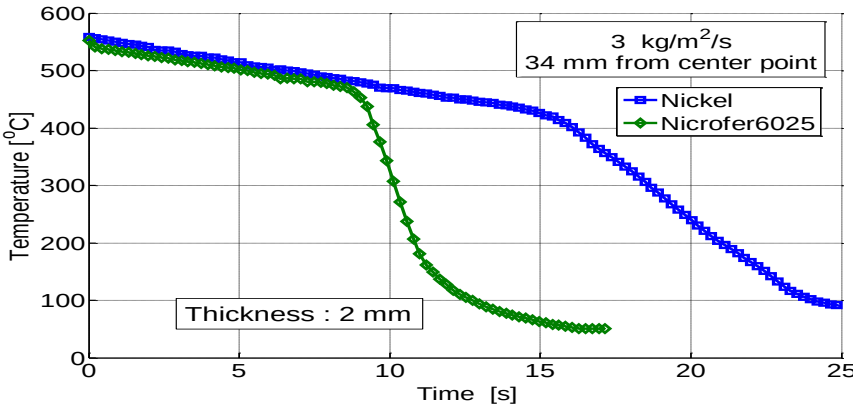

Figure A.32: Temperature profiles of metals with the thickness of 2 mm at 34 mm from center point

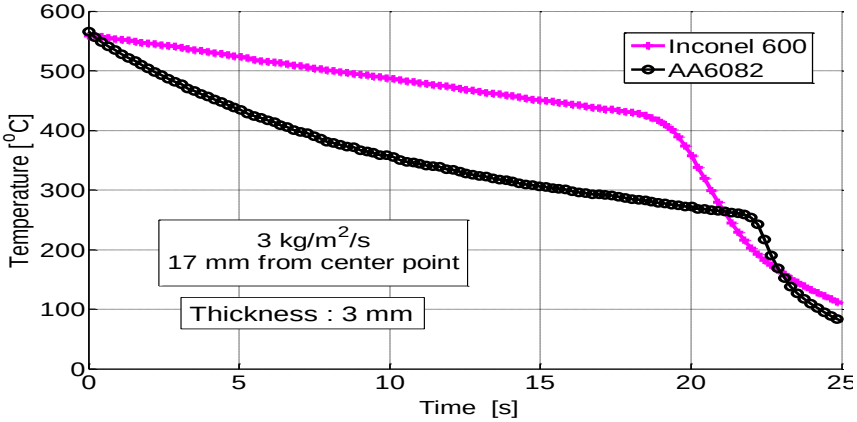

Figure A.33: Temperature profiles of metals with the thickness of 3 mm at 17 mm from center point

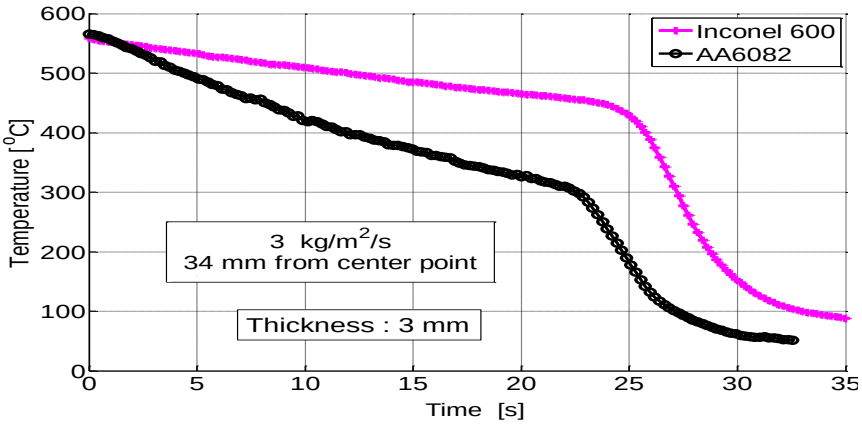

Figure A.34: Temperature profiles of metals with the thickness of 3 mm at 34 mm from center point

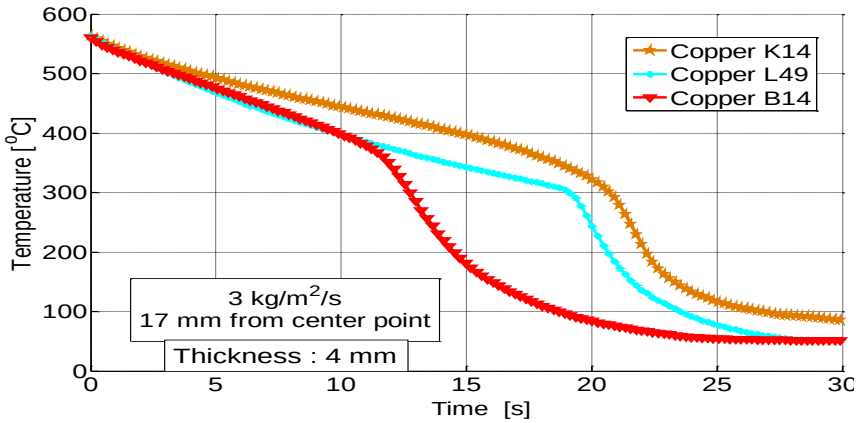

Figure A.35: Temperature profiles of metals with the thickness of 4 mm at 17 mm from center point

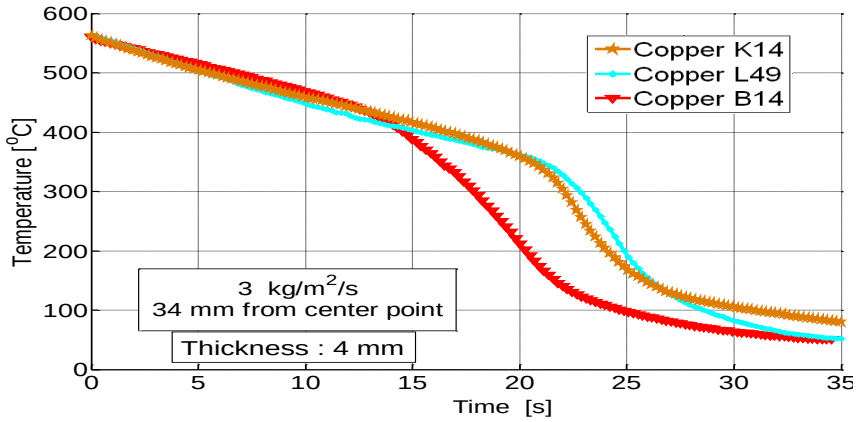

Figure A.36: Temperature profiles of metals with the thickness of 4 mm at 34 mm from center point

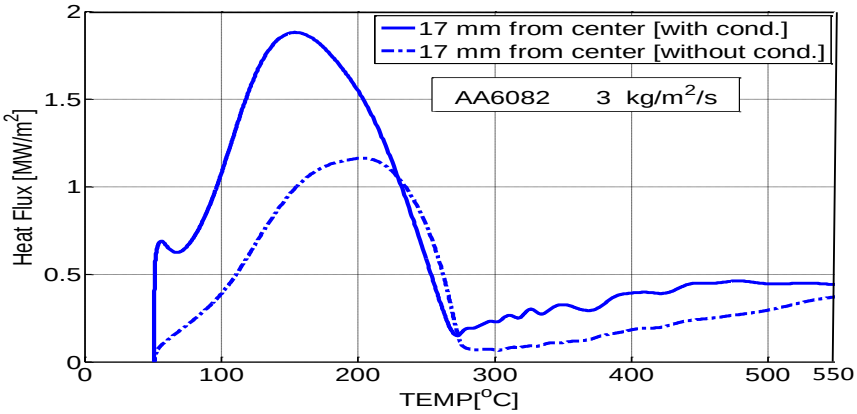

Figure A.37: Heat flux with dependence on the surface temperature for AA6082 at 17 mm from center point

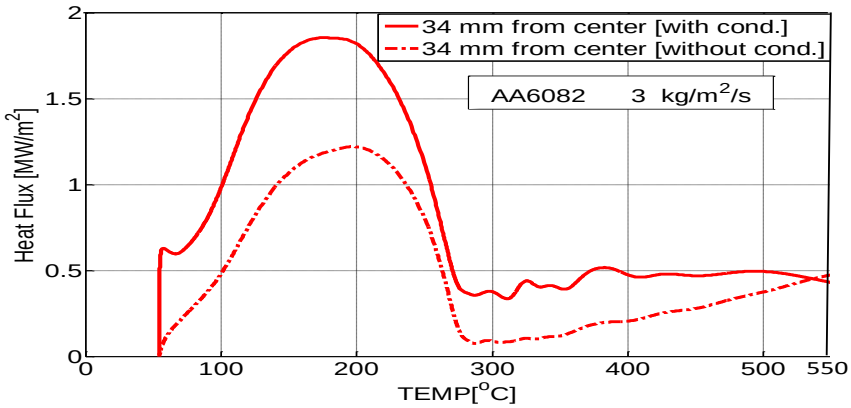

Figure A.38: Heat flux with dependence on the surface temperature for AA6082 at 34 mm from center point

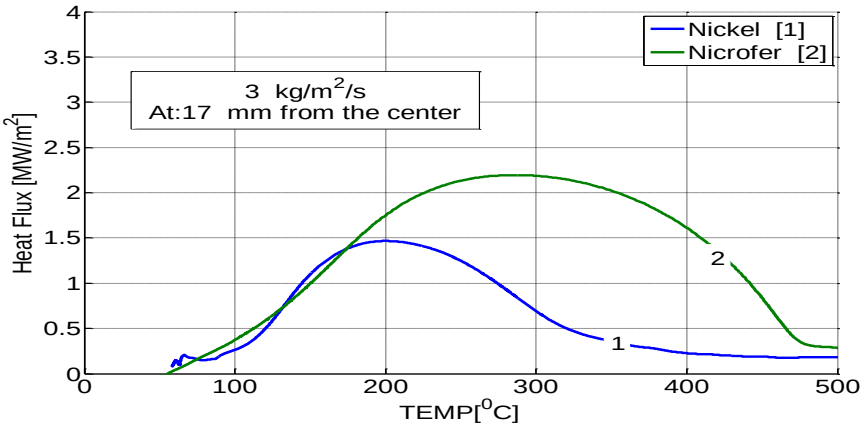

Figure A.39: Heat flux of Nickel and Nicrofer plates with the thickness of 2 mm at 17 mm from center point

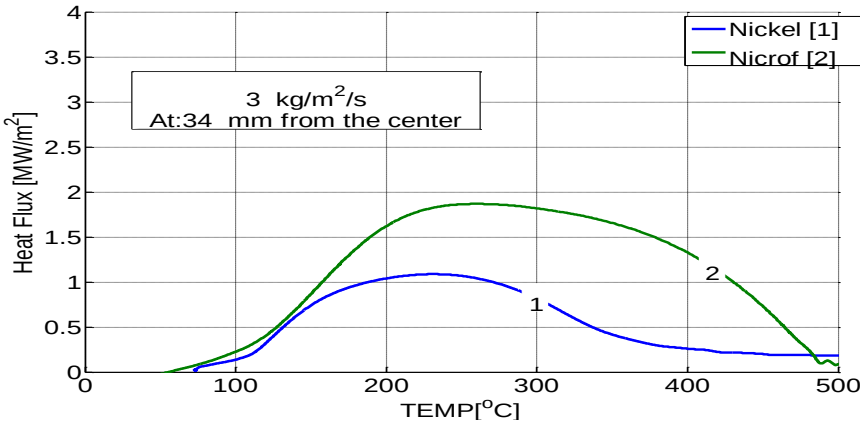

Figure A.40: Heat flux of Nickel and Nicrofer plates with the thickness of 2 mm at 34 mm from center point

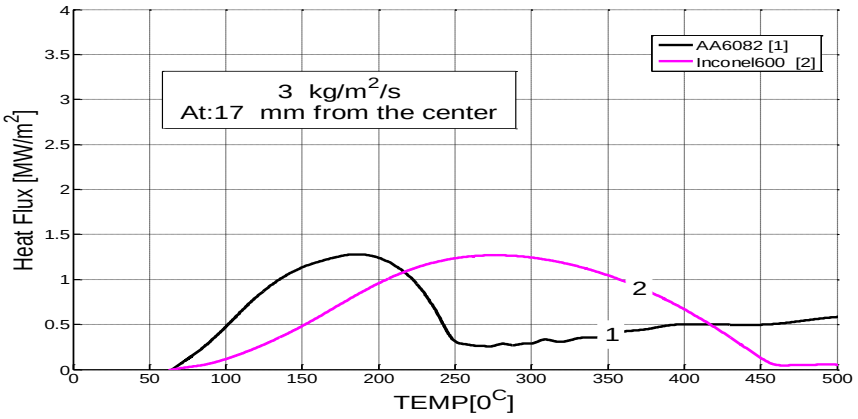

Figure A.41: Heat flux of AA6082 and Inconel plates with the thickness of 3 mm at 17 mm from center point

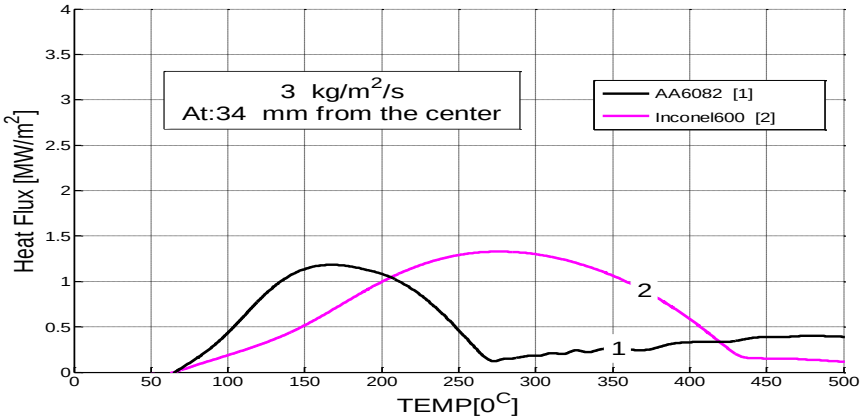

Figure A.42: Heat flux of AA6082 and Inconel plates with the thickness of 3 mm at 34 mm from center point

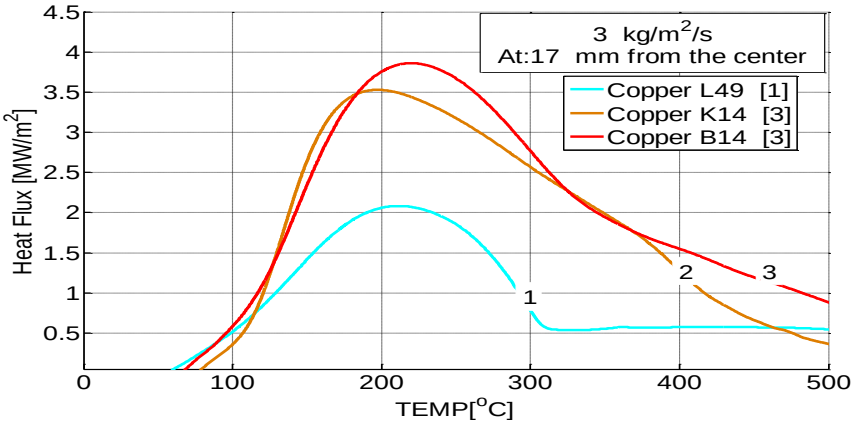

Figure A.43: Heat flux of Copper alloys L49, K14 and B14 with the thickness of 4 mm at 17 mm from center point

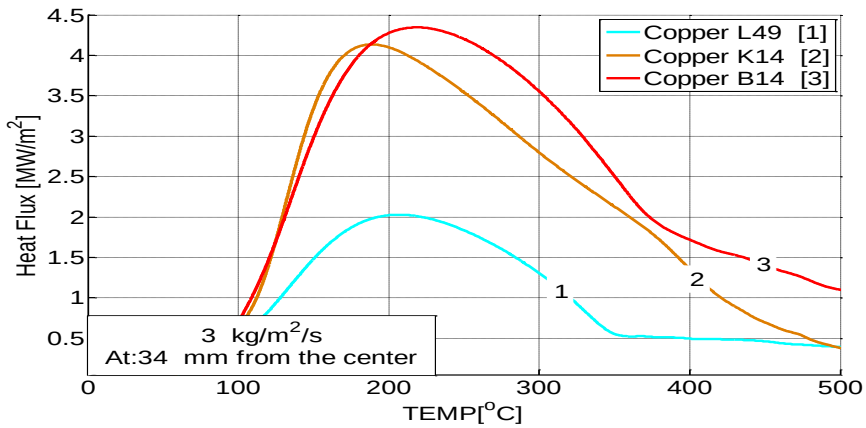

Figure A.44: Heat flux of Copper alloys L49, K14 and B14 with the thickness of 4 mm at 34 mm from center point

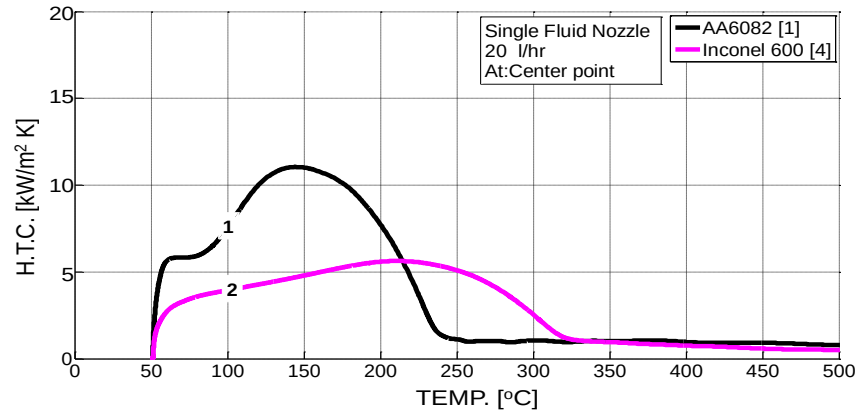

Figure A.45: Heat transfer coefficient of Nickel and Nicrofer at 17 mm from center poin

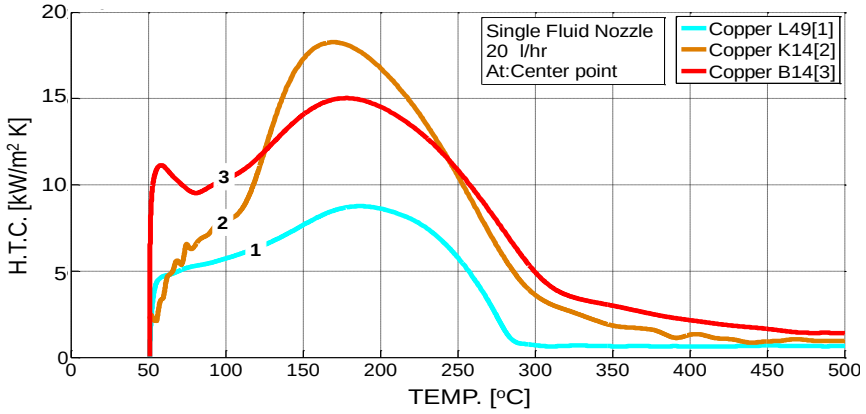

Figure A.46: Heat transfer coefficient of Nickel and Nicrofer at 34 mm from center poin

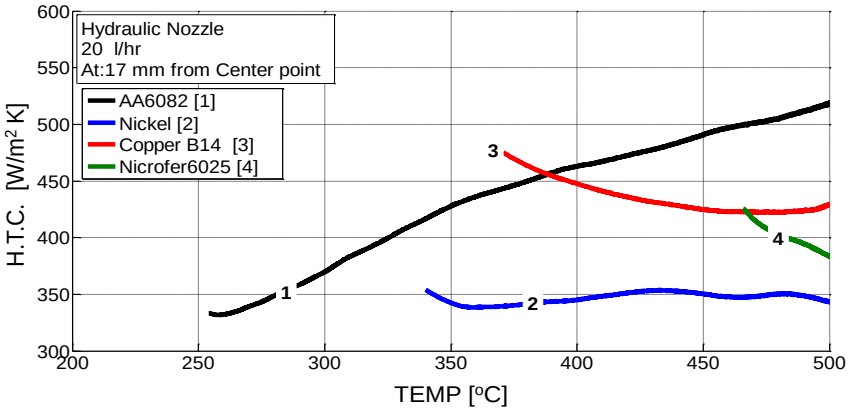

Figure A.47: Heat transfer coefficient in film boiling region of metal plates used at 17 mm from center point

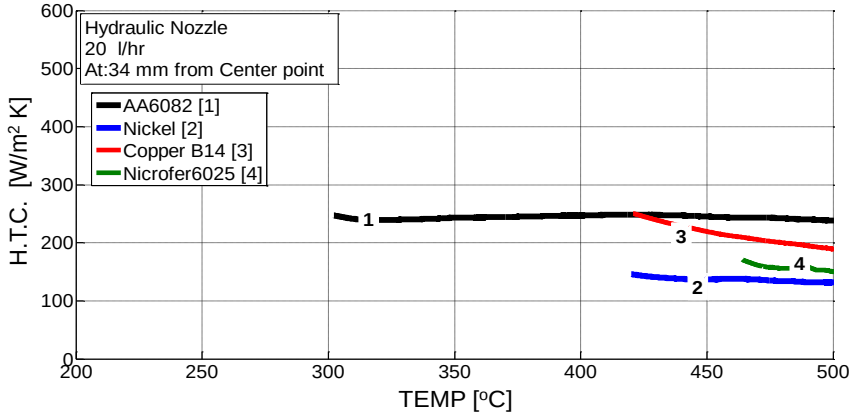

Figure A.48: Heat transfer coefficient in film boiling region of metal plates used at 34 mm from center point

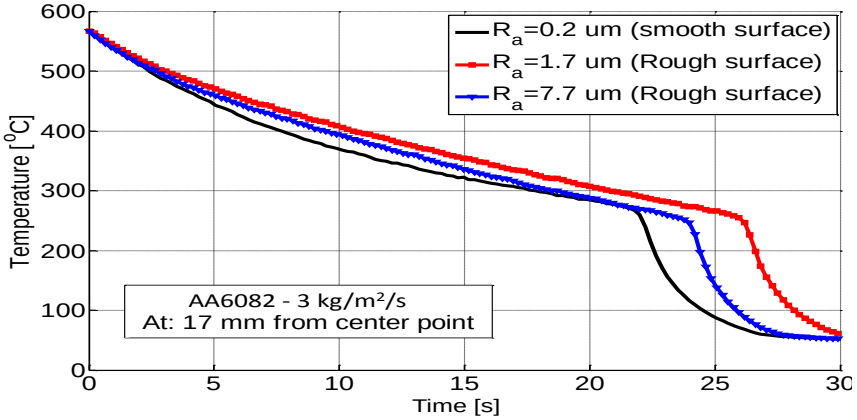

Figure A.49: Temperature profile of rough AA6082 surfaces at 17 mm from center point

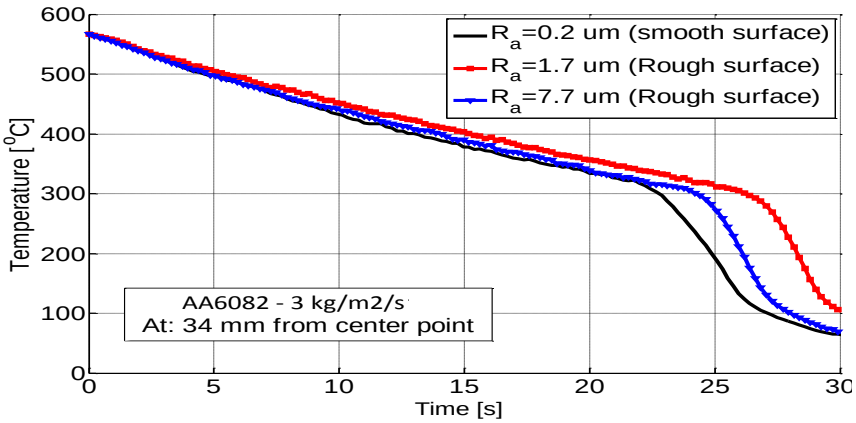

Figure A.50: Temperature profile of rough AA6082 surfaces at 34 mm from center point

Curriculum Vitae

First name	**Khalid Haroun Mohamed**
Family name	**Abdalrahman**
Nationality	Egypt
Date of birth	17–06–1976
Place of birth	Qena, Egypt.
Marital status	Married (2 Daughters)
Email	khharoun@yahoo.com

1994 - 1996	Higher Secondary Certificate, Red Sea, Egypt.
1997 - 2001	Bachelor of Mechanical Engineering, May 2001 (Very good with honor's degree by 82%).
2002 - 2003	Military Service
2004 - 2007	Assistant lecturer in Dept. of Mechanical Power Engineering and Energy , Faculty of Engineering, , Minia University, Egypt.
2004 - 2007	Master of Science in Mechanical Engineering, Egypt 2007.
2008 - 2012	Ph.D student, Institute of Fluid Dynamics and Thermodynamics, Otto von Guericke University, Magdeburg, Germany.

List of Publications

(a) Abdalrahman, Khalid, Alam, U., Nallathambi, A.K., Specht, E.: **"Aluminum quenching by array of water jets"**, 1st Mediterranean conference on heat treatment and surface engineering December 1-3, 2009, Sharm El-Sheikh, Egypt.

(b) Abdalrahman, Khalid, Alam, U., Specht, E.: **"Wetting front tracking during metal quenching using array of jets"**, 2010 14th International Heat Transfer Conference, IHTC14, pp. 475-484.

(c) Alam, U.,Abdalrahman, Khalid, Specht, E.: **"Experimental investigation of influence of dissolved salts and surfactant on heat transfer in atomized spray quenching of metal"**, 2010 14th International Heat Transfer Conference, IHTC14, pp. 779-786.

(d) Specht, E., Alam, U.,Abdalrahman, Khalid: **"Influence of quality of water on the heat transfer in secondary cooling zone during continuous casting"**, Symposium Stranggiessen, November 15-17 2010, Neu Ulm Germany.